ENGINEERING OF CATHODE MATERIALS FOR SODIUM-ION BATTERIES

Ph.D. Thesis

By

JENA AKASH KUMAR SATRUGHNA

DEPARTMENT OF PHYSICS

INDIAN INSTITUTE OF TECHNOLOGY INDORE

AUGUST 2025

ENGINEERING OF CATHODE MATERIALS FOR SODIUM-ION BATTERIES

A THESIS

Submitted in partial fulfillment of the
requirements for the award of the degree
of
DOCTOR OF PHILOSOPHY

by

JENA AKASH KUMAR SATRUGHNA

DEPARTMENT OF PHYSICS
INDIAN INSTITUTE OF TECHNOLOGY INDORE
AUGUST 2025

INDIAN INSTITUTE OF TECHNOLOGY INDORE

CANDIDATE'S DECLARATION

I hereby certify that the work which is being presented in the thesis entitled **"ENGINEERING OF CATHODE MATERIALS FOR SODIUM-ION BATTERIES"** in the partial fulfillment of the requirements for the award of the degree of **DOCTOR OF PHILOSOPHY** and submitted in the **DEPARTMENT OF PHYSICS, Indian Institute of Technology Indore**, is an authentic record of my own work carried out during the time period from August 2020 to August 2025 under the supervision of Dr. Parasharam M. Shirage, Professor, Department of Metallurgical Engineering and Materials Science and Dr. Preeti A. Bhobe, Professor, Department of Physics, Indian Institute of Technology Indore.

The matter presented in this thesis has not been submitted by me for the award of any other degree of this or any other institute.

Akash Kumar Jena

11/10/2025

Signature of the student with date

JENA AKASH KUMAR SATRUGHNA

This is to certify that the above statement made by the candidate is correct to the best of our knowledge.

13/10/2025

Signature of Thesis Supervisor with date

Prof. (Dr.) PARASHARAM M. SHIRAGE

13/10/2025

Signature of Administrative Supervisor with date

Prof. (Dr.) PREETI A. BHOBE

JENA AKASH KUMAR SATRUGHNA has successfully given his Ph.D. Oral Examination held on **10th October 2025**.

13/10/2025

Signature of Thesis Supervisor with date

Prof. (Dr.) PARASHARAM M. SHIRAGE

13/10/2025

Signature of Administrative Supervisor with date

Prof. (Dr.) PREETI A. BHOBE

ACKNOWLEDGEMENTS

First and foremost, I express my sincere and profound gratitude to my thesis supervisor, **Prof. Dr. Parasharam M. Shirage**, Professor, Department of Metallurgical Engineering and Materials Science, Indian Institute of Technology Indore (IIT Indore). His exceptional guidance, visionary supervision, invaluable mentorship, and unfaltering support have been the foundation of my Ph.D. journey and the completion of this thesis work. I am deeply indebted to him for his patient counsel, unceasing encouragement, critical insights, and for generously investing his valuable time and expertise to refine and shape my research work. His solid passion for research has been an enduring source of motivation for me to strive for excellence throughout this research work.

My sincere gratitude to my administrative supervisor, **Prof. Dr. Preeti A. Bhobe**, Professor, Department of Physics, IIT Indore, for her incessant support in managing the administrative matters. Her constant advice, encouragement, and unwavering support have been instrumental throughout my Ph.D. journey.

I extend my heartfelt gratitude to my PG Student Progress Committee (PSPC) members **Prof. Dr. Rupesh R. Devan**, Professor, Department of Metallurgical Engineering and Materials Science, IIT Indore, and **Prof. Dr. Krushna R. Mavani**, Professor, Department of Physics, IIT Indore for their diligent evaluation, perceptive advices, and valuable suggestions for my research work that profoundly improved the quality and clarity of my research.

I sincerely thank the current director, **Prof. Suhash S. Joshi**, and the founding director, **Prof. Pradeep Mathur**, for enriching the research environment at IIT Indore. I am thankful to the Department of Physics, Department of Metallurgical Engineering and Materials Science, and Sophisticated Instrumentation Centre (SIC) at IIT Indore for providing access to the experimental facilities. I am thankful to the technical and academic staff for their invaluable assistance in technical and non-technical matters.

I am thankful to the **Department of Science and Technology (DST)** of the Government of India for providing me the financial support through DST **INSPIRE fellowship (Fellowship ID. IF190546)** to carry out my research work.

I would like to express my sincere thanks to my international collaborators **Dr. Yuta Ito, Dr. Atsushi Ogura, Dr. Hyunju Lee** (Meiji University, Kawasaki, Japan), **Dr. Yoshio Ohshita** (Toyota Technological Institute Nagoya, Japan), **Dr. Sawanta S. Mali**, **Jyoti V. Patil**, **Dr. Chang Kook Hong** (Chonnam National University, South Korea) for their valuable collaborations and for providing XPS, Raman, and HRTEM instrumental facilities.

I am truly blessed to have shared this Ph.D. journey with my collaborators and colleagues from the Advanced Functional Materials Research Group (AFMRG), Dr. Subhash Chand Yadav, Dr. Manish Kumar Tiwari, Archana R. Kanwade, Abhishek Srivastava, Shraddhha M. Rajore, and Anushka Singh. Their continuous support, stimulating discussions, and inspiration have greatly enriched both my personal and professional efficiency.

Finally, I owe my heartfelt appreciation to my parents and siblings, whose continuous support, boundless love, enduring patience, inspiration, and steadfast belief in my dreams have been my real strength and may not be completely expressed in words. My sincere gratitude to my companion, Subhasini Sahoo, whose unwavering patience, unfaltering belief, and selfless care have been instrumental throughout my research journey. I also extend my heartfelt gratitude to my friends whose companionship and support are invaluable.

Date: 5th August 2025 **Jena Akash Kumar Satrughna**

DEDICATED TO

MY BELOVED FAMILY

&

ALL WELL-WISHERS

ABSTRACT

The continuously increasing worldwide demand for cost-efficient, eco-friendly, and sustainable energy storage devices has driven the search beyond traditional lithium-ion batteries. Among several energy storage systems, sodium-ion batteries have become a potential candidate due to the natural availability, abundant supply, and affordable nature of sodium resources, together with similar electrochemistry to lithium-ion batteries. Though these have the advantages listed, sodium-ion batteries are hindered by critical issues due to the larger ionic radius and increased molar mass of Na^+ ion, leading to phase instability, slow diffusion kinetics, and lower energy density. Here, the cathode material is the most critical ingredient as it determines the overall capacity, operating voltage, energy density, and cycle life performance of the battery. The current thesis is dedicated to engineering, optimization, and thorough assessment of several cathode materials for sodium-ion batteries through tailoring structure, substituting elements, and defect engineering.

Systematic studies were conducted on polyanionic, layered, and tunnel-structured cathode materials. Sodium-deficient polyanionic $Na_{0.8}Fe(SO_4)_2$ exhibited enhanced Na^+ ion mobility and improved cycling stability. High crystalline and phase-pure $NaCoO_2$ exhibited a discharge capacity as high as 155.85 mAh/g and a high energy density of 466 Wh/kg at 0.1C. Multi-transition-metal co-substitution in $Na_xCo_{0.5}Fe_{0.25}Mn_{0.25}O_2$

stabilized the layered structure, suppressed irreversible phase transitions, and offered long cycle life. In addition, chromium-based systems, such as $Na_{1.35}CrO_4$ and tunnel-structured $Na_4Mn_{7.2}Cr_{1.8}O_{18,}$ were investigated for sodium-ion batteries. The partial substitution of Jahn-Teller inactive Cr^{3+} in $Na_4Mn_{7.2}Cr_{1.8}O_{18}$ cathode reduced the Jahn-Teller distortion effect of Mn^{3+}. These approaches led to enhanced Na^+ ion diffusion channels, redox stability, enhanced cycling stability, and better electrochemical performance.

Systematic characterization of the above cathode materials through sophisticated physicochemical and electrochemical techniques revealed significant correlations between crystal structure, oxidation states, ion diffusion, and electrochemical performance. The findings emphasized the fundamental role of sodium deficiency, synthesis condition optimization, element substitution, and tunnel-structure stabilization towards capacity retention and energy density.

Overall, this doctoral thesis provides new insights into the sodium-ion battery by proving feasible methods for adjusting the structure-property correlation of the cathode materials. The results not only progress the understanding of electrochemical phenomena in polyanionic, layered, and tunnel structures but also offer effective routes to design high-capacity, energy-efficient, and long-cycle-life cathodes. These advances unlock the possibilities for the realization of sodium-ion batteries as a green power source in the case of large-scale energy storage.

LIST OF PUBLICATIONS
(From the Thesis Work)

[1]. J. A. K. Satrughna, A. R. Kanwade, S. M. Rajore, M. K. Tiwari, Y. Ito, A. Ogura, H. Lee, Y. Ohshita, P. M. Shirage, Sol-gel based synthesis of high-capacity-$NaCoO_2$ cathode for advanced sodium-ion batteries, *Electrochim. Acta*, 2024, 507, 145201. **(IF: 5.6)**
DOI: https://doi.org/10.1016/j.electacta.2024.145201

[2]. J A K Satrughna, A R Kanwade, S M Rajore, M K Tiwari, Y Ito, A Ogura, H Lee, Y Ohshita, S S Mali, J V Patil, C K Hong, P M Shirage, Unveiling the physicochemical and electrochemical features of sodium deficient-$Na_{0.8}Fe(SO_4)_2$ as cathode for sodium-ion batteries, *Next Res.,* 2025, 2, 100210. DOI: https://doi.org/10.1016/j.nexres.2025.100210

[3]. J. A. K. Satrughna, A. R. Kanwade, P. M. Shirage, Synergistic effect of multi-transition metal co-substitution in high cycle life performance of $Na_xCo_{0.5}Fe_{0.25}Mn_{0.25}O_2$ cathode for sodium-ion batteries, *Sustain. Energy Fuels,* 2025, 9, 3354-3373. **(IF: 4.1)**
DOI: https://doi.org/10.1039/D5SE00107B

[4]. J. A. K. Satrughna, A. R. Kanwade, S. M. Rajore, P. M. Shirage, Exploring the characteristics of $Na_{1.35}CrO_4$ as active electrode for energy storage application in sodium-ion batteries, *Phys. Status Solidi-Rapid Res. Lett.,* 2025, 2500079. **(IF: 2.0)**
DOI: https://doi.org/10.1002/pssr.202500079

[5]. J. A. K. Satrughna, A. R. Kanwade, S. M. Rajore, P. M. Shirage, Tunnel-structure $Na_4Mn_{7.2}Cr_{1.8}O_{18}$ metal oxide as a potential cathode for energy storage application in sodium-ion batteries, *ACS Appl. Energy Mater.,* 2025. **(IF: 5.5)** DOI: https://doi.org/10.1021/acsaem.5c01281

LIST OF PUBLICATIONS

(Other than thesis work)

1. A. Kanwade, S. Gupta, A. Kankane, M. K. Tiwari, A. Srivastava, **J. A. K. Satrughna**, S. C.Yadav, P. M. Shirage, Transition metal oxides as a cathode for indispensable Na-ion batteries, *RSC Adv.,* 2022, 12, 23284-23310. **(IF: 4.6)**
   DOI: https://doi.org/10.1039/D2RA03601K
2. M. K. Tiwari, S. C. Yadav, A. Srivastava, A. R. Kanwade, **J. A. K. Satrughna**, S. S. Mali, J. V. Patil, C. K. Hong, and P. M. Shirage, Enhancement of CO gas sensing performance by Mn-doped porous $ZnSnO_3$ microspheres, *RSC Adv.*, 2022, 12, 32249–32261. **(IF = 4.6)** DOI: https://doi.org/10.1039/D2RA06785D
3. A. Srivastava, B. S. Chauhan, S. C. Yadav, M. K. Tiwari, **J. A. K. Satrughna**, A. Kanwade, K. Bala, and P. M. Shirage, Performance of dye-sensitized solar cells by utilizing Codiaeum Variegatum Leaf and Delonix Regia Flower as natural sensitizers, *Chem. Phys. Lett.*, 2022, 807, 140087. **(IF = 3.1)**
   DOI: https://doi.org/10.1016/j.cplett.2022.140087
4. A. Srivastava, **J. A. K. Satrughna**, M. K. Tiwari, A. Kanwade, S. C. Yadav, K. Bala, P. M. Shirage, Effect of $Ti_{1-x}Fe_xO_2$ photoanodes on the performance of dye-sensitized solar cells utilizing natural betalain pigments extracted from Beta vulgaris (BV), *Energy Adv.*, 2023, 2, 148–160. **(IF=4.3)**
   DOI: https://doi.org/10.1039/D2YA00197G
5. M. K. Tiwari, A. R. Kanwade, S. C. Yadav, A. Srivastava, **J. A. K. Satrughna**, and P. M. Shirage, NASICON-type $Na_3Fe_2(PO_4)_3$ material for an excellent room temperature CO sensor, *J. Mater. Chem. C*, 2023, 11, 5469-5480. **(IF = 5.1)**
   DOI: https://doi.org/10.1039/D3TC00300K

6. M. K. Tiwari, S. C. Yadav, A. Kanwade, **J. A. K. Satrughna**, S. M. Rajore and P. M. Shirage, Advancements in lanthanide-based perovskite oxide semiconductors for gas sensing applications: a focus on doping effects and development, *Anal. Methods*, 2023, 15, 5754-5787. **(IF = 2.6)** DOI: https://doi.org/10.1039/D3AY01420G
7. A. S. Teja, A. Srivastava, **J. A. K. Satrughna**, M. K. Tiwari, A. Kanwade, S. C. Yadav and P. M. Shirage, Optimal processing methodology for futuristic natural dye-sensitized solar cells and novel applications, *Dye. Pigment.,* 2023, 210, 110997. **(IF= 4.2)** DOI: https://doi.org/10.1016/j.dyepig.2022.110997
8. A. Srivastava, **J. A. K. Satrughna**, M. K. Tiwari, A. Kanwade, S. C. Yadav, K. Bala and P. M. Shirage, Lead metal halide perovskite solar cells: Fabrication, advancement strategies, alternatives, and future perspectives, *Mater. Today Commun.*, 2023, 35, 105686. **(IF = 4.5)** DOI: https://doi.org/10.1016/j.mtcomm.2023.105686
9. A S Teja, A Srivastava, **J A K Satrughna**, M K Tiwari, A Kanwade, H Lee, A Ogura, and P M Shirage, Synergistic co-sensitization of environment-friendly chlorophyll and anthocyanin-based natural dye-sensitized solar cells: An effective approach towards enhanced efficiency and stability, *Solar Energy*, 2023, 261, 112-124. **(IF = 6.6)** DOI: https://doi.org/10.1016/j.solener.2023.06.004
10. A. S. Shaikh, S. C. Yadav, A. Srivastava, A. Kanwade, M. K. Tiwari, S. M. Rajore, **J. A. K. Satrughna**, M. Dhonde, and P. M. Shirage, Dynamic synergy of tin in the electron-transfer layer and absorber layer for advancing perovskite solar cells: a comprehensive review, *Energy Adv.*, 2024, 3, 1505-1552. **(IF = 4.3)** DOI: https://doi.org/10.1039/D4YA00204K
11. A. R. Kanwade, **A. K. Satrughna Jena**, S. M. Rajore, S. S. Mali, J. V. Patil, C. K. Hong, P. M. Shirage, Revealing the potential of graphene-embedded $Na_3Fe_2(PO_4)_3$ for enhanced sodium-ion battery performance, *J. Mat. Sci.,* 2024, 59, 8956-8972. **(IF = 3.9)**

DOI: https://doi.org/10.1007/s10853-024-09698-y

12. M. K. Tiwari**,** A. R. Kanwade, S. M. Rajore, **J. A. K. Satrughna**, H. Lee, Y. Ohshita, A. Ogura, S. S. Mali, J. V. Patil, C. K. Hong, and P. M. Shirage, $W_{18}O_{49}$ Nanofibers Functionalized with Graphene as a Selective Sensing of NO_2 gas at Room Temperature, *ACS Appl. Mater. Interfaces*, 2024, 16, 49520-49532. **(IF = 8.2)** DOI: https://doi.org/10.1021/acsami.4c10014
13. S M Rajore, A R Kanwade, **J A K Satrughna**, M K Tiwari**,** and P M Shirage, A comprehensive review on advancements in catalysts for aluminum-air batteries, *J. Power Sources,* 2024, 616, 235101. **(IF = 7.9)** DOI: https://doi.org/10.1016/j.jpowsour.2024.235101
14. A S Shaikh, A R Kanwade, **J A K Satrughna**, M K Tiwari, S M Rajore, S C Yadav, Y Ito, H Lee, Y Ohshita, A Ogura, P M Shirage, Ambient condition synthesis of $Cs_2AgBiBr_6$-double perovskite and its solar cell performances, *J. Power Sources,* 2025, 65, 23771. **(IF = 7.9)** DOI: https://doi.org/10.1016/j.jpowsour.2025.237717
15. A. R. Kanwade, **J. A. K. Satrughna**, S. M. Rajore, P. Pawar, S. S. Mali, J. V. Patil, C. K. Hong, R. C. Dutta, P. M. Shirage, Heteroatom Doping Strategy for Enhanced Sodium-Ion Storage in $Na_2Fe_{1.5}Mn_{1.5}(PO_4)_3$, *Small,* 2025, 2502979. **(IF = 12.1)** DOI: https://doi.org/10.1002/smll.202502979

LIST OF CONFERENCE/WORKSHOP/COURSES ATTENDED

1. Poster presentation at the International Symposium on Theoretical and Computational Physics (IISTCP-2025), organized by the Department of Physics, Madanpalle Institute of Technology & Sciences (MITS), Madanpalle, Andhra Pradesh, held from 1st to 3rd April 2025.
2. Workshop on Quantum Computations and Its Application in Molecular Structure, organized by Centre for Computational and Data Sciences & Nodal Centre for Training in HPC & AI, under the aegis of the National Supercomputing Mission at IIT Kharagpur on 5th March 2025.
3. Training session on How to Publish with Oxford Journals, by Oxford University Press on 12th February 2025.
4. Poster presentation in the International Union of Materials Research Societies – International Conference in Asia, 2024 (IUMRS_ICA 2024) held on 3rd–6th December 2024, at Indore, India.
5. Online Training Workshop on Quantum Technology Spin Qubit Semiconductor Modeling & Simulation Using "QTCAD" TCAD Software from Nanoacademic Technologies, 2024.
6. International workshop on "Energy Conversion and Sustainable Future", 2024.
7. 20th School on "Neutron as Probe of Condensed Matter (NPCM-2024)" organized by UGC_DAE Consortium for Scientific Research, Mumbai Centre & Solid-State Physics Division, Bhabha Atomic Research Centre (BARC), Mumbai during February 05-10, 2024.

8. 1st DFT-M Workshop/Hands-on-Training on Density Functional Theory Modeling of Materials: Nanoparticles, Thin Films, Unit Cells using Quantum Espresso, Centre for Advanced Computational Studies, New Delhi, India, 30th July-5th August 2023.

9. SERB-sponsored Karyashala (High-End Workshop) on "Energy Material Synthesis, Characterization, and Device Fabrication" Organized by Prof. Parasharam M. Shirage, Department of Metallurgical Engineering and Materials Science during 03-08 July 2023.

10. Faculty Development Program on "Recent Development in Energy Materials for Sustainable Future" approved by ATAL AICTE and organized by the Indian Institute of Technology Indore, held from November 21 to December 02, 2022.

11. Oral presentation at "*International Conference on Advanced Materials Synthesis, Characterization and Applications (AMSCA Maverick-2022)*", Department of Physics, Savitribai Phule Pune University, Pune-07, Maharashtra, India, 18th-20th October 2022.

12. SPARC-sponsored one-week course on Introduction to the Search for Extra-Terrestrial Intelligence conducted at IIT Indore on 9th-15th September 2022 by Prof. Erik Zackrisson from Uppsala University, Sweden.

13. TEQIP III sponsored E-Training Program/Short-term course on "Advanced Energy Science and Technology" in the Department of Physics from 7th to 9th December 2020 at IIT Indore.

TABLE OF CONTENTS

LIST OF FIGURES

LIST OF TABLES

ACRONYMS/ABBREVIATIONS

2D	Two-dimensional
3D	Three-dimensional
BE	Binding energy
CB	Carbon black
CMC	Carboxymethyl cellulose
CPE	Constant phase element
CV	Cyclic voltammetry
DEC	Diethyl carbonate
DI-water	De-ionized water
DMC	Dimethyl carbonate
DRT	Distribution of relaxation times
DSC	Differential Scanning Calorimetry
DTG	Derivative of thermogravimetric
EC	Ethylene carbonate
EDS/EDX	Energy dispersive X-ray spectroscopy
EES	Electrochemical energy storage
EIS	Electrochemical impedance spectroscopy
EMC	Ethyl methyl carbonate
ESS	Energy storage systems
FEC	Fluoroethylene carbonate
FESEM	Field emission scanning electron microscopy
FWHM	Full-width half maxima
HC	Hard carbon
HR-TEM	High Resolution Transmission Electron Microscopy
ICP-OES	Inductively coupled Plasma-Optical Emission Spectroscopy
IL	Ionic liquid
JCPDS	Joint committee on powder diffraction standards

LIB	Lithium-ion battery
LTMOs	Layered transition metal oxides
MAP	Maximum A Posteriori
NMP	N-methyl-2-pyrrolidone
OCV	Open circuit voltage
PAA	Polyacrylic acid
PBA	Prussian blue analog
PC	Propylene carbonate
PE	Polyethylene
PP	Polypropylene
ppb	parts per billion
ppm	parts per million
PVDF	Polyvinylidene difluoride
RHE	Reference hydrogen electrode
SAED	Selected Area Electron Diffraction
SBR	Styrene-butadiene rubber
SEI	Solid electrolyte interphase
SIB	Sodium-ion battery
TEM	Transmission Electron Microscopy
TGA	Thermogravimetric Analysis
TM	Transition metal
TMO	Transition metal oxide
XPS	X-Ray Photoelectron Spectroscopy
XRD	X-Ray Diffraction

CHAPTER 1

Introduction

This chapter provides a comprehensive introduction to rechargeable battery technology with a special focus on sodium-ion batteries. Its components and fundamental working principle are briefly discussed, with a particular emphasis on cathode materials. A detailed literature review is presented on various types of cathode materials, outlining their advantages and limitations. Special attention is given to layered, tunnel-structured, and polyanionic-based materials. Finally, the chapter outlines the research gaps, scope, and objectives of this thesis. Further, this chapter presents a detailed structure of the thesis work.

1.1 Background and Motivation

In the current times, the continuous growth in technological development, urbanization, and industrialization has significantly increased the energy demand, relying on sustainable energy sources, including electricity [1–3]. India, as one of the largest developing countries, consumes a high amount of energy for its economic growth. Its further development and economic growth demand a continuous rise in energy supplies. For many centuries, fossil fuels, including coal, petroleum, and natural gas, have been used to satisfy energy requirements worldwide. However, the combustion of these fossil fuel energy sources releases huge amounts of hazardous greenhouse gases, including methane (CH_4) and carbon dioxide (CO_2), leading to unavoidable climate change [4,5]. Besides these environmental demerits, the high dependence on these fossil fuels brings geopolitical and economic vulnerabilities, especially for India, where around USD 132.4 billion foreign exchange was spent on crude oil imports alone in the fiscal year 2023-2024 [6]. Further, the finite nature of these fossil fuels requires an urgent alternative solution for a sustainable energy supply. Environmental, clean, renewable energy sources are possible alternatives to fossil fuels. However, the nonuniform distribution and localized dependent nature of these resources bring major problems in the continuous and stable energy supply throughout the year. These issues could be resolved with the development of energy storage systems (ESS) that can bridge the gap between energy production and energy consumption [1,7,8]. ESS stores energy in various forms, and electrical energy is the most required one. Electrochemical energy storage (EES) devices, such as batteries and supercapacitors, can efficiently store electric energy [9–11]. Batteries are preferred due to their redox reaction and can deliver this stored electrical energy on demand. Based on electrochemical reversibility, batteries are categorized as primary (non-rechargeable) and secondary (rechargeable) batteries. Secondary batteries, such as lead-acid, nickel-metal hydride, nickel-cadmium, and lithium-ion batteries (LIBs), are

commercially used in various applications due to their unique properties and cycle life performance. LIBs are lightweight, possess high energy density, and have long cycle life stability, among other rechargeable batteries [12,13]. As a result, they have revolutionized the energy storage market, especially in portable electronic devices and electric vehicles. However, the scarcity of lithium sources, the cost of the raw material, uneven geographical distribution, and environmental concerns related to mining and processing bring constraints to the widespread adoption of lithium-ion (Li^+-ion) technology [3,14]. Further, countries like India do not even have significant reserves of lithium resources [15].

To tackle such challenges, research interest is focused on alternative sustainable technology showing similar chemistry to that of LIBs. Sodium-ion batteries (SIBs) have gained significant research attention as a promising secondary ESS [3,16,17]. Sodium (Na) is the sixth most abundant element on Earth, with widespread distribution. Further, Na shares similar electrochemical properties to lithium (Li). As a result, SIBs are considered the most sustainable and cost-effective alternative to LIBs [1,5,16]. The limitation of SIBs over LIBs is the larger ionic radius and mass of sodium ions (Na^+-ions) than lithium ions (Li^+-ions). As a result, Na^+-ions show low capacity, sluggish ionic diffusion, high-capacity fading, and structural instability. The development of sustainable SIBs requires addressing the above challenges. This could be achieved with the development of potential electrode materials with high capacity, rate performance, energy density, Na^+-ion kinetics, capacity retention, and low volume change [3,4,14]. Among electrodes, the cathode (as the positive electrode) is important in determining the cost and electrochemical performance of SIBs. Among various types of cathode materials, sodiated metal oxides and polyanionic compounds have emerged as potential positive electrodes [3,14]. Worldwide research has been focused on the development of advanced cathode materials, including sodiated metal oxides and polyanionic compounds.

1.2 What is a Battery?

A battery is a single or a combination of electrochemical cells in a parallel or series connection that converts the chemical energy stored in its active material into electric energy through the redox process [3]. This electric energy from the battery is drawn as an electric current at a certain voltage equal to the electrode potential difference. Every redox reaction is related to the standard cell potential E^0_{cell}, as shown in **equation 1.1**. It assumes a reversible redox reaction under standard, isothermal, and ideal conditions where only electrical work is performed.

$$E^0{}_{cell} = \frac{-\Delta G^0}{n\,F} \qquad \text{….. ….. ….. (1.1)}$$

Where ΔG^0 = standard Gibbs free energy, n = moles of electrons transferred, and F = Faraday's constant. The overall theoretical voltage of a cell (ΔE^0_{cell}) is given as the standard cell potential difference of the cathode ($E^0_{cathode}$) and the anode (E^0_{anode}) as given in **equation 1.2**.

$$\Delta E^0_{cell} = E^0_{cathode} - E^0_{anode} \qquad \text{….. ….. ….. (1.2)}$$

For a spontaneous reaction, $\Delta E^0_{cell} > 0$.

1.3 Types of Batteries

Primary Batteries: Primary batteries are also known as non-rechargeable batteries. Here, the electrochemical reactions are irreversible; as a result, these batteries cannot be further charged once they are discharged. Hence, these batteries are discarded after a single use. Some primary batteries include the Zinc-Carbon, Alkaline-Manganese, Zinc-Air, *etc.*

Secondary Batteries: They are also called rechargeable batteries, where the electrochemical reactions at the electrodes are reversible in nature. They can be charged and discharged several times. Some secondary batteries include Lead-Acid, Ni-Cd, Ni-Metal Hydride, LIB, SIBs, *etc.* From the Ragone plot shown in **Figure 1.1,** the gravimetric and volumetric energy densities of rechargeable batteries increase with the decrease in the weight and size of the ions [18].

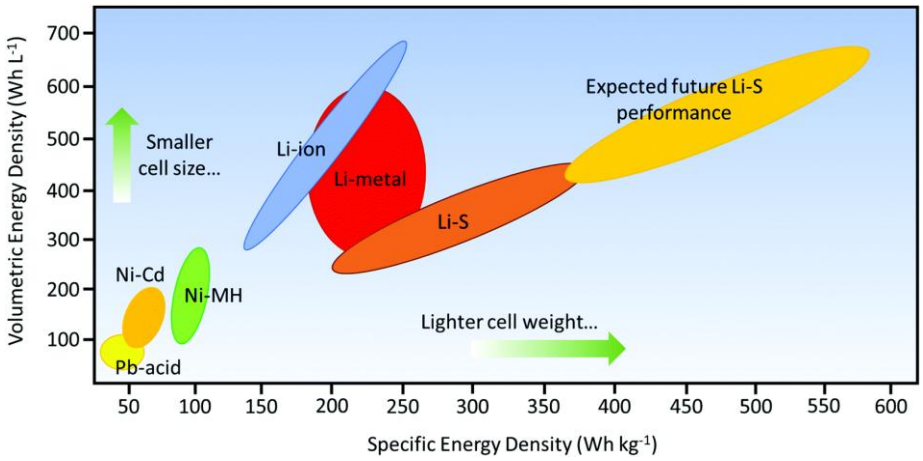

Figure 1.1 Specific and volumetric energy densities of batteries [18].

1.4 History of Battery Technology

In early 1748, Benjamin Franklin coined the term "battery" for a group of Leyden jars used to store static electricity. In 1780, Luigi Galvani (an Italian scientist) discovered battery principles. A breakthrough in battery came in 1800 when Alessandro Volta (Italian scientist) invented the voltaic pile, an alternative stacking of Cu and Zn discs separated by brine-soaked cloth as the first electrochemical battery, producing a continuous flow of electric current [19]. In 1836, John Frederic Daniell, UK chemist, invented the Daniell cell, which was the more reliable and stable version of the voltaic pile, comprised of copper sulfate solution-filled copper pot. In 1859, the lead-acid battery was invented as the first rechargeable battery by Gaston Planté. This lead-acid battery used lead plates and sulphuric acid. By reversing the current flow, it could be recharged. In 1868, a French scientist, Leclanche, developed the original version of the dry cell [3]. Whereas in 1885, a Japanese scientist, Sakizo Yai, invented a dry cell. Following this, the nickel-cadmium (Ni-Cd) battery, the early form of an alkaline battery, was invented by a Swedish scientist, Waldemar Jungner, in 1899. The Ni-Cd battery could deliver improved cycle life and stability compared to the lead-acid battery. The commercialization of Ni-Cd alkaline batteries started in 1964.

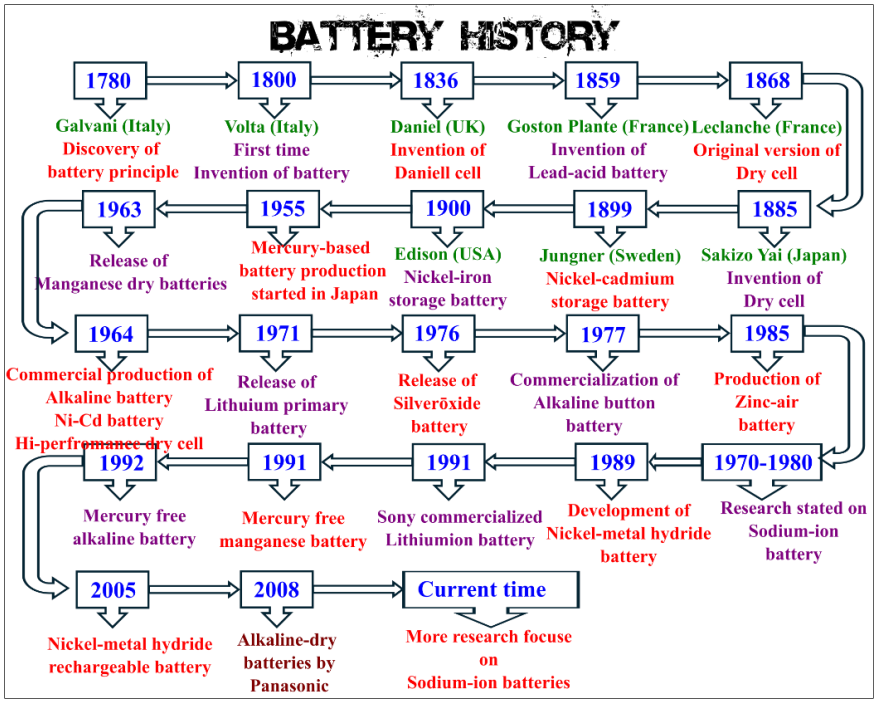

Figure 1.2 Schematic representation of the history of batteries.

At the start of the 20th century, several commercialized batteries were developed based on the new battery chemistry. In 1980, nickel-metal hydride (NiMH) batteries were introduced into the battery market and could deliver higher energy density and improved safety compared to Ni-Cd batteries. In 1991, Sony Corporation commercially introduced LIBs that revolutionized the portable electronics industry. These LIBs are relatively lightweight and have a high capacity, energy density, and long cycle life. In parallel with the LIBs, the research on SIBs was also initiated in the 1970s and 1980s [3,19]. However, the commercialization of LIBs dominated further research on SIBs. LIBs dominate the current portable electronics and electric vehicle market, but there are several limitations associated with LIBs. The cost and nonuniform distribution of lithium resources have increased the research interest in alternative energy storage devices such as SIBs. In the last few decades, SIBs have regained research interest as a promising alternative to LIBs due to the high abundance and low cost of sodium for large-scale energy storage applications [3,19]. Now, SIBs are on the verge of commercialization and will provide a cost-effective, safer,

and sustainable solution. **Figure 1.2** represents a brief history of batteries. Sodium metal has a high negative redox potential of -2.71 V with respect to the standard reference hydrogen electrode (RHE). Low Na atomic weight (22.99 g/mol) provides a high theoretical capacity of 1166 mAh/g as a promising element for energy storage. Additionally, Na is abundant on Earth (2.64%); as a result, it is cheaper and approximately 20 times less expensive than lithium. Despite the many benefits of SIBs, they have not been commercialized. This presents a significant scope for the researchers to advance and refine the technology toward the practical and commercial applications of SIBs. This requires rigorous research on the various components of SIBs. Among them, electrode materials, especially cathodes, have gained a lot of interest.

1.5 Advantages of SIBs over LIBs

SIBs show several advantages over LIBs. Sodium is cheaper than lithium due to its abundance, widespread distribution, and low processing cost, making it a more sustainable and cost-effective option for large-scale ESSs. As shown in **Figure 1.3 (a),** SIBs exhibit better thermal stability, enhanced safety, and low dendrite formation than LIBs. SIBs show promising performance over a wide temperature range, where LIBs tend to struggle. SIB electrodes are often less toxic. Both the SIBs and LIBs demonstrate almost similar energy density. While LIBs still dominate portable electronics due to their higher energy density, the continued development of efficient cathode and electrolyte materials for SIBs is reducing this gap.

1.6 Components of SIBs

The structural components of SIBs are similar to those of other rechargeable batteries. The five major components of SIBs comprise anode, cathode, electrolyte, current collectors, and separator, as shown in **Figure 1.3(b)**. Each component plays a vital role in battery operation and has its own advantages and selection criteria [3,9].

1.6.1 Cathode

The cathode, also known as the positive electrode of the battery, undergoes reduction during discharging and accepts electrons from the external circuit. The cathode is one of the deterministic components of SIBs, as it significantly affects the cost, cycle life, safety, specific capacity, energy, and power density of the battery. The cathode materials for SIBs typically follow the formula of $Na_xM_yN_z$, where M is a single or multiple transition metal (TMs), and N represents an anion (usually oxides or polyanions $(XO_4)^{n-}$). Cathodes possess several significant and unique properties for the optimal performance of SIBs [3,9].

Required features of cathode materials:

1. It should contain redox-active ions in its lattice structure.
2. Should exhibit high chemical, mechanical, and thermal stability.
3. Suitable structural morphology for easy Na^+ ion migration.
4. It needs to have good electronic and ionic conductivity.
5. Capable of operating within the electrolyte potential window.
6. It should be cost-effective and environmentally friendly.

Various layered transition metal oxides (LTMOs), tunnel-based transition metal oxides (TMOs), and polyanionic-type cathodes have been extensively explored for SIBs owing to their favorable Na^+ ion intercalation characteristics. Various layered cathodes, including MoS_2, TaS_2, TiS_2, and sodium-containing LTMOs of the form Na_xMO_2 (M=single / multiple TMs) have been investigated for SIBs. A diverse family of TM-based salts containing oxoanion compounds such as phosphates, sulfates, fluorophosphates, and fluorides, and Prussian blue analogs (PBA) (hexa-cyanoferrates) has also been explored for SIBs [3,9]. A comprehensive discussion on the development and evolution of various cathode materials for SIBs will be given in the subsequent sections.

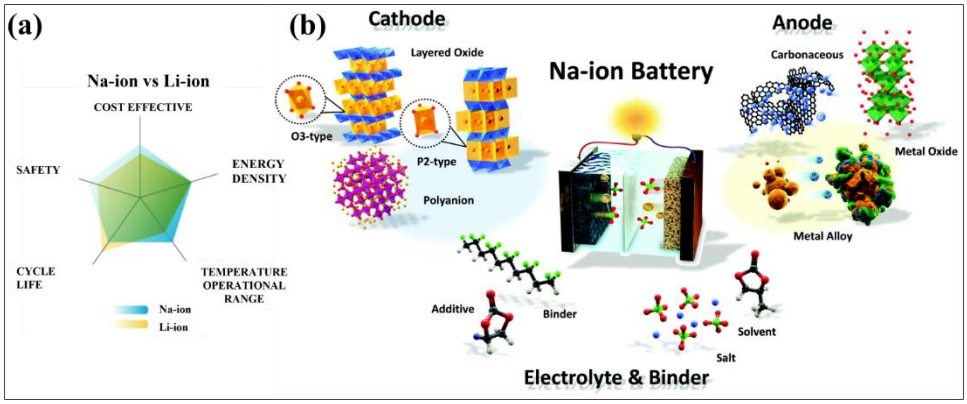

Figure 1.3 (a) Comparison of SIBs and LIBs, **(b)** Components of SIBs [9].

1.6.2 Anode

The anode works as the negative electrode, where oxidation takes place during discharge, and the Na atoms lose electrons that flow through the external circuit to provide an electric current. Sodium metal has a low redox potential (-2.71 V vs. SHE) and offers a high theoretical specific capacity and energy density [3,20]. Hence, from the thermodynamic point of view, sodium metal is an ideal anode material for SIBs. However, it is highly reactive to most liquids, resulting in the formation of dendrites that can pierce the separator and will result in the internal short circuit and thermal runaway. As a result, the use of metallic sodium anode is limited to research aspects and is not commercially available for SIBs [3,20].

To address these safety issues, research is being carried out to develop anode materials showing a better sodium storage mechanism [21]. Among several explored anodes, carbon-based anode materials, particularly hard carbon (HC), are another choice of anode for SIBs. Graphite has an interlayer spacing of ~3.35 Å and is hence used as an anode material in LIBs. However, this interlayer spacing of graphite is not sufficient to accommodate and easily transfer Na^+ with a diameter of ~2.04 Å [3,22]. Density functional theory has also revealed that graphite possesses unfavorable energies for the intercalation of sodium; as a result, graphite has limitations as an anode material for SIBs. Although NaC_x could form compounds of NaC_{15}, NaC_{30}, and NaC_{70}, it can accommodate a very small

amount of Na in its lattice structure. Glucose-derived HC exhibited pseudo-intercalation behavior for both LIBs and SIBs [23]. In SIBs, it exhibited a reversible capacity of ~300 mAh/g. Since then, research has focused on improving the HC anode for SIBs [3]. Based on the working mechanism, the anode materials can be classified as

1. **Intercalation-type anodes:** Accommodate Na^+ without significant structural rearrangements. HC, Titanium dioxide (TiO_2), sodium titanate ($Na_2Ti_3O_7$), *etc*.
2. **Conversion-type anodes:** Undergo a redox reaction with a complete change of chemical phase upon sodiation. Iron (III) oxide (Fe_2O_3), Transition metal dichalcogenides.
3. **Alloy-type anodes:** Form sodium-based alloys on sodium insertion with a significant volume change. Tin-based compounds (SnS, SnO_2), Sb_2O_4, *etc*.

While anode material is crucial, the present thesis primarily focuses on the development of cathode materials for SIBs with the use of Na metal chips as anode and reference electrode in Na-half cell configuration.

1.6.3 Electrolyte

Electrolytes act as Na^+-ion conducting channels between electrodes. Although electrolytes have no direct involvement in energy storage, their physicochemical properties critically affect the battery's performance. Electrolytes can be in liquid, solid, or gel form. However, liquid electrolytes currently dominate due to their high ionic mobility and facile electrode wetting. The electrolyte is desired to have the following properties [3,24].

1. Wide electrochemical stability window.
2. High ionic conductivity (preferably above 10^{-3} S/cm).
3. Low electronic conductivity to reduce self-discharge/short-circuit.
4. Thermally and chemically stable with other cell components.
5. Low viscosity and high wettability for better ion transport.
6. Low-toxic, non-flammable, and cost-effective.
7. Formation of a Stable Solid Electrolyte Interphase (SEI).

Various liquid electrolytes consisting of sodium salts and organic solvents, often with functional additives, have been developed for SIBs [24]. The sodium salts for electrolytes include Sodium perchlorate ($NaClO_4$), Sodium hexafluorophosphate ($NaPF_6$), Sodium bis (trifluoromethanesulfonyl) imide (NaTFSI), Sodium bis (fluorosulfonyl) imide (NaFSI), and Sodium fluoroalkylsulfonylimide derivatives commonly dissolved in mixtures of cyclic organic solvents like Ethylene carbonate (EC), Propylene carbonate (PC), and linear solvents like Dimethyl carbonate (DMC), Diethyl carbonate (DEC), Ethyl methyl carbonate (EMC), *etc* to enhance viscosity, dielectric constant, and ion solvation properties [24,25].

Further, the functional additive, such as fluoroethylene carbonate (FEC), is added to tailor the interfacial chemistry as it improves the reversibility of Na^+ ion insertion due to the stable formation of SEI and reduction in parasitic reactions. Ionic liquids (ILs) as electrolytes for SIBs have also gained attention due to their high thermal stability, non-flammability, and wide electrochemical windows. However, they are in limited use due to their high viscosity and high cost [3,24,25].

1.6.4 Current Collector and Separator

Current collectors at the electrode are important to collect the electrons produced during the redox process and to conduct them to the external circuit. The selection of the current collector is based on the properties of conductivity, corrosion resistance, electrochemical stability, mechanical strength, and cost. Basically, copper (Cu) and Aluminium (Al) are used as anode and cathode current collectors, respectively, owing to their high conductivity and low cost. Initially, Cu was used as an anode current collector. However, it is costly and heavier than Al. Recently, Al has also been used as the anode current collector for SIBs, further reducing the cost and weight of the battery [3,26,27].

The separator is electrochemically inert and is used to physically separate the positive and negative electrodes of the battery to prevent a short

circuit. It also acts as the electrolyte reservoir, facilitating ionic transport and allowing free movement of Na^+. Separators should have high porosity (~40-60%), low pore size (~1 μm) to reduce dendrite penetration, high electrolyte wettability for better electrolyte absorption and ionic conductivity, be electrically insulating, and have high mechanical and thermal stability. The common separators are borosilicate glass fiber, microporous polypropylene (PP), and polyethylene (PE). Polymer composites and ceramic-coated films are other emerging separators.

1.6.5 Other Important Components

Other components are conductive additives, polymer binders, and solvents for electrode slurry preparation. To compensate for the intrinsic nonconductivity of the polymer binder and to enhance the conductivity of the active material, conductive additives are added. The conductive carbons are carbon black (CB), activated carbon, and Super C-65 due to their high surface area and fine particle size. Recently, single and multi-walled carbon nanotubes, carbon nanofibers, reduced graphene oxide, and graphene-conductive carbon have been explored owing to their superior electrical conductivity and mechanical flexibility [3]. These not only improve electron transport but also act as mechanical buffers, accommodating volumetric changes. Electrodes for SIBs use about 10–20 wt% of conductive additive, though reducing this quantity is desirable to increase the energy density by reducing the dead mass of the battery [3,27].

Polymeric binders maintain the mechanical integrity of the electrodes by adhering the conductive carbon and active material to the current collectors and withstand the mechanical stresses during Na^+ ions insertion/extraction. Generally, 5-10 wt% of binder is used. The common binders are Polyvinylidene difluoride (PVDF), Carboxymethyl cellulose (CMC), Sodium alginate, polyacrylic acid (PAA), and styrene-butadiene rubber (SBR). Among them, PVDF is widely used for SIBs due to its chemical stability and compatibility with N-methyl-2-pyrrolidone (NMP) solvent.

1.7 Working Principle of a SIB

SIBs store electrochemical energy *via* reversible migration of Na^+ between electrodes through the electrolyte. Its functionality is governed by the rocking chair, similar to LIBs. The operational mechanism is based on a redox process. The electrons are transported externally through a closed circuit, whereas the Na^+ ions migrate through the electrolyte. The charging process is accompanied by the deintercalation of Na^+ ions from the cathode, transported through the electrolyte to the anode, and then intercalated into it. During the same time, the electrons migrate from the cathode to the anode through the external circuit, thereby storing electrical energy in chemical form. During the discharging process, the reverse flow of electrons and Na^+ ions takes place. Na^+ ions from the anode are released to the electrolyte, which migrates and intercalates into the cathode. Simultaneously, the electrons power the external device as they pass through it from anode to cathode [3]. The redox process for SIB, consisting of $NaCoO_2$ cathode and HC anode, is shown in **Figure 1.4**.

Cathode half-cell: $NaCoO_2 \leftrightarrow Na_{1-x}CoO_2 + xNa^+ + xe^-$

Anode half-cell: $xNa^+ + xe^- + HC \leftrightarrow Na_xHC$

Overall cell reaction: $NaCoO_2 + HC \leftrightarrow Na_{1-x}CoO_2 + Na_xHC$

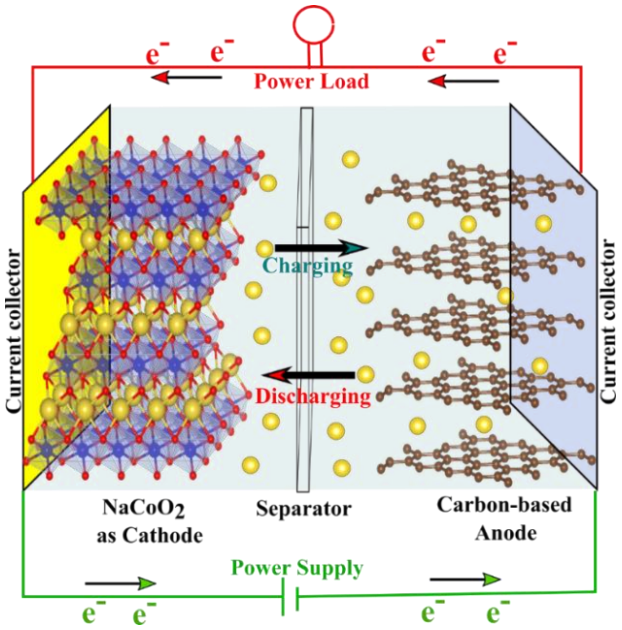

Figure 1.4 Schematic for the working mechanism of SIBs.

1.8 Electrochemical Parameters and Performance Matrices

(i) Cell Voltage

Cell voltage is an important and fundamental parameter of batteries. It is defined as the difference in electrochemical potential between its electrodes. Under ideal conditions, mathematically,

$$V = E_{cell} = E_{Cathode} - E_{Anode}$$

In standard conditions, these cell potentials are termed the standard cell potentials and are calculated as follows:

$$E^0_{Electrode} = \frac{-\Delta G^0}{n\,F}$$

In equilibrium conditions (no external current is connected), it is called the open-circuit voltage. The voltage is affected by electrode redox potentials.

(ii) Theoretical Capacity (Q_{th})

Capacity is the total charge a battery can store due to the redox process. Mathematically, it is given as follows.

$$Q = \int_0^t I\,dt$$

Capacity is basically expressed in Coulombs (C). However, in the material research, this capacity is normalized to specific capacity, the amount of charge stored by the battery per unit mass of the active material, and is expressed in the unit of mAh/g. The theoretical specific capacity (Q_{th}) of an active material is calculated from its molecular weight (M) as follows.

$$Q_{th} = \frac{n\,.\,F}{3.6\,M} \qquad \text{(in mAh/g)}$$

where n = number of electrons in redox process, and F = Faraday's constant.

(iii) C-Rate

The charge and discharge rates of a battery are usually expressed in terms of C-rates. 1C, 0.5, and 2C indicate that the battery gets charged or discharged fully in 1h, 2h, and 30 minutes, respectively.

(iv) Energy Density (W)

The amount of energy delivered per unit mass of the active material is known as the energy density and can be expressed as the integral of the

power output over time, which is the equivalent of the product of experimental capacity and average voltage (V_{avg}). It is expressed in volumetric energy density (Wh/L) or specific energy density (Wh/kg).

$$W = \int_o^t V \, . I \, dt = Q . V_{avg}$$

(v) Energy Efficiency

It is the ratio of usable energy output to energy input during the charge-discharge cycle of the battery system.

(vi) Power (P)

Power is the rate of energy delivered. In practical applications, power density is used and can be expressed in terms of specific power (W/kg) or volumetric power (W/L).

$$P = I . V$$

(vii) Power Efficiency (η)

Power efficiency is the ratio of power output from the system to the power input to the battery system.

$$\eta = \frac{P_{out}}{P_{in}} \times 100\%$$

(viii) Cycle Life

Cycle life or cyclability refers to the number of complete charge-discharge cycles that a battery can undergo before its capacity decreases by more than 80%. It is directly associated with the electrode stability, electrolyte decomposition, and SEI formation of the battery.

(ix) Coulombic Efficiency (CE)

It is the ratio of discharge to charge capacity (if the charging process is performed 1st) or the ratio of charge to discharge capacity (if the discharging process is performed 1st). Ideally, it should approach 100%. Low coulombic efficiency represents parasitic side reactions such as SEI formation and electrolyte decomposition.

$$CE = \frac{Q_{dischrage}}{Q_{charge}} \times 100\% \qquad \text{or} \qquad CE = \frac{Q_{chrage}}{Q_{discharge}} \times 100\%$$

1.9 Cathode Materials for SIBs

Cathodes, the positive electrode of SIBs, play a pivotal role. It significantly determines specific capacity, operating voltage window, energy density, overall stability, and cycle life performance of the battery. In the current stage of research on SIBs, most of the cathode materials are similar to the cathodes for LIBs [3,28]. For the past couple of decades, in the context of SIBs, significant research efforts have been devoted to the development of optimized and suitable cathode materials. There are mainly four types of cathode materials, such as polyanionic compounds, PBAs, organic compounds, and Na-containing LTMOs, which are explored for SIBs, as shown in **Figure 1.5**.

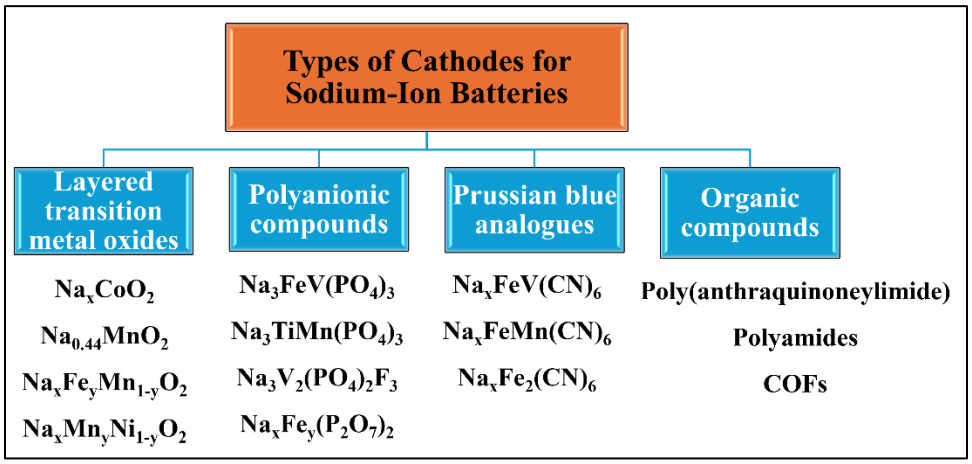

Figure 1.5 Various types of promising cathode materials for SIBs.

1.9.1 Polyanionic Compounds

Different types of polyanionic compounds, such as NASICON, abbreviated for sodium superionic conductors, having the general form of $Na_xM_2(XO_4)_3$ (where M = transition metals and X = P, S, Si, Mo, W, *etc.*), olivine with a general formula of $NaMPO_4$ (M = Fe^{2+}, Mn^{2+}, Co^{2+}, Ni^{2+}, *etc.*), pyrophosphates with general formula $Na_2MP_2O_7$, mixed polyanions with a general formula of $Na_xM_y(PO_4)_2P_2O_7$ (where, M = Fe, Mn, Cr, Ti, V, *etc. e.g.* $Na_4Fe_3(PO_4)_2P_2O_7$), and alluaudite with general formula of $Na_{2+\delta}M_2(PO_4)_3$ have been investigated as cathode materials for SIBs [3,28]. The polyanionic cathodes with an intrinsic 3D crystal framework for Na^+

ion migration exhibit high thermal, structural, and electrochemical stability, fairly high operating potential, and usually rapid sodium transport kinetics. The rigid 3D structure offers open Na^+ ion diffusion pathways and strong covalent bonding, which reduces oxygen evolution at high voltages and enhances cycling stability. The highly electronegative polyanions give rise to the inductive effect, which increases the redox potential of the TM center. As a result, the operational potential of the polyanionic cathodes becomes higher compared to other cathode materials for SIBs [3,28,29].

NASICON-type cathodes have shown satisfactory performance for SIBs [30–32]. Further, various advanced strategies such as carbon coating, nanosizing, and partial doping have been adopted to mitigate their inherent drawbacks [31-32]. In addition to the desired properties of high operational voltage, thermal and structural integrity, polyanionic cathodes show poor intrinsic electronic conductivity, limited rate capability, and synthesis complexity, limiting their practical use. Furthermore, these materials have a limited number of Na^+ ions during the discharging process, resulting in a limited specific capacity, which is generally lower than other cathodes for SIBs [33,34]. At certain crystallographic sites, the NASICON-type polyanionic cathodes possess sluggish Na^+ diffusion as well as redox instabilities at high voltage, resulting in a high capacity fading during the cycle life performance [32]. Although a lot of research is still being done to enhance the properties of polyanionic cathode materials for SIBs, the above limitations have motivated the research community to further develop and thoroughly investigate alternative cathode materials for SIBs.

1.9.2 $NaFe(SO_4)_2$ as Polyanionic Compounds

$NaFe(SO_4)_2$ is an oxoanion group-based polyanionic compound that has been studied as a cathode material for SIB owing to its high potential window, 3D structural framework, and high stability. P. Singh *et al.* [35] investigated the electrochemical performances of $NaFe(SO_4)_2$ (shown in **Figure 1.6)** as a low-cost positive electrode for rechargeable SIBs with reversible sodium ion insertion capability at 3.2 V vs. Na/Na^+ due to the

active Fe^{3+} /Fe^{2+} redox couple. This polyanion-based cathode material, on the other hand, has a decreased sodium insertion rate, resulting in limited specific energy. A. Banerjee *et al.* [36] performed a DFT investigation on $Na_xFe(SO_4)_2$ ($0 \leq x \leq 2$). It exhibited only 8% of the volume change with full desodiation. Trussov *et al.* [37] investigated pristine $NaFe(SO_4)_2$ and its derivatives doped with SeO_4, PO_3F, and HPO_4. They observed that $NaFe(SO_4)_2$ demonstrated the highest capacity of 63 mAh/g compared to $NaFe(SO_4)_{1.5}(SeO_4)_{0.5}$, $NaFe(HPO_4)_{1.5}(SeO_4)_{0.5}$, $NaFe(SO_4)_{1.5}(PO_3F)_{0.5}$. Further, pristine $NaFe(SO_4)_2$ has better cycling performance compared to its polyanionic substituted derivatives. However, the study of $NaFe(SO_4)_2$ is mostly limited to theoretical studies due to the low electronic conductivity, limited specific capacity, and limited energy density.

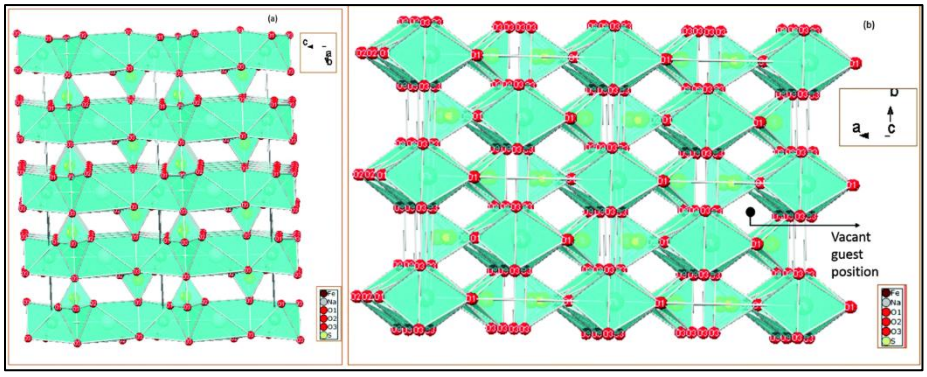

Figure 1.6 $NaFe(SO_4)_2$ crystal (a) planner and (b) vertical views [35].

1.9.3 Prussian Blue Analogues (PBAs)

PBAs are the coordination polymers having a general formula of $Na_xMM'(CN)_6$ (M/M' = TMs), where the TM ions are linked to cyanide ligands, forming a 3D crystal framework with Na^+ ions accommodated at the interstitial sites. Unique features, including rigid and tuneable structure, aqueous-based synthesis, and low cost, make them attractive cathode materials for SIBs [3,38,39]. Several PBAs, including $Na_4Fe(CN)_6$, $Na_xCoFe(CN)_6$, $Na_xNiFe(CN)_6$, and many more, have demonstrated potential performance for SIBs with a reversible capacity of ~150 mAh/g and satisfying cycling stability.[38] Further, defect engineering strategies

such as carbon coating, composite formation, partial elemental doping, and vacancy formation have enhanced electronic conductivity and structural stability. In addition, the removal of interstitial water molecules and $[Fe(CN)_6]^{4-}$ vacancies has been employed to enhance electrochemical performance [3,38,39].

Despite the above advancements, PBA suffers from severe challenges such as low operational voltage, the presence of interstitial H_2O, and low energy density due to high molecular weight, as well as relatively low operating voltage. Cyanide in their lattice framework is considered very toxic to nature. Furthermore, the poor intrinsic electronic conductivity, sluggish Na^+ ion diffusion, $[Fe(CN)_6]^{4-}$ vacancies, and coordinated H_2O molecules result in a high capacity fading during the high-rate cycling process, limiting their practical application [39]. As a result, the current research is focused on alternative cathode materials.

1.9.4 Organic Compound Cathode Materials

Organic compounds including carbonyl compounds (Quinones, ketones, carboxylates, anhydrides, and amides containing C=O group), imides (R-C(O)-N(R)-C(O)-R structure), azo derivatives (N=N group), and Schiff-bases and pteridine derivatives (C=N group) have been explored as cathode for SIBs [3,40,41]. The intrinsic advantages, such as an abundance of natural sources, sustainability, stable redox properties, availability of multi-electron charge storage, and structural tunability, make them suitable for SIBs. Several other organic compound materials, such as disodium rhodizonate ($Na_2C_6O_6$), quinone derivatives, organometallic polymers, conjugated microporous polymers, and covalent organic frameworks, demonstrated multi-electron redox reactions and high theoretical capacities. Heavy organic cathodes such as nitroxyl radical polymers, metal-organic frameworks, and hydrogen-bonded organic frameworks have exhibited suitable porosity and active redox units [3,40,41].

Still, organic compound cathodes suffer from the disadvantages of high dissolution in electrolytes, limited operating voltage, low electrical

conductivity, and poor structural stability. As a result, they show rapid capacity fading and self-discharge [3,40,41]. Hence, over the last two decades, high research interest has been given to the development of more robust inorganic alternative materials such as sodiated layered and tunnel-structured TMO cathodes for SIBs. Sodiated LTMO cathodes offer facile synthesis, higher structural stability, wider voltage windows, improved Na^+-ion mobility, superior conductivity, and favorable electrochemical performance for advanced SIBs. However, these materials absorb moisture, often show irreversible phase transitions, and have low reaction kinetics. A detailed discussion on the sodiated LTMO cathodes is given in the next section. **Figure 1.7** shows the various design strategies for synthesizing high-performance cathode materials for SIBs.

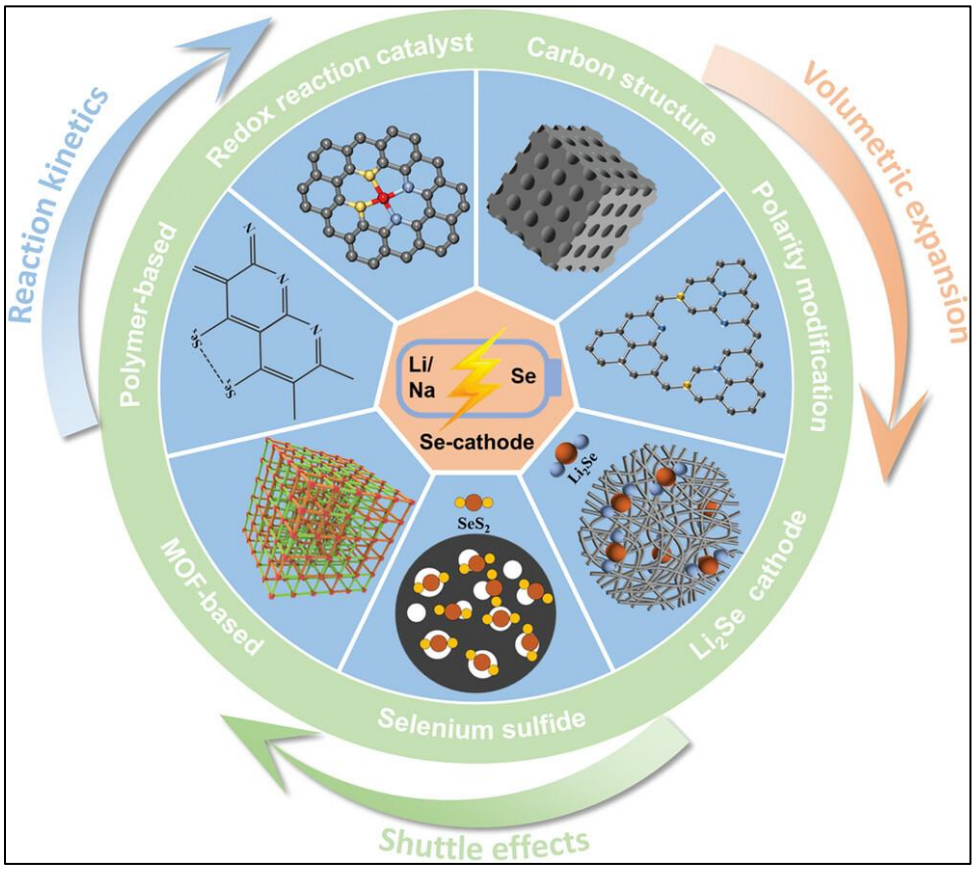

Figure 1.7 Various design strategies for synthesizing high-performance cathode materials for SIBs [3].

1.10 Sodiated Layered Transition Metal Oxide Cathodes

Among different cathodes for SIBs, sodiated LTMO with a general formula of Na_xMO_2 (M = single/multiple TMs such as Fe, Mn, Cr, Co, Ni) has gained significant research interest due to its similarity with Li-based analogues for LIBs. These types of cathodes have several advantages compared to other cathode systems, such as easy synthesis, high theoretical capacity, structural tunability, and good sodium storage capability [3,14].

1.10.1 Structural Classification of Sodiated LTMO Cathodes

The structural unit of sodiated LTMO is composed of Na^+ cations present in an alternate arrangement with two-dimensional (2D) anionic sheets of MO_6 slabs (M = TMs). These TMs form octahedra with six neighboring oxygens. Here, the TM can be made up of single or multiple TM elements. Based on the coordination of Na between the MO_6 layers, they can form an octahedral (*O*) or a Prismatic (*P*) structure. After the letters *O* and *P*, the numbers 1, 2, and 3 are used to indicate the stacking sequence of MO6 slabs or the oxygen-ion layers, as shown in **Figure 1.8** [42]. For example, in the *P*2-Na_xMO_2, the Na^+ ions are situated in prismatic order between the MO_6 layers of AB-BA stacking. In this structural arrangement, the Na^+-ions can be occupied at two prismatic sites, (1) Na_1 or Na_f: prismatic Na^+ sharing its face with two MO_6 octahedra, and (2) Na_2 or Na_e: prismatic Na^+ sharing its edges with two MO_6 octahedra units of the adjacent layers. Furthermore, in the *P*2 structure of Na_xMO_2, the Na^+ ions cannot reside at both the Na_1 and Na_2 sites owing to the coulombic interactions; as a result, inherently *P*2-Na_xMO_2 can have x~0.67 to 0.7 per unit formula [3,42,43].

*P*2-Na_xMO_2 provides direct sodium transport from one *P*-site to another, resulting in a high Na^+ diffusion and high-rate performance, which is one of the most desired features of the cathode material for SIBs. For alkali metal-ion batteries like SIBs, the cathode material with a high reservoir of sodium is preferred; however, *P*2-Na_xMO_2 cathodes have the major drawbacks of containing low sodium content ($x < 0.7$), which results in low specific capacity and energy density [3,42,43].

One more important and stable sodiated layered metal oxide is the *O*3-Na_xMO_2, where the Na^+ ions are located at the octahedral sites formed by the three different stacking of MO_6 octahedral of AB-CA-BC stacking as shown in **Figure 1.8**. In the *O*3-Na_xMO_2, the Na^+ can have only the Na_e locations in which the octahedral of Na shares the edges with the adjacent MO_6 slabs. Unlike *P*2-Na_xMO_2, which can accommodate the sodium $x < 0.7$, *O*3-Na_xMO_2 can have higher sodium content with $(0.7 \leq x \leq 1)$ per unit formula, exhibiting higher specific capacity and energy density [9,11,44,45]. However, the *O3* phases of Na_xMO_2 are vulnerable to moisture and suffer from multiple phase transitions, Jahn-Teller distortion due to Ni^{3+} and Mn^{3+}, and high phase instability due to significant layer-sliding, hindering the long-term durability and high-capacity fading. Hence, although *O*3-Na_xMO_2 cathodes exhibit higher initial capacities, their cycling stability is inferior to *P*2-Na_xMO_2 cathodes. Overcharging at higher voltage can also induce structural transitions of *P*2 or *O*3 phases into the undesired *O*2 phase [44,45].

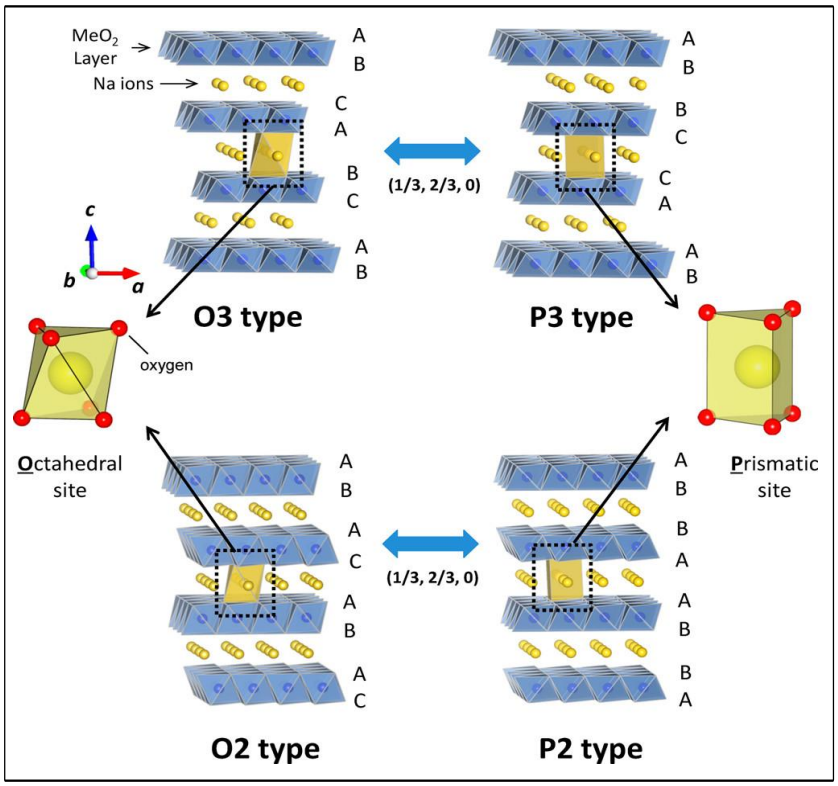

Figure 1.8 Structural classification of sodiated LTMO cathodes [42].

1.11 Issues with Sodiated LTMO Cathodes for SIBs

There are two major problems, mainly environmental and electrochemical instability with LTMO cathodes. The following sections briefly describe these issues, mechanisms, and strategies to overcome them.

1.11.1 Environmental Instability of Na_xMO_2 Cathodes

Na_xMO_2 exhibits significant environmental instability. On exposure to moisture, O_2, and CO_2, they undergo spontaneous surface reactions. This forms undesired and insulating byproducts such as sodium carbonate (Na_2CO_3), sodium hydroxide (NaOH), and sodium bicarbonate ($NaHCO_3$), with the decrease of reversible sodium in the material [46]. These insulating byproducts increase impedance, reduce Na^+ ion diffusion, induce voltage hysteresis, limit rate capability, and affect electrochemical performance. A humid environment promotes judicious hydration and Na^+/H^+ exchange. It reduces the mechanical strength and ionic integrity of the cathode due to microcracks. Surface hydroxides react with CO_2 and form passivation layers of carbonates. Low-voltage cathode systems based on the Mn^{3+}/Mn^{4+} redox are more susceptible to Na^+ ion loss compared to those of the high-voltage cathodes based on Ni^{2+}/Ni^{4+} redox.

The oxidation states of TMs also increase due to the spontaneous extraction of Na^+ ions that induce structural changes and reduce the reversible capacity. The sliding of interlayer MO_6 slabs takes place with prolonged exposure, facilitating irreversible phase transition prior to cell fabrication, which affects the structural stability and electrochemical performance [47,48]. It also complicates the electrode processing, increases the electrode slurry pH, causes partial impurity dissolution in NMP, defluorination of PVDF binder, slurry gelation, Al current collector, and poor adhesion, leading to peeling and cracking of the electrode. The presence of undesired sodium compounds as impurities degrades Al and produces CO_2 and CO byproducts, causing cell swelling and explosion during the charge/discharge process. All these mentioned instability issues reduce the electrochemical performance. Many research has been

performed to understand and address instability issues through several advanced defect engineering techniques, such as multitransitional-metal co-substitution, composite formation, controlled processing, protective coatings, *etc*., which are discussed in detail below [47,48].

1.11.2 Instability Mechanism of with Environment Species

- **Na^+/H^+ exchange and Hydration on O_2 and H_2O exposure:**

When Na_xMO_2 is exposed to air or moisture, H_2O and CO_2 from the air get adsorbed onto it and react to form carbonic acid (H_2CO_3). This acid dissociates into anions and cations of H^+, OH^-, CO_3^{2-}, and HCO_3^-, which react with the surface Na^+ to form the residual byproducts of NaOH, Na_2CO_3, and $NaHCO_3$ as shown in **Figure 1.9**. At the same time, H^+ can partially replace Na^+ through hydrolysis.[49]

$$Na_xMO_2 + xH_2O \rightarrow Na_{1-x}H_xMO_2 + xNaOH$$

Partial Na^+ exchange with H^+ increases the oxidation state of TMs, resulting in secondary surface metal oxide phases as impurities. Prolonged exposure results in the penetration of H_2O into sodium layers and interlayer spacing expansion, causing swelling and mechanical strength degradation.

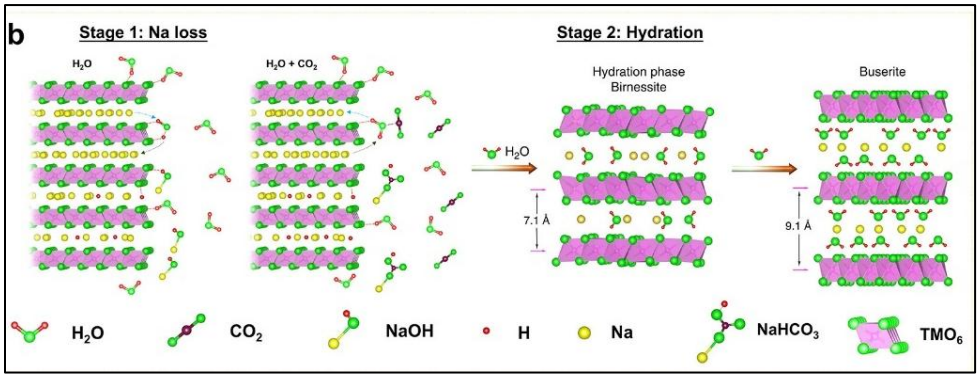

Figure 1.9 Schematic for the H_2O and O_2 exposure of Na_xMO_2 [49].

- **Surface carbonation and CO_2 reactivity:**

NaOH, as the surface residual, reacts with atmospheric CO_2 and forms the insulating layers of sodium carbonate (Na_2CO_3). The presence of this Na_2CO_3 significantly reduces the capacity and increases the impedance of the cathode material. For example, the capacity of *O*3-$NaCrO_2$ and

$NaNi_{0.33}Mn_{0.33}Co_{0.33}O_2$ significantly reduces to ~40% of the initial capacity after 48 hours due to the presence of the Na_2CO_3 passivation layer [50,51].

$$CO_2 + 2NaOH \rightarrow Na_2CO_3 + H_2O$$

In the case of *O*3-Na_xMO_2, carbonation is surface-limited; however, in *P*2-Na_xMO_2, such as *P*2-$Na_{0.67}Mn_{0.5}Fe_{0.5}O_2$, can incorporate the CO_3^{2-} into the MO_6 slabs with the formation of CO_4 tetrahedra. CO_4 units alter local coordination and form secondary phase and Na-deficient species.

1.11.3 Approach for Improving Environmental Stability

Several advanced engineering strategies, including surface coatings, elemental doping, structural tuning, post-synthesis treatments, *etc.*, have been adopted to solve the environmental instability issue and to enhance long-term structural and electrochemical performance.

- **Partial Elemental Doping**

Partial elemental doping at both Na and TM sites helps in structural and electronic modifications. Partial doping of Ti and Ni at the Mn site of $NaMnO_2$ results in the surface segregation of Ti with the formation of the spinel-TiO_2 protective layer [52]. Partial Nb-doping improves the air stability [53]. Partial Cu-substitution has significantly improved air and moisture stability by maintaining structural and electrochemical integrity [54]. Partial co-doping of Cu and Mg has shown outstanding air and moisture stability [55]. Other elemental doping, such as Sb, Al, and Zn, has also been shown to improve environmental stability. Partial substitution of Al^{3+} reduces volume strain and Jahn–Teller distortions of Mn^{3+}. Sb incorporation provides air resistance by enhancing the structural ordering.

Partial elemental doping at the Na-site is also an effective strategy to enhance environmental stability. Ca-doping shows reduced Na-loss and irreversible phase transitions due to stronger Ca-O bonding [56]. Co-doping of Li and F reduces H_3O^+/H_2O intake and lattice oxygen loss [57].

- **Surface Modification:**

It is one of the widely used strategies. Carbon-based coating shows significant improvement in air and moisture stability. About ~2–3 wt% of

carbon layer significantly reduces NaOH byproduct formation and retains a stable *O*3 phase [57]. ZrO_2 coating has also been shown to reduce the capacity fading due to reduced interfacial degradation. Al_2O_3 thin layer deposition also protects the cathode from air and moisture by reducing its reactivity with CO_2 and H_2O.

- **Washing Treatments:**

Washing the electrode thoroughly provides a complementary strategy to remove Na_2CO_3, NaOH, and $NaHCO_3$. Aqueous washing of the electrode degrades the air-sensitive cathodes; gentle ethanol washing can remove surface impurities significantly without damaging the cathode structure. This provides an easy strategy to reduce moisture sensitivity and enhance reversible capacity and cycling stability.

- **Compositional-Structural Modifications**

Proper elemental substitution can provide a compositional structural modification to enhance air and moisture stability. The hexagonal honeycomb structure of *P*2-$Na_{0.67}Ni_{0.33}Mn_{0.67}O_2$ reduces the moisture intake [57]. In such materials, Co substitution degrades the material due to the disruption of this ordering; Cu substitution preserves the superstructure due to similar radii of Cu^{2+} and Ni^{2+}.

- **Post Heat Treatments**

Post-heat treatment of the cathodes after synthesis is also an effective strategy to improve air and moisture stability. Air-exposed materials on re-calcination under inert conditions at 200-300°C decompose the dehydrated byproducts and restore the phase-pure material. Hot-roller mechanical pressing of the electrode reduces surface area and forms a compact electrode that lowers the adsorption of water.

1.11.4 Electrochemical Instability of Na_xMO_2 Cathodes

*O*3-Na_xMO_2 as sodiated LTMO cathodes show high initial capacity and favorable redox potentials. However, these types of cathode materials exhibit critical electrochemical instability during the continuous charging/discharging process due to structural degradation and interfacial

reactions in SIBs. *O*3-Na_xMO_2 cathode materials are more prone to electrochemical instability compared to *P*2-Na_xMO_2 due to their lower interlayer spacing and unsuitable Na^+ diffusion pathways.[50,51] *O*3-type $NaFeO_2$, $NaMnO_2$, $NaCoO_2$, and $NaNiO_2$, as single TMO, exhibit poor cycling stability [3,27,58–60]. *O*3-type α-$NaFeO_2$ shows a reversible capacity of about 80 mAh/g corresponding to 0.3-mole extraction of Na with a cut-off voltage of 3.4 V. However, beyond 3.5 V, it shows a high-capacity fading owing to the irreversible phase transitions associated with the migration of Fe^{3+} from octahedral to tetrahedral sites of the Na-layer, destabilizing the structure and blocking Na^+ diffusion pathways [61]. The electrochemical performance of $NaFeO_2$ is also affected by H^+/Na^+ ion exchange in the air. *O*3-Na_xCoO_2 shows a reversible phase transition of O3↔O′3↔P′3 for the x-values of 1.00↔0.83↔0.67 [62]. The *P*2-Na_xCoO_2 is found to exist in $0.68 \leq x \leq 0.76$ as shown in **Figure 1.10**.

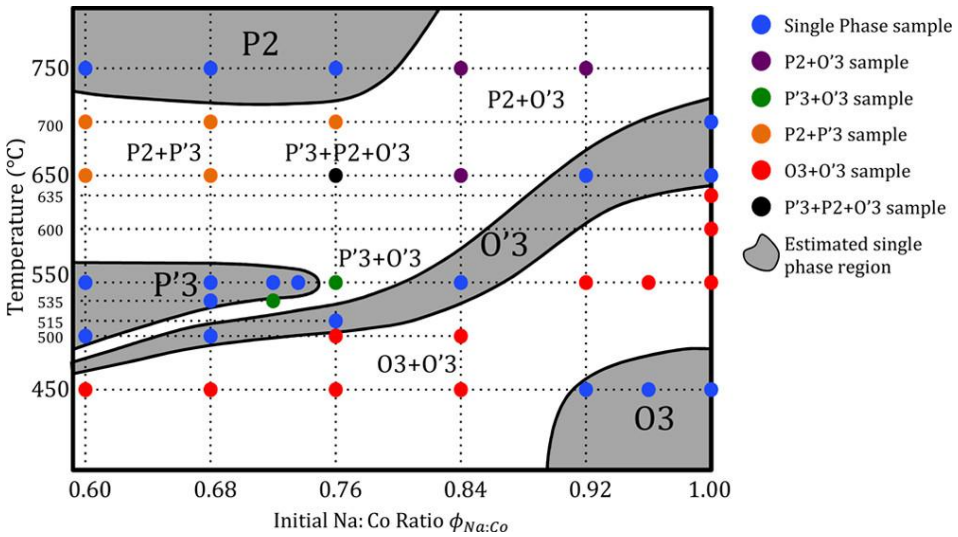

Figure 1.10 Phase diagram of Na_xCoO_2 [62].

The Jahn-Teller distortion from high-spin Mn^{3+} in O'3-Na_xMnO_2 results in critical structural instability. Although the *P*2-Na_xMnO_2 exhibits a high reversible capacity of ~150 mAh/g, it still shows high-capacity fading [3,63]. O3-Na_xCoO_2 has high energy barriers of ~180 meV for the Na^+ hopping in the octahedral–tetrahedral–octahedral site, whereas *P*2 has an energetically favorable prismatic route [64]. The irreversible phase

transition of O3-$NaNiO_2$ (O'3→P'3→P"3→O"3→O"'3) leads to significant capacity loss and Jahn-Teller distortion. Elemental substitution stabilizes these materials by changing oxidation states or structure goodness [65,66]. Several binary and multiple TM oxides have been explored to overcome the inherent limitations of single-TM systems. The synergistic effect can significantly reduce Jahn-Teller distortion and improve the structure. Ti^{4+}, Ni^{2+}, Mg, Li, and Cu^{2+}doping suppresses the multiple-step phase transitions and improve material stability [9,67-68].

Despite several advancements, the challenges still remain. Jahn-Teller distortion due to Mn^{3+} and electrolyte decomposition in the Mn-rich cathode is completely unavoidable [69,70]. Interfacial degradation, formation of disordered surface layers, electrolyte decomposition, and gas evolution remain the major challenges, significantly affecting capacity fading and cyclability. Hence, further optimizing the balance between structural integrity, redox activity, and interfacial stability is important in improving the electrochemical performance [71].

1.11.5 Problems with Na-deficiency in *P*2-Na_xMO_2

*P*2-Na_xMO_2 with x<0.7 limits the available Na, restricting the capacity and a low average operating voltage of <3.2 V (**Figure 1.11)** [72]. Hence, the energy density of *P*2 is lower compared to *O*3-Na_xMO_2. The structure and cycle life performance of *P*2-type cathodes is affected by the multiple phase transitions of *P*2→*O*2/OP4/Z, Na^+ vacancy, and TM-ordering [3,27,73]. The doping of electrochemically inactive or partially active cations, such as Ti^{4+}, Al^{3+}, Cu^{2+}, Mg^{2+}, Li^+, *etc.,* is adopted to mitigate these challenges. However, doing so reduces the specific capacity due to the reduction in redox-active elements. Alternatively, doping with multivalent redox-active ions such as Co^{3+}, Fe^{3+}, Mn^{3+}, *etc.,* can enhance capacity, although it compromises energy density due to low working voltage [3,27,73]. Therefore, the development of Na_xMO_2 cathodes with higher initial Na content, reversible structural transitions, high specific capacity, and energy density is desired for advancing SIBs.

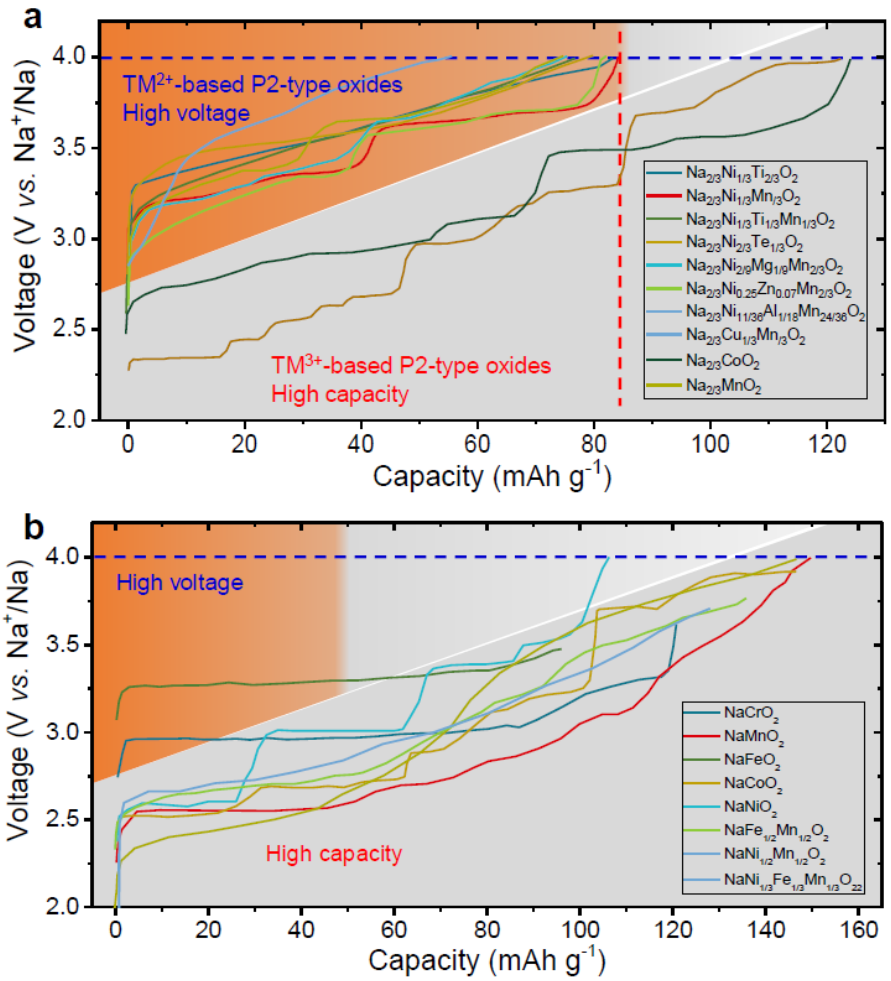

Figure 1.11 Electrochemical performance of typical *P*2/*O*3-Na_xMO_2 [72].

1.12 Tunnel-Structured LTMO Cathodes for SIBs

In addition to layered Na_xMO_2, the tunnel-structured TMO cathodes, such as orthorhombic-$Na_4Mn_9O_{18}$ (also known as $Na_{0.44}MnO_2$), have emerged as a potential cathode for SIBs [74]. These compounds contain S-shaped tunnels for the unidirectional Na^+ migration along the *c*-axis formed by the edge-sharing of MnO_6 octahedra and MnO_5 pyramids in the orthorhombic symmetry, as shown in **Figure 1.12** [75]. The rigid framework structure of these cathodes results in high structural stability, fast Na^+ ion diffusion, cycling stability, and rate capability, outperforming layered counterparts. The tunnel structure enables these cathodes for reversible Na^+ ion insertion/extraction with minimal lattice change, leading to reversible capacities of 86-188 mAh/g depending on composition and

modification. $Na_4Mn_9O_{18}$ with a tunnel geometry delivers 100-120 mAh/g in a 2-4 V voltage window vs. Na/Na^+. Further, the Ti, Cu, Fe, Ni, and B doping have enhanced the rate performance and structural stability via altered Na^+ ion diffusion pathways and stronger M-O bonding. Surface coatings, composite architectures, and advanced synthesis conditions have been found to significantly improve the electrochemical performance of these cathode materials for SIBs. However, a more stable electrolyte is required for the extraction of high sodium at higher voltages. The extraction of Na^+ ions is often limited to <0.24 Na^+ per unit formula, reducing practical capacity. Further, the poor air stability and low voltage (~2.9 V) issues need to be resolved [74].

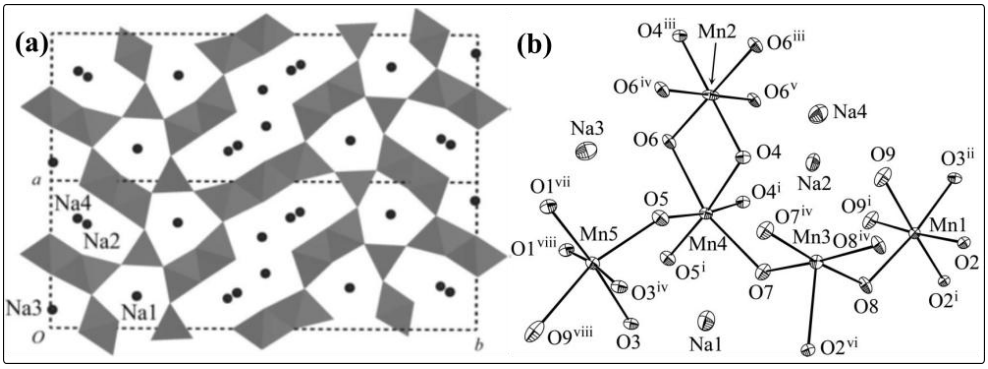

Figure 1.12 (a) Tunnel-crystal structure of $Na_4Mn_9O_{18}$ and (b) Mn coordination environment in $Na_4Mn_9O_{18}$ cathode for SIBs [75].

Hence, the development and characterization of cathodes involves a balance between the cathode's structural stability, electrochemical performance, and electrolyte compatibility. Layered and tunnel-structured TMOs and polyanionic compound cathodes are gaining significant research attention in the current SIB technology. Further advancement of cathode material design, optimization, doping approach, sodium deficiency, and electrolyte engineering is important to advance sustainable SIBs.

1.13 Scope and Aims of the Thesis Work

The rapidly increasing demand for cost-effective and sustainable ESSs has stimulated research interest in SIBs. The similar alkali-ion intercalation chemistry of Na^+ with Li^+, the earth's abundance of sodium precursors, easy processing, and low cost signify the strategic advantages of SIBs over LIBs. The relatively larger ionic size of Na^+ compared to Li^+, sluggish Na^+ diffusion kinetics, air and moisture instability, the lower standard potential of the electrode, electrochemical instability, *etc.,* are fundamental challenges for the development of advanced and high-performance cathodes for SIBs. The cathode determines specific capacity, voltage output, energy density, and cycle life performance. Considerable progress has been made in exploring several classes of cathode materials for SIBs; still, this field remains in its infancy, with a limited number of promising cathode materials capable of delivering high reversible electrochemistry. Consequently, there is a compelling need to explore and develop advanced cathode materials in their pristine and defect-engineered forms, such as composite, partial, co-doped TMs, and Na-vacancy-based forms. These advanced cathode materials could exhibit the promising characteristics of favorable structural attributes, reversible multivalent redox processes, and enhanced electrochemical features for SIBs.

In this context, this thesis is devoted to the engineering of cathode materials, such as synthesis, optimization, characterization, mechanistic understanding, half-cell fabrication, and electrochemical properties analyses of cathode materials for SIBs, with an emphasis on layered and tunnel-type Na_xMO_y and sodium-deficient $Na_xM(SO_4)_2$. The research strategy, moreover, concentrates on the rational design of sodiated metal oxides and sulfates, employing simple and scalable material synthesis methods, such as sol-gel and solid-state. The thesis focuses on the comprehensive physicochemical analyses of these cathode materials, followed by their electrochemical evaluation in half-cell configurations for the next-generation SIBs.

1.14 Thesis Objectives

The primary aim of this thesis work is to experimentally synthesize, optimize, and analyze cathodes for SIBs. Our main goal concentrates on applying defect engineering, such as synthesis optimization, Na-deficiency, and multiple TM cosubstitution, to explore cathode materials capable of exhibiting better electrochemical performances, including high specific capacity, energy density, rate capability, voltage window, structural stability, and long cycle life performance. The major objectives are:

1. To study the effect of sodium ions deficiency on the structural stability and working-voltage profile of $Na_{0.8}Fe(SO_4)_2$.
2. To study the effect of calcination temperature on morphology and electrochemical performance of $NaCoO_2$.
3. Engineering the multi-TMs substituted $Na_xCo_{0.5}Fe_{0.25}Mn_{0.25}O_2$ through solid-state synthesis and investigating in detail the synergistic effects of multiple redox species in the life cycle performance.
4. To study the 3D $Na_{1.35}CrO_4$ and tunnel-structured $Na_4Mn_{7.2}Cr_{1.2}O_{18}$ and examine their structural and Cr-doping effect on Jahn-Teller effect mitigation, Na^+ diffusion kinetics, and cycle life performance.
5. To synthesize the cathode materials, perform physicochemical characterizations to understand the thermal behavior, stoichiometry, phase formation, morphology, and atomic and chemical environment.
6. To carry out electrochemical analyses: redox process investigation, Na^+ ion kinetics, capacity retention, and cycle life performance of the cathode materials.
7. To investigate the compatibility of the above cathode materials in a half-cell configuration of sodium-based anodes and propose future directions for full-cell fabrication.

1.15 Structure of the Thesis

Chapter 1: Introduction

This chapter briefly introduces the urgent global need for sustainable, cost-effective energy storage, batteries, their history, and the motivation for using SIBs as a promising alternative to LIBs. The critical components and working principle of SIBs, followed by a discussion of various parameters used to evaluate battery performance. Several classes of cathode materials for SIBs with a special focus on metal oxides and sulphate-based polyanions are given. The challenges and the approach to overcome them are explained. The challenges and opportunities in developing cathodes. The scope, aim, and objectives of the present thesis work are clearly defined.

Chapter 2: Experimental Methods and Characterization Techniques

This chapter clearly discusses the preparation methodologies of various cathodes, including both sol-gel and solid-state routes. It briefly discusses the electrode preparation, coin-cell assembly, advanced physicochemical and electrochemical characterization techniques used to assess the physical, chemical, and electrochemical properties of cathode materials.

Chapter 3: Sodium-Deficient-Based $Na_{0.8}Fe(SO_4)_2$ Cathode: A Novel Polyanionic Framework for Enhanced Na^+ Ion Migration

This chapter provides a detailed synthesis of sodium-deficient $Na_{0.8}Fe(SO_4)_2$ through the sol-gel method, focusing on enhancing the Na^+ ion diffusion and electrochemical performance. This chapter reveals the effect of sodium deficiency in polyanionic-type cathodes for SIBs. It demonstrates how the sodium deficiency results in the lattice shrinkage, d-spacing reduction, and enhanced Na^+ ion diffusion.

Chapter 4: Optimization of Layered $NaCoO_2$ Cathode for High-Capacity SIBs

This chapter presents a systematic study of the synthesis of phase-pure $NaCoO_2$ by optimizing the calcination temperature through the sol-gel method. The effects of calcination temperature on phase formation, morphology, stoichiometry, and crystallinity are thoroughly discussed. This

chapter also explains electrochemical analyses of $NaCoO_2$, revealing high initial specific capacity, consistency in capacity performance, excellent C-rate performance, and energy density compared to its present Na_xCoO_2 derivatives as a promising cathode for high-performance SIBs.

Chapter 5: Multi-Transition Metal Co-substituted-$Na_xCo_{0.5}Fe_{0.25}Mn_{0.25}O_2$ as a High Cycle Life Cathode for SIBs

This chapter includes the synthesis of a multi-transition metal co-substituted layered $Na_xCo_{0.5}Fe_{0.25}Mn_{0.25}O_2$, designed to utilize the synergistic multiple redox effects and improve structural stability for SIBs. The solid-state synthesis, physicochemical, and electrochemical analyses demonstrating promising capacity retention and rate capability are discussed.

Chapter 6: 3D Channel-Based $Na_{1.35}CrO_4$ and Tunnel-Structured $Na_4Mn_{7.2}Cr_{1.8}O_{18}$ Metal Oxide Electrodes for SIBs

This chapter has been divided into two parts: Part A and Part B. Part A explores the effect of particle nano-structuring on the physicochemical and electrochemical properties of $Na_{1.35}CrO_4$ electrode in SIBs. Part B describes the features of the tunnel-structured $Na_4Mn_{7.2}Cr_{1.8}O_{18}$ cathode. It explains the merits of using a combination of TMs in $Na_4Mn_9O_{18}$ for reducing the Jahn-Teller effect of Mn^{3+} and describes how the interconnected tunnel structure facilitates the efficient Na^+ ion transport and the redox synergy between Mn and Cr in the cycle life enhancements.

Chapter 7: Conclusions and Scope for Future Work

This chapter summarizes and finalizes the key findings of the thesis and critically assesses the performance of the developed cathode materials for SIBs. The chapter concludes with perspectives on future strategies for advancing cathode material and achieving commercial-based SIBs.

By addressing the outlined objectives, this thesis aims to significantly contribute to the advancement of SIB technology through the rational design and development of advanced cathode materials.

1.16 References

[1] M. Sawicki, L.L. Shaw, Advances and challenges of sodium ion batteries as post lithium ion batteries, RSC Adv. 5 (2015) 53129–53154. https://doi.org/10.1039/c5ra08321d.

[2] X. Wang, S. Roy, Q. Shi, Y. Li, Y. Zhao, J. Zhang, Progress in and application prospects of advanced and cost-effective iron (Fe)-based cathode materials for sodium-ion batteries, J. Mater. Chem. A. 9 (2021) 1938–1969. https://doi.org/10.1039/d0ta10610k.

[3] J. Feng, S. Yu, C. Shi, X. Tang, X. Zhao, S. Chen, and J. Song, Advanced Cathode Designs for High-EnergyLithium/Sodium–Selenium Battery, Adv. Funct. Mater. (2025), 35, 2422013. https://doi.org/10.1002/adfm.202422013.

[4] M. Armand, P. Axmann, D. Bresser, M. Copley, K. Edström, C. Ekberg, D. Guyomard, B. Lestriez, P. Novák, M. Petranikova, W. Porcher, S. Trabesinger, M. Wohlfahrt-Mehrens, H. Zhang, Lithium-ion batteries – Current state of the art and anticipated developments, J. Power Sources. 479 (2020) 228708. https://doi.org/10.1016/j.jpowsour.2020.228708.

[5] M.A. Khan, D. Han, G. Lee, Y. Il Kim, Y.M. Kang, P2/O3 phase-integrated Na0.7MnO2 cathode materials for sodium-ion rechargeable batteries, J. Alloys Compd. 771 (2019) 987–993. https://doi.org/10.1016/j.jallcom.2018.09.033.

[6] T.E. Times, India's crude oil import bill drops 16% but import dependency hits new high, The Economic Times. (2024). https://economictimes.indiatimes.com/news/economy/foreign-trade/indias-crude-oil-import-bill-drops-16-but-import-dependency-hits-new-high/articleshow/109373640.cms.

[7] S. Wang, C. Sun, N. Wang, Q. Zhang, Ni- and/or Mn-based layered transition metal oxides as cathode materials for sodium ion batteries: Status, challenges and countermeasures, J. Mater. Chem. A. 7 (2019) 10138–10158. https://doi.org/10.1039/c8ta12441h.

[8] S. Wang, G. Wang, X. Che, S. Wang, C. Li, D. Li, Y. Zhang, Q. Dong, J. Qiu, Enhancing the capacitive deionization performance of NaMnO2 by interface engineering and redox-reaction, Environmental Science: Nano. 6 (2019) 2379–2388. https://doi.org/10.1039/c9en00545e.

[9] J.Y. Hwang, S.T. Myung, Y.K. Sun, Sodium-ion batteries: Present and future, Chem. Soc. Rev. 46 (2017) 3529–3614. https://doi.org/10.1039/c6cs00776g.

[10] V. Palomares, P. Serras, I. Villaluenga, K.B. Hueso, J. Carretero-

González, T. Rojo, Na-ion batteries, recent advances and present challenges to become low cost energy storage systems, Energy Environ. Sci. 5 (2012) 5884–5901. https://doi.org/10.1039/c2ee02781j.
[11] T. Hosaka, K. Kubota, A.S. Hameed, S. Komaba, Research Development on K-Ion Batteries, Chemical Reviews. 120 (2020) 6358–6466. https://doi.org/10.1021/acs.chemrev.9b00463.
[12] T. Kim, W. Song, D.Y. Son, L.K. Ono, Y. Qi, Lithium-ion batteries: outlook on present, future, and hybridized technologies, J. Mater. Chem. A. 7 (2019) 2942–2964. https://doi.org/10.1039/C8TA10513H.
[13] A. Maheshwari, M. Heck, M. Santarelli, Cycle aging studies of lithium nickel manganese cobalt oxide-based batteries using electrochemical impedance spectroscopy, Electrochimica Acta. 273 (2018) 335–348. https://doi.org/10.1016/j.electacta.2018.04.045.
[14] A. Kanwade, S. Gupta, A. Kankane, M.K. Tiwari, A. Srivastava, J.A. Kumar Satrughna, S. Chand Yadav, P.M. Shirage, Transition metal oxides as a cathode for indispensable Na-ion batteries, RSC Adv. 12 (2022) 23284–23310. https://doi.org/10.1039/d2ra03601k.
[15] Lithium Reserves by Country 2025, (2024). https://worldpopulationreview.com/country-rankings/lithium-reserves-by-country.
[16] S. Guo, P. Liu, H. Yu, Y. Zhu, M. Chen, M. Ishida, H. Zhou, A layered P2- and O3-type composite as a high-energy cathode for rechargeable sodium-ion batteries, Angew. Chem. Int. Ed. 54 (2015) 5894–5899. https://doi.org/10.1002/anie.201411788.
[17] Y.-F. Liu, K. Han, D.-N. Peng, L.-Y. Kong, Y. Su, H.-W. Li, H.-Y. Hu, J.-Y. Li, H.-R. Wang, Z.-Q. Fu, Q. Ma, Y.-F. Zhu, R.-R. Tang, S.-L. Chou, Y. Xiao, X.-W. Wu, Layered oxide cathodes for sodium-ion batteries: From air stability, interface chemistry to phase transition, InfoMat. 5 (2023) e12422. https://doi.org/https://doi.org/10.1002/inf2.12422.
[18] E. Cha, M. Patel, S. Bhoyate, V. Prasad, W. Choi, Nanoengineering to achieve high efficiency practical lithium – sulfur batteries, Nanoscale Horiz. 5 (2020) 808–831. https://doi.org/10.1039/c9nh00730j.
[19] Panasonic Energy, A simple history of batteries, (n.d.). https://www.panasonic.com/global/energy/study/academy/history.html (accessed May 24, 2025).
[20] T. Chen, B. Ouyang, X. Fan, W. Zhou, W. Liu, K. Liu, Oxide

cathodes for sodium-ion batteries: Designs, challenges, and perspectives, Carbon Energy. 4 (2022) 170–199. https://doi.org/10.1002/cey2.153.

[21] Y. Liu, W. Li, Y. Xia, Recent Progress in Polyanionic Anode Materials for Li (Na)-Ion Batteries, Electrochem. Energy Rev. 4 (2021) 447–472. https://doi.org/https://doi.org/10.1007/s41918-021-00095-6.

[22] X. Luo, C. Yang, Y. Peng, N. Pu, M. Ger, C. Hsieh, J. Chang, Graphene nanosheets, carbon nanotubes, graphite, and activated carbon as anode materials for sodium-ion batteries, J. Mater. Chem. A. 3 (2015) 10320–10326. https://doi.org/10.1039/c5ta00727e.

[23] J.A.K. Satrughna, A.R. Kanwade, S.M. Rajore, P.M. Shirage, Exploring the Characteristics of Na1.35CrO4 as Active Electrode for Energy Storage Application in Sodium-Ion Batteries, Phys. Status Solidi RRL. (2025) 2500079. https://doi.org/10.1002/pssr.202500079.

[24] N. Aslfattahi, L. Samylingam, M. Sadat, K. Kadirgama, V. Kulish, M. Schmirler, Z. Said, State-of-the-art review on electrolytes for sodium-ion batteries : Potential recent progress and technical challenges, J. Energy Storage. 72 (2023) 108781. https://doi.org/10.1016/j.est.2023.108781.

[25] F. Cheng, M. Cao, Q. Li, C. Fang, J. Han, Y. Huang, Electrolyte Salts for Sodium-Ion Batteries: NaPF6 or NaClO4?, ACS Nano. 12 (2023) 18608−18615. https://doi.org/10.1021/acsnano.3c07474.

[26] S.M. Rajore, A.R. Kanwade, J.A.K. Satrughna, M.K. Tiwari, P.M. Shirage, A comprehensive review on advancements in catalysts for aluminum-air batteries, J. Power Sources. 616 (2024) 235101. https://doi.org/10.1016/j.jpowsour.2024.235101.

[27] J.A.K. Satrughna, A.R. Kanwade, S.M. Rajore, M. Kumar, Y. Ito, A. Ogura, H. Lee, Y. Ohshita, P.M. Shirage, Sol-gel-based synthesis of high-capacity-NaCoO2 cathode for advanced sodium-ion batteries, Electrochim. Acta. 507 (2024) 145201. https://doi.org/10.1016/j.electacta.2024.145201.

[28] M. Chen, Q. Liu, S.W. Wang, E. Wang, X. Guo, S.L. Chou, High-Abundance and Low-Cost Metal-Based Cathode Materials for Sodium-Ion Batteries: Problems, Progress, and Key Technologies, Adv. Energy Mater. 9 (2019) 1–41. https://doi.org/10.1002/aenm.201803609.

[29] A. Kanwade, S. Gupta, A. Kankane, A. Srivastava, S.C. Yadav, P.M. Shirage, Phosphate-based cathode materials to boost the

electrochemical performance of sodium-ion batteries, Sustainable Energy Fuels. 6 (2022) 3114–3147. https://doi.org/10.1039/d2se00475e.

[30] J. Ou, H. Wang, H. Deng, H. Zhang, Gelatin and Graphene Co-Modified Na3v2(Po4)2f3 Prepared by Water-Based Hydrothermal for High Performance Sodium Ion Battery, SSRN Electronic Journal. 2 (2022). https://doi.org/10.2139/ssrn.4081216.

[31] M.T. Ahsan, Z. Ali, M. Usman, Y. Hou, Unfolding the structural features of NASICON materials for sodium-ion full cells, Carbon Energy. (2022) 1–44. https://doi.org/10.1002/cey2.222.

[32] C. Heubner, S. Heiden, M. Schneider, A. Michaelis, In-situ preparation and electrochemical characterization of submicron sized NaFePO4 cathode material for sodium-ion batteries, Electrochim. Acta. 233 (2017) 78–84. https://doi.org/10.1016/j.electacta.2017.02.107.

[33] I. Rey, M. Iturrondobeitia, O. Akizu-Gardoki, R. Minguez, E. Lizundia, Environmental Impact Assessment of Na 3 V 2 (PO 4) 3 Cathode Production for Sodium-Ion Batteries, Adv. Energy Sustainability Res. 2 (2022) 2200049. https://doi.org/10.1002/aesr.202200049.

[34] Y. Li, Y. Li, X. Liang, G. Zhong, C. Wang, S. Wu, K. Xu, C. Yang, Fiber-Shape Na3V2(PO4)2F3@N-Doped Carbon as a Cathode Material with Enhanced Cycling Stability for Na-Ion Batteries, ACS Appl. Mater. Interfaces. 12 (2020) 25920–25929. https://doi.org/10.1021/acsami.0c05490.

[35] P. Singh, K. Shiva, H. Celio, J.B. Goodenough, Eldfellite, NaFe(SO4)2: an intercalation cathode host for low-cost Na-ion batteries, Energy Environ. Sci. 8 (2015) 3000–3005. https://doi.org/10.1039/c5ee02274f.

[36] A. Banerjee, R.B. Araujo, R. Ahuja, Unveiling the thermodynamic and kinetic properties of NaxFe(SO4)2 (x = 0-2): toward a high-capacity and low-cost cathode material, J. Mater. Chem. A. 4 (2016) 17960–17969. https://doi.org/10.1039/c6ta05330k.

[37] I.A. Trussov, S.T. Kokhmetova, L.L. Driscoll, R. Smith, F.J. Berry, J.F. Marco, A.K. Galeyeva, A.P. Kurbatov, P.R. Slater, Synthesis, structure and electrochemical performance of Eldfellite, NaFe(SO4)2, doped with SeO4, HPO4 and PO3F, Journal of Solid State Chemistry. 289 (2020) 1–11. https://doi.org/10.1016/j.jssc.2020.121395.

[38] J. Qian, M. Zhou, Y. Cao, X. Ai, H. Yang, Nanosized Na 4 Fe(CN)

6/C composite as a low-cost and high-rate cathode material for sodium-ion batteries, Adv. Energy Mater. 2 (2012) 410–414. https://doi.org/10.1002/aenm.201100655.

[39] B. Xie, B. Sun, T. Gao, Y. Ma, G. Yin, P. Zuo, Recent progress of Prussian blue analogues as cathode materials for nonaqueous sodium-ion batteries, Coord. Chem. Rev. 460 (2022) 214478. https://doi.org/10.1016/j.ccr.2022.214478.

[40] Y. Huang, G. Jiang, J. Xiong, C. Yang, Q. Ai, H. Wu, S. Yuan, Recrystallization synthesis of disodium rhodizonate-conductive polyaniline composite with high cyclic performance as cathode material of sodium-ion battery, Appl. Surf. Sci. 499 (2020) 143849. https://doi.org/10.1016/j.apsusc.2019.143849.

[41] H. Lyu, C.J. Jafta, I. Popovs, H.M. Meyer, J.A. Hachtel, J. Huang, B.G. Sumpter, S. Dai, X.G. Sun, A dicyanobenzoquinone based cathode material for rechargeable lithium and sodium ion batteries, J. Mater. Chem. A. 7 (2019) 17888–17895. https://doi.org/10.1039/c9ta04869c.

[42] N. Yabuuchi, K. Kubota, M. Dahbi, S. Komaba, Research Development on Sodium-Ion Batteries, Chem. Rev. 114 (2014) 11636−11682. https://doi.org/10.1021/acs.chemrev.9b00463.

[43] C. Delmas, J.-J. Braconnier, C. Fouassier, P. Hagenmuller, ELECTROCHEMICAL INTERCALATION OF SODIUM IN NaxCoO2 BRONZES, Solid State Ion. 3/4 (1981) 165–169. https://doi.org/10.1016/0167-2738(88)90351-7.

[44] X. Ma, H. Chen, G. Ceder, Electrochemical Properties of Monoclinic NaMnO2, J. Electrochem. Soc. 158 (2011) A1307. https://doi.org/10.1149/2.035112jes.

[45] J. Song, B. Xiao, Y. Lin, K. Xu, X. Li, Interphases in Sodium-Ion Batteries, Adv. Energy Mater. 8 (2018) 1–24. https://doi.org/10.1002/aenm.201703082.

[46] M.H. Han, N. Sharma, E. Gonzalo, J.C. Pramudita, H.E.A. Brand, J.M. Lopez, D. Amo, T. Rojo, Moisture exposed layered oxide electrodes as Na- ion battery cathodes, J. Mater. Chem. A. 4 (2016) 18963–18975. https://doi.org/10.1039/c6ta07950d.

[47] B.S. Kumar, A. Pradeep, A. Dutta, A. Mukhopadhyay, Water-stable O3-type layered Na transition metal oxides enabling environment friendly ‘aqueous processing’ of electrodes with long-term electrochemical stability, J. Mater. Chem. A. 8 (2020) 18064–18078. https://doi.org/10.1039/d0ta05169a.

[48] Z. Lu, J.R. Dahn, Intercalation of Water in P2, T2 and O2 Structure

Az[CoxNi1/3-xMn2/3]O2, Chem. Mater. 13 (2001) 1252–1257. https://doi.org/10.1021/cm000721x.

[49] W. Zuo, A. Innocenti, M. Zarrabeitia, D. Bresser, Y. Yang, S. Passerini, Layered Oxide Cathodes for Sodium-Ion Batteries: Storage Mechanism, Electrochemistry, and Techno-economics, Acc. Chem. Res. 56 (2023) 284−296. https://doi.org/10.1021/acs.accounts.2c00690.

[50] S. Boyd, R. Dhall, J.M. Lebeau, V. Augustyn, Charge storage mechanism and degradation of P2-type sodium transition metal oxides in aqueous electrolytes, J. Mater. Chem. A. 6 (2018) 22266–22276. https://doi.org/10.1039/c8ta08367c.

[51] M. Sathiya, K. Hemalatha, K. Ramesha, J.-M. Tarascon, A.S. Prakash, Synthesis, Structure, and Electrochemical Properties of the Layered Sodium Insertion Cathode Material: NaNi1/3Mn1/3Co1/3O2, Chem. Mater. 24 (2012) 1846−1853.

[52] S. Guo, Q. Li, P. Liu, M. Chen, H. Zhou, Environmentally stable interface of layered oxide cathodes for sodium-ion batteries, Nat. Commun. 8 (2017) 135. https://doi.org/10.1038/s41467-017-00157-8.

[53] Q. Shi, R. Qi, X. Feng, J. Wang, Y. Li, Z. Yao, Q. Li, X. Lu, J. Zhang, Y. Zhao, X. Wang, Q. Li, X. Lu, J. Zhang, Y. Zhao, 1234567890():, Niobium-doped layered cathode material for high-power and low-temperature sodium-ion batteries, Nat. Commun. 13 (2022) 3205. https://doi.org/10.1038/s41467-022-30942-z.

[54] L. Mu, S. Xu, Y. Li, Y. Hu, H. Li, L. Chen, Prototype Sodium-Ion Batteries Using an Air-Stable and Co / Ni-Free O3-Layered Metal Oxide Cathode, Adv. Mater. 27 (2015) 6928–6933. https://doi.org/10.1002/adma.201502449.

[55] Y.-F. Liu, H.-Y. Hu, J.-Y. Li, H. Wang, Y. Zhao, J. Wang, Y.-B. Wu, Y.-J. Li, G.-Y. Zhang, Q.-Q. Sun, Y.-F. Zhu, R.-R. Tang, X.-W. Wu, J.-Z. Wang, S.-X. Dou, S.-L. Chou, Y. Xiao, An air-stable single-crystal layered oxide cathode based on multifunctional structural modulation for high-energy-density sodium-ion batteries, Sci China Chem. 67 (2024) 4242–4250.

[56] H. Yao, Air-stability of sodium-based layered-oxide cathode materials, Sci. China. Chem. 65 (2022) 1076–1087.

[57] Z. Lu, J.R. Dahn, Intercalation of Water in P2 , T2 and O2 Structure Az[CoxNi1/3-xMn2/3]O2, Chem. Mater. 13 (2001) 1252–1257.

[58] K. Shiprath, H. Manjunatha, R. Venkata Nadh, T. Anil Babu, S. Ramesh, K. Chandra Babu Naidu, M. Ramesha, Synthesis and

Electrochemical Characterization of NaCoO2 as Cathode Material in 2M NaOH Aqueous Electrolyte, ChemistrySelect. 6 (2021) 1874–1881. https://doi.org/10.1002/slct.202100294.

[59] V.R. Reddy Boddu, M. Palanisamy, L. Sinha, S.C. Yadav, V.G. Pol, P.M. Shirage, Hysteresis abated P2-type NaCoO2 cathode reveals highly reversible multiple phase transitions for high-rate sodium-ion batteries, Sustain. Energy Fuels. 5 (2021) 3219–3228. https://doi.org/10.1039/d1se00490e.

[60] Y. Takeda, K. Nakahara, M. Nishijima, N. Imanishi, O. Yamamoto, M. Takano, R. Kanno, Sodium deintercalation from sodium iron oxide, Materials Research Bulletin. 29 (1994) 659–666. https://doi.org/10.1016/0025-5408(94)90122-8.

[61] J. Zhao, J.E. Soc, J. Zhao, L. Zhao, N. Dimov, S. Okada, T. Nishida, Electrochemical and Thermal Properties of α- NaFeO 2 Cathode for Na-Ion Batteries, J. Electrochem. Sac. 160 (2013) A3077–A3081. https://doi.org/10.1149/2.007305jes.

[62] Y. Lei, X. Li, L. Liu, G. Ceder, Synthesis and Stoichiometry of Di ff erent Layered Sodium Cobalt Oxides, Chem. Mater. 26 (2014) 5288−5296.

[63] J.A.K. Satrughna, A.R. Kanwade, P.M. Shirage, Synergistic effect of multi-transition metal co- substitution in high cycle life performance of NaxCo0.5Fe0.25Mn0.25O2 cathode for sodium-ion batteries, Sustain. Energy Fuels. (2025). https://doi.org/10.1039/d5se00107b.

[64] S.P. Ong, V.L. Chevrier, G. Hautier, A. Jain, C. Moore, S. Kim, X. Ma, G. Ceder, Voltage, stability and diffusion barrier differences between sodium-ion and lithium-ion intercalation materials, Energy Environ. Sci. 4 (2011) 3680–3688. https://doi.org/10.1039/c1ee01782a.

[65] F. Wei, Q. Zhang, P. Zhang, W. Tian, K. Dai, L. Zhang, J. Mao, G. Shao, Review—Research Progress on Layered Transition Metal Oxide Cathode Materials for Sodium Ion Batteries, J. Electrochem. Soc. 168 (2021) 050524. https://doi.org/10.1149/1945-7111/abf9bf.

[66] Q. Wang, S. Chu, S. Guo, Progress on multiphase layered transition metal oxide cathodes of sodium ion batteries, Chin. Chem. Lett. 31 (2020) 2167–2176. https://doi.org/10.1016/j.cclet.2019.12.008.

[67] Z. Lua, J.R. Dahn, In Situ X-Ray Diffraction Study of P2-Na2/3[Ni1/3Mn2/3]O2, J. Electrochem. Soc. 148 (2001) A1225–A1229. https://doi.org/10.1149/1.1407247.

[68] A. Banerjee, N. Khossossi, W. Luo, R. Ahuja, Promise and reality of organic electrodes from materials design and charge storage

perspective, J. Mater. Chem. A. (2022). https://doi.org/10.1039/d2ta00896c.

[69] M. Leng, J. Bi, Z. Xing, W. Wang, X. Gao, J. Wang, A new perspective on the composition-structure-property relationships on Nb/Mo/Cr-doped O3-type layered oxide as cathode materials for sodium-ion batteries, Chemical Engineering Journal. (2020) 127824. https://doi.org/10.1016/j.cej.2020.127824.

[70] W.L. Pang, X.H. Zhang, J.Z. Guo, J.Y. Li, X. Yan, B.H. Hou, H.Y. Guan, X.L. Wu, P2-type Na2/3Mn1-xAlxO2 cathode material for sodium-ion batteries: Al-doped enhanced electrochemical properties and studies on the electrode kinetics, J. Power Sources. 356 (2017) 80–88. https://doi.org/10.1016/j.jpowsour.2017.04.076.

[71] Q.C. Wang, E. Hu, Y. Pan, N. Xiao, F. Hong, Z.W. Fu, X.J. Wu, S.M. Bak, X.Q. Yang, Y.N. Zhou, Utilizing Co2+/Co3+ Redox Couple in P2-Layered Na0.66Co0.22Mn0.44Ti0.34O2 Cathode for Sodium-Ion Batteries, Adv. Sci. 4 (2017) 1–8. https://doi.org/10.1002/advs.201700219.

[72] C. Zhao, Z. Yao, Q. Wang, H. Li, J. Wang, M. Liu, S. Ganapathy, M. Wagemaker, Y. Lu, J. Cabana, B. Li, X. Bai, L. Chen, Y. Hu, Revealing High Na-Content P2-Type Layered Oxides as Advanced Sodium-Ion Cathodes, J. Am. 142 (2020) 5742−5750. https://doi.org/10.1021/jacs.9b13572.

[73] Y. Wang, Y. Ding, L. Pan, Y. Shi, Z. Yue, Y. Shi, G. Yu, Understanding the Size-Dependent Sodium Storage Properties of Na2C6O6-Based Organic Electrodes for Sodium-Ion Batteries, Nano Lett. 16 (2016) 3329–3334. https://doi.org/10.1021/acs.nanolett.6b00954.

[74] Z. Shan, Y. He, T. Tan, Y. Zhang, X. Wang, Preparation of Na4Mn9O18/carbon nanotube/reduced graphene oxide by spray drying as cathode materials for sodium ion batteries, Solid State Sci. 94 (2019) 77–84. https://doi.org/10.1016/j.solidstatesciences.2019.05.019.

[75] Q. Chu, X. Wang, Q. Li, X. Liu, The tunnel manganese oxide Na4.32Mn9O18: A new Na+ site discovered by single-crystal X-ray diffraction, Acta Cryst. 67 (2011) i10–i12. https://doi.org/10.1107/S0108270110052856.

CHAPTER 2

Experimental Methods and Characterization Techniques

This chapter presents the experimental methodologies adopted for the synthesis and sophisticated advanced characterizations used for the comprehensive physicochemical and electrochemical characterization of advanced cathode materials developed for SIB applications. Layered tunnel-type TMO and polyanionic compounds, including $NaCoO_2$, $Na_{0.8}Fe(SO_4)_2$, $Na_xCo_{0.5}Fe_{0.25}Mn_{0.25}O_2$, $Na_{1.35}CrO_4$, *and* $Na_4Mn_{7.2}Cr_{1.8}O_{18}$, *were successfully synthesized via sol-gel and solid-state methods under controlled conditions. The physicochemical properties of the as-synthesized materials were systematically investigated using a range of advanced techniques such as X-ray diffraction (XRD), scanning and transmission electron microscopy (SEM/TEM), energy-dispersive X-ray spectroscopy (EDX), Fourier-transform infrared spectroscopy (FTIR), Raman spectroscopy, and thermogravimetric analysis (TGA). Electrode preparation, coin-cell fabrication, and electrochemical characterization comprising galvanostatic charge-discharge (GCD) measurements, cyclic voltammetry (CV), and electrochemical impedance spectroscopy (EIS) are described in detail. This chapter establishes the foundation for interpreting structure-performance relationships in the cathode materials discussed in subsequent chapters.*

2.1 Chemicals and Precursors Used

The selection of high-purity chemical precursors is crucial in developing advanced cathode materials for SIBs, as the stoichiometry and quality of the starting chemicals can severely affect the structure, performance, and stability. All the chemicals were purchased from Alfa Aesar and Merck Specialties Pvt. Ltd. and directly used as received without any further purification to retain the original stoichiometry.

2.1.1 Chemicals for Cathode Synthesis

Analytical grade precursors of sodium nitrate ($NaNO_3$), cobalt nitrate hexahydrate ($Co(NO_3)_2.6H_2O$), citric acid monohydrate ($C_6H_8O_7.H_2O$), iron(III) nitrate nonahydrate ($Fe(NO_3)_3.9H_2O$), ammonium sulphate ($(NH_4)_2SO_4$), sodium carbonate (Na_2CO_3), manganese(III) oxide (Mn_2O_3), ferric oxide (Fe_2O_3), tricobalt tetraoxide (Co_3O_4), chromium(III) oxide (Cr_2O_3), chromium (III) nitrate nonahydrate ($Cr(NO_3)_3.9H_2O$), and manganese(II) carbonate ($MnCO_3$) were utilized for the synthesis of $NaCoO_2$, $Na_{0.8}Fe(SO_4)_2$, $Na_xCo_{0.5}Fr_{0.25}Mn_{0.25}O_2$, $Na_{1.35}CrO_4$, and $Na_4Mn_{7.2}Cr_{1.8}O_{18}$ electrodes for SIBs. We used deionized water as the universal solvent, as well as ethanol and acetone, for cleaning purposes.

2.1.2 Chemicals for Electrode Fabrication

Our synthesized materials worked as the primary active materials for electrode fabrication. In addition, PVDF was used as the thermoplastic-based molecular binder, and Super P-CB was used as a conductive additive for electrode preparation. The solvent NMP was used to prepare the electrode slurry. Pure battery-grade aluminum (Al) and copper (Cu) foils were used as current collectors. Highly pure Na metal chips were used as the counter anode material with respect to our synthesized active materials as cathodes. The Na-metal chief acted as both the counter and reference electrode, and all the measurements were performed with respect to Na/Na^+ in the sodium-half cell configuration.

2.2 Material Synthesis Methods

The synthesis methods adopted for the preparation of cathode materials play a crucial role in determining various properties of the cathode materials, including the structural, morphological, and electrochemical properties of SIBs. In this thesis work, mainly two principal synthesis approaches, (i) sol-gel [1,2] and (ii) solid-state reaction [3–5] methods were used due to their respective advantages for the preparation of phase-pure and compositionally controlled sodium-based TMO and sulfate cathode materials. The subsequent sections briefly elaborate on these synthesis approaches.

2.2.1 The Sol-Gel Synthesis Method

Sol-gel synthesis is a commonly used wet-chemical method for the preparation of sodiated metal oxides and phosphates-based cathodes for SIBs [1,2,6–9]. In this method, the metal precursors are dissolved in an appropriate solvent, such as DI water, and chelated by adding complexing agents, such as citric acid or ethylene glycol, to form a stable sol. By gradually heating the sol at around 80-120ºC, the evaporation and polymerization process takes place, which converts the sol into gel. The gel is further dried and calcined at high temperatures to produce crystalline materials in powder form. The controlled mixing at the molecular level provides a uniform elemental distribution and fine particle morphology.

Compared to other synthesis methods, sol-gel has several key benefits. It requires lower synthesis temperatures due to the homogeneous precursor distribution, reducing energy cost and preventing phase segregation. It has better control over the particle size, morphology, and crystallinity, which is crucial for improving ionic/electronic conductivity and cycling stability. Further, it allows for the addition of dopants at atomic-scale accuracy. These benefits make the sol-gel method one of the most appropriate for high-performance cathode synthesis for SIBs. Hence, we adopted this synthesis method for the preparation of $NaCoO_2$, $Na_{0.8}Fe(SO_4)_2$, and $Na_{1.35}CrO_4$ for SIBs, as discussed below.

2.2.1.1 Synthesis of $NaCoO_2$ through Sol-Gel

The detailed synthesis approach for the preparation of $NaCoO_2$ through the sol-gel technique is represented in **Figure 2.1** [2]. Initially, 100 mL of DI water was divided into 40, 40, and 20 mL in separate beakers. Stoichiometric amounts of $NaNO_3$ (977.39 mg), $Co(NO_3)_2{\cdot}6H_2O$ (2910.3 mg), and $C_6H_8O_7{\cdot}H_2O$ (2101.4 mg) in a ratio of 1.15:1:1 were dissolved in separate beakers containing 40, 40, and 20 mL of DI water, respectively, to make their complete miscible solutions. The extra Na precursor was used to compensate for Na loss at the higher calcination temperature. $NaNO_3$ solution and $Co(NO_3)_2{\cdot}6H_2O$ solution were mixed in a single beaker and allowed for continuous stirring at 30ºC for about 3 h. Subsequently, the $C_6H_8O_7{\cdot}H_2O$ solution was added, and the mixture was heated to 9 ºC with continuous stirring until it formed a gel. The gel was then transferred to a muffle furnace at 125ºC for about 12 h to dry the gel, resulting in an ash-like powder, which was ground and proceeded for calcination at 700, 800, and 900ºC to identify the optimal synthesis calcination temperature. The final calcined powders were ground and stored in a moisture-free environment.

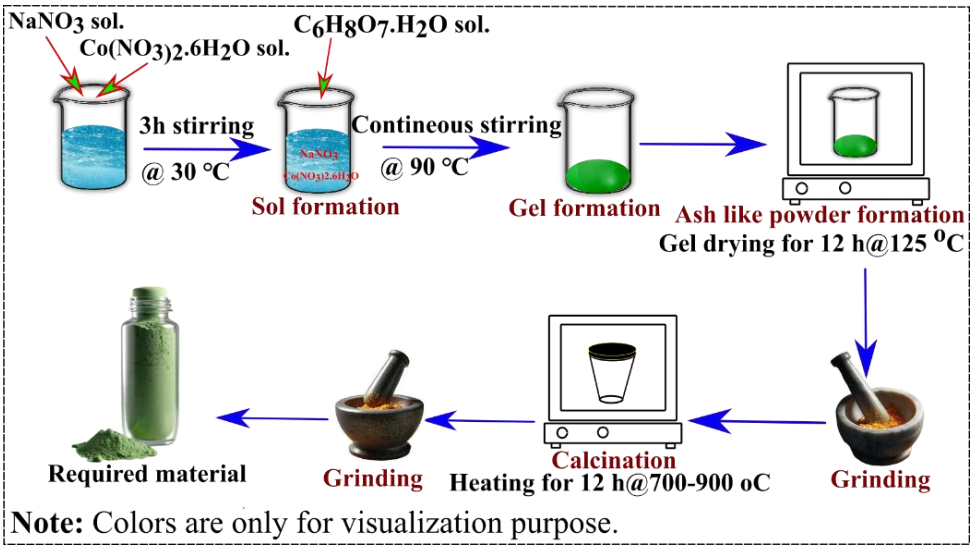

Figure 2.1 Sol-gel synthesis scheme for $NaCoO_2$ [2].

2.2.1.2 Synthesis of $Na_{0.8}Fe(SO_4)_2$ through Sol-Gel

$Na_{0.8}Fe(SO_4)_2$ cathode for SIBs was synthesized *via* citric acid-assisted simple sol-gel method as shown in **Figure 2.2(a)**. The precursors $NaNO_3$, $Fe(NO_3)_3 \cdot 9H_2O$, $(NH_4)_2SO_4$, and $C_6H_8O_7.H_2O$ were taken in 0.9:1:2:1 molar ratio. The excess ~10% of sodium source material was taken to balance the sodium loss during the heat treatment. In the beginning, a highly pure DI water of 100 mL was taken and separated into four beakers, each containing 25 mL. 764.9523 mg, 4040 mg, 2642.8 mg, and 2101.4 mg of $NaNO_3$, $Fe(NO_3)_3 \cdot 9H_2O$, $(NH_4)_2SO_4$, and $C_6H_8O_7.H_2O$, respectively, were added to the separate beakers, each containing 25 mL DI water, and stirred at room temperature. Then the $NaNO_3$, $Fe(NO_3)_3 \cdot 9H_2O$, and $(NH_4)_2SO_4$ solutions were mixed and allowed to continuously mix through a magnetic stirrer for about 2 hrs in a silicone oil bath at 50°C until a homogenized solution was formed, as shown in **Figure 2.2(a)**.

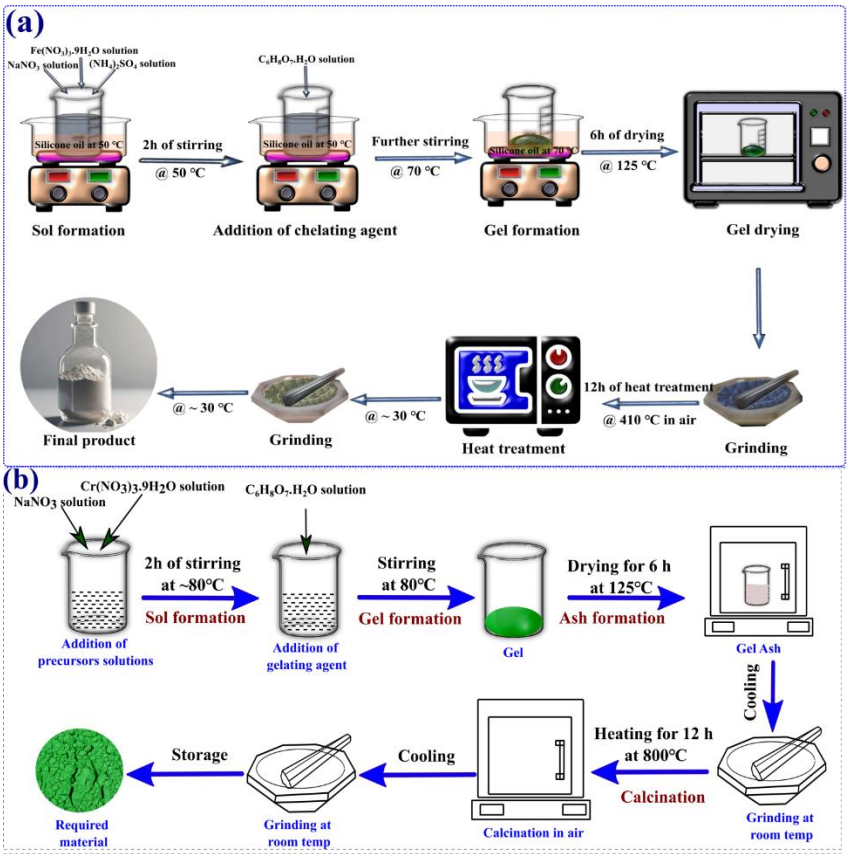

Figure 2.2 Sol-gel-based synthesis of **(a)** $Na_{0.8}Fe(SO_4)_2$ and **(b)** $Na_{1.35}CrO_4$.

Here, the silicone oil bath was used to provide a uniform temperature to the solution from all around. After that, $C_6H_8O_7.H_2O$ solution as the chelating agent was added dropwise. Then, with continuous stirring, the temperature of the silicon bath was raised to 70°C until a gel-like form was achieved. Then the gel solution was dried for the next 6 hrs at 125°C in the furnace. Once the gel was completely dried, it turned into an ash-like form, which was ground and taken in an alumina crucible and allowed for calcination at 410°C with a ramping rate of 5°C/min for 12 hrs in a tube furnace to achieve the final materials. After calcination, the material was thoroughly ground into fine particles at room temperature and stored in a desiccator for further characterization.

2.2.1.3 Synthesis of $Na_{1.35}CrO_4$ through Sol-Gel

The synthesis of $Na_{1.35}CrO_4$ electrode for SIBs through a simple citric acid-assisted sol-gel method is illustrated in **Figure 2.2(b)**. A total of 100 mL of DI water as solvent was taken in three portions of 40 mL, 40 mL, and 20 mL to prepare the solutions of $NaNO_3$, $Cr(NO_3)_3$, and $C_6H_8O_7$**,** respectively, using their stoichiometric amounts. The $NaNO_3$ and $Cr(NO_3)_3$ solutions are mixed in a single beaker and stirred at 80°C for about 2 hours to obtain a homogeneous solution. Subsequently**,** the $C_6H_8O_7$ solution as a chelating agent was added, followed by stirring at 80°C until a gel-like semisolid phase formed. The resulting gel was dried in a muffle furnace at 125°C for about 6 hours, forming an ash-like compound, then finely ground. The dried powder was annealed at 800°C for 12 hours in the air to form phase-pure $Na_{1.35}CrO_4$ material. The resultant product was thoroughly ground into fine particles to obtain the final $Na_{1.35}CrO_4$ material.

2.2.2 The Solid-State Synthesis Method

Solid-state synthesis is one of the most commonly used methods for the preparation of SIBS cathodes. This method has the advantages of simplicity in operation and scalability, making it suitable for mass production. In this synthesis method, stoichiometric amounts of solid precursors, usually metal oxides, carbonates, or sulfates, are thoroughly

mixed by ball milling or grinding and then subjected to high-temperature calcination to promote solid-state reactions and phase development. The high temperatures of heating (700-1000°C) allow for diffusion and crystallization, resulting in extremely stable and well-defined crystallinity. This method is less costly, environmentally friendly, and compatible with materials that need high thermal energy. It is particularly beneficial for synthesizing high-strength structures such as tunnel-type and layered oxides, where high-temperature calcination enhances crystallinity and structural integrity. Solid-state synthesis also avoids the utilization of drying, gelation, or chelating agents, simplifying the synthesis process. Large-scale preparation and industrial translation are facilitated by its scalability and reproducibility, rendering it a useful method [10,11]. Hence, inspired by the above, we prepared $Na_xCo_{0.5}Fe_{0.25}Mn_{0.25}O_2$ and $Na_4Mn_{7.2}Cr_{1.8}O_{18}$ cathodes through this synthesis method for their better phase purity, crystallinity, and electrochemical performance for SIBs.

2.2.2.1 Synthesis of $Na_xCo_{0.5}Fe_{0.25}Mn_{0.25}O_2$

$Na_xCo_{0.5}Fe_{0.25}Mn_{0.25}O_2$ was synthesized through a conventional and simple solid-state method by a two-step heating approach, as shown in **Figure 2.3**. Initially, stoichiometric amounts of Na_2CO_3, Co_3O_4, Fe_2O_3, and Mn_2O_3 in a molar ratio of 0.5:0.167:0.125:0.125, having, were mixed and ground properly for 45 minutes in a mortar and pestle. Then, the first step of heating was performed by annealing the powder at 750°C for 2 h in a muffle furnace.t The powder was ground at room temperature, followed by the 2nd step of the heating process of calcination at 700°C for 10h in air. The obtained final material was ground into fine particles for further analysis.

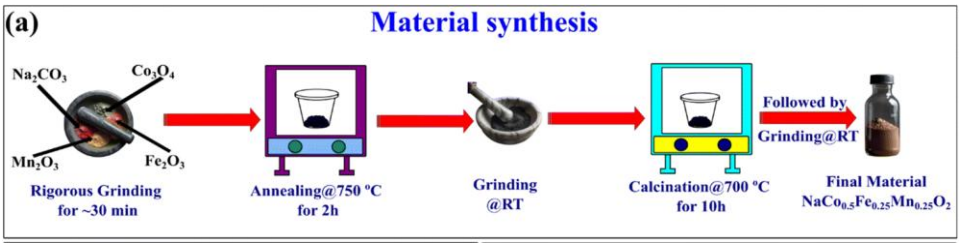

Figure 2.3 Synthesis of $Na_xCo_{0.5}Fe_{0.25}Mn_{0.25}O_2$ cathode for SIBs [12].

2.2.2.2 Synthesis of $Na_4Mn_{7.2}Cr_{1.8}O_{18}$

$Na_4Mn_{7.2}Cr_{1.8}O_{18}$ as active cathode material for SIBs was synthesized through a conventional and straightforward solid-state method, as shown in **Figure 2.5**. A precisely weighted (Na_2CO_3, $MnCO_3$, and Cr_2O_3 in a molar ratio of 0.4:0.8:0.1 was thoroughly mixed and ground in an agate mortar and pestle for approximately one hour until a homogeneous fine powder was achieved. The extra precursor of Na was taken to balance the loss of sodium during the high-temperature heating process. The first heating step of annealing was performed for the resulting powder at 750°C for 12 h in a muffle furnace, using an alumina crucible. After cooling to room temperature, the resulting product was ground again for about 15 minutes to break any formed agglomerates and ensure consistent particle size. Then, the second heating process of calcination is carried out by heat treatment for 12 h at temperatures of 700, 800, and 900°C. This prolonged heat treatment facilitates the formation of the desired crystalline phase of $Na_4Mn_{7.2}Cr_{1.8}O_{18}$ while ensuring the complete reaction between the precursors. The final resulting materials were further ground to obtain a fine, uniform powder, as shown in **Figure 2.4**. This two-step heating approach ensures the material's high phase purity and structural integrity as a cathode material for SIBs. **Table 2.1** represents the materials synthesis methods, key precursors, and final calcination temperature.

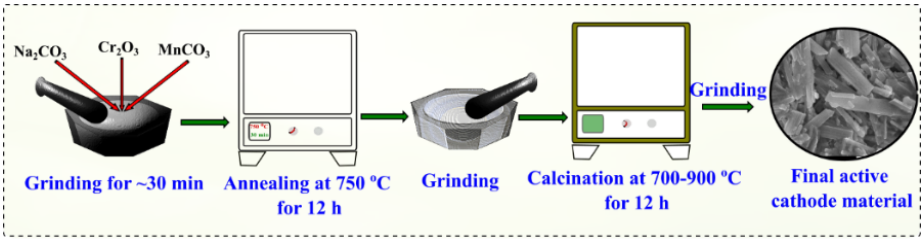

Figure 2.4 Solid state-based synthesis of $Na_4Mn_{7.2}Cr_{1.8}O_{18}$ cathode.

2.3 Electrode Fabrication and Coin Cell Assembly

Before evaluating the electrochemical performance of the cathode materials in SIBs, there is a series of systematic processes that must be followed for electrode fabrication and cell assembly, as discussed below.

Table 2.1: List of cathode materials, their synthesis methods, precursors used, and final calcination temperature.

Material	Method	Key Precursors	Calcination
$NaCoO_2$	Sol-gel	$NaNO_3$, $Co(NO_3)_2$, $C_6H_8O_7.H_2O$	700-900°C
$Na_{0.8}Fe(SO_4)_2$	Sol-gel	$NaNO_3$, $Fe(NO_3)_3$, $(NH_4)_2SO_4$, $C_6H_8O_7.H_2O$	410°C
$Na_{1.35}CrO_4$	Sol-gel	$NaNO_3$, $Cr(NO_3)_3.9H_2O$, $C_6H_8O_7.H_2O$	800°C
$Na_xCo_{0.5}Fe_{0.25}Mn_{0.25}O_2$	Solid-state	Na_2CO_3, Co_3O_4, Fe_2O_3, Mn_2O_3	700-750°C
$Na_4Mn_{7.2}Cr_{1.8}O_{18}$	Solid-state	Na_2CO_3, $MnCO_3$, Cr_2O_3	700-900°C

2.3.1 Electrode Fabrication

The fabrication of electrodes from the active cathode materials plays a pivotal role in assessing their intrinsic properties. This involves several systematic procedures as explained below. Each of these steps has its importance to ensure reproducibility and reliable battery performance data.

2.3.1.1 Electrode Slurry Preparation

Slurry was prepared by mixing active material with CB as a conductive additive and PVDF as a polymeric binder in NMP solvent. The ratio of these materials was used in their optimal proportion by taking the ratios of active material: PVDF: CB as 8:1:1 (for $NaCoO_2$, $Na_{1.35}CrO_4$, and $Na_xCo_{0.5}Fe_{0.25}Mn_{0.25}O_2$), 7:1.5:1.5 (for $Na_{0.8}Fe(SO_4)_2$), and 7:1:2 ($Na_4Mn_{7.2}Cr_{1.2}O_{18}$). **Figure 2.5** shows the slurry preparation process.

2.3.1.2 Coating on Current Collectors

The homogeneously mixed slurries were uniformly coated onto battery-grade Al foil current collector substrates using a doctor blade technique to control the thickness of the electrode, as shown in **Figure 2.5**.

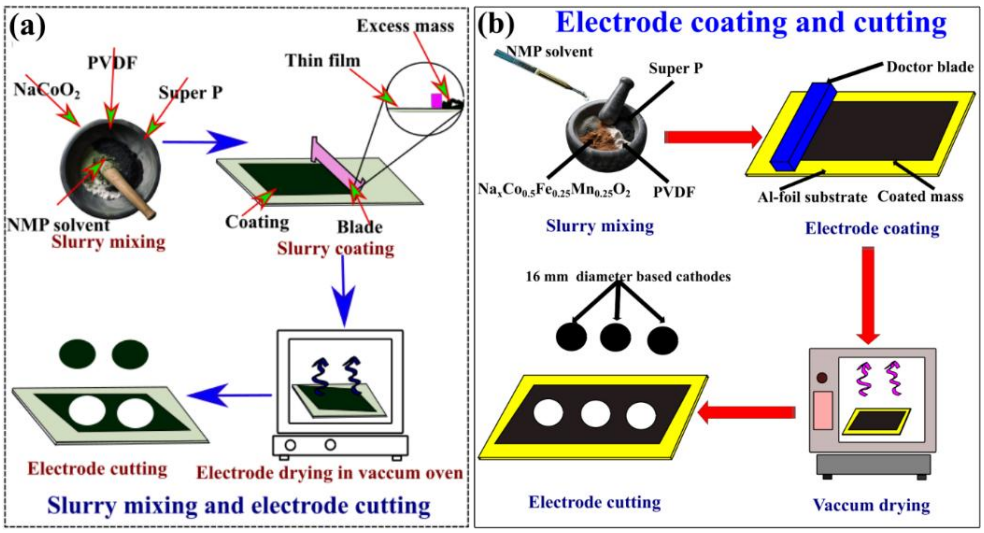

Figure 2.5 Electrode slurry preparation process for (a) $NaCoO_2$ [2] and (b) $Na_xCo_{0.5}Fe_{0.25}Mn_{0.25}O_2$ [12] materials.

2.3.1.3 Drying and Hot Roller Pressing

The coated electrodes were dried inside the vacuum oven at 120°C for 12 hours to remove residual NMP solvent and to enhance binder adhesion, as shown in **Figure 2.5**. After drying, the electrodes were uniformly pressed via a hot roller press to obtain uniform thickness, better adhesion with the current collector, and better particle-to-particle contact.

2.3.1.4 Electrode Cutting and Active Mass Calculation

The electrodes were punched into circular discs of 1.6 cm diameter with the help of a precision electrode punch, as shown in **Figure 2.5**, and the active mass coated on each electrode was measured. The typical active mass loading per electrode was measured to be in the range of 1.5–2.5 mg/cm^2. All electrode discs were stored in a dry, inert atmosphere (argon-filled glove box) until cell assembly to prevent moisture and air degradation.

2.4 Coin Cell Assembly

The CR2032-type coin cells, having a dimension of 20 mm in diameter and 3.2 mm in thickness, were assembled in an N_2 gas-filled glove box to carry out the electrochemical performance. These coin cells were assembled in a sodium half-cell configuration, where highly pure sodium

metal chips were used as both the counter and reference electrodes. In the cell assembly process, the glass microfiber was used as a separator, whereas 1M $NaClO_4$ in PC and EC in 1:1 v/v were used as electrolytes. In addition, we have optimized the performance of $Na_{0.8}Fe(SO_4)_2$ with different electrolytes, which will be discussed in Chapter 4. All of these important components of SIBs are precisely assembled in a coin cell configuration. **Figure 2.6** represents the sequence of the Na-half coin cell assembling process. The whole coin cell assembly process was carried out inside the N_2-filled glove box by maintaining O_2 and H_2O levels below 0.1 ppm to prevent side reactions. The coin cells were sealed using a hydraulic crimping machine and rested for 12 h [12–15].

The ideal conditions for electrodes used in estimating cell voltage required (i) use of highly pure and stable sodium-metal as counter/reference electrodes, (ii) careful assembly under an inert atmosphere (such as argon or nitrogen) glove box to avoid moisture and oxygen contamination, (iii) uniform electrode-electrolyte contact to minimize interfacial contact, (iv) maintaining stable electrolyte composition to prevent side reactions, and (v) all electrodes must provide reversible and reliable electrochemical responses for accurate voltage estimation in SIBs studies. Under these controlled conditions, the measured potentials reliably represent the redox activity of the cathode materials against the Na/Na^+.

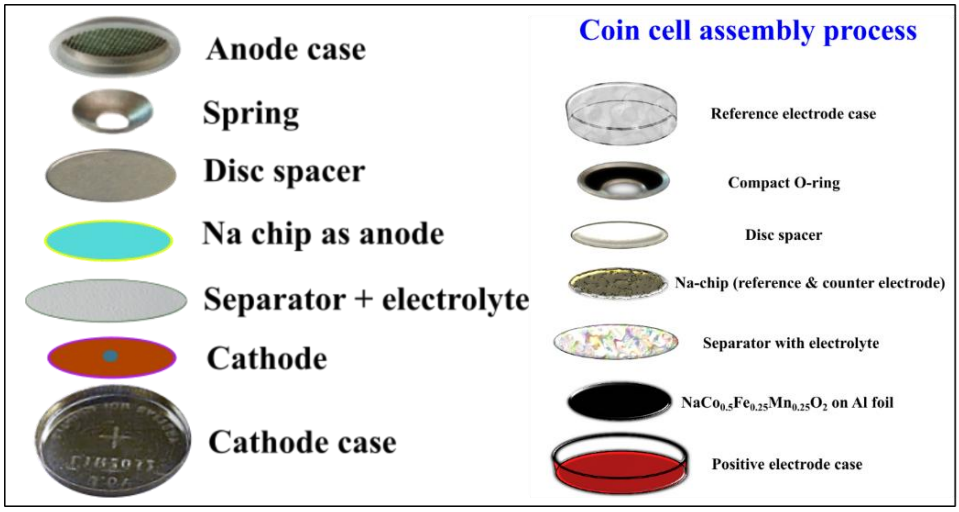

Figure 2.6 Sodium half-cell assembly process [12].

2.5 Physicochemical Characterization Techniques

A comprehensive suite of advanced physicochemical characterization techniques was employed to thoroughly investigate the physical properties, such as phase, symmetry, thermal behavior, particle size, surface morphology, atomic arrangement, and chemical features such as stoichiometry, elemental oxidation states, chemical environment, *etc.,* of the synthesized cathode material for SIBs. TGA, Derivative Thermogravimetric (DTG), and Differential Scanning Calorimetry (DSC) were used to investigate thermal behaviors such as thermal stability, decomposition of the precursors, and phase-pure synthesis of cathode materials. Powder XRD, having Cu-Kα radiation with wavelength $\lambda = 1.542$ Å, was used to analyze the phase purity, crystalline structure, and lattice parameters. Field Emission Scanning Electron Microscopy (FESEM) integrated with Energy Dispersive X-ray Spectroscopy (EDS) was used to explore the particle and surface morphology, particle size distribution, elemental homogeneity, and empirical stoichiometry. However, the exact stoichiometry and elemental composition of the synthesized cathode material were further confirmed by Inductively Coupled Plasma Optical Emission Spectroscopy (ICP-OES). Raman spectroscopy analysis was used to study the bonding nature and the vibrational features. High-resolution imaging, atomic structural arrangements, lattice interplanar spacing, and structural details at the atomic level in the nanoscale range were understood through TEM, High-Resolution TEM (HRTEM), and Selected Area Electron Diffraction (SAED) patterns. The chemical states and oxidation environments of the elements in the cathode material were investigated through X-ray Photoelectron Spectroscopy (XPS). A brief discussion of these advanced techniques is given in the following subsections.

2.5.1 Thermal Analysis Techniques: TGA, DTG, and DSC

The thermal behaviors of the synthesized cathode materials for SIBs were analyzed with the help of TGA, DTG, and DSC. These analyses were performed through the PerkinElmer STA8000 system under N_2 gas flow at

a heating rate of 5 °C/min to 10°C/min in the temperature range of room temperature to up to 1000 °C. The mass change of a sample with respect to temperature in a controlled environment (oxidative or inert) could be understood by TGA, allowing direct investigation of thermal stability, decomposition mechanisms, residual organics, and inorganic content. The basic operational principle of a TGA device consists of suspending the sample (loaded into a Pt or Al_2O_3 crucible) on a highly sensitive balance protectively placed inside a thermally controlled furnace, in which heat-induced changes like desorption, pyrolysis, oxidation, and structure decomposition cause measurable mass loss [16]. TGA profile mainly exhibits three predominant mass-loss regimes, 1st mass loss between 50-200°C corresponding to the evaporation of physically adsorbed or the water molecules trapped inside the lattice; 2nd mass loss between 200-600°C attributed to the thermal decomposition of precursors; and the 3rd major mass loss beyond 600°C representing the thermal degradation or the crystallographic reordering of the material [16,17].

The DTG curve defines the precise temperature at which the decomposition processes occur. Whereas the DSC is used to identify endothermic and exothermic processes. The detailed analyses of TGA, DTG, and DSC provide a comprehensive thermal characterization of cathode materials for SIB cathodes [18–20].

2.5.2 X-ray Diffraction (XRD) for Phase Analysis

XRD is a widely used, versatile non-destructive characterization tool that is commonly used to study the structure and phase characteristics of crystalline materials. It provides valuable information on the crystallinity, phase purity, and lattice parameters. It is useful in determining the successful synthesis of targeted cathode material for SIBs. The working principle of XRD is based on Bragg's Law, which defines the constructive interference of monochromatic X-rays diffracted by parallel atomic planes in a crystal lattice and is given by:

$$n\lambda = 2\ d\ sin\theta$$

where n is a positive integer representing the order of reflection, λ is the wavelength of the X-rays (usually 1.5406 Å for Cu-Kα X-rays radiation), d is the interplanar distance, and θ is the angle of incidence with the lattice planes. Under this condition, sharp diffraction peaks are generated corresponding to the specific crystallographic structure and phase of the material [21–23]. The working principle of an XRD and its common components of the device are shown in **Figure 2.7**.

The XRD generates a sharp diffracted peak pattern corresponding to the distinctive crystallographic planes. Peaks are compared against standard reference data to determine crystalline phases and assess phase purity. In more intricate or multiphase systems, Rietveld refinement is utilized to retrieve precise structural parameters, including unit cell parameters, atomic positions, and phase proportions, by adapting the experimental pattern to a computed model. XRD can also calculate the crystallite size (L) through the Scherrer equation, as given below, which assumes that peak broadening is solely due to small crystallite size, the crystals are strain-free and uniformly sized, and X-rays are monochromatic with instrumental broadening corrected.

$$L = \frac{k\,\lambda}{\beta\,\cos\theta}$$

Where K is a shape factor (approximately 0.9), β is the full width at half maximum (FWHM) of the diffraction peak (in radians), and θ is the Bragg angle. Although XRD has some drawbacks in identifying amorphous or complicated overlapping phases, it is still a crucial tool for structural identification in many fields. In the current thesis, XRD, as a physicochemical characterization technique, was utilized to confirm the formation, purity, and crystallinity of the cathode materials for SIBs.

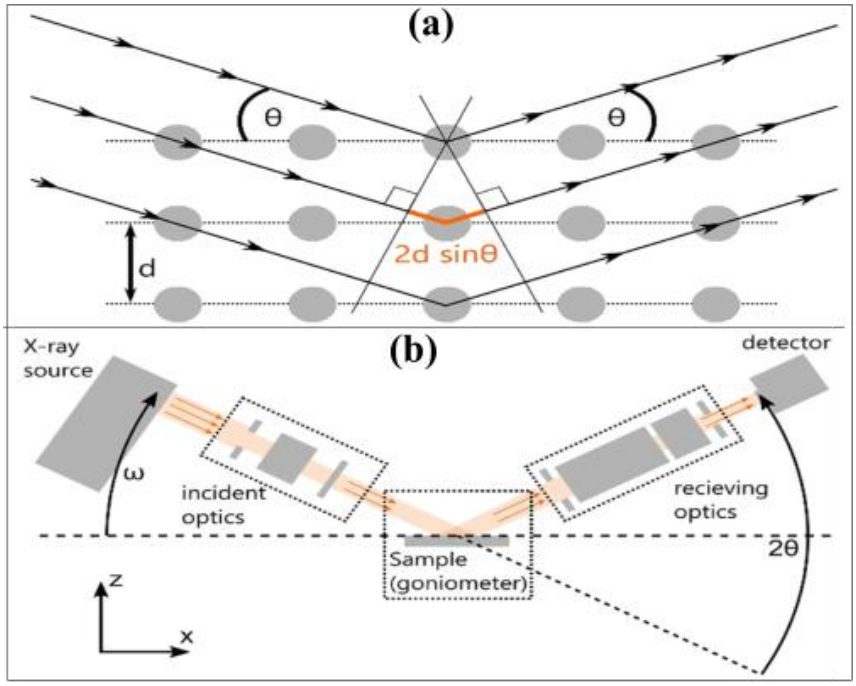

Figure 2.7 (a) Working principle based on Bragg's Law, and (b) Basic components of XRD [24].

2.5.3 FESEM, Color Mapping, and EDX/EDS

FESEM combined with EDS is one of the fundamental analysis tools for high-resolution morphological and compositional investigation of nanostructured materials, including cathodes for SIBs. FESEM uses a field emission gun that produces a high-brightness, narrow, coherent electron beam, allowing imaging resolutions as low as ~1.5 nm at magnifications of up to 300,000×. It works at low accelerating voltages of about 0.5–30 kV, which helps to reduce the charging of the samples and avoid frequent usage of conductive coatings. It helps to retain the surface details. The electron scattering in FESEM is shown in **Figure 2.8 (a)** [25], where the electron beam interacts with the specimen to produce backscattered electrons (BSEs), secondary electrons (SEs), and characteristic X-rays. SEs provide topographic contrast, while BSEs provide information on compositional variations in atomic number differences. This allows for precise imaging of particle morphology and surface texturing. FESEM is integrated with EDS, which monitors element-specific X-ray emissions due to inelastic

scattering. Elemental mapping and line scans provide compositional gradients, phase distribution, and impurities [26–28]. **Figure 2.8 (b)** shows FESEM-EDS instrumentation. JSM-7610F Plus, JEOL FESEM was utilized in this research. EDS analysis provides elemental composition

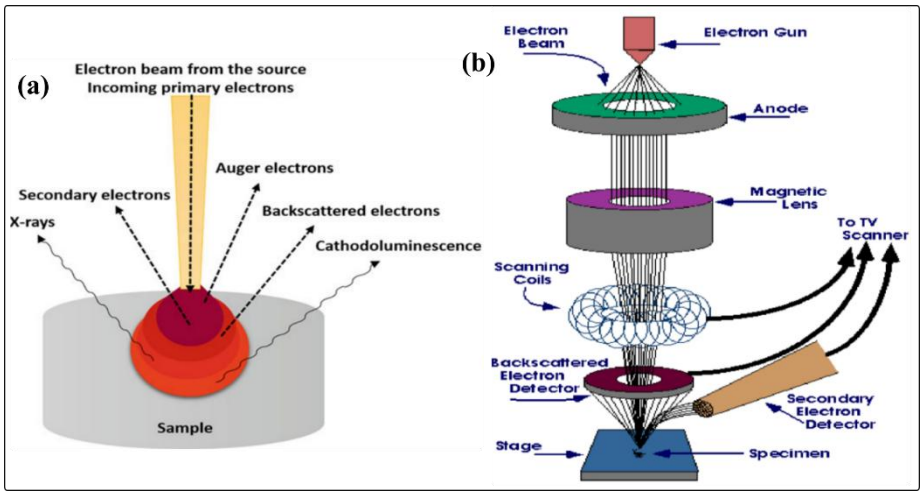

Figure 2.8 (a) Interaction of electron beam with sample in FESEM [25]. (b) Schematic for FESEM-EDS instrumentation [27].

2.5.4 ICP-OES for Quantitative Stoichiometry Analysis

ICP-OES is a strong, high-throughput quantitative multi-element analytical technique. It is primarily used to quantitatively detect many elements, even in extremely low concentrations of parts per billion (ppb) to parts per million (ppm) range. Hence, it is an important quantitative tool in material science to evaluate bulk composition, dopant concentration, and contamination. In ICP-OES, the sample in a solution of diluted nitric acid is nebulized into an aerosol, which is carried into a high-temperature argon plasma (6000-10,000 K) maintained by a radiofrequency (RF) induction coil. In this high-temperature-based plasma, the atoms and ions are thermally excited; on returning to the ground state, they emit element-specific photons. The radiated light is scattered with a diffraction grating and measured with a photomultiplier tube (PMT) or charge-coupled device (CCD) [2,15,28–30]. The intensity of every spectral line is proportional to the concentration of the respective element, determined through calibration

with standard solutions. **Figure 2.9** schematically shows the components of the ICP-OES.

ICP-OES was utilized to quantitatively determine the elemental content and stoichiometry of cathode materials. For this, the powder cathode samples were properly digested by diluted HNO_3 and HCL acid in a 3:1 ratio (~96% of DI water and ~4% of acids). Further, the solution for the calibration process is formed by preparing the standard solution with different concentrations. ICP-OES possesses several advantages over surface-sensitive methods, such as EDS, with the benefits of bulk elemental analysis and better sensitivity for light and trace elements [2,15,28–30].

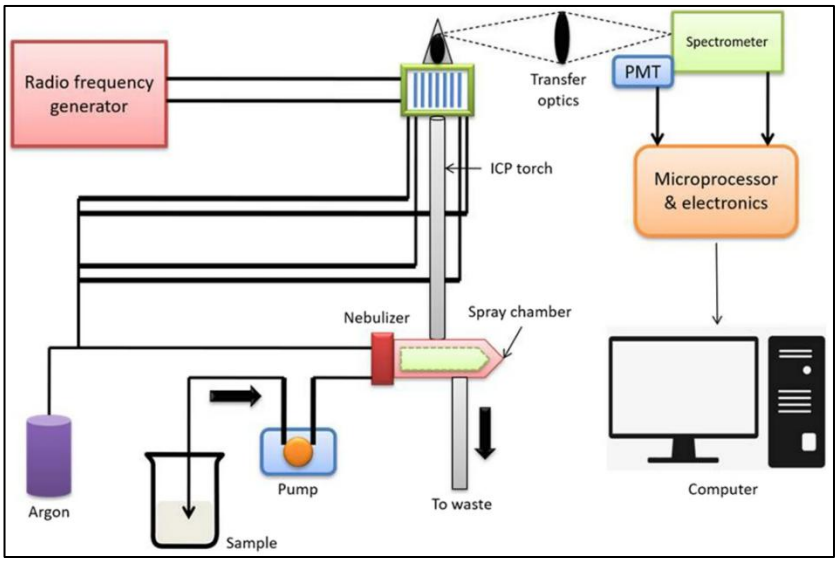

Figure 2.9 Schematic for the instrumentation of the ICP-OES [30].

2.5.5 Raman Spectroscopy

Raman spectroscopy is a non-destructive vibrational spectroscopic method that provides crucial information about the molecular structure, phase composition, and bonding features of the materials by analyzing the inelastic scattering of monochromatic light. The underlying principle of Raman spectroscopy is inelastic scattering (Raman scattering) of photons, in which the incident photons interact with phonons (which are the molecular vibrations) or other excitations in the sample. A small portion of the scattered light undergoes an energy shift, Stokes or anti-Stokes shifts,

which corresponds to specific vibrational modes of the molecules or crystal lattice. In Raman spectroscopy, a monochromatic laser (typically 532 nm or 785 nm) is focused onto the sample surface. The light that has been scattered off the sample is collected, filtered for removal of Rayleigh (elastic) scattering, and subsequently dispersed by a grating onto a CCD detector. The resultant Raman spectrum in the form of a plot between the intensity and Raman shift (in cm^{-1}) serves as a fingerprint of the molecular and structural features of the material [31–33]. In this thesis work, Raman spectroscopy was used to investigate the vibrational modes and structural integrity of the cathode materials for SIBs.

2.5.6 TEM, HRTEM, and SAED

TEM is one of the important physicochemical analysis tools that is widely used for the characterization of advanced materials, including cathodes for SIBs. TEM can image the internal structures of the material even at the nanoscale. In contrast to SEM, which shows surface morphology, TEM facilitates the atomic level resolution for the direct observation of internal morphology, particle size, crystallinity, lattice defects, and phase boundaries. In TEM, a high-energy (60-300 keV) coherent electron beam is passed through an ultrathin specimen (<100 nm thick). The electrons scatter, absorb, or transmit upon interaction with the atoms of the material. Mass-thickness, diffraction, and phase differences lead to contrast based on these interactions, indicating morphological and crystallographic details like particle morphology and grain boundaries.

HRTEM is an upgraded version of TEM, which uses aberration-corrected optics to reach a sub-angstrom resolution (<0.1 nm), enabling the visualization of atomic arrangements, atomic structures, and lattice fringes directly. HRTEM is important in determining the interplanar spacing *d*-spacing viewing dislocations [34,35]. SAED enhances the TEM imaging capability by providing crystallographic information from limited areas of interest (usually 50–500 nm in diameter). By placing a chosen area aperture in the back focal plane of the objective lens, a diffraction pattern is

produced, comprising bright spots or rings corresponding to the crystal planes of the material. SAED is essential for phase identification, observing polycrystalline, nanocrystalline, or amorphous domains, and measuring interplanar spacing *d*-spacing [36,36]. **Figure 2.10** shows a schematic diagram of TEM. When a high-energy electron beam illuminates a thin sample, the electrons are scattered elastically or inelastically from the sample. Transmitted electrons are magnified through a sequence of electromagnetic lenses to produce an image or diffraction pattern. Either high-resolution structural information or crystallographic data is recorded, depending on the detector mode. In this thesis work, TEM analysis was performed using a JEOL JEM-2100 Field Emission TEM, operated at 200 keV. This instrument enabled atomic-scale imaging and crystallographic characterization of the synthesized cathode materials for SIBs. TEM, HRTEM, and SAED were used to examine morphology, particle connectivity, lattice ordering, *d*-spacing, and orientation analysis.

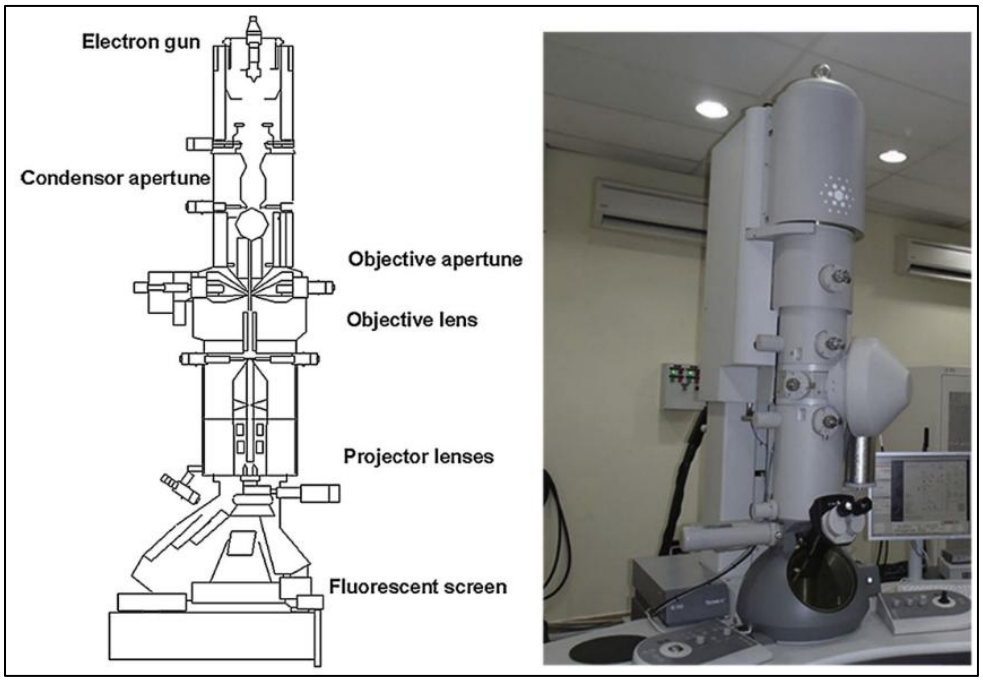

Figure 2.10 Schematic diagram of TEM [37].

2.5.7 X-ray Photoelectron Spectroscopy (XPS).

XPS is a surface analytical tool with high sensitivity, commonly used to investigate the chemical composition, oxidation states, and electronic environments of elements on the top few nanometres of the surface of a material. It studies the surface phenomena like degradation, ion migration, and interfacial reactions that impact the electrochemical performance and cycling stability of cathode materials for SIBs [38–40]. XPS operates based on the well-known photoelectric effect, wherein monochromatic X-rays irradiate the sample, causing the ejection of core-level electrons from the atoms at or near the surface. The kinetic energy (KE) of the emitted electrons is measured by an electron energy analyzer, and the binding energy (BE) of each electron is calculated as:

$$BE = h\nu - KE - \Phi$$

Where $h\nu$ = incident X-ray photon energy (Al Kα, 1486.6 eV), and Φ = work function of the spectrometer. The survey and high-resolution scan XPS spectra provide element-specific fingerprint peaks. Survey spectra provide an overview of all the elements present (excluding H and He), whereas high-resolution scans analyze subtle shifts in BE, which help to distinguish various oxidation states and local chemical surroundings. **Figure 2.11** shows a schematic of a typical XPS instrument and its major components. The X-rays are incident on the sample, photoelectrons are emitted from surface atoms, their KE is measured, and BE is calculated for elemental identification and chemical state analysis. Besides quantification of elements, XPS also allows Chemical shift analysis: Changes in BE as a function of oxidation state or bonding, and interface studies such as SEI layer analysis. In this thesis, XPS analyses were carried out to verify the oxidation states of transition metals, check the surface composition, and verify the phase purity of the synthesized cathode materials. Deconvolution at the peak level was carried out to understand overlapping components and evaluate mixed valence states.

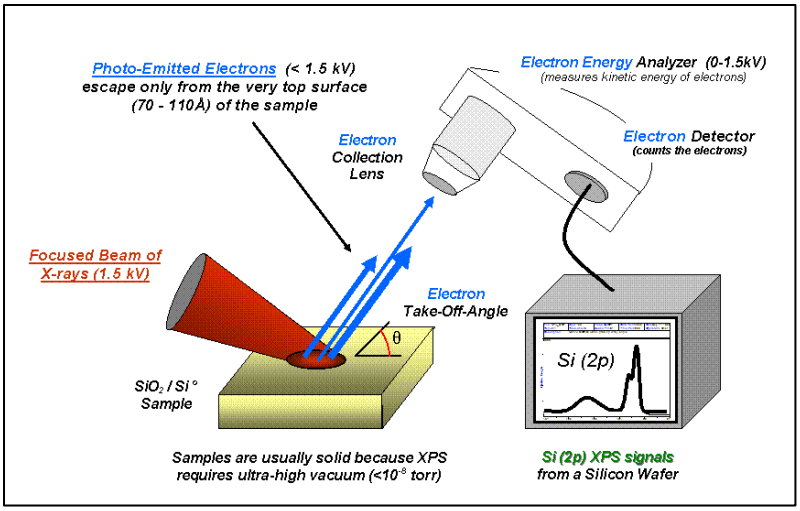

Figure 2.11 Schematic for monochromatic XPS basic components [41].

2.6 Electrochemical Characterization Techniques

Electrochemical characterization of the cathode materials is crucial for assessing the electrochemical performance and degradation mechanisms of the overall battery system. It provides important insights into the charge storage kinetics, specific capacity, energy, and power density, interfacial events, cycle life performance, and long-term stability of cathode materials. It further explains the redox activity, Na^+-ion diffusion dynamics, and phase transformations of the cathode materials. We carried out CV, galvanostatic charge-discharge (GCD), EIS, and distribution of relaxation time (DRT) analyses of the cathode material in the Na-half cell.

CV explains redox couples, electrochemical reversibility, and kinetics through current-voltage peak shape and position analysis. EIS investigates the resistive and capacitive properties of the electrode-electrolyte interface, such as charge transfer resistance, Na^+-ion diffusion impedance, and SEI formation. GCD was used to study the specific capacity, cycling stability, and coulombic efficiency. Rate capability tests were also carried out through GCD. The CV and EIS were performed using Autolab electrochemical workstation (**Figure 2.12 (a)**), and an 8-channel battery tester (**Figure 2.12 (b)**) for GCD and other battery testing.

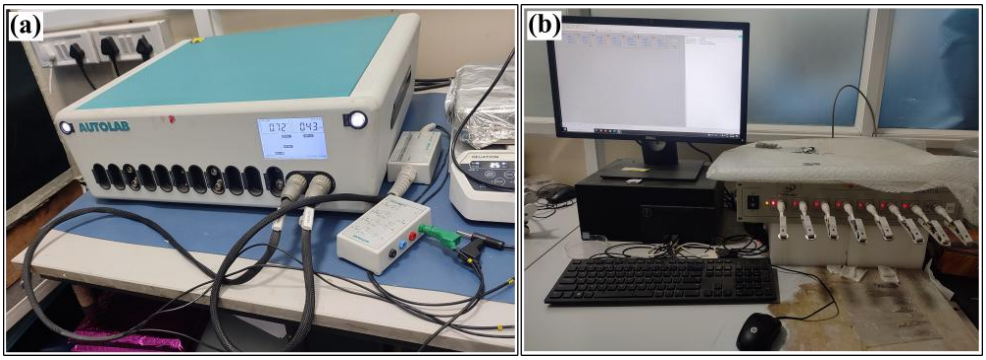

Figure 2.12 (a) Autolab electrochemical workstation and **(b)** 8-channel battery tester, MATAB.

2.6.1 Cyclic Voltammetry (CV)

CV is an important electrochemical method that was used for exploring redox behavior, reaction kinetics, and the reversibility nature of synthesized layered and tunnel structure TM oxides and polyanionic cathode materials for SIBs [42–44]. During CV, a linearly changing potential was applied across the cell, and the resulting current was measured to produce a cyclic voltammogram, which is an electrochemical fingerprint for the cathode material. In a CV, the oxidation and reduction peaks result from the insertion and extraction of Na^+-ions and reflect redox-active sites and structural development on the cycling of the material. Important analytical parameters like peak potential separation $\Delta E = E_{cathode} - E_{anode}$ and peak current ratio (I_c/I_a) are very useful in understanding the reversibility of the redox process and the kinetics of sodium intercalation/deintercalation. The scan-rate-dependent phenomenon of peak currents also reveals the charge storage mechanisms. As per the Randles–Sevcik equation, the peak current (i_p) is found to vary as the square root of the scan rate ($v^{1/2}$) as [42–44],

$$i_p = 2.69 \times 10^5 . A . C . n^{\frac{3}{2}} . D^{\frac{1}{2}} v^{\frac{1}{2}}$$

Where n is the number of electrons, A is the electrode area, D is the diffusion coefficient of Na^+ ion, and C is the concentration of Na^+ ion. A linear relationship between i_p and $v^{1/2}$ indicates a diffusion-controlled

process, usually found in well-crystallized layered/tunnel-structured metal oxides or polyanionic structures. To distinguish between diffusion-controlled (battery type) and surface-controlled (capacitor type) contributions of the cathode material, the log(i_p) *vs.* log(v) analysis provides the slope b-value from the equation below.

$$i_p = a\, v^b$$

Where b ≈ 0.5 implies diffusion control, and b ≈ 1.0 implies capacitive or pseudocapacitive storage. Intermediate b-values indicate mixed charge storage mechanisms, which are generally desired to realize both high power and energy densities.

CV can also determine phase transitions in sodiation/desodiation, e.g., the *P*2 to *O*3 or *O*′3 to *O*1 phase transformations usual in Na-based layered oxides. They appear as changes in peak shape, position, and symmetry throughout cycles. In addition, CV allows for the estimation of parasitic side reactions by assessing coulombic efficiency as given below.

$$\eta = \frac{Q_{discharge}}{Q_{charge}} \times 100\%$$

CV analysis enables an in-depth electrochemical understanding of the electrochemical activity of the cathode materials. Therefore, CV is not only a diagnostic means but also an effective means for directing rational design and optimization of high-rate, high-stability SIB cathode materials.

2.6.2 Galvanostatic Charge-Discharge (GCD)

GCD is an important electrochemical characterization method used for the assessment of the specific capacity, rate capability, reversibility, and long-term cycling stability of cathode materials in SIBs. In GCD experiments, a steady current is passed through the cell while the voltage is measured as a function of time, producing charge-discharge profiles that provide crucial information about major electrochemical reactions. They provide information on phase transitions, multi-step redox reactions, overpotentials, and ion diffusion limitations [45–48]. Voltage plateaus of the above curves are usually characteristic of two-phase transitions, for

example, *P*2-*O*2 transformations in layered oxides, whereas sloping profiles typically reflect single-phase solid-solution behavior. The specific capacity in mAh/g is calculated as below.

$$Q = \frac{I \times \Delta t}{m}$$

where I is the applied current (in mA), Δt is the discharge time (in h), and m is the mass of active material (in g). The reversibility of the cathode material is quantified by the coulombic efficiency as given below. Which is usually higher than 99% in advanced cathode material for several hundred cycles, showing less side reaction and structural degradation. Long-term capacity retention is an important electrochemical parameter in assessing cathode stability and is given as

$$R_{cycle} = \frac{Q_n}{Q_{initial}} \times 100\%$$

High upper cutoff voltages (*e.g.,* 4.5 V) can trigger extra capacity from high-voltage redox couples but potentially hasten degradation by irreversible phase transformation and electrolyte decomposition, as indicated by a sharp fall to 88.3% retention within 40 cycles.

Differential capacity analysis (dQ/dV *vs.* V) enhances the interpretation of GCD curves by resolving overlapping redox processes. Spikes in dQ/dV plots are associated with a particular redox couple, e.g., Mn^{3+}/Mn^{4+} and Fe^{3+}/Fe^{4+} in layer-type oxides occur around 3.6 V and 4.1 V, respectively. Such analysis is also used to identify parasitic processes and follow electrode evolution with time. Further, GCD testing at different current densities allows the measurement of rate capability. Therefore, GCD cycling not only provides a useful benchmark for electrochemical performance but also an excellent diagnostic tool to improve SIB cathodes for high-energy, long-cycling, and fast-charging battery systems [19,49].

2.6.3 Electrochemical Impedance Spectroscopy (EIS)

EIS is an analytical, frequency-domain, non-destructive method essential for investigating charge transfer kinetics, interfacial effects, and

mass transport limitations in the cathode materials of SIBs. EIS involves the superimposition of a small sinusoidal voltage perturbation (often 5-10 mV) over a broad frequency range (100 kHz to 10 mHz) and records the current response, producing complex impedance spectra.[50–53] The Nyquist plot (imaginary impedance Z'' vs. real impedance Z') shows characteristic semicircles and slopes for electrochemical processes: high-frequency intercepts are ohmic resistance (R_s, electrolyte/contact resistances), mid-frequency semicircles are charge transfer resistance (R_{ct}) in parallel with double-layer capacitance (C_{dl}), and low-frequency Warburg tails are Na^+-ion diffusion. The Randles equivalent circuit models these processes:

$$Z(\omega) = R_s + \frac{1}{\frac{1}{R_s} + j\omega C_{dl}} + \sigma\omega^{-\frac{1}{2}}(1 - j)$$

where σ is the Warburg coefficient, associated with the sodium diffusion coefficient (D_{Na^+}) via:

$$\sigma = \frac{R\,T}{n^2\,F^2\,A\,\sqrt{2}} \cdot \frac{1}{C\sqrt{D_{Na^+}}}$$

Here, R is the gas constant, T is temperature (K), n is electron transfer number, F is Faraday's constant, A is electrode area (cm^2), and C is Na^+ concentration (mol/cm^3).

2.6.4 Distribution of Relaxation Times (DRT)

Although the EIS is a potential electrochemical tool capable of understanding the interfacial and bulk properties of the electrode, analyzing the complex impedance involving the overlapping of semicircles within the same frequency domain becomes difficult or inaccurate. The EIS typically uses the models of equivalent circuits composed of several resistive and capacitive elements; however, their interpretation becomes increasingly difficult due to the problem of isolating the individual contributions of distinct electrochemical processes [54]. To tackle these limitations, the DRT, an advanced mathematical tool, has evolved to deconvolute the impedance spectra into discrete relaxation processes in the time domain [54]. Mathematically, DRT assumes an infinite Voigt circuit composed of an infinite series of RQ elements, each RQ pair contributing to a unique

relaxation process whose time constant (τ) is derived from the equation below [54]. Here, α represents the deviation from ideal capacitive behavior.

$$\tau = (RQ)^{\frac{1}{\alpha}}$$

The DRT approach calculates a normalized distribution function γ(τ) representing the contribution of each relaxation process across the time constant (τ) domain. The relation between impedance Z(ω) and the DRT function γ(τ) is given in equation below [54].

$$Z(\omega) = R_s + R_p \int_{-\infty}^{\infty} \frac{\gamma(\tau)}{1+j\omega\tau} d \ln \tau$$

R_s represents the uncompensated solution resistance at the high-frequency range, and R_p represents the total resistance due to the polarization contribution at the low-frequency range. To ensure that the area under each DRT peak corresponds quantitatively to the associated relaxation process, the DRT function γ(τ) is normalized as in equation below.

$$\int_{-\infty}^{\infty} \gamma(\tau) d \ln \tau = 1$$

Considering any i^{th} DRT peak representing a discrete electrochemical process, the location of each peak reveals the characteristic relaxation time, while its area and intensity correspond to the magnitude of the resistance R_i. The capacitance C_i is calculated by below **equation**. This decomposition helps to understand individual kinetic processes [54].

$$C_i = \frac{T_i}{R_1}$$

The time constant τ domain represents various resistances and their respective physical processes. The location of $\tau \leq 10^{-3}$ s corresponds to the resistance between particle-current collector and particle-particle of the electrode, between $10^{-3} < \tau < 10^{-2}$ s represents the resistance by the active ion transport through SEI (*i.e.,* resistance due to SEI layer formation), $10^{-2} < \tau < 10^{-1}$ s represents the charge transfer resistance, and $\tau \geq 10^{-1}$ s correspond to the active ion diffusion process in the bulk electrode.

2.7 References

[1] C.I. Priyadharsini, G. Marimuthu, T. Pazhanivel, P.M. Anbarasan, V. Aroulmoji, V. Siva, L. Mohana, Sol – Gel synthesis of Co3O4 nanoparticles as an electrode material for supercapacitor applications, J Solgel Sci Technol. 96 (2020) 416–422. https://doi.org/10.1007/s10971-020-05393-x.

[2] J.A.K. Satrughna, A.R. Kanwade, S.M. Rajore, M. Kumar, Y. Ito, A. Ogura, H. Lee, Y. Ohshita, P.M. Shirage, Sol-gel-based synthesis of high-capacity-NaCoO2 cathode for advanced sodium-ion batteries, Electrochim. Acta. 507 (2024) 145201. https://doi.org/10.1016/j.electacta.2024.145201.

[3] L. Durai, S. Badhulika, Facile synthesis of large area pebble-like β-NaFeO2 perovskite for simultaneous sensing of dopamine , uric acid , xanthine and hypoxanthine in human blood, Mater. Sci. Eng. C. 109 (2020) 110631. https://doi.org/10.1016/j.msec.2020.110631.

[4] X. WANG, W. WANG, B. ZHU, F. QIAN, Z.F. FANG, Mo-doped Na3V2(PO4)3@C composites for high stable sodium ion battery cathode, Front. Mater. Sci. 12 (2018) 53–63. https://doi.org/10.20964/2019.03.36.

[5] Z. Jian, L. Zhao, H. Pan, Y.S. Hu, H. Li, W. Chen, L. Chen, Carbon coated Na3V2(PO4)3 as novel electrode material for sodium ion batteries, Electrochem. Commun. 14 (2012) 86–89. https://doi.org/10.1016/j.elecom.2011.11.009.

[6] D. Bokov, A. Turki Jalil, S. Chupradit, W. Suksatan, M. Javed Ansari, I.H. Shewael, G.H. Valiev, E. Kianfar, Nanomaterial by Sol-Gel Method: Synthesis and Application, Adv. Mater. Sci. Eng. 2021 (2021) 1–21. https://doi.org/10.1155/2021/5102014.

[7] P. Szołdra, M. Frąc, W. Pichór, Effect of sol composition on the properties of TiO2 powders obtained by the sol-gel method, Powder Technol. 387 (2021) 261–269. https://doi.org/10.1016/j.powtec.2021.04.037.

[8] J.A.K. Satrughna, A.R. Kanwade, S.M. Rajore, M.K. Tiwari, Y. Ito, A. Ogura, H. Lee, Y. Ohshita, S.S. Mali, J. V Patil, C.K. Hong, P.M. Shirage, Unveiling the physicochemical and electrochemical features of sodium deficient-Na0.8Fe(SO4)2 as cathode for sodium-ion batteries, Next Research. 2 (2025) 100210. https://doi.org/10.1016/j.nexres.2025.100210.

[9] V.R. Reddy Boddu, M. Palanisamy, L. Sinha, S.C. Yadav, V.G. Pol, P.M. Shirage, Hysteresis abated P2-type NaCoO2 cathode reveals highly reversible multiple phase transitions for high-rate sodium-ion

batteries, Sustain. Energy Fuels. 5 (2021) 3219–3228. https://doi.org/10.1039/d1se00490e.

[10] E. Lee, D.E. Brown, E.E. Alp, Y. Ren, J. Lu, J.J. Woo, C.S. Johnson, New Insights into the Performance Degradation of Fe-Based Layered Oxides in Sodium-Ion Batteries: Instability of Fe3+/Fe4+ Redox in α-NaFeO2, Chem. Mater. 27 (2015) 6755–6764. https://doi.org/10.1021/acs.chemmater.5b02918.

[11] K. Kaliyappan, Z. Chen, Facile solid-state synthesis of eco-friendly sodium iron silicate with exceptional sodium storage behaviour, Electrochim. Acta. 283 (2018) 1384–1389. https://doi.org/10.1016/j.electacta.2018.07.034.

[12] J.A.K. Satrughna, A.R. Kanwade, P.M. Shirage, Synergistic effect of multi-transition metal co- substitution in high cycle life performance of NaxCo0.5Fe0.25Mn0.25O2 cathode for sodium-ion batteries, Sustain. Energy Fuels. (2025). https://doi.org/10.1039/d5se00107b.

[13] B. Hu, C. Li, M. Shen, B. Hu, X. Lou, X. Zhang, W. Tong, High-energy nanostructured Na3V2(PO4)2O1.6F1.4 cathodes for sodium-ion batteries and a new insight into their redox chemistry, J. Mater. Chem. A. 6 (2018) 8340–8348. https://doi.org/10.1039/c8ta00568k.

[14] P. Zhan, K. Jiao, J. Wang, Z. Hu, R. Ma, H. Zhu, S. Jiao, Titanium-Substituted Na 0.44 MnO 2 Nanorods as Cathode Materials for High Performance Sodium-Ion Batteries , Journal of The Electrochemical Society. 162 (2015) A2296–A2301. https://doi.org/10.1149/2.0521512jes.

[15] J.A.K. Satrughna, A.R. Kanwade, S.M. Rajore, P.M. Shirage, Exploring the Characteristics of Na1.35CrO4 as Active Electrode for Energy Storage Application in Sodium-Ion Batteries, Phys. Status Solidi RRL. (2025) 2500079. https://doi.org/10.1002/pssr.202500079.

[16] Q.A.T. Technology, Thermogravimetric Analyzer TGA: A Comprehensive Overview and APplications, (n.d.). https://www.worldoftest.com/articles/tga-thermogravimetric-analyzer (accessed May 28, 2025).

[17] S. Kumar, R. Mondal, R. Prakash, P. Singh, Eldfellite-structured NaCr(SO4)2: a potential anode for rechargeable Na-ion and Li-ion batteries, Dalton Transactions. 51 (2022) 11823–11833. https://doi.org/10.1039/d2dt00573e.

[18] R.R. Samigullin, O.A. Drozhzhin, E. V. Antipov, Comparative Study of the Thermal Stability of Electrode Materials for Li-Ion and Na-Ion Batteries, ACS Appl. Energy Mater. 5 (2022) 14–19.

https://doi.org/10.1021/acsaem.1c03151.

[19] K. Shiprath, H. Manjunatha, R. Venkata Nadh, T. Anil Babu, S. Ramesh, K. Chandra Babu Naidu, M. Ramesha, Synthesis and Electrochemical Characterization of NaCoO2 as Cathode Material in 2M NaOH Aqueous Electrolyte, ChemistrySelect. 6 (2021) 1874–1881. https://doi.org/10.1002/slct.202100294.

[20] S.M. Oh, J. Song, S. Lee, I.C. Jang, Effect of current rate on the formation of the solid electrolyte interphase layer at the graphite anode in lithium-ion batteries, Electrochim. Acta. 397 (2021) 139269. https://doi.org/10.1016/j.electacta.2021.139269.

[21] M. Sathiya, K. Hemalatha, K. Ramesha, J.-M. Tarascon, A.S. Prakash, Synthesis, Structure, and Electrochemical Properties of the Layered Sodium Insertion Cathode Material: NaNi1/3Mn1/3Co1/3O2, Chem. Mater. 24 (2012) 1846−1853.

[22] B. Pandit, B. Fraisse, L. Stievano, L. Monconduit, M.T. Sougrati, Carbon-coated FePO4 nanoparticles as stable cathode for Na-ion batteries: A promising full cell with a Na15Pb4 anode, Electrochim. Acta. 409 (2022) 139997. https://doi.org/10.1016/j.electacta.2022.139997.

[23] S. Vafakhah, M. Saeedikhani, M. Tanhaei, S. Huang, L. Guo, S.Y. Chiam, H.Y. Yang, An energy efficient bi-functional electrode for continuous cation-selective capacitive deionization, Nanoscale. 12 (2020) 22917–22927. https://doi.org/10.1039/d0nr05826b.

[24] G.F. Harrington, J. Santiso, Back-to-Basics tutorial: X-ray diffraction of thin films, J. Electroceramics. 47 (2021) 141–163. https://doi.org/10.1007/s10832-021-00263-6.

[25] K. Akhtar, S.A. Khan, S.B. Khan, A.M. Asiri, Scanning Electron Microscopy: Principle and Applications in Nanomaterials Characterization, in: Handbook of Materials Characterizatio, 2018: pp. 113–145. https://doi.org/https://doi.org/10.1007/978-3-319-92955-2_4.

[26] P. Bhojane, A. Sharma, M. Pusty, Y. Kumar, S. Sen, P. Shirage, Synthesis of ammonia-assisted porous nickel ferrite (NiFe2O4) nanostructures as an electrode material for supercapacitors, J. Nanosci. Nanotechnol. 17 (2017) 1387–1392. https://doi.org/10.1166/jnn.2017.12666.

[27] R.S. Prabhu, R. Priyanka, M. Vijay, G.R.K. Vikashini, Field Emission Scanning Electron Microscopy (Fesem) with A Very Big Future in Pharmaceutical Research, Int. J. Pharm. Biol. Sc. 11 (2021) 183–187. https://doi.org/10.21276/ijpbs.2021.11.2.21.

[28] I. Michalak, K. Chojnacka, K. Marycz, Using ICP-OES and SEM-EDX in biosorption studies, Microchim Acta. 172 (2011) 65–74. https://doi.org/10.1007/s00604-010-0468-0.

[29] A. Alomary, S. Belhadj, S. Obeidat, I. Al-momani, A. Attiyat, A comparison of SEM-EDS with ICP-OES for the Quantitative Elemental Determination of Algerian Mediterranean Sea Sediments, Jordan J. Chem. 7 (2012) 383–391. https://jjc.yu.edu.jo/index.php/jjc/article/view/199.

[30] S. Raza, K. Babita, S. Pooja, A.C. Rohit, Inductively Coupled Plasma Optical Emission Spectrometry (ICP-OES): a Powerful Analytical Technique for Elemental Analysis, Food Anal. Methods. 15 (2022) 666–688. https://doi.org/10.1007/s12161-021-02148-4.

[31] M.A. Khan, D. Han, G. Lee, Y. Il Kim, Y.M. Kang, P2/O3 phase-integrated Na0.7MnO2 cathode materials for sodium-ion rechargeable batteries, J. Alloys Compd. 771 (2019) 987–993. https://doi.org/10.1016/j.jallcom.2018.09.033.

[32] F. Xiao, M. Cao, R. Chu, X. Hu, W. Shi, Y. Chen, Novel Perylene-3, 4, 9, 10-tetracarboxylic dianhydride modified Zr-MOFs/Graphene oxide membrane for dye wastewater treatment, J. Colloid Interface Sci. 610 (2022) 671–686. https://doi.org/10.1016/j.jcis.2021.11.113.

[33] D. Bin, Y. Wang, A.G. Tamirat, P. Zhu, B. Yang, J. Wang, J. Huang, Y. Xia, Stable High-Voltage Aqueous Zinc Battery Based on Carbon-Coated NaVPO4F Cathode, ACS Sustainable Chem. Eng. 9 (2021) 3223–3231. https://doi.org/10.1021/acssuschemeng.0c08651.

[34] J. Billaud, R.J. Clement, A.R. Armstrong, J. Canales-Vazquez, P. Rozier, C.P. Grey, P.G. Bruce, β-NaMnO2 : A High-Performance Cathode for Sodium-Ion Batteries., J. Am. Chem. Soc. 136 (2014) 17243−17248. https://doi.org/10.1002/chin.201514014.

[35] Y. Zuo, J. Yue, Z. Ma, Z. Zuo, Facile fabrication of carbon-encapsulated NaVPO4F nanocomposite as a high-rate and long-cycle life cathode material for sodium energy storage, J. Phys. Chem. Solids. 160 (2022) 110354. https://doi.org/10.1016/j.jpcs.2021.110354.

[36] S. Guo, P. Liu, H. Yu, Y. Zhu, M. Chen, M. Ishida, H. Zhou, A layered P2- and O3-type composite as a high-energy cathode for rechargeable sodium-ion batteries, Angew. Chem. Int. Ed. 54 (2015) 5894–5899. https://doi.org/10.1002/anie.201411788.

[37] C.Y. Tang, Z. Yang, Transmission Electron Microscopy (TEM), Elsevier B.V., 2017. https://doi.org/10.1016/B978-0-444-63776-

5.00008-5.
[38] U. Nisar, M.H. Gulied, R.A. Shakoor, R. Essehli, Z. Ahmad, A. Alashraf, R. Kahraman, S. Al-Qaradawi, A. Soliman, Synthesis and performance evaluation of nanostructured NaFexCr1-X(SO4)2 cathode materials in sodium ion batteries (SIBs), RSC Adv. 8 (2018) 32985–32991. https://doi.org/10.1039/c8ra06583g.
[39] J.J. Ding, Y.N. Zhou, Q. Sun, X.Q. Yu, X.Q. Yang, Z.W. Fu, Electrochemical properties of P2-phase Na0.74CoO2 compounds as cathode material for rechargeable sodium-ion batteries, Electrochim. Acta. 87 (2013) 388–393. https://doi.org/10.1016/j.electacta.2012.09.058.
[40] L. Shen, H. Yang, Y. Jiang, J. Ma, T. Sun, M. Zhang, N. Zhu, NASICON-Structured Na2VTi(PO4)3@C for Symmetric Aqueous Rechargeable Na-Ion Batteries with Long Lifespan, ACS Sustain. Chem. Eng. 9 (2021) 3490–3497. https://doi.org/10.1021/acssuschemeng.0c07755.
[41] W. Contributors, X-ray photoelectron spectroscopy, (2025).
[42] K. Kaliyappan, J. Liu, B. Xiao, A. Lushington, R. Li, T.K. Sham, X. Sun, Enhanced Performance of P2-Na0.66(Mn0.54Co0.13Ni0.13)O2 Cathode for Sodium-Ion Batteries by Ultrathin Metal Oxide Coatings via Atomic Layer Deposition, Adv. Funct. Mater. 27 (2017) 1–8.
[43] N. Raeisi-Kheirabadi, A. Nezamzadeh-Ejhieh, H. Aghaei, Cyclic and Linear Sweep Voltammetric Studies of a Modified Carbon Paste Electrode with Nickel Oxide Nanoparticles toward Tamoxifen: Effects of Surface Modification on Electrode Response Kinetics, ACS Omega. 7 (2022) 31413–31423. https://doi.org/10.1021/acsomega.2c03441.
[44] M.J. Aragón, P. Lavela, G.F. Ortiz, J.L. Tirado, Effect of Iron Substitution in the Electrochemical Performance of Na 3 V 2 (PO 4) 3 as Cathode for Na-Ion Batteries, J. Electrochem. Soc. 162 (2015) A3077–A3083. https://doi.org/10.1149/2.0151502jes.
[45] U. Nisar, R.A. Shakoor, R. Essehli, R. Amin, B. Orayech, Z. Ahmad, P.R. Kumar, R. Kahraman, S. Al-Qaradawi, A. Soliman, Sodium intercalation/de-intercalation mechanism in Na4MnV(PO4)3 cathode materials, Electrochim. Acta. 292 (2018) 98–106. https://doi.org/10.1016/j.electacta.2018.09.111.
[46] X. Wu, Y. Li, Y. Xiang, Z. Liu, Z. He, X. Wu, Y. Li, L. Xiong, C. Li, J. Chen, The electrochemical performance of aqueous rechargeable battery of Zn/Na0.44MnO2 based on hybrid electrolyte,

Journal of Power Sources. 336 (2016) 35–39. https://doi.org/10.1016/j.jpowsour.2016.10.053.

[47] C.L. Jakobsen, M. Brighi, B.P. Andersen, G. Ducrest, R. Černý, D.B. Ravnsbæk, Expanded solid-solution behavior and charge-discharge asymmetry in NaxCrO2 Na-ion battery electrodes, J. Power Sources. 535 (2022) 231317.

[48] B.V. Rami Reddy, R. Ravikumar, C. Nithya, S. Gopukumar, High performance NaxCoO2 as a cathode material for rechargeable sodium batteries, J. Mater. Chem. A. 3 (2015) 18059–18063.

[49] C. Pastor-Fernández, K. Uddin, G.H. Chouchelamane, W.D. Widanage, J. Marco, A Comparison between Electrochemical Impedance Spectroscopy and Incremental Capacity-Differential Voltage as Li-ion Diagnostic Techniques to Identify and Quantify the Effects of Degradation Modes within Battery Management Systems, Journal of Power Sources. 360 (2017) 301–318.

[50] N.K. Tailor, N. Parikh, P. Yadav, S. Satapathi, Dielectric Relaxation and Polaron Hopping in Cs2AgBiBr6Halide Double Perovskites, Journal of Physical Chemistry C. 126 (2022) 10199–10208. https://doi.org/10.1021/acs.jpcc.2c02073.

[51] A.C. Lazanas, M.I. Prodromidis, Electrochemical Impedance Spectroscopy-A Tutorial, ACS Meas. Sci. Au. 3 (2023) 162−193. https://doi.org/10.1021/acsmeasuresciau.2c00070.

[52] L. Wang, J. Zhao, X. He, J. Gao, J. Li, C. Wan, C. Jiang, Electrochemical Impedance Spectroscopy (EIS) study of LiNi 1/3Co 1/3Mn 1/3O 2 for Li-ion batteries, International Journal of Electrochemical Science. 7 (2012) 345–353.

[53] R.L. Smith, A. V. Bray, D.K. Coates, Impedance spectroscopy as a technique for monitoring aging effects in nickel hydrogen and nickel-metal hydride batteries, Proceedings of the 35th International Power Sources Symposium. (1992) 156–159. https://doi.org/10.1109/IPSS.1992.282005.

[54] J. Pati, R.S. Dhaka, Mixed polyanionic NaFe1.6V0.4(PO4)(SO4)2@CNT cathode for sodium-ion batteries: Electrochemical diffusion kinetics and distribution ofrelaxation time analysis at different temperatures, J. Power Sources. 609 (2024) 234646. https://doi.org/10.1016/j.jpowsour.2024.234646.

CHAPTER 3

Sodium-Deficient-Based $Na_{0.8}Fe(SO_4)_2$ Cathode: A Novel Polyanionic Framework for Enhanced Na^+ Ion Migration

This chapter presents the successful synthesis of sodium-deficient-$Na_{0.8}Fe(SO_4)_2$ using citric acid abetted sol-gel technique, followed by a comprehensive exploration of its physicochemical and electrochemical performances as a cathode material for SIBs. Its electrochemical performances revealed significant insights into sodium-ion insertion and the impact of 20% sodium deficiency. It exhibits a reduction in lattice parameters, unit cell volume, and interplanar d-spacing, operating at an average voltage of ~3.1 to 3.15 V. The material delivered a high specific discharge capacity of ~41.17 mAh/g with a specific energy of 107.61 Wh/kg at 0.2 C within a 1.5-4.5 V voltage window vs. Na/Na^+. Additionally, it demonstrates excellent capacity retention, maintaining ~98% and ~70% of its initial capacity after 45 cycles at 1 C and 0.1 C, respectively. Despite lower specific capacity, sodium deficiency in $Na_{0.8}Fe(SO_4)_2$ enhances sodium ion diffusion, charge kinetics, voltage window, and capacity retention at higher C-rates. These findings position it as a promising candidate for SIBs.

3.1 Introduction

SIBs present a viable option to LIBs for large-scale energy storage [1–3]. To be a viable option for energy storage, SIBs must have a low cost, high cyclability, and excellent rate capability [4–6]. Over the last two decades, extensive research on intercalation materials for SIBs has been carried out to develop a rechargeable and sustainable SIB system [7,8]. Among them, layer structure-based sodiated TM oxides have shown impressive results in terms of specific capacity and rate performance as potential cathode material for SIBs, owing to their low molecular weight [4,9–12]. Surface modification engineering, such as defect, doping, partial metal-ion substitution, and co-doping, has enhanced the electrochemical performance of these types of layered cathode materials [10–14]. However, they possess several disadvantages, including multiple phase transitions, moisture sensitivity, and limited working voltage. Hence, although LTMOs for SIBs have shown significant improvements in electrode performance, there is a growing research interest in alternative materials having oxoanion groups due to their 3D-frame work and highly stable structure [1]. As the demand for SIBs grows, there is a renewed interest in the substantial study of a wide range of new cathode materials based on oxoanion groups such as $NaFe(SO_4)_2$, Na_2FeSiO_4, $Na_xFe_y(SO_4)_3$, $Na_3V_2(PO_4)_3$, $Na_3V_2O_2(PO_4)_2F$, $NaFePO_4$, *etc.* owing to their high potential window, 3D structural framework, and high stability. Many of these polyanion-based cathode materials encounter issues such as restricted theoretical capacity due to high molecular weight and sluggish sodium insertion rates, which can have a severe effect on the overall performance of SIBs [15]. To achieve optimal device performance, we need cathodes to have high potential, fast sodium-ion diffusion, good stability, and excellent cyclability. Maximizing the capacity and rate capability is critical for realizing the full potential of SIBs as an energy storage option [16–18].

P. Singh *et al.* [19] studied the electrochemical performances of eldfellite $NaFe(SO_4)_2$ as a low-cost positive electrode for rechargeable SIBs

with reversible Na^+-ion insertion capability at 3.2 V *vs.* Na/Na^+ due to the active Fe^{3+}/Fe^{2+} redox couple. This cathode material delivered a high capacity of about 80 mAh/g at 0.1 C in a Na half-cell with 1M $NaClO_4$ as electrolyte. This polyanion-based cathode material, on the other hand, has a decreased sodium insertion rate, resulting in limited specific energy. A. Banerjee *et al.* [20] performed a theoretical study to investigate the phase stability of $Na_xFe(SO_4)_2$ (with $0 \leq x \leq 2$) cathode material. As per their study, the material of interest showed outstanding structural stability with only 8% volume change with full desodiation. They found that the materials exhibited an energy band gap of about 1.54 to 3.19 eV for half to the fully-sodiated materials. In 2020, Trussov *et al.* [15] investigated the electrochemical properties of the pristine $NaFe(SO_4)_2$ and the eldfellite $NaFe(SO_4)_2$ doped with SeO_4, PO_3F, and HPO_4. They observed that $NaFe(SO_4)_2$ demonstrated the highest capacity of 63 mAh/g compared to 45 mAh/g, 39 mAh/g, and 39 mAh/g capacities of $NaFe(SO_4)_{1.5}(SeO_4)_{0.5}$, $NaFe(HPO_4)_{1.5}(SeO_4)_{0.5}$, and $NaFe(SO_4)_{1.5}(PO_3F)_{0.5}$ respectively. Again, the pristine $NaFe(SO_4)_2$ exhibited better cycling performance compared to its polyanionic substituted ones, performed for 30 cycles.

Although a justified amount of theoretical work had been successfully reported on $NaFe(SO_4)_2$, it was limited to a few experimental investigations due to the low electronic conductivity, limited specific capacity, and limited energy density of $NaFe(SO_4)_2$ in the commercially available electrolyte [15,19–22]. Even though numerous theoretical studies, along with a few experimental investigations, were conducted on $NaFe(SO_4)_2$, none of them demonstrated the various characteristics of any sodium-deficient $NaFe(SO_4)_2$ materials, such as $Na_{0.8}Fe(SO_4)_2$ for SIBs. Further reducing sodium content by 20% to 25% found to enhance the stability and sodium-ion movement in many sodiated TM oxide cathode materials. Given the importance of the structural modification and sodium deficiency of the cathode materials in determining the potential window, sodium diffusion kinetics, and performance of SIBs, a detailed study of

sodium-deficient $Na_xFe(SO_4)_2$ was desired. Hence, detailed physicochemical and electrochemical analyses were required to provide a meaningful mechanism for driving ionic diffusion to fully grasp the sodium insertion kinetics of $Na_{0.8}Fe(SO_4)_2$ cathode.

In this chapter, we investigated the synthesis of $Na_{0.8}Fe(SO_4)_2$ via a citric acid-abetted sol-gel method to study its various properties. Further, we extended our investigations on its electrochemical performance by fabricating CR2032 Na/1M $NaClO_4$/$Na_{0.8}Fe(SO_4)_2$ half-cells. A thorough investigation of the reversible Na^+-ion insertion and the effect of 20% sodium deficiency of $Na_{0.8}Fe(SO_4)_2$ was carried out. $Na_{0.8}Fe(SO_4)_2$ showed significant shrinkage in the lattice parameters, volume, and *d*-spacing. The material operated at an average voltage of 3.1-3.15 V, which corresponding to sodium intercalation and deintercalation. It showed a discharge-specific capacity of ~41.17 mAh/g and a specific energy of 107.61 Wh/kg at a rate of 0.2 C, within a voltage range of 1.5-4.5V vs Na/Na^+. Further, $Na_{0.8}Fe(SO_4)_2$ as the cathode material for SIBs showed remarkable capacity retention by retaining ~99% and ~70% initial capacities after 45 cycles at 1 C and 0.1 C, respectively. Along with this, sodium deficiency in $Na_{0.8}Fe(SO_4)_2$ helped to provide a better Na^+-ion diffusion than its pristine one during the charging/discharging process. Hence, Na^+-ion deficiency had significantly improved the sodium diffusion kinetics, working potential window, and remarkable capacity retention at higher C-rates.

3.2 Experimental Section

The experimental details, such as the selection of precursors, synthesis methodology, slurry making process, electrode preparation, cell fabrication, physicochemical profiling techniques, and the electrochemical analyses techniques for the $Na_{0.8}Fe(SO_4)_2$ cathode was discussed in **Chapter 2** in detail. The physicochemical characterizations for $Na_{0.8}Fe(SO_4)_2$ cathode included TGA, DSC, Powder-XRD, FESEM, EDX, XPS, Raman Spectroscopy, and HRTEM.

Before proceeding with the evaluation of the electrochemical performance of $Na_{0.8}Fe(SO_4)_2$ in CR2032 half-cells, we optimized the electrolyte system using various formulations. Six electrolytes were tested: (1) $NaPF_6$ in a 1:1 volume ratio of DMC and EC; (2) $NaClO_4$ with 2% FEC in PC; (3) $NaClO_4$ with 10% FEC in PC; (4) $NaClO_4$ in a 1:1 ratio of DMC and EC; (5) $NaClO_4$ with 5% FEC in PC; and (6) $NaClO_4$ in a 1:1 ratio of EC and PC. Among these, $Na_{0.8}Fe(SO_4)_2$ exhibited significant electrochemical performance only in electrolytes (5) and (6), with the best results in the electrolyte (6). Therefore, further studies utilized the Na/1M $NaClO_4$/$Na_{0.8}Fe(SO_4)_2$ system, referring to the cell fabricated with 1M $NaClO_4$ in a 1:1 volume ratio of EC and PC as the electrolyte.

3.3 Results and Discussion

3.3.1 Physicochemical Analyses

3.3.1.1 TGA & DSC Analyses:

It was well known that the SO_4^{2-} polyanions decompose at a temperature of more than 600℃ with the evolution of SO_2, [19] as a result, we performed a TGA-DSC study to determine the required calcination temperature. **Figure 3.1** represents the TGA and DSC spectrum for $Na_{0.8}Fe(SO_4)_2$, signifying the percentage weight loss, thermal behaviour, decomposition, and the desired calcination temperature for the material of interest. The dark blue coloured line corresponds to the TGA (*i.e.,* percentage-wise mass loss) and the dark-yellow line represents DSC, signifying the heat flow and decomposition of the material at the respective temperatures. From the TGA and DSC, it was observed that there was a short mass loss (~3.48% of the initial mass) at about 133℃, which was associated with the loss/evaporation of the trapped or absorbed water molecules in the material. Further, 2nd mass loss of about 6.93% of the initial mass of the material took place at around 357℃, which was attributed to the gas evolution of nitrate precursors and the formation of the desired phase of $Na_{0.8}Fe(SO_4)_2$. Here, the weight losses were very small indicating the

high thermal stability of the compound. From the DSC and TGA, it is observed that there was no further significant decomposition and significant mass loss took place after 400°C, which revealed that the required material can be synthesized in between these two temperature limits of 400°C to 600°C. As a result, we selected 410ºC as the calcination temperature for the synthesis of $Na_{0.8}Fe(SO_4)_2$ to achieve a relatively highly stable material.

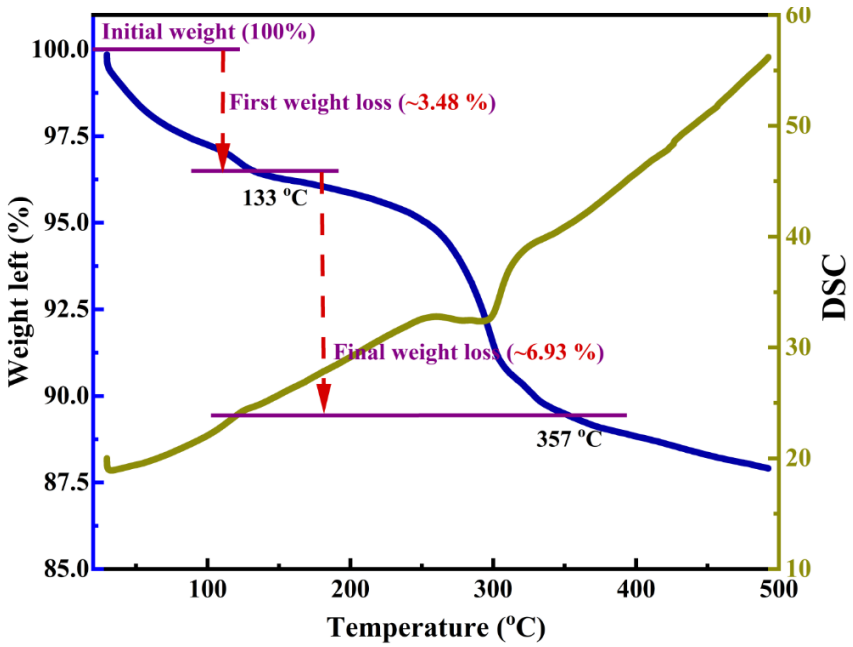

Figure 3.1 TGA-DSC curve for $Na_{0.8}Fe(SO_4)_2$.

3.3.1.2 Powder-XRD Analysis

Figures 3.2 (a-b) represent the powder XRD pattern for $Na_{0.8}Fe(SO_4)_2$. The red peaks in **Figure 3.2 (a)** represent the prominent intensity peaks with their respective Miller indices of 00-027-0718 Joint committee on powder diffraction standards (JCPDS) card file, indicating the formation of phase-pure sodium-deficient $Na_{0.8}Fe(SO_4)_2$ with the space group *C2/m1* of the monoclinic symmetry. Similarly, the dark blue peaks in **Figures 3.2 (a-b)** are the reference peaks representing the standard peaks of the pristine $NaFe(SO_4)_2$ with the same symmetry. These reference peaks (*i.e.,* blue peaks in **Figures 3.2 (a-b)**) were taken from the materials project "mp-1102092" cif file for the pristine $NaFe(SO_4)_2$ with *C2/m1* symmetry.

From the peak position of these two materials, a significant peak shift was observed. **Figure 3.2 (b)** represents the relative peak shift and peak position of our synthesized $Na_{0.8}Fe(SO_4)_2$ materials with that of pristine $NaFe(SO_4)_2$ (mp-1102092). The highest intense peak was obtained for the (*hkl*) value of *(11-1)* 2θs of about 24.328º followed by other low-intense peaks. The relative peak intensity of our synthesized $Na_{0.8}Fe(SO_4)_2$ remained almost the same as that of the relative intensity of $NaFe(SO_4)_2$. In addition to the characteristic XRD peaks of $Na_{0.8}Fe(SO_4)_2$, a few additional impurity peaks were observed, marked by (***) in **Figure 3.2 (a)**. These impurity peaks correspond to the presence of $Fe_2(SO_4)_3$ [23,24] and $FeSO_4 \cdot H_2O$ [25]. The formation of these impurities was attributed to a localized deficiency of sodium in $Na_{0.8}Fe(SO_4)_2$ compared to the stoichiometric composition of pristine $NaFe(SO_4)_2$. The existence of $FeSO_4.H_2O$ is especially significant due to the structural water molecule in this phase. Such water content can result in unwanted consequences in electrochemical cycling, such as gas evolution, electrode/electrolyte interface instability, and potential decomposition reactions at high potentials. These side reactions can negatively impact the initial Coulombic efficiency and long-term cycling stability of the electrode material. Nevertheless, it must be stressed that peaks of the observed $FeSO_4.H_2O$ were extremely low in intensity, which corresponded to a trace impurity in the resultant material. Its presence was minimized by optimizing the synthesis conditions through the careful regulation of calcination temperature and precursor drying. Accordingly, although this impurity is recognized as being potentially harmful, its low amount should not have a major effect on the overall electrochemical performance of $Na_{0.8}Fe(SO_4)_2$.

This peak position shifting towards higher 2θ of $Na_{0.8}Fe(SO_4)_2$ results in low *d*-spacing as per **equation 3.1** which further reduced the crystal parameters of sodium deficient $Na_{0.8}Fe(SO_4)_2$ compared to that of the pristine $NaFe(SO_4)_2$. These parameters reduction in $Na_{0.8}Fe(SO_4)_2$ due to the sodium deficiency that resulted in the shrinkage of the lattice

parameters and unit cell volume, which further reduced the *d*-spacing and increased the peak position at various 2θ values compared to $NaFe(SO_4)_2$. Hence, the reduced unit cell volume of $Na_{0.8}Fe(SO_4)_2$ compared to the reported $NaFe(SO_4)_2$ is due to the sodium deficiency. To further investigate this observation of volume shrinkage and higher 2θ shifting in the XRD pattern, we performed the calcination process at various temperatures of 310, 410, and 510ºC. From the XRD analysis of the materials calcinated at these temperatures, we observed that, as the calcination temperature increased from 310ºC to 510ºC there was a noticeable higher 2θ shifting of XRD peaks, which was due to the shrinkage in both the lattice parameters and the unit cell volume. Hence, there was a significant reduction in the lattice parameters and the unit cell volume of the material of interest with the successive increase in the calcination temperature.

Bragg's law: $$d_{(hkl)} = \frac{n\lambda}{2\sin(\theta)} \qquad \ldots\ldots\ldots (3.1)$$

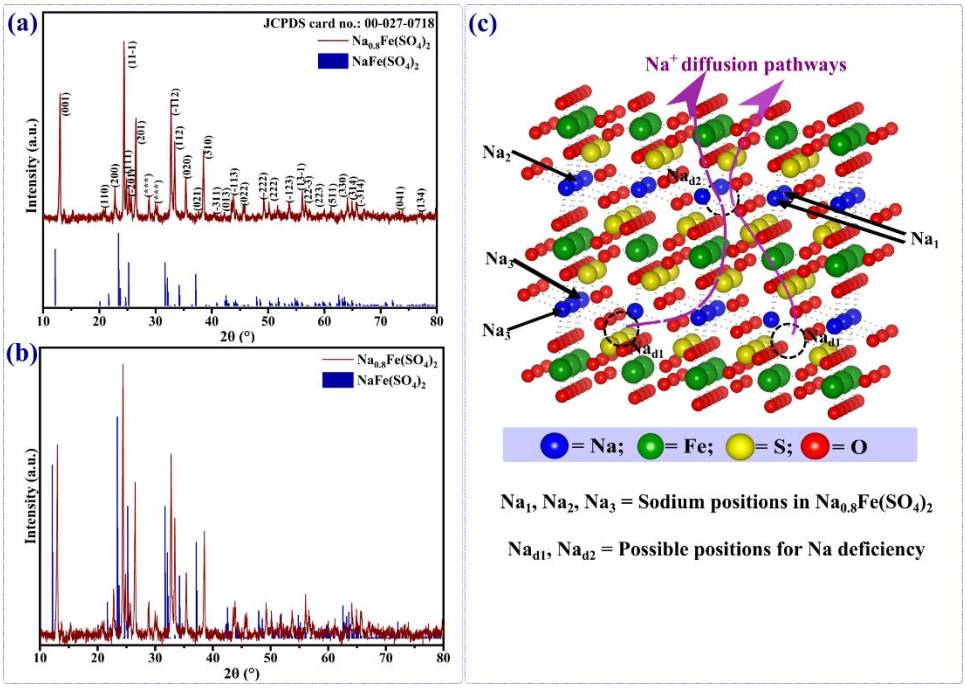

Figure 3.2 (a-b) XRD pattern for the synthesized $Na_{0.8}Fe(SO_4)_2$ calcinated at 420º for 12 h, and (c) Possible crystal structure of sodium deficient $Na_{0.8}Fe(SO_4)_2$ representing the possible feasible sodium-ion and sodium deficient locations and the new possible sodium ion diffusion pathway.

Further the interplanar spacing formula (**equation 3.2**) for the monoclinic structure, *d*-spacing, and (*hkl*) values were used to find out lattice parameters and β (angle between *a* and *c* axes) values for sodium deficient $Na_{0.8}Fe(SO_4)_2$.

$$\frac{1}{d_{hkl}^2} = \frac{h^2}{a^2\, sin^2(\beta)} + \frac{k^2}{b^2} + \frac{l^2}{c^2\, sin^2(\beta)} - \frac{2\, h\, l \cos(\beta)}{a\, c\, sin^2(\beta)} \qquad \ldots\ldots\ldots\ldots \quad (3.2)$$

Further, the unit cell volume for sodium deficient $Na_{0.8}Fe(SO_4)_2$ lattice was calculated with the help of **equation 3.3**.

$$V = abc\sqrt{1 - cos^2(\alpha) - cos^2(\beta) - cos^2(\gamma) + 2\cos(\alpha)\cos(\beta)\cos(\gamma)} \quad \ldots (3.3)$$

For a monoclinic crystal system with $\alpha = \gamma = 90\circ$ and only $\beta \neq 90°$, the unit cell volume reduces as follows:

$$V\ (in\ A^{\circ 3}) = abc\ \sin(\beta) \qquad \ldots\ldots\ldots\ldots (3.4)$$

Where β is in radian and calculated as,

$$\beta(in\ radian) = \frac{\pi}{180} \text{x}\ \beta(in\ degree) \ldots\ldots\ldots\ldots\ldots (3.5)$$

With the help of the above equations, we calculated the lattice parameters, interaxial angles, and unit cell volume for $Na_{0.8}Fe(SO_4)_2$ material synthesized via the sol-gel method. These calculated parameters are summarized in **Table 3.1** and compared with those of pristine $NaFe(SO_4)_2$ (CIF file: mp-1102092 from the materials project and early reported data for $NaFe(SO_4)_2$).

Figure 3.2 (c) represents the crystal structure of sodium-deficient $Na_{0.8}Fe(SO_4)_2$, representing the possible sodium atom and Na^+-ion position inside the crystal. Three specific sodium positions represented by Na_1 (sodium atom at the centre of the unit cell), Na_2 (sodium atom situated between the centre and the crystal side), and Na_3 (sodium atoms at the corner of the crystal) were observed as shown in **Figure 3.2 (c)**. The dotted circles (represented by Na_{d1} and Na_{d2}) in **Figure 3.2 (c)** represent the possible position of sodium deficiency in $Na_{0.8}Fe(SO_4)_2$, which results in an additional pathway for Na^+-ion diffusion during the intercalation/deintercalation process. With these additional pathways, it was

expected that the $Na_{0.8}Fe(SO_4)_2$ would demonstrate higher Na^+-ion diffusion coefficients and charge kinetics, which were one of the crucial parameters for battery performance.

Table 3.1: EDX, crystallographic, and structure parameters/data for $Na_{0.8}Fe(SO_4)_2$ and $NaFe(SO_4)_2$.

Parameter Description	$Na_{0.8}Fe(SO_4)_2$ (synthesized)	$NaFe(SO_4)_2$ (mp-1102092)	$NaFe(SO_4)_2$ (early reported)
***a* (Å)**	7.835	8.176	8.120 [20]
***b* (Å)**	5.085	5.232	5.230 [20]
***c* (Å)**	6.841	7.252	7.190 [20]
***α* (º)**	90.000	90.000	90.000 [20]
***β* (º)**	73.609	91.445	90.750 [20]
***γ* (º)**	90.000	90.000	90.000 [20]
Unit cell volume (Å^3)	261.465	310.169	305.66 [20]
Atomic % from EDX (Na, Fe, S, O)	8.4, 10.3, 19.8, 61.6	-	-

3.3.1.3 Particle Size and Surface Morphology Analysis

The particle size and surface morphology of $Na_{0.8}Fe(SO_4)_2$ as cathode, synthesized by the citric acid abetted sol-gel technique with a calcination heat treatment of 410ºC for about 12 h are shown in **Figure 3.3**. Both the microstructural particle size and surface morphology were studied with the help of FESEM, as shown in **Figures 3.3 (a-c).** It was observed that $Na_{0.8}Fe(SO_4)_2$ compound possessed particles with an undefined size and shape. Most of the $Na_{0.8}Fe(SO_4)_2$ particles lay in the particle size range of 0.5-1 μm, having unexpected agglomeration as shown in **Figure 3.3 (a-c)** for the different scale views of the surface morphology of $Na_{0.8}Fe(SO_4)_2$.

Further, EDX analysis was performed to analyse the atomic-wise existence of Na, Fe, S, and O elements in $Na_{0.8}Fe(SO_4)_2$, atomic, molecular, and chemical composition to match the nominal proportion of $Na_{0.8}Fe(SO_4)_2$, and the nature of elemental distribution in the material of

interest. From **Figure 3.3 (d)** it can be observed that Na, Fe, S, and O elements were uniform and evenly distributed throughout the $Na_{0.8}Fe(SO_4)_2$ cathode. Similarly, **Figure 3.3 (e)** demonstrates the EDX plotting for the presence of various elements in a percentage manner, representing the nominal composition of the synthesized material. Furthermore, **Figures 3.3 (f-i)** correspond to the uniform distribution and the color mapping of various atoms present in the synthesized $Na_{0.8}Fe(SO_4)_2$. Interestingly, EDX demonstrated the nominal composition of Na, Fe, and S present in the material of interest as per our stoichiometry requirement. Further, all the elements (*i.e.,* Na, Fe, S, and O) were uniformly spanned throughout the material, representing the synthesis of the required compound in a better manner.

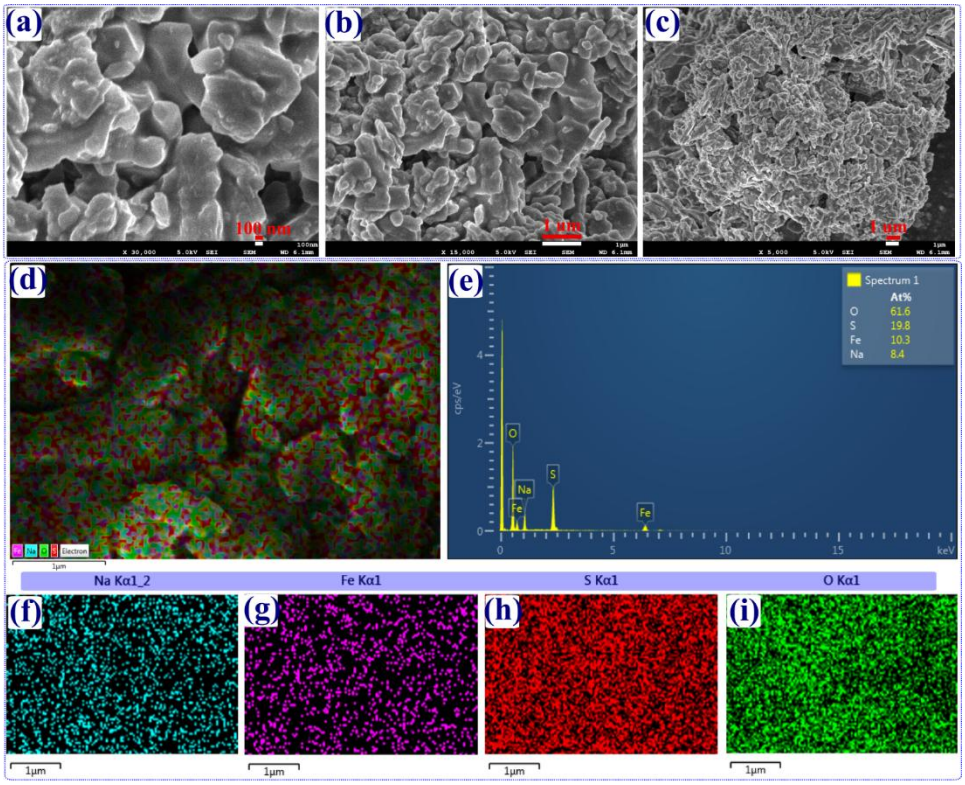

Figure 3.3 (a-c) Various scale view FESEM imaging, (d) Elemental distribution for Na, Fe, S, and O, (e) EDX mapping, and (f-i) Uniform spanning and color mapping of various elements in the synthesized $Na_{0.8}Fe(S)_4)_2$ compound.

4.3.1.4 XPS Analysis of $Na_{0.8}Fe(SO_4)_2$

To carry out a more in-depth investigation on the redox couple, oxidation state, and chemical composition, an XPS study was performed for $Na_{0.8}Fe(SO_4)_2$, as shown in **Figure 3.4**. The XPS survey scan of $Na_{0.8}Fe(SO_4)_2$ in **Figure 3.4 (a)** demonstrated the presence of all the elements belonging to the material of interest. An additional peak of C *1s* was present as the carbon-coated Cu grid was used as the substrate for the sample holder in the XPS study. The C_{KLL}, O_{KLL}, and Fe_{LMM} peaks were also observed due to the Auger electrons. Smooth scan XPS of Na 1*s*, Fe 2*p*, S 2*p*, and O 1*s* are shown in **Figures 3.4 (b-e)**.

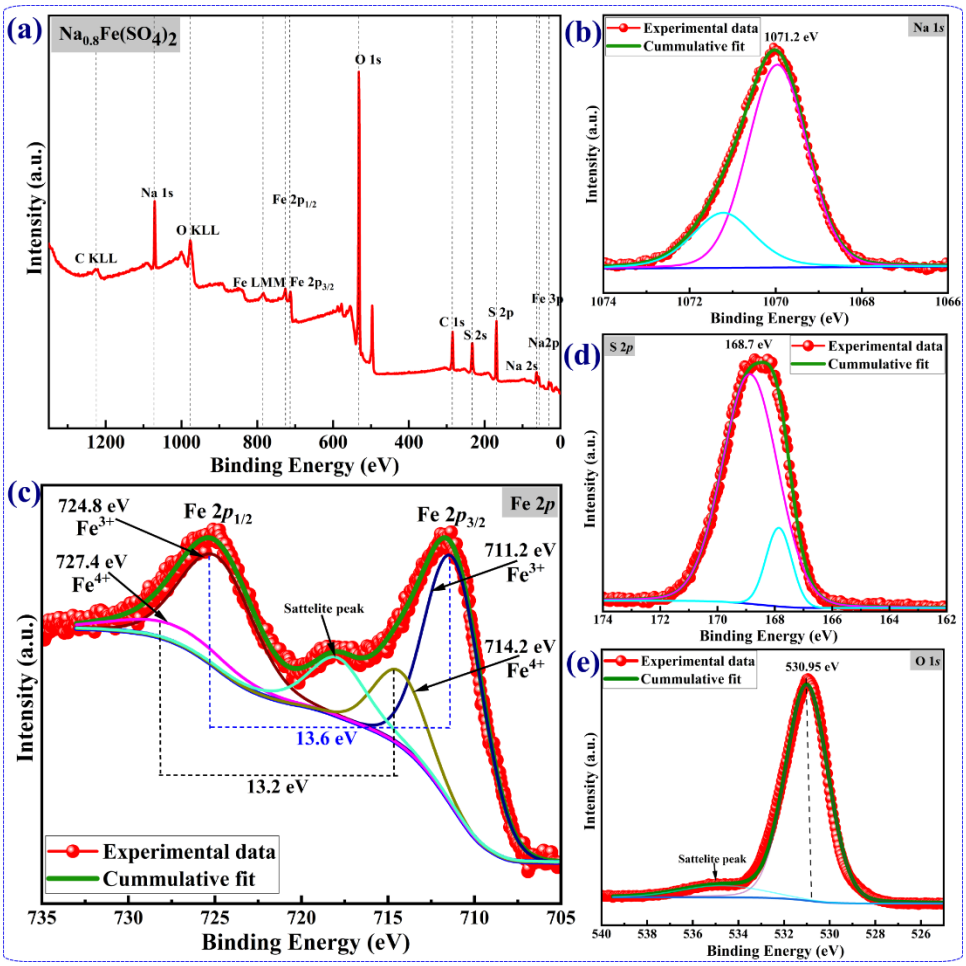

Figure 3.4 (a) XPS survey scan of $Na_{0.8}Fe(SO_4)_2$, smooth XPS survey scan of (b) Na 1s, (c) Fe 2p, (d) S 2p, and (e) O 1s orbitals.

The BE for electrons in Na 1*s* was found at 1071.2 eV. We performed the deconvolution of the Fe 2*p* orbital as shown in **Figure 3.4 (c)**. It was observed that Fe in $Na_{0.8}Fe(SO_4)_2$ coexists in both Fe^{3+} and Fe^{4+} oxidation states, with the Fe^{3+} state being dominant. The presence of Fe^{4+} could be attributed to the sodium deficiency in the local structure, leading to partial 4+ oxidation of Fe. The smooth scan XPS of Fe revealed a spin-orbital splitting of Fe $2p_{3/2}$ and Fe $2p_{1/2}$ with binding energies of 711.2 eV and 724.8 eV, respectively for Fe^{3+}, and binding energies of 714.2 eV and 727.4 eV, respectively for Fe^{4+} oxidation states. These resulted in a spin-orbit splitting BE difference of 13.6 and 13.2 eV for Fe^{3+} and Fe^{4+}, respectively. This analysis revealed that the electrochemical performances of $Na_{0.8}Fe(SO_4)_2$ were mostly dominated by Fe^{3+}/Fe^{4+} redox couple during the deintercalation/intercalation process. Additionally, a partial occurrence of Fe^{4+} is due to the presence of a small amount of materials with Na-deficiency. The additional high-intensity satellite peak corresponded to the characteristic for Fe^{3+} oxidation state in Fe *2p* orbital was also observed. Similarly, the smooth scan XPS for S (**Figure 3.4 (d)**) showed the BE of the electron in S *2p* orbital was about 168.7 eV and that of the electron in O 1*s* (**Figure 3.4 (e)**) was about 531 eV.

3.3.1.5 Raman Analysis of $Na_{0.8}Fe(SO_4)_2$

Raman spectra studies for $Na_{0.8}Fe(SO_4)_2$ were performed to explore more information about the material through the vibrational modes of the material as presented in **Figure 3.5 (a)**. Three significant peaks were observed at 1005.36, 1020.129, and 1072.84 cm^{-1} wave numbers corresponding to the symmetric vibration (υ_{sym}) of S-O in sulphate polyanions (SO_4) tetrahedral unit. Similarly, the asymmetric vibration (υ_{asym}) of S-O in the SO_4 was found at the corresponding wave number of 1294.81 cm^{-1}. These υ_{sym} and υ_{asym} vibration modes for $Na_{0.8}Fe(SO_4)_2$ were observed to be shifted towards a slightly higher wave number than the early reported literature of pristine $NaFe(SO_4)_2$.[15] The Raman peak shifting

was due to the formation of local disorder on those sites, which had resulted from the presence of sodium deficiency in $Na_{0.8}Fe(SO_4)_2$ cathode material. This data interpretation revealed crucial information regarding the local chemical interaction and the integrity of structural retention of $Na_{0.8}Fe(SO_4)_2$, particularly in the SO_4 tetrahedral group.

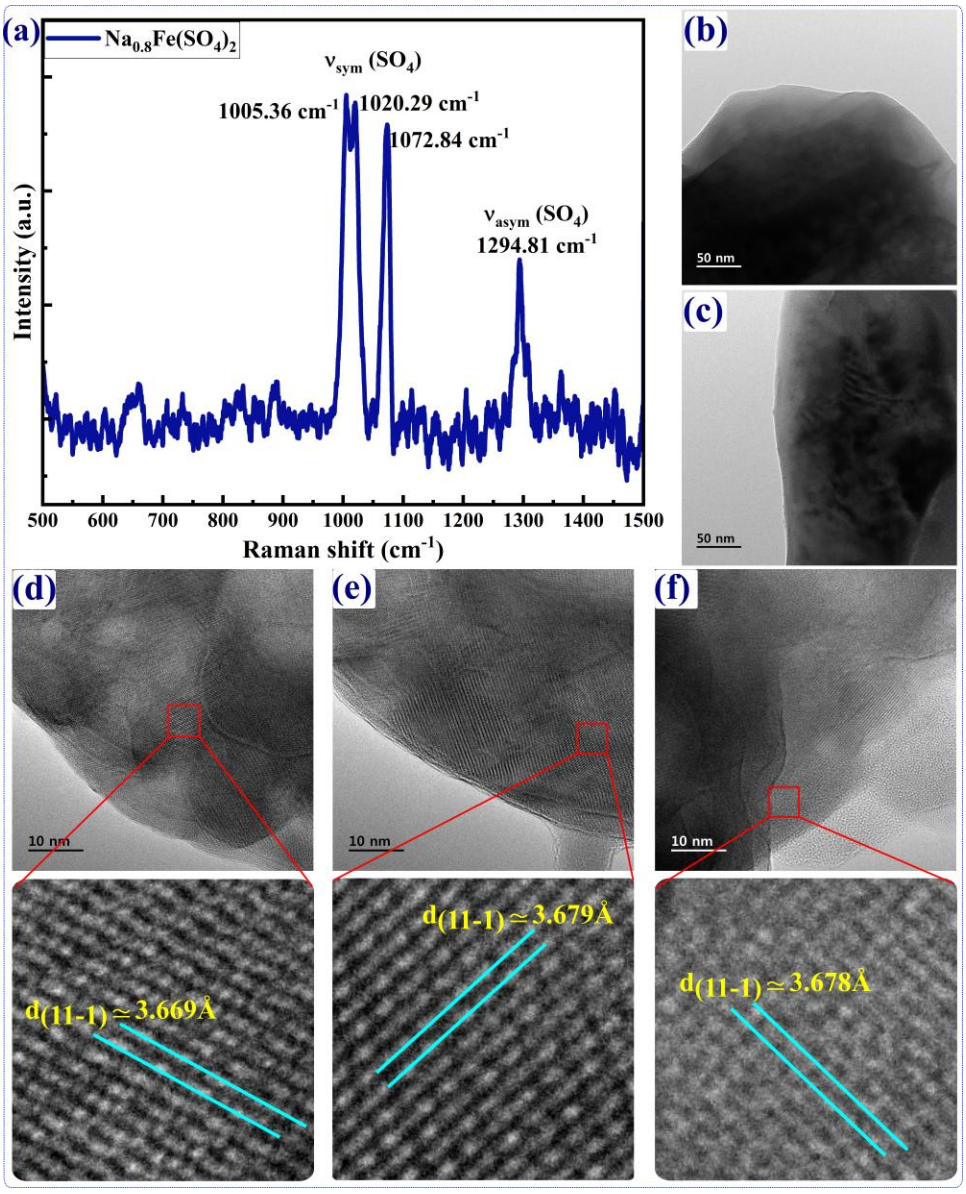

Figure 3.5 (a) Raman spectra of $Na_{0.8}Fe(SO_4)_2$, (b-c) TEM images, and (d-f) HRTEM images of $Na_{0.8}Fe(SO_4)_2$ particles at various locations.

3.3.1.6 Atomic Arrangement Analyses: HRTEM/TEM

Figures 3.5 ***(b-c)*** represent the TEM images of $Na_{0.8}Fe(SO_4)_2$ at different locations, representing the morphological features of the material of interest. The surface morphologies of the particles displayed a relatively homogeneous distribution and irregular shape, which was consistent with FESEM analysis. The particle size of the synthesized $Na_{0.8}Fe(SO_4)_2$ through TEM was found to be in the range of 500-1000 nm (0.5-1 μm). Further, HRTEM was performed to investigate the internal atomic arrangements and ordered lattice fringes for $Na_{0.8}Fe(SO_4)_2$. The HRTEM images in **Figures 3.5 (d-f)** display the ordered atomic arrangement and ordered lattice fringes of $Na_{0.8}Fe(SO_4)_2$ at a different location. The upscaled portion of the respective **Figures 3.5 (d-f)** displays a clear view of the uniform and ordered arrangement of atoms in a particular direction and orientation.

These lattice fringes and their corresponding interplanar spacing of ordered atomic arrangement were used to calculate the interplanar *d*-spacing as displayed in the upscaled portion of **Figures 3.5 (d-f)**. We observed a *d*-spacing of ~3.7 Å, consistent with (*hkl*) of the highest intense lattice plane of (*11-1*) as shown in the XRD pattern. This additionally revealed the high crystallinity of $Na_{0.8}Fe(SO_4)_2$. This obtained d = ~3.7 Å of $Na_{0.8}Fe(SO_4)_2$ was slightly lower than that of the pristine $NaFe(SO_4)_2$ having d = 3.79 Å corresponding to the same *(11-1)* plane. This decrease in *d* value was due to sodium deficiency and is resonant with those of XRD results, as explained above, XRD-section. This investigation lighted on a crucial insight into the ordered atomic arrangement, signifying high crystalline nature and minimal sodium defects within the particles of $Na_{0.8}Fe(SO_4)_2$. The distinct and crisp lattice fringes in **Figures 3.5 (d-f)** indicated a better-ordered arrangement of atomic layers, crucial for enhancing the electrochemical characteristics of the cathode materials. Hence, the combined TEM and HRTEM investigations provided a thorough insight into the structural surface morphology and integrity of $Na_{0.8}Fe(SO_4)_2$, emphasizing its potential as an SIB cathode.

3.3.2 Electrochemical Performance Analyses

3.3.2.1 CV Analysis

Na/1M-$NaClO_4$/$Na_{0.8}Fe(SO_4)_2$ CR2032 coin-cell demonstrated an open-circuit voltage of ~3.12V *vs.* Na/Na^+ before performing the CV analysis, highlighting the suitability of $Na_{0.8}Fe(SO_4)_2$ for high-performance cathode material for energy storage applications. **Figure 3.6 (a)** represents the CV pattern of Na/1M-$NaClO_4$/$Na_{0.8}Fe(SO_4)_2$ at the scan rates of 0.1 mV/s, 0.25 mV/s, and 0.5 mV/s in the working voltage range of 1.5 - 4.5 V having a high voltage window of 3 V. A consistent presence of a single redox pair corresponding to the Fe^{4+}/Fe^{3+} transition during the oxidation/reduction was observed at all scan rates within the voltage range of 1.5-4.5 V. The specific anodic peaks at 3.505, 3.483, and 3.483 V and cathodic peaks at 3.136, 3.116, 3.102V at the corresponding scan rates of 0.1 mV/s, 0.25 mV/s, and 0.5 mV/s, respectively indicated consistency in redox peak positions of $Na_{0.8}Fe(SO_4)_2$ material in Na/1M-$NaClO_4$/$Na_{0.8}Fe(SO_4)_2$ revealing its excellent reversibility of redox reaction. Furthermore, the high current density values for the anodic and cathodic peaks in **Figure 3.6 (a)** represent the fast electron transfer and diffusion control mechanism of the cathode material during the charge/discharge process. This enhanced performance could be attributed to the presence of sodium deficiency of $Na_{0.8}Fe(SO_4)_2$ cathode material.

The reaction kinetics of $Na_{0.8}Fe(SO_4)_2$ as a cathode material was further characterized using the power-law equation **(equation 3.6)** that relates the oxidation/reduction peak current (i), scan rate (v), and 'a and b' as two constant parameters as follows.

$$i = av^b \qquad \text{…. …. …. (3.6)}$$

Here, the value of 'b' was achieved by taking the slope of the straight line drawn for the logarithm of the redox peak of current densities (*i.e., log(I_p)* and the logarithm of scan rates (*i.e., log(v)*) as shown in **Figure 3.6 (b)**. Here, the value of b theoretically reveals the capacitive or battery-type performance of $Na_{0.8}Fe(SO_4)_2$. The obtained values of 'b' for the cathode of

$Na_{0.8}Fe(SO_4)_2$ in Na/1M $NaClO_4$/$Na_{0.8}Fe(SO_4)_2$ through CV analysis were found to be 0.887 and 0.792 for the cathodic and anodic peaks, respectively. This suggests that $Na_{0.8}Fe(SO_4)_2$ exhibited favorable kinetics for both battery as well as supercapacitor applications indicating the efficient charge transfer and redox reactions of $Na_{0.8}Fe(SO_4)_2$ during cycling.

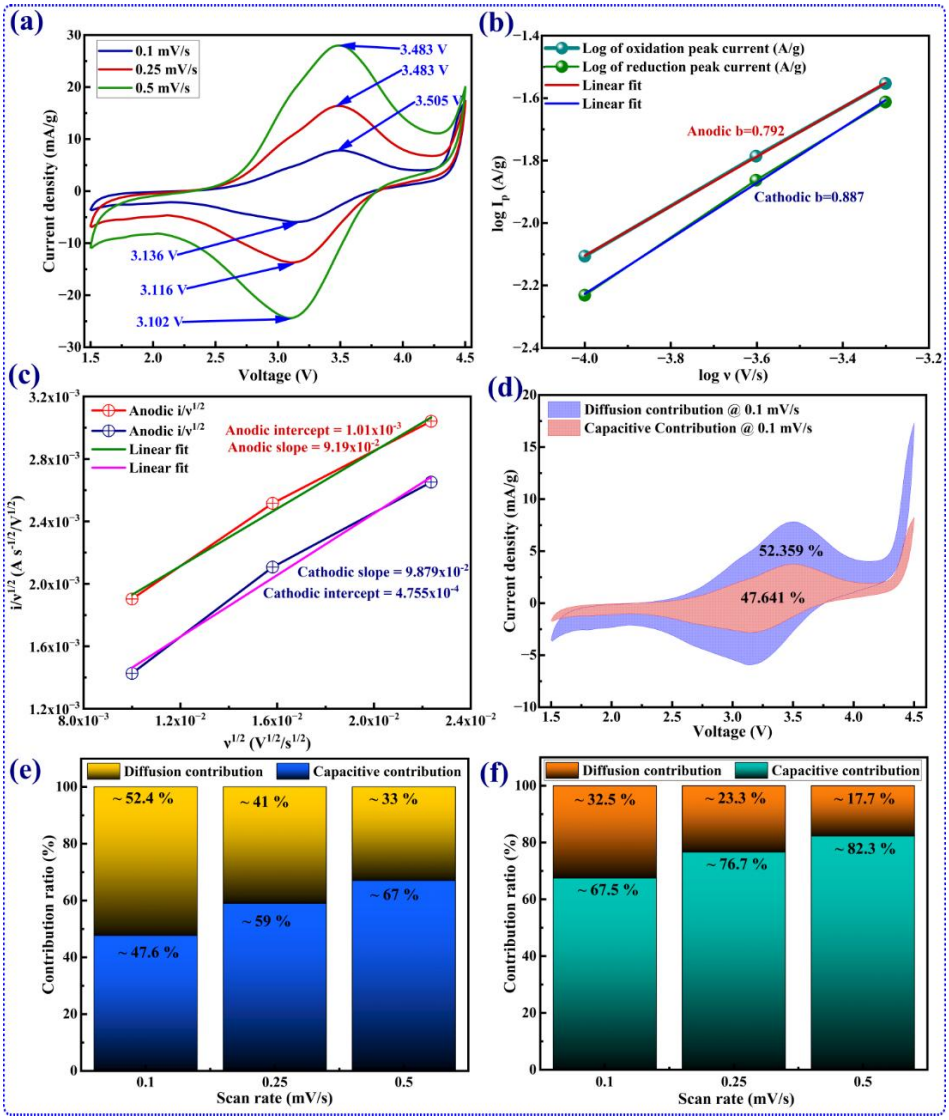

Figure 3.6 (a) CV curve at 0.1, 0.25, and 0.5 mV/s scan rates, (b) Linear relation of log(I_p) vs. log (υ), (c) Linear relation of $i/\upsilon^{1/2}$ vs. $\upsilon^{1/2}$, (d) Contribution of diffusion and capacitive behavior, (e) Bar diagram for the contribution of diffusion and capacitive behavior at anodic, and (f) Bar diagram for the contribution of diffusion and capacitive behavior at cathodic peak for $Na_{0.8}Fe(SO_4)_2$ cathode in Na/1M $NaClO_4$/$Na_{0.8}Fe(SO_4)_2$ cell.

The CV analysis was extended for Na^+-ion diffusion coefficient (represented by D_{Na+})calculation for the oxidation peaks with the assistance of the Randles-Sevcik equation as given below in **equation 3.7** [26].

$$i_p = 0.446\, n\, F\, A\, C \left(\frac{n\, F\, \upsilon\, D_{Na+}}{RT}\right)^{\frac{1}{2}} \quad \ldots\ldots\ldots (3.7)$$

Where i_p (in A) represents the peak current of anodic/cathodic peaks, n represents the number of electrons transferred (here n=1 for the material of interest), F is Faraday constant, A represents electrode surface area (2.011 cm^2), C represents the concentration of sodium ions in the unit of mol/cm^3 for our material, υ represents the respective scan rate, R is the universal gas constant, and T is the absolute temperature. By substituting the values of F, R, and T at room temperature of 25°C, the above equation of the sodium ion diffusion coefficient (D_{Na+}) is reduced to:

$$i_p = 2.69\text{x}10^5\, n^{\frac{3}{2}}\, A\, C\, \sqrt{D_{Na+}\, \upsilon}$$

$$D_{Na+} = \frac{{i_p}^2}{7.236\text{x}10^{10}\, n^3\, A^2 C^2\, \upsilon} \quad \ldots\ldots\ldots (3.8)$$

Followed by **equation 3.8**, the average D_{Na+} of the charging process was calculated to be about $1.413\text{x}10^{-13}$ cm^2/s. The D_{Na}^+ values for $Na_{0.8}Fe(SO_4)_2$ cathode material are presented in **Table 3.2** and are compared with those of the early reported literature for the pristine $NaFe(SO_4)_2$ and polyanion group-doped cathode materials. **Table 3.2** demonstrates that $Na_{0.8}Fe(SO_4)_2$ shows an improved sodium diffusion than the pristine $NaFe(SO_4)_2$ and polyanionic group substituted $NaFe(SO_4)_{1.5}(SeO_4)_2$, $NaFe(SO_4)_{1.5}(PO_3F)_2$, $NaFe(SO_4)_{1.5}(HPO_4)_2$. This improved sodium diffusion was due to the presence of sodium deficiency, which resulted in the formation of additional Na^+-ion diffusion that helped to improve the Na^+-ion and electron kinetics inside the host cathode material, which was a crucial requirement for a secondary ESS.

Table 3.2: Sodium diffusion coefficients for $Na_{0.8}Fe(SO_4)_2$.

Materials	Average D_{Na^+} (cm^2/s)	Ref.
$NaFe(SO_4)_2$	$1.4x10^{-13}$ (from CV); $5.53x10^{-19}$ (from EIS)	[15]
$NaFe(SO_4)_{1.5}(HPO_4)_{0.5}$	$1.4x10^{-14}$ (from CV), $1.15x10^{-16}$ ((from EIS)	[15]
$NaFe(SO_4)_{1.5}(PO_3F)_{0.5}$	$3.1x10^{-13}$ (from CV), $2.76x10^{-13}$ (from EIS)	[15]
$NaFe(SO_4)_{1.5}(SeO_4)_{0.5}$	$3.8x10^{-14}$ (from CV), $1.32x10^{-18}$ (from EIS)	[15]
$Na_{0.8}Fe(SO_4)_2$	**$1.413x10^{-13}$**	**This work**

The diffusion-controlled and capacitive characteristics of $Na_{0.8}Fe(SO_4)_2$ cathode were calculated through CV analysis using power-law (**equation 3.9**) and Dunn plots (**Figure 3.6 (d)**). In **equation 3.9**, i(V) represents the current at fixed voltage *vs.* Na/Na^+, and k_1 and k_2 are the constants [27]. The first term $k_1\upsilon$ corresponds to the capacitive contribution, and the second term $k_2\upsilon^{0.5}$ corresponds to the diffusion-controlled contribution towards to total current of the cathode material. A linear plot of $i/\upsilon^{1/2}$ *vs.* $\upsilon^{1/2}$ was used to find out the values for k_1 and k_2 for both the oxidation and reduction processes as shown in **Figure 3.6 (c).**

$$i(V) = k_1\upsilon + k_2\nu^{\frac{1}{2}} \qquad \ldots\ldots\ldots\ldots (3.9)$$

The pictorial representation of these combined behaviour known as Dunn's plot, is shown in **Figure 3.6 (d)** for a 0.1 mV/s scan rate. At this scan, $Na_{0.8}Fe(SO_4)_2$ showed about 52.36% diffusion-controlled and 47.64% of capacitive characteristics for energy storage. The current contribution values for other scan rates as shown in the form of a bar diagram in **Figure 3.6 (e)** for charging and **Figure 3.6 (f)** for discharging, respectively.

3.3.2.2 Galvanostatic Charge Discharge Analysis

Electrochemical features of $Na_{0.8}Fe(SO_4)_2$ cathode material were further analyzed through GCD as shown in **Figure 3.7.** The voltage window chosen for GCD analysis was 1.5-4.5 V, which was the same as that used for the CV analysis. As demonstrated in **Figure 3.7**, the GCD analysis was performed at various C-rates of 0.2, 0.25, 0.5, 1, and 2C for five cycles. The

GCD curve in **Figure 3.7 (a)** demonstrated a couple of almost horizontal plateau-like charging and discharging behaviour, indicating the electrochemical reversibility and the lower polarizability of $Na_{0.8}Fe(SO_4)_2$ as cathode material for SIBs. The consistency in the GCD curves pattern across all C-rates for both charging and discharging processes in **Figure 3.7 (a)** strongly indicates the high electrochemical reversibility process and the structural integrity retention of $Na_{0.8}Fe(SO_4)_2$ during the intercalation/deintercalation of Na^+ ions. This consistency suggested that the redox reactions were highly efficient and reversible. Furthermore, the minimal gap between the charge and discharge profiles in GCD reflected lower polarizability, which was attributed to the material's 3D structural features resulted due to sodium deficiency, including a stable crystalline framework, and efficient charge transfer kinetics. These properties collectively enhanced the electrochemical stability and performance of the cathode material. $Na_{0.8}Fe(SO_4)_2$ in Na/1M-$NaClO_4$/$Na_{0.8}Fe(SO_4)_2$ cell exhibited a discharge specific capacity of 41.17 mAh/g, 30.8 mAh/g, 22.06 mAh/g, 15.11 mAh/g, and 9.12 mAh/g at 0.2C, 0.25C, 0.5C, 1C and 2C, respectively. The lower discharge capacity of $Na_{0.8}Fe(SO_4)_2$ than $NaFe(SO_4)_2$ was mainly due to its lower theoretical capacity (~80.49 mAh/g) compared to $NaFe(SO_4)_2$ (~98.91 mAh/g). While electrolyte decomposition could contribute slightly, the primary reason for the reduced capacity was the inherent electrochemical properties of $Na_{0.8}Fe(SO_4)_2$ itself. These discharge-specific capacities were almost equal to their respective charge capacity values, representing a high Coulombic efficiency for the charge/discharge process of the cathode material. These specific capacity values of $Na_{0.8}Fe(SO_4)_2$ cathode material are given in **Table 3.3,** and its performance was compared with several of the early reported pristine $NaFe(SO_4)_2$ and its polyanion group tuned materials. The decrease of specific capacities at higher C-rates was due to the higher resistance encountered by the ions, which results in a slower ion diffusion. Again, the reduced contact of the ions with the electrolyte hindered the efficient

transfer of charge. The decrease in specific capacities in $Na_{0.8}Fe(SO_4)_2$ was due to the presence of sodium deficiency. The line chart in **Figure 3.7 (b)** represented the average voltage of Na/1M-$NaClO_4$/$Na_{0.8}Fe(SO_4)_2$ cell for all five cycles corresponding to their C-rates. The average voltage for the 1st charge-discharge cycle at 0.2 C was about 3.26 V, which then saturated to about 3.15 V for other cycles at 0.2 C. The average voltage for other C-rates remained between 3.1 V to 3.15 V as shown in **Figure 3.7 (b)**. Again, **Figure 3.7 (c)** represents the *dQ/dV vs.* voltage (V) profile for various C-rates ranging from 0.2 to 2 C. The *dQ/dV vs.* V curve in **Figure 3*c*** demonstrates similar charge and discharge peak positions at the same voltages, similar to the CV profile for intercalation/deintercalation processes. This further revealed the consistency of GCD with CV and the high reversibility of the electrochemical characteristics of $Na_{0.8}Fe(SO_4)_2$ cathode material.

Table 3.3: Electrochemical performance of $Na_{0.8}Fe(SO_4)_2$ relative to other reported materials.

Material Name	Specific capacity (mAh/g)	Capacity retention (%)	Voltage range (V)	Ref.
$NaFe(SO_4)_2$	63 mAh/g at 0.1C	-	2 - 4.25	[15]
$NaFe(SO_4)_2$	78 mAh/g at 0.1C	-	2 - 4.2	[19]
$NaFe(SO_4)_2$	78 mAh/g at 0.1C	-	1.5 - 4.5	[28]
$NaFe(SO_4)_{1.5}(SeO_4)_{0.5}$	45 mAh/g at 0.1C	~50% after 5 cycles@0.1 C	2 - 4.25	[15]
$NaFe(SO_4)_{1.5}(PO_3F)_{0.5}$	39 mAh/g at 0.1C	~70% after 30 cycles	2 - 4.25	[15]
$NaFe(SO_4)_{1.5}(HPO_4)_{0.5}$	39 mAh/g at 0.1C	-10% after 30 cycles @0.1C	2 - 4.25	[15]
$Na_{0.8}Fe(SO_4)_2$	41.17 mAh/g at 0.2 C	~70% after 45 cycles@0.1C & ~98% @1.0C	1.5 - 4.5	This work

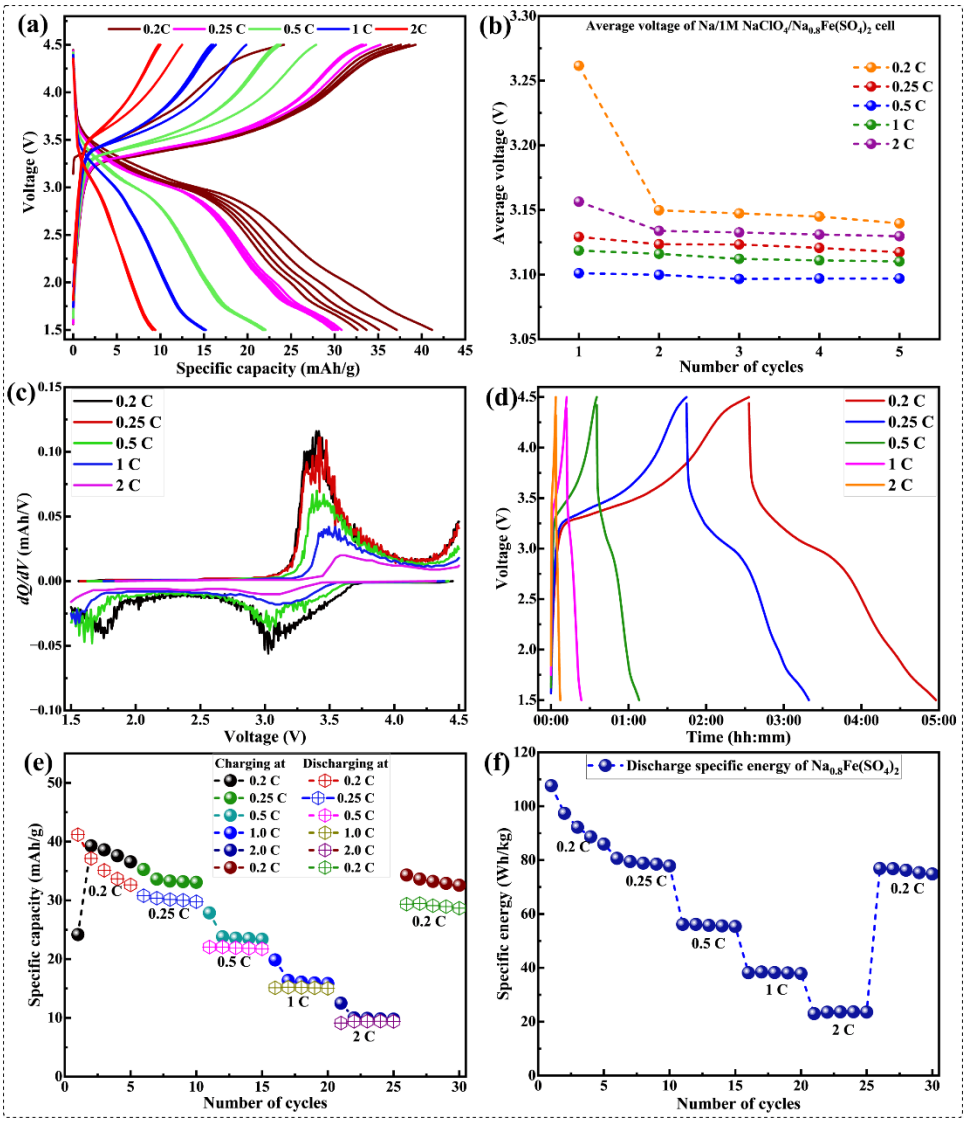

Figure 3.7 (a) GCD profile at various C-rates, (b) Average working voltage at various C-rates, (c) dQ/dV curve at various C-rates, (d) The charge-discharge time profile, (e) Rate performance, and (f) Specific energy for $Na_{0.8}Fe(SO_4)_2$ cathode in Na/1M-$NaClO_4$/$Na_{0.8}Fe(SO_4)_2$ cell.

Figure 3.7 (d) represents the charge-discharge time profile of Na/1M-$NaClO_4$/$Na_{0.8}Fe(SO_4)_2$ cell for various C-rates. The rate performance of $Na_{0.8}Fe(SO_4)_2$ at 0.2, 0.25, 0.5, 1, 2, and 0.2 C are represented in **Figure 3.7 (e)**. Interestingly, the material of interest exhibited good rate capability even at the higher C-rates of 1 C and 2 C. The discharge-specific capacities corresponding to five cycles of their respective

C-rates remained almost the same, indicating the highly electrochemically reversible nature of the cathode material. Additionally, it demonstrated an average discharge specific capacity of ~31 mAh/g at 0.25 C and 22.06 mAh/g at 0.5 C, corresponding to the initial specific capacity of 41.17 mAh/g at the first cycle of 0.2 C. With further rise in the current density (*i.e.,* C-rate values) the average specific capacity decreased as shown in **Figure 3.7 (e)**. During the entire rate performance, the Coulombic efficiency was also good and remained between 85-100%. It possessed the highest specific capacity of ~30 mAh/g on further proceeding to 0.2C. The specific energy for the material of interest was found to be ~107.61 Wh/kg at 0.2 C and ~79.4 Wh/kg at 0.25 C as shown in **Figure 3.7 (f)**.

3.3.2.3 Capacity Retention Analysis

The cyclic stability and the specific capacity retention of $Na_{0.8}Fe(SO_4)_2$ cathode are illustrated in **Figure 3.8(a)**. Although the specific capacity exhibited by $Na_{0.8}Fe(SO_4)_2$ was lower than its pristine $NaFe(SO_4)_2$, it demonstrated remarkable cycling stability and initial discharge capacity retention. It retained around 70% of its initial discharge capacity at the 45^{th} cycle at 0.1C. This capacity retention was much better than $NaFe(SO_4)_{1.5}(X)_{0.5}$ (X= SeO_4, PO_3F, HPO_4) and is comparable with $NaFe(SO_4)_2$. However, $Na_{0.8}Fe(SO_4)_2$ exhibited an incredible capacity retention at 1C. It retained about 98% of its initial discharge capacity even after 45 charge/discharge cycles as shown in **Figure 3.8 (a)**. These capacity retentions are compared in **Table 3.3**. The observed higher capacity retention at 1 C compared to 0.1 C was primarily due to the formation of a more stable solid-electrolyte interphase layer at faster cycling rates, which could reduce the side reactions that occur at slower rates. At 0.1C, longer cycles might allow more electrolyte decomposition, leading to a decrease in capacity retention over time. This superior capacity retention of $Na_{0.8}Fe(SO_4)_2$ at a higher C-rate represented its potential application as a long-term energy storage device irrespective of its low specific capacity.

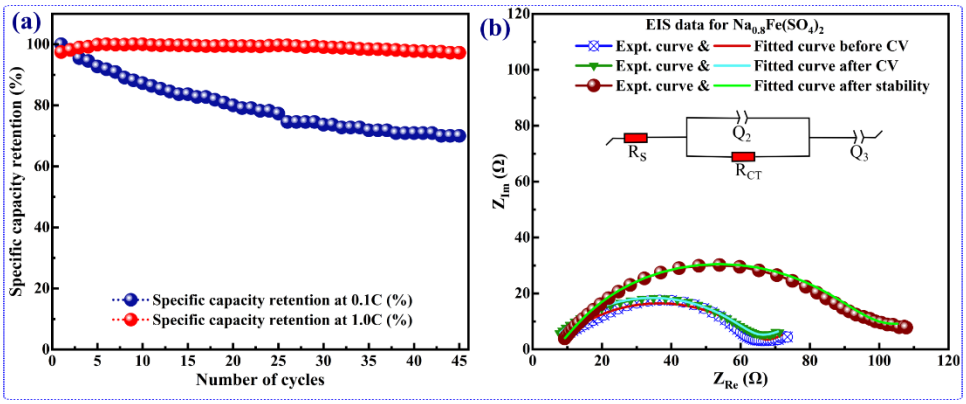

Figure 3.8 (a) Capacity retention behavior and (b) EIS analysis of $Na_{0.8}Fe(SO_4)_2$ cathode in Na/1M-$NaClO_4$/$Na_{0.8}Fe(SO_4)_2$ cell configuration.

3.3.2.4 EIS Studies

The charge kinetics, state of health, and ion diffusion activity of $Na_{0.8}Fe(SO_4)_2$ in Na/1M-$NaClO_4$/$Na_{0.8}Fe(SO_4)_2$ cells were explored through the EIS. **Figure 3.8 (b)** depicts the Nyquist plot relating the real part of impedance as a resistive component along the x-axis and the imaginary part of impedance as reactive components along the y-axis in a frequency covering from 1 Hz to 100,000 Hz. The EIS studies were performed before CV, after CV, and after stability tests as shown in **Figure 3.8 (b)**. These three curves had a similar pattern representing the high electrochemical reversibility. A well-fitted electrochemical circuit model corresponding to these experimentally obtained data is shown in **Figure 3.8 (b)** and is given by **equation 3.10**.

$$Equivalent\ circuit = R_s + \frac{Q_2}{R_{CT}} + Q_3 \qquad \ldots\ldots\ldots (3.10)$$

The total impedance (Z_{total}) of the above-fitted circuit as a function of applied frequency (υ) is given by the **equation 3.11**. Where, $j = \sqrt{-1}$ is the imaginary number, a_1 and a_2 are the exponent constants.

$$Z_{total}(\upsilon) = R_S + \frac{1}{\frac{1}{R_{CT}} + Q_2(j\upsilon)^{a_1}} + \frac{1}{Q_3(j\upsilon)^{a_2}} \qquad \ldots\ldots\ldots (3.11)$$

The values for these impedance parameters are tabulated in **Table 3.4** based on the fitted equivalent circuit with the experimentally obtained EIS data for $Na_{0.8}Fe(SO_4)_2$.

Table 3.4: Fitted impedance parameters of $Na_{0.8}Fe(SO_4)_2$ cathode in Na/1M-$NaClO_4$/$Na_{0.8}Fe(SO_4)_2$ cell.

Parameters	Before CV	After CV	After Stability
R_S (ohm)	6.076 (6)	3.822 (9)	3.323 (7)
R_{CT} (ohm)	59.279 (3)	57.641 (8)	78.996 (3)
Q_2 ($F.s^{(a-1)}$)	36. 25 (3)	12.321 (4)	10.521 (7)
a_1	0.636 (7)	0.7 (3)	0.778 (3)
Q_3 ($F.s^{(a-1)}$)	0.054 (5)	0.024 (1)	0.016 (1)
a_2	0.371 (9)	0.321 (7)	0.186 (5)

The solution resistance before CV analysis was found to be 6.076 Ω which was reduced to 3.822 Ω after CV. This reduction in the solution resistance was due to the formation of electrode/electrolyte interphase. After the CV study, the ions preferably followed a suitable pathway resulting a lower in resistance offered by the electrolyte. This solution resistance remained almost the same at 3.323 Ω after stability, indicating that the resistance offered by the electrolytes remains the same as the resistance offered by electrode/electrolyte interphase after the formation of the SEI layer. $Na_{0.8}Fe(SO_4)_2$ demonstrated a similar value for the charge transfer resistance offered by the SEI layer. However, this charge transfer resistance after stability analysis varied noticeably, indicating that the SEI layers compounds exhibited variation in their chemical composition after several charge/discharge processes. However, this R_{CT} value after stability was not significantly higher after several cycles than the R_{CT} before and after CV analysis. This indicated that the ions have good charge transfer kinetics due to the high reversible diffusion activity and the electrode exhibits a good state of health for Na^+ migration from the cathode to the electrolyte and vice-versa during intercalation and deintercalation.

3.4 Conclusions

In conclusion, in this chapter, we successfully synthesized sodium-deficient $Na_{0.8}Fe(SO_4)_2$ using a citric acid-abetted sol-gel process, and for the first time, unveiled its diverse physicochemical and electrochemical properties and performance as a cathode for SIBs. $Na_{0.8}Fe(SO_4)_2$ with monoclinic symmetry in the space group of *C2/m1* exhibited a reduction in lattice parameters, interplanar *d*-spacing, and the unit cell volume than its pristine $NaFe(SO_4)_2$, along with undefined particle shape and sizes ranging from 0.5 to 1 μm. The electrochemical properties of $Na_{0.8}Fe(SO_4)_2$ were attributed to the Fe^{4+}/Fe^{3+} redox couple during charging/discharging. It operated at an equilibrium voltage of 3.1-3.15 V within a voltage range of 1.5 - 4.5 V *vs.* Na/Na^+. The material showed high reversibility for redox reactions, rapid charge kinetics, and a combination of diffusion-controlled and capacitive behaviour for energy storage. Notably, $Na_{0.8}Fe(SO_4)_2$ exhibited a superior sodium diffusion coefficient compared to $NaFe(SO_4)_2$ and its polyanion-substituted derivatives. While $Na_{0.8}Fe(SO_4)_2$ had lower specific capacity than pure $NaFe(SO_4)_2$ it offered a comparable specific capacity to $NaFe(SO_4)_{1.5}X_{0.5}$ (X= SeO_4, PO_3F, HPO_4). Despite its lower specific capacity, $Na_{0.8}Fe(SO_4)_2$ stood out due to its high charge kinetics, wide voltage window, remarkable electrochemical reversibility, good cycling performance, excellent capacity retention, and low solution and charge transfer resistance. In short, this chapter focused on the systematic exploration of sodium deficiency as a design strategy, specifically investigating its impact on the structural, physicochemical, and electrochemical performance of the material. These attributes made $Na_{0.8}Fe(SO_4)_2$ a promising cathode for SIBs. This chapter provided valuable insights for the future development of long-cycle life, high C-rate SIBs tailored to meet specific requirements. We believe that our work contributed to the materials science and energy storage community by shedding light on how sodium deficiency impacted the overall properties of Na-based cathodes, paving the way for future advancements in this direction.

3.5 References

[1] A. kanwade, S. Gupta, A. Kankane, A. Srivastava, S.C. Yadav, P.M. Shirage, Phosphate-based Cathode Materials to boost the electrochemical performance of Sodium-ion Battery, Sustain. Energy Fuels. 6 (2022) 3114–3147. https://doi.org/10.1039/d2se00475e.

[2] V.R.R. Boddu, D. Puthusseri, P.M. Shirage, P. Mathur, V.G. Pol, Layered NaxCoO2-based cathodes for advanced Na-ion batteries: review on challenges and advancements, Ionics. 27 (2021) 4549–4572. https://doi.org/10.1007/s11581-021-04265-w.

[3] H. Shi, T. Li, Y. Liu, T. Yu, Z. Zhao, L. Hou, C. Yuan, Three-dimensional faveolate porous N-doped carbon skeleton embodied with nano Bi toward stable less-Na sodium metal batteries, J. Power Sources. 602 (2024) 234375. https://doi.org/10.1016/j.jpowsour.2024.234375.

[4] A. Kanwade, S. Gupta, A. Kankane, M.K. Tiwari, A. Srivastava, J.A. Kumar Satrughna, S. Chand Yadav, P.M. Shirage, Transition metal oxides as a cathode for indispensable Na-ion batteries, RSC Adv. 12 (2022) 23284–23310. https://doi.org/10.1039/d2ra03601k.

[5] V.R. Reddy Boddu, M. Palanisamy, L. Sinha, S.C. Yadav, V.G. Pol, P.M. Shirage, Hysteresis abated P2-type NaCoO2 cathode reveals highly reversible multiple phase transitions for high-rate sodium-ion batteries, Sustain. Energy Fuels. 5 (2021) 3219–3228. https://doi.org/10.1039/d1se00490e.

[6] M. Palanisamy, V.R. Reddy Boddu, P.M. Shirage, V.G. Pol, Discharge State of Layered P2-Type Cathode Reveals Unsafe than Charge Condition in Thermal Runaway Event for Sodium-Ion Batteries, ACS Appl. Mater. Interfaces. 13 (2021) 31594–31604. https://doi.org/10.1021/acsami.1c04482.

[7] C. Delmas, Sodium and Sodium-Ion Batteries: 50 Years of Research, Adv. Energy Mater. 8 (2018) 1703137.

https://onlinelibrary.wiley.com/doi/abs/10.1002/aenm.201703137%0Ainternal-pdf://843/aenm.html.

[8] K. Chayambuka, G. Mulder, D.L. Danilov, P.H.L. Notten, From Li-Ion Batteries toward Na-Ion Chemistries: Challenges and Opportunities, Adv. Energy Mater. 10 (2020) 2001310. https://doi.org/10.1002/aenm.202001310.

[9] L. Liang, X. Sun, D.K. Denis, J. Zhang, L. Hou, Y. Liu, C. Yuan, Ultralong Layered NaCrO2 Nanowires: A Competitive Wide-Temperature-Operating Cathode for Extraordinary High-Rate Sodium-Ion Batteries, ACS Appl. Mater. Interfaces. 11 (2019) 4037−4046. https://doi.org/10.1021/acsami.8b20149.

[10] K. Hashimotoa, K. Kubotaa, I. Ikeuchia, I. Saadoune, S. Komaba, P2-type Nax[Fe, Ni, Mn]02 for high capacity Na-ion batteries, 02 (2014) 1–4.

[11] T. Chen, B. Ouyang, X. Fan, W. Zhou, W. Liu, K. Liu, Oxide cathodes for sodium-ion batteries: Designs, challenges, and perspectives, Carbon Energy. 4 (2022) 170–199. https://doi.org/10.1002/cey2.153.

[12] P. Gupta, S. Pushpakanth, M.A. Haider, S. Basu, Understanding the Design of Cathode Materials for Na-Ion Batteries, ACS Omega. 7 (2022) 5605–5614. https://doi.org/10.1021/acsomega.1c05794.

[13] X. Li, L. Liang, M. Su, L. Wang, Y. Zhang, J. Sun, Y. Liu, L. Hou, C. Yuan, Multi-Level Modifications Enabling Chemomechanically Stable Ni-Rich O3-Layered Cathode toward Wide- Temperature-Tolerance Quasi-Solid-State Na-Ion Batteries, Adv. Energy Mater. 13 (2023) 2203701. https://doi.org/10.1002/aenm.202203701.

[14] F. Wei, Q. Zhang, P. Zhang, W. Tian, K. Dai, L. Zhang, J. Mao, G. Shao, Review—Research Progress on Layered Transition Metal Oxide Cathode Materials for Sodium Ion Batteries, J. Electrochem. Soc. 168 (2021) 050524. https://doi.org/10.1149/1945-7111/abf9bf.

[15] I.A. Trussov, S.T. Kokhmetova, L.L. Driscoll, R. Smith, F.J. Berry,

J.F. Marco, A.K. Galeyeva, A.P. Kurbatov, P.R. Slater, Synthesis, structure and electrochemical performance of Eldfellite, NaFe(SO4)2, doped with SeO4, HPO4 and PO3F, J. Solid State Chem. 289 (2020) 1–11. https://doi.org/10.1016/j.jssc.2020.121395.

[16] M. Yuan, H. Liu, F. Ran, Fast-charging cathode materials for lithium & sodium ion batteries, Mater. Today. 63 (2023) 360–379. https://doi.org/10.1016/j.mattod.2023.02.007.

[17] Z. Pan, X. Liu, J. Yang, X. Li, Z. Liu, X.J. Loh, J. Wang, Aqueous Rechargeable Multivalent Metal-Ion Batteries: Advances and Challenges, Adv. Energy Mater. 11 (2021) 2100608. https://doi.org/10.1002/aenm.202100608.

[18] X.L. Huang, C. Zhou, W. He, S. Sun, Y.L. Chueh, Z.M. Wang, H.K. Liu, S.X. Dou, An Emerging Energy Storage System: Advanced Na-Se Batteries, ACS Nano. 15 (2021) 5876–5903. https://doi.org/10.1021/acsnano.0c10078.

[19] P. Singh, K. Shiva, H. Celio, J.B. Goodenough, Eldfellite, NaFe(SO4)2: an intercalation cathode host for low-cost Na-ion batteries, Energy Environ. Sci. 8 (2015) 3000–3005. https://doi.org/10.1039/c5ee02274f.

[20] A. Banerjee, R.B. Araujo, R. Ahuja, Unveiling the thermodynamic and kinetic properties of NaxFe(SO4)2 (x = 0-2): toward a high-capacity and low-cost cathode material, J. Mater. Chem. A. 4 (2016) 17960–17969. https://doi.org/10.1039/c6ta05330k.

[21] T. Balić-Žunic, A. Garavelli, P. Acquafredda, E. Leonardsen, S.P. Jakobsson, Eldfellite, NaFe(SO4)2 , a new fumarolic mineral from Eldfell volcano, Iceland, Mineral. Mag. 73 (2009) 51–57. https://doi.org/10.1180/minmag.2009.073.1.51.

[22] M. Reynaud, M. Ati, S. Boulineau, M.T. Sougrati, B.C. Melot, G. Rousse, J.-N. Chotard, J.-M. Tarascon, Bimetallic Sulfates A2M(SO4)2·nH2O (A = Li, Na and M = Transition Metal) as New Attractive Electrode Materials for Li- and Na-ion Batteries, ECS

Trans. 50 (2013) 11–19. https://doi.org/10.1149/05024.0011ecst.

[23] J. Yao, T. Jin, Y. Li, S. Xiao, B. Huang, J. Jiang, Electrochemical performance of Fe2(SO4)3 as a novel anode material for lithium-ion batteries, J. Alloys Compd. 886 (2021) 161238. https://doi.org/10.1016/j.jallcom.2021.161238.

[24] J. Shirakawa, M. Nakayama, M. Wakihara, Y. Uchimoto, Changes in Electronic Structure upon Lithium Insertion into Fe2(SO4)3 and Fe2(MoO4)3 Investigated by X-ray Absorption Spectroscopy, J. Phys. Chem. B. 111 (2007) 1424–1430. https://doi.org/10.1021/jp065802g CCC:

[25] A. Van Alboom, V.G. De Resende, E. De Grave, J.A.M. Gómez, Hyperfine interactions in szomolnokite (FeSO4. H2O), J. Mol. Struct. 924–926 (2009) 448–456. https://doi.org/10.1016/j.molstruc.2008.10.049.

[26] N. Elgrishi, K.J. Rountree, B.D. McCarthy, E.S. Rountree, T.T. Eisenhart, J.L. Dempsey, A Practical Beginner's Guide to Cyclic Voltammetry, J. Chem. Educ. 95 (2018) 197–206. https://doi.org/10.1021/acs.jchemed.7b00361.

[27] A.R. Kanwade, A.K.S. Jena, S.M. Rajore, S.S. Mali, J. V Patil, C.K. Hong, P.M. Shirage, Revealing the potential of graphene-embedded Na3Fe2(PO4)3 for enhanced sodium-ion battery performance, J. Mater. Sci. Energy. 59 (2024) 8956–8972. https://doi.org/10.1007/s10853-024-09698-y.

[28] U. Nisar, M.H. Gulied, R.A. Shakoor, R. Essehli, Z. Ahmad, A. Alashraf, R. Kahraman, S. Al-Qaradawi, A. Soliman, Synthesis and performance evaluation of nanostructured NaFexCr1-X(SO4)2 cathode materials in sodium ion batteries (SIBs), RSC Advances. 8 (2018) 32985–32991. https://doi.org/10.1039/c8ra06583g.

CHAPTER 4

Optimization of Layered $NaCoO_2$ Cathode for High-Capacity Sodium-Ion Batteries

In chapter 3, sodium deficiency in the polyanionic compounds such as $Na_{0.8}Fe(SO_4)_2$ enhanced the Na^+-ion diffusion kinetics and cycle life performance of the cathode. However, the sodium deficiency in the polyanionic compound could not enhance the specific capacity and energy density due to the inherent lower theoretical capacity of the polyanionic compound. Hence, this chapter presents a successful synthesis of layered phase-pure $NaCoO_2$ by improving the sol-gel-based calcination temperature, yielding a highly crystalline, well-ordered material with $P6_3/mmc$ hexagonal symmetry, ideal for reversible, high-capacity, and energy density-based SIBs. Advanced physicochemical techniques confirmed its pure hexagonal crystal structure along with the desired stoichiometry. It demonstrated multiple redox peaks due to Co^{3+}/Co^{4+} redox couple, signifying stable multiphase transitions and exhibited exceptional structural and electrochemical stability. It demonstrated a high discharge specific-capacity of 155.85 mAh/g at 0.1C with outstanding discharge capacity retention of 136.98, 100.6, 84.78, 78.31, and 72.46 mAh/g at the C-rates of 0.15, 0.2, 0.3, 0.5, and 1.0C, respectively, outperforming previously reported values. It showed a remarkable discharge-energy density of 466.04 Wh/kg at 0.1C. These results revealed that $NaCoO_2$ is a high-performance and high-capacity cathode material for lightweight and compact SIBs.

4.1 Introduction

In chapter 3, the sodium deficiency in the polyanionic compounds enhanced Na^+-ion diffusion kinetics, working voltage window, and cycle life performance of the polyanionic cathode. However, the sodium deficiency in the polyanionic compound could not enhance the specific capacity and energy density due to the inherent lower theoretical capacity of the polyanionic compound. Hence, in this chapter, we have explored a LTMO cathode for SIBs due to its high theoretical capacity and energy density. Among the various cathode materials explored for SIBs, LTMOs, specifically of the chemical form Na_xMO_2 (where M =TM) have attracted significant attention [1–3]. These materials are structurally similar to the well-established Li_xCoO_2 used in LIBs and offer high theoretical capacity (>235 mAh/g) and potential for high energy storage [4,5]. The *P2* and *P3* phase structures of Na_xCoO_2 are particularly promising due to their structural stability and reversible sodium intercalation properties [6]. However, the performance of *P2* or *P3*-type Na_xCoO_2 as cathode materials for SIBs is hindered by issues including multiple phase transitions and volume expansion during the intercalation/deintercalation process, leading to capacity fading and structural deterioration [6,7]. To address these challenges, recent research efforts have focused on optimizing the synthesis techniques and engineering the structural features of *P2*-type Na_xCoO_2 cathodes [8,9]. Moreover, the improved electrochemical performances of $NaCoO_2$ can be achieved due to the formation of the stabilized structure of Co^{3+} with oxygen. Several theoretical and experimental works for the performance of $NaCoO_2$ as cathode material in aqueous as well as non-aqueous electrolytes for SIBs have been reported. For instance, the theoretical calculation performed by Nina Mattila and Antti Karttunen revealed that $NaCoO_2$ possesses higher in-plane and cross-plane lattice thermal conductivity than the counterpart $LiCoO_2$, representing the better thermal sustainability of $NaCoO_2$ than $LiCoO_2$ [10]. In 2021, Shiprath *et al.* carried out the electrochemical performance of $NaCoO_2$ in an aqueous

electrolyte of NaOH by fabricating $NaTi_2(PO_4)_3$/2M-NaOH/$NaCoO_2$ cell [11]. This cell system demonstrated a discharge-specific capacity of 89 mAh/g at 0.1C and retained about 34 mAh/g discharge-specific capacity at the 55^{th} cycle at a constant current rate of 1C. Gao *et al.* adopted the hydrothermal process to synthesize the *P3*-$Na_{0.67}CoO_2$ on Ni substrate which provided an arrear capacity of 1.66 mAh/cm^2 at 0.33C in a voltage window of 2.0-3.8V [12]. Boddu *et al.* adopted the sol-gel technique and synthesized the *P2*-Na_xCoO_2 with the highest specific capacity of about 99 mAh/g at 0.1C [13]. Reddy *et al.* carried out a micro-emulsion method and synthesized Na_xCoO_2 cathode material which represented discharge capacities of 161 and 80 mAh/g at 0.1 and 0.2C, respectively, within the voltage window of 2.0-4.2V owing to the Co^{3+}/Co^{4+} redox couple [14].

Since 2010s, extensive research have been conducted on various cathode materials, including $NaCoO_2$, for SIBs. Although numerous synthesis techniques have been explored to harness the excellent electrochemical performance of $NaCoO_2$ as a cathode material, most of them rely on advanced and costly processing techniques. Developing a simple, scalable, and cost-effective synthesis method capable of producing high discharge capacity and exhibiting good C-rate for $NaCoO_2$ cathodes remains a compelling challenge for the research community. This research gap must be addressed to fabricate a sustainable SIB system. Among the various approaches, the sol-gel method stands out as one of the most promising due to its simplicity and versatility. However, achieving the optimal conditions for temperature and calcination period during the sol-gel process to yield high-capacity $NaCoO_2$ cathodes remains challenging. There is a pressing need to refine the sol-gel synthesis parameters to enhance the electrochemical performance of $NaCoO_2$, with a particular focus on improving specific capacity and C-rate performance. In this chapter, *P2*-$NaCoO_2$ as cathode for SIBs is synthesized by improving the calcination temperature, which exhibited an impressive discharge specific capacity exceeding 155 mAh/g at 0.1C and demonstrated an outstanding C-

rate performance, irrespective of high reversible multiphase transitions. By iterating the temperature scale, the sol-gel calcination temperature was improved to provide a highly pure hexagonal phase of $NaCoO_2$. The Na/1M-$NaClO_4$/$NaCoO_2$ coin cell demonstrated an enhanced Na^+-ion diffusion, robust state of health, excellent diffusion-controlled behaviour, improved discharge specific capacities, and outstanding C-rate performance, primarily attributed to the Co^{3+}/Co^{4+} redox couple. These advancements not only marked a significant step towards the development of SIBs but are also important for more sustainable and cost-effective energy storage solutions. By harnessing the potential of $NaCoO_2$ through improved sol-gel synthesis, we believe it to open a new avenue for high-performance battery technologies that may assist in fulfilling the growing energy demands of the future.

4.2 Experimental and Characterization Section

The experimental details such as the selection of raw chemical ingredients, approach for material synthesis, slurry, and electrode preparation for $NaCoO_2$ cathode material was briefly explained in **Chapter 2**. After the synthesis of a series of $NaCoO_2$ cathode materials with varying the calcination temperature in the solgel synthesis method, their physicochemical properties were characterized by various advanced techniques. Further to carryout the electrochemical properties of $NaCoO_2$ cathode, sodium half-cell with Na/1M $NaClO_4$/$NaCoO_2$ CR2032-cells configurations were fabricated in the glove box. These cells were composed of 16 mm diameter-based disc-shaped Na metal chips as the counter and reference electrode, 1M-$NaClO_4$ sodium salt in 1:1 volume ratio of EC:PC solvents as the electrolyte, 19 mm diameter-based disc-shaped glass fibre separators, and $NaCoO_2$ as the active cathode material. After fabrication, the electrochemical properties of the coin cells were carried out through CV (in a voltage window of 2.0-4.2V), EIS (in 0.01Hz to 100 kHz), and GCD. Both the CV and EIS studies were performed through an electrochemical

workstation (PGSTAT032N from Metrohm), whereas the GCD studied were carryout through an 8-channel battery analyzer (LAND CT3001A) in a voltage window of 2.0-4.0V.

4.3 Results and Discussion Section

4.3.1 Physicochemical Assessments

4.3.1.1 Thermal Comportment Analysis: TGA & DSC

The weight retention behaviour of $NaCoO_2$ material with increasing temperature is presented in **Figure 4.1 (a & b).** The TGA in **Figure 4.1 (a)** revealed three significant mass losses. The initial mass loss of about 2.9% at 100-150ºC corresponded to the loss of absorbed and trapped water from the material [13]. The 2nd major mass loss of ~7.3% at ~150-350ºC was attributed to the decomposition as well as the gas evolution processes . The final and 3rd mass loss of ~2.9% took place between 350 ºC to 600 ºC and might be associated with the process of nucleation and the formation of the desired phase. After these stages, the material retained approximately 87.2% of its initial mass. Beyond 600°C, no further significant mass loss was observed, indicating the formation of the stable phase. Based on these findings, calcination temperatures of 700°C, 800°C, and 900°C were chosen for synthesizing materials for greater stability.

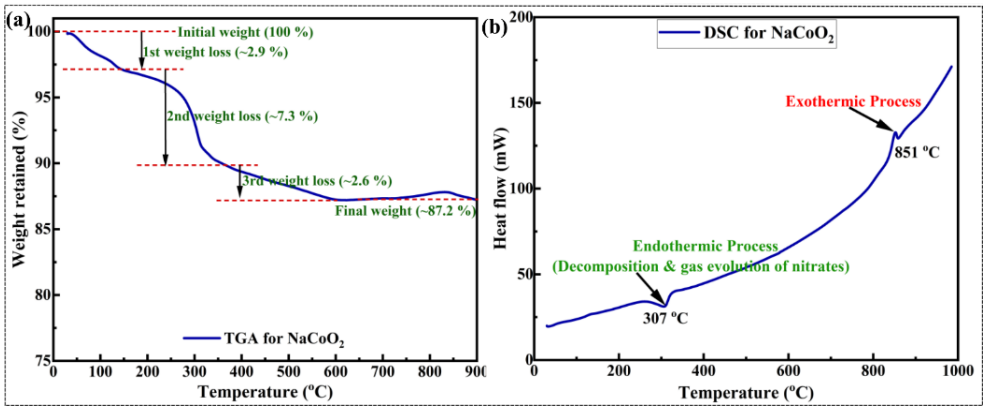

Figure 4.1 (a) (a) TGA, and (b) DSC profiles of $NaCoO_2$.

DSC results shown in **Figure 4.1 (b)**, indicated the decomposition and gas release processes of nitrate precursors and citric acid follow an

endothermic reaction, mainly occurring around 307°C [15]. Interestingly, a mass gain anomaly was observed in the TGA at around 850°C, which was explained by an exothermic event detected at 851°C in the DSC analysis. This exothermic process provided further insight into the possible change of material composition beyond this temperature.

4.3.1.2 Powder XRD Analysis

The phase purity synthesis analysis of $NaCoO_2$ calcinated at various temperatures of 700, 800, and 900 °C was performed with the help of powder XRD. **Figure 4.2 (a)** depicts the XRD pattern of $NaCoO_2$ before calcination (blue), calcinated at 700°C (red), 800°C (green), and 900°C (violet) samples. The respective peaks of the synthesized samples were indexed with the standard JCPDS card of 87-0274. Compared to the samples after calcination, the material before calcination showed a minimal number of peaks situated at different 2θ values compared to the calcinated ones. This was due to the process of nucleation and the formation of phase pure material with calcination. The $NaCoO_2$ material calcinated at 800°C showed phase purity formation of the desired material without the presence of any impurities, and all the peaks were well matched and indexed with the referenced data of the JCPDS card. The highest intense peak was observed at around 2θ value of 16.51º corresponding to the (002) plane followed by the 2nd intense peak at 40.33º for (102), and so on. However, compared to $NaCoO_2$ calcinated at 800°C, the sample calcinated at 700°C possessed a few additional impurity peaks corresponding to $Na_3CO_3.H_2O$, and CO_3O_4 in addition to the main peaks of the material, indicating that this temperature was not sufficient for the phase pure formation of the sample. Whereas the sample calcinated at 900ºC exhibited a completely different XRD spectrum profile. This revealed that some other material different than the required $NaCoO_2$ material was formed at 900ºC of calcination temperature. With the calcination temperature of 900ºC, many additional impurity peaks were observed along with the deficiency of desired peaks corresponding to the

required materials. This analysis revealed that 800ºC is the improved phase pure material synthesis temperature for further physicochemical and electrochemical analyses.

From the above discussion, the material calcinated at 800ºC showed better phase pure formation compared to samples calcinated at other temperatures. Following this conclusion we performed the XRD data structural refinement for $NaCoO_2$ calcinated at 800ºC with the assistance of FullProf-Suite software by using linear interpolation between the background selected points and the pseudo voigt function for the profile shape as shown in **Figure 4.2 (b)**. The observed XRD profile of $NaCoO_2$ nicely fitted with the calculated XRD data of the '1532939.cif' file from the Crystallography Open Database having the hexagonal symmetry of "*$P6_3/mmc$*" of the international space group number 194. All the peaks of the observed data were well-fitted with the calculated data with a chi-square 1.44. **Figure 4.2(c-e)** represents the lattice structures for $NaCoO_2$ calcinated at 800ºC obtained from the structural refinement. The polyhedral (**Figure 4.2 (c)**) and ball-and-stick type view (**Figure 4.2 (d)**) of $NaCoO_2$ showed the *P2*-phase formation in AB-BA-AB type stacking of the CoO_6 metal oxide layers. The sodium atoms are sandwiched between these metal oxide layers in a prismatic manner through metallic bonding [10,13]. **Figure 4.2 (e)** represents the single CoO_6 and NaO_6 units, where CoO_6 are present in the octahedral pattern with a Co-O bond length of 1.91 Å, and NaO_6 units form the prismatic structure with a Na-O bond length of 2.39 Å. Both polyhedral units had symmetric metallic bond lengths with oxygen.

The lattice parameters for $NaCoO_2$ obtained from the structural refinement are represented in **Table 4.1** and are compared with previously reported data. The unit cell of $NaCoO_2$ had the lattice parameters of about a=2.832 Å, b=2.832 Å, c=10.913 Å, with the interaxial angles as $\alpha = \beta = 90.00^o$, $\gamma = 120.00^o$ and unit cell volume V=75.809 $Å^3$ (**Table 4.1**). Owing to these crystallographic parameters, $NaCoO_2$ formed a hexagonal structure

with a space group symmetry of *P6₃/mmc*. The experimental volume of the unit cell in Å^3 was calculated through **equation (4.1).**

$$V = abc\sqrt{1 - cos^2(\alpha) - cos^2(\beta) - cos^2(\gamma) + 2cos(\alpha)cos(\beta)cos(\gamma)} \quad \ldots. (4.1)$$

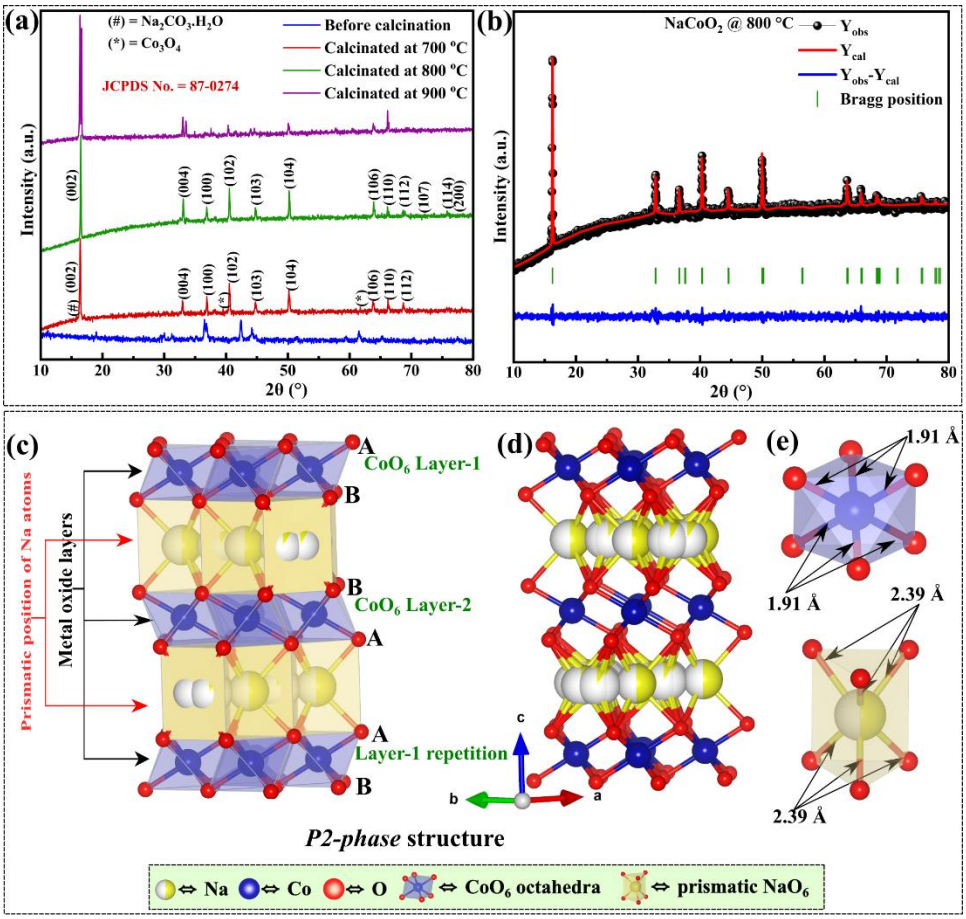

Figure 4.2 (a) (a) XRD spectra of $NaCoO_2$ before calcination (blue), calcinated at 700ºC (red), 800ºC (green), and 900ºC (violet), (b) Structural refinement of $NaCoO_2$ calcinated at 800ºC, (c-e) Crystal structures for $NaCoO_2$ calcinated at 800ºC.

The atomic positions (in fractional coordinates), occupancy, and multiplicity values for all the elements obtained from the structural refinement of $NaCoO_2$ calcinated at 800ºC, are provided in **Table 4.2**. The relation among the fractional coordinates (*x, y, z*) and the cartesian coordinates (X, Y, Z) is given in **equation 4.2**.

Table 4.1: Crystallographic parameters for $NaCoO_2$ obtained from structural refinement.

Parameters	Previously reported parameters		Refined parameters (This work)
	Experimentally	Theoretically	
***a* (Å)**	2.82 [16], 2.833 [17]	2.87 [10]	2.832 ± 0.0001
***b* (Å)**	2.82 [16], 2.833 [17]	2.87 [10]	2.832 ± 0.0001
***c* (Å)**	10.89 [16], 10.880 [17]	15.62 [10]	10.913 ± 0.0003
α (º)	90.00 [13,16,17],	90.00 [10]	90.000 ± 0.0
β (º)	90.00 [13,16,17],	90.00 [10]	90.000 ± 0.0
γ (º)	120.00 [13,16,17],	120.00 [10]	120.000 ± 0.0
V (Å^3)	75.07 [13,16,17],	111.42	75.809 ± 0.005
P (g/cm^3)	-	-	5.257 g/cm3
Symmetry, space group	Hexagonal [13,16,17], *P6₃/mmc* [13,16,17]	Hexagonal [10], *P6₃/mmc* [10]	Hexagonal, *P6₃/mmc*

The atomic positions (in fractional coordinates), occupancy, and multiplicity values for all the elements obtained from the structural refinement of $NaCoO_2$ calcinated at 800ºC, are provided in **Table 4.2**. The relation between the fractional coordinates (*x, y, z*) and the Cartesian coordinates (X, Y, Z) is given in **equation 4.2**. The negative fractional coordinate for Na1 in **Table 4.2** reflects crystallographic convention during structural refinement. Fractional coordinates are periodic, and a negative value simply means that the atom is slightly beyond the origin chosen for the unit cell but is identical to a positive value on translation by the lattice vector.

$x = \frac{X}{a},\ y = \frac{Y}{b},\ z = \frac{Z}{c},$ (*a*, *b*, and *c* are lattice parameters) ……..(4.2)

Table 4.2: Atomic coordinates, multiplicity, and occupancy of various elements in $NaCoO_2$.

Atoms	Occupancy of atoms	Fractional coordinates			Multiplicity
		x	*y*	*z*	
O1	1.76430	0.33330	0.66670	0.09024	4
Co1	0.96379	0.00000	0.00000	0.00000	2
Na2	0.31759	0.00000	0.00000	0.25000	2
Na1	0.58874	0.59957	-0.54480	0.25000	14

The XRD analysis was further used to measure the crystallite size (*D*) with the help of the Debye-Scherrer formula[18] as given in **equation 4.3**.

$$D = \frac{0.9\,\lambda}{\beta \cos(\theta)} \quad \ldots\ldots\ldots\ldots (4.3)$$

Here λ = 0.15418 nm (X-ray wavelength), β = FWHM of the prominent diffraction peaks (in radians), and θ = angle corresponding to the diffraction peaks (in radians). With these specified values the average crystallite size from the XRD analysis waas found to be *D* = 34.88 nm.

4.3.1.3 Particle Morphology & Composition Analysis

From the above XRD analysis, it was concluded that the hexagonal symmetry-based phase pure synthesis of *P2*-$NaCoO_2$ took place at 800ºC. To further analyse the surface morphology and the nominal chemical composition of the synthesized materials, further analyses were extended with the help of FESEM, EDS, and ICP-OES. **Figure 4.3** represents the particle surface morphology and size of $NaCoO_2$ synthesized by calcinating at 700, 800, and 900ºC.

Various scale view FESEM images of $NaCoO_2$ synthesized at 700 ºC in **Figure 4.3 (a-d)** revealed that the particles are mostly of undefined shape and size with very few numbers of particles in the hexagonal shape. This could be due to the presence of a large number of amorphous particles with a few quantities of hexagonal $NaCoO_2$. This indicated that a higher temperature was required for the nucleation of those amorphous particles to form the hexagonal-shaped particles. **Figure 4.3 (e-h)** represents the FESEM images at various magnifications for $NaCoO_2$ synthesized at a calcination temperature of 800ºC. At this temperature, it was observed that the particles were well nucleated and formed better defined hexagonal shape. Interestingly almost all the particles at this calcination temperature were observed to have a hexagonal shape. This further supported the XRD analysis, indicating the formation of the desired hexagonal symmetry-based *P2* phase of $NaCoO_2$ at 800ºC. These hexagonal particles were formed in a

particle size range of 5.07-23.99 µm with an average particle size of 12.091 µm. On the other hand, $NaCoO_2$ synthesized with a calcination temperature of 900ºC exhibited a completely different scenario for particle morphology as shown in **Figure 4.3 (i-l)**. The particle at this calcination temperature possessed a solid cylindrical structure with a diameter of about 100 nm and a length falling between 0.5-1.5 µm. The anomaly for the complete transformation of the hexagonal particle to the solid cylindrical shape could be attributed to the formation of other compounds than the desired $NaCoO_2$ at this calcination temperature as explained in the XRD analysis section.

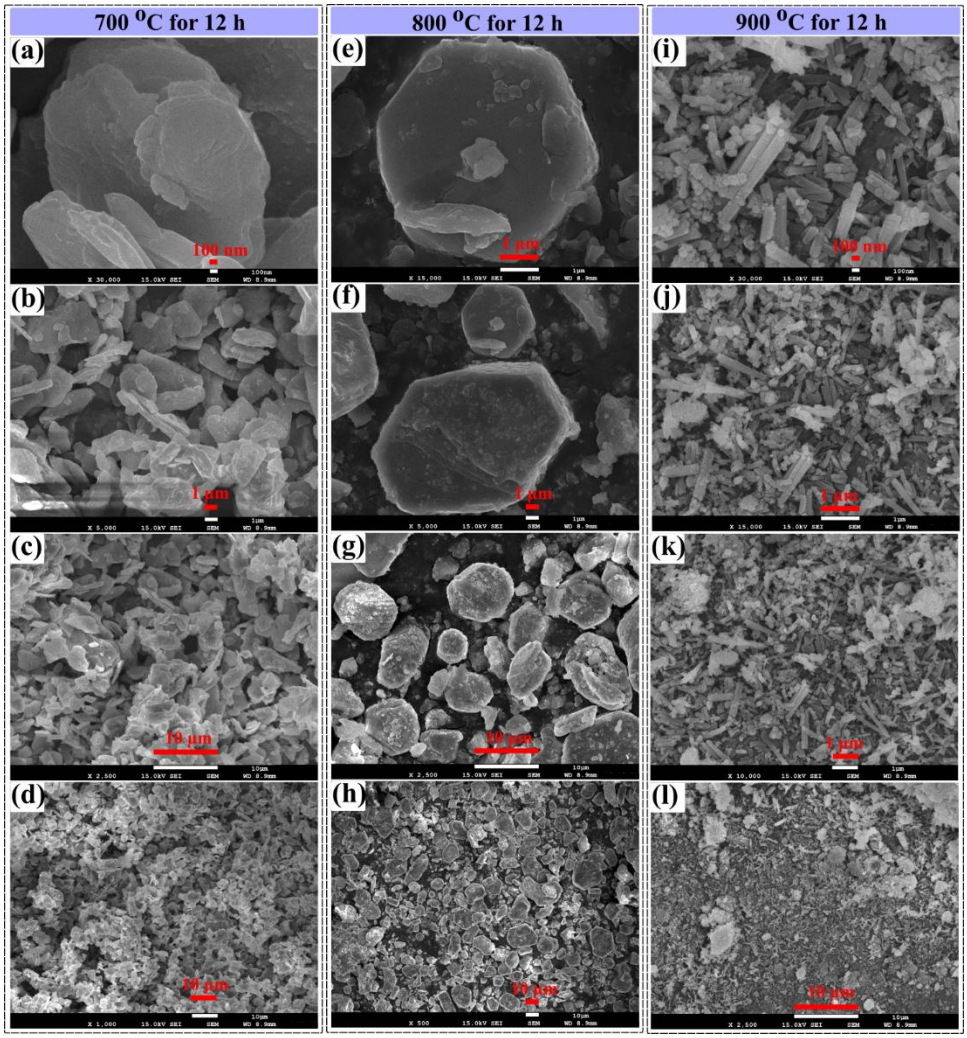

Figure 4.3 Various magnification FESEM images of $NaCoO_2$ synthesized via sol-gel with a calcination temperature of (a-d) 700ºC, (e-h) 800ºC, and (i-l) 900ºC, respectively.

Nominal elemental composition and distribution of elements in $NaCoO_2$ were analysed using EDS, as depicted in **Figure 4.4**. The EDS spectrum of $NaCoO_2$ synthesized at 700ºC (**Figure 4.4 (a)**) confirmed the presence of elements in near-stoichiometric. **Figures 4.4 (b-c)** demonstrated that Na, Co, and O were uniformly distributed throughout the material. At 800ºC (**Figure 4.4 (d)**), EDS analysis showed the desired nominal values for all elements, with color mapping over the hexagonal particles indicated uniform elemental distribution (**Figure 4.4 (f)**). However, $NaCoO_2$ calcined at 900ºC presented a different scenario (**Figure 4.4 (g)**), where a significant loss of Na was observed. This Na loss at high calcination temperatures likely resulted in the formation of particles with varying shapes and sizes, as explained in the FESEM analysis, and led to the creation of a new phase, primarily Co_2O_3, as indicated in the XRD analysis. Although the color mapping (**Figures 4.4 (h-i)**) showed a uniform distribution of all elements, Na mapping was negligible compared to Co and O at 900ºC, confirming the significant reduction of Na at this temperature. The atomic percentages of elements in these materials through EDS are summarized in **Table 4.3**.

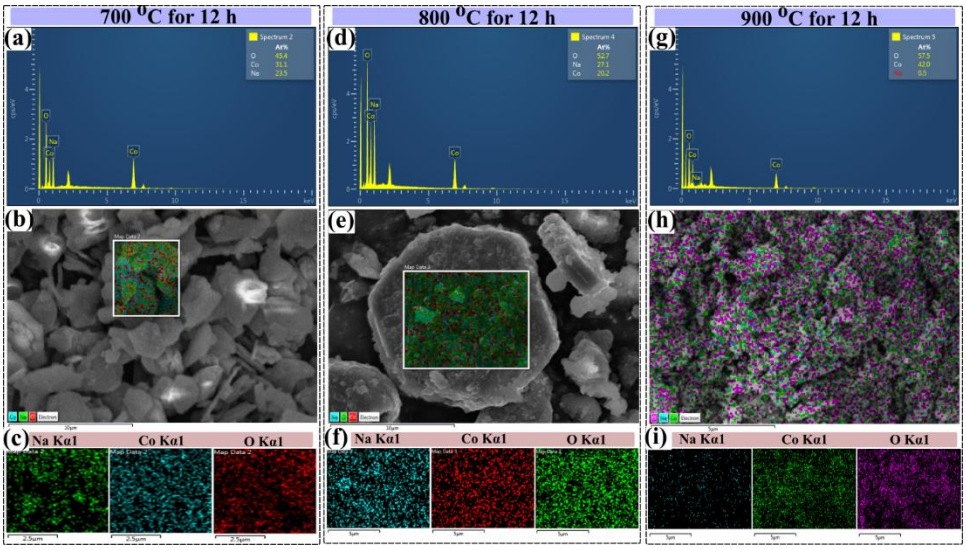

Figure 4.4 EDS spectrum $NaCoO_2$ calcinated at **(d)** 700ºC, **(g)** 900ºC, Elemental distribution and color mapping of elements in $NaCoO_2$ calcinated at **(b-c)** 700ºC, **(e-f)** 800ºC, and **(h-i)** 900ºC.

Table 4.3: Atomic-%-wise presence of elements in $NaCoO_2$ synthesized at 700, 800, and 900ºC.

Atomic % of elements	$NaCoO_2$@700 ºC	$NaCoO_2$@800 ºC	$NaCoO_2$@900 ºC
Na	24.9	26.3	22.2
Co	20.4	20.0	55.2
O	54.7	53.7	22.6

The stoichiometry and composition of $NaCoO_2$ materials synthesized at calcination temperatures of 700-900ºC were further determined through ICP-OES, as given in **Table 4.4**. The ICP-OES results indicated that the $NaCoO_2$ sample calcinated at 800ºC exhibited a molecular formula of $Na_{1.05}CoO_2$, which is more favourable and desired stoichiometry compared to those calcinated at 700ºC and 900ºC.

Table 4.4: ICP-OES for $NaCoO_2$ calcinated at 700, 800, and 900ºC.

Samples	Concentration (ppm)		Moles		Stoichiometry (Na : Co)	Molecular formula
	Na	Co	Na	Co		
$NaCoO_2$ @700	2.16	4.32	0.094	0.073	1.28:1.00	$Na_{1.28}CoO_2$
$NaCoO_2$ @800	3.36	8.23	0.146	0.139	1.05:1.00	$Na_{1.05}CoO_2$
$NaCoO_2$ @900	2.46	7.59	0.107	0.129	0.83:1.00	$Na_{0.83}CoO_2$

From the above discussions (XRD, FESEM, EDS, and ICP-OES), it was concluded that $NaCoO_2$ synthesized with a calcination temperature of 800ºC demonstrated a better phase pure formation with the required surface morphology and the desired stoichiometry compared to $NaCoO_2$ materials calcinated at 700 and 900ºC. Hence further physicochemical and electrochemical analyses from this point onwards were performed for $NaCoO_2$ material calcinated at 800ºC to work as the active cathode material for SIBs.

4.3.1.4 Chemical State Analysis via XPS

XPS spectra for $NaCoO_2$ synthesized with a calcination temperature of 800ºC are shown in **Figure 4.5**. The smooth scan XPS in **Figure 4.5 (a)**, covered a wide range of BE from 0 eV to 1200 eV, confirmed the presence of all constituent elements of $NaCoO_2$ in their anticipated orbitals. A few additional peaks were also observed corresponding to the peaks resulting in due to the augur electrons. In addition to the primary elements of $NaCoO_2$, an additional peak for carbon 'C' is observed due to the use of a carbon-coated Cu grid for sample-holding purposes.

The high-resolution scan XPS for all the individual elements in $NaCoO_2$ calcinated at 800 ºC are represented in **Figures 4. 5(b-d)**. Na is found in the Na-*1s* orbital with an electron BE of 1070.45 eV as represented by Na_e in **Figure 4.5 (b)**. The additional peak of 'Na-O-Co' was due to the presence of the metallic bond of Na with O. The high-resolution scan XPS of Co-*2p* indicated that Co was present in the Co^{3+} oxidation state in the sample. Due to the *2p* orbital of Co, a spin-orbit coupling took place with the splitting of Co-*2p* orbital into Co-$2p_{1/2}$ and Co-$2p_{3/2}$ at the electro-binding energies of 794.45 and 779.4 eV, respectively with a BE difference of $\Delta E = 14.9$ eV. The Co^{3+} oxidation state of the uncharged $NaCoO_2$ cathode gets oxidized to Co^{4+} during the charging process. Hence the electrochemical process of $NaCoO_2$ cathode in SIBs was due to the Co^{3+}/Co^{4+} redox activity. The high-resolution scan XPS of oxygen was observed for the electron in the O-*1s* orbital with a BE of 530.7 eV. The low intense peaks corresponding to the O-Na, and O-Co were also observed. **Figure 4.5 (e)** represents the high-resolution XPS spectrum for C-*1s* orbital, which was used as substrate and the reference data to calculate the relative BE for other elements. The significant peak of C-*1s* was observed at the standard BE of 284.8 eV with the presence of other neighbouring peaks at 289.1 eV representing the formation of O-C=O bonding as the surface carbon contamination.

The electrochemical performance of $NaCoO_2$ is primarily dominated by the Co^{3+}/Co^{4+} redox couple. The Co^{3+} species ($t_{2g}^6 e_g^0$, low-spin, S = 0) can be oxidized to Co^{4+} ($t_{2g}^5 e_g^0$, low-spin, S = ½) at charging. This change does not disturb the layered structure or cause Jahn-Teller distortion. Even though Co ions can theoretically exhibit various spin states, the ΔE = 14.9 eV agrees with low-spin Co^{3+} and Co^{4+} for octahedral coordination, ascertaining that mixed Co valence states give way mainly through stable low-spin redox activity. Therefore, enhanced electrochemical performance is not only due to its layered $P6_3/mmc$ structure but also the favorable spin-state stabilization of Co. However, detailed spin-state analysis is beyond the scope of the present work.

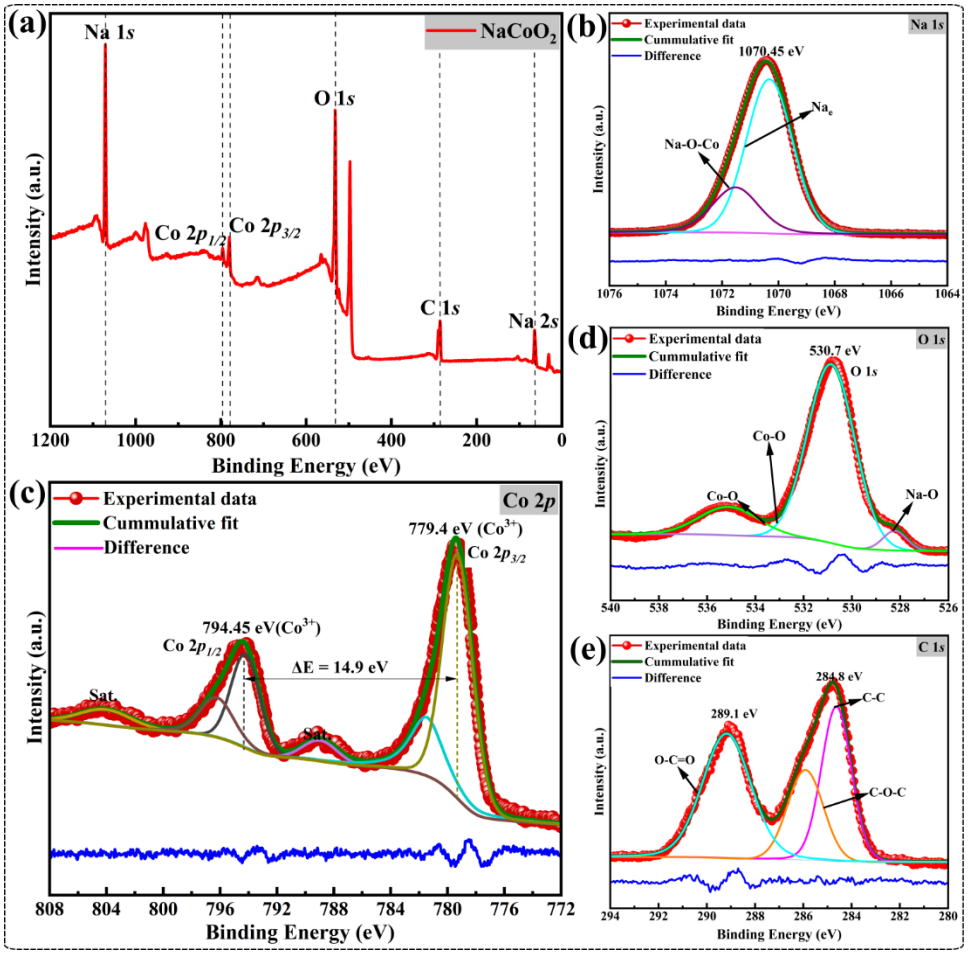

Figure 4.5 (a) Smooth scan XPS of $NaCoO_2$ calcinated at 800ºC; and high-resolution XPS of **(b)** Na-1*s*, **(c)** Co-2*p*, **(d)** O-1*s*, and **(e)** C-1*s* orbitals.

4.3.1.5 TEM and HRTEM Analyses

Figure 4.6 (*a*) represents the TEM images of $NaCoO_2$, which were performed to reveal the morphology, particle spheres, and size characteristics of the synthesized cathode material. These particles had a hexagonal shape, and the particle size was in resonance with the results shown by FESEM, suggesting a consistent synthesis process. Further to explore more details on the internal structure of $NaCoO_2$ at the atomic level, the HRTEM was performed. SAED pattern for $NaCoO_2$ is shown in **Figure 4.6 (b)** representing the lattice of $NaCoO_2$ in the reciprocal lattice plane. The '*d*-spacing' from the SAED pattern was found to be 2.3 Å, which corresponds to the (*hkl)* value of (*102*) lattice plane of $NaCoO_2$ with the hexagonal symmetry. **Figures 4.6 (*c-d*)** represents the HRTEM images of the synthesized $NaCoO_2$ at various locations. The magnified images of **Figures 4.6 (c-*d*)** represented a clear view of the ordered lattice fringes and atomic arrangements in an unfirm order and orientation.

These distinct lattice fringes and the interplanar spacing were further used to calculate *d*-spacing values as shown in the magnified portion of **Figures 4.6 (c-*d*).** In most of the cases, we observed an interplanar *d*-spacing value of between 2.2-2.3 Å, which was in good agreement with that of the SAED pattern and the (*hkl*) value of the highest intense (*102*) plane as shown in the XRD pattern. This further confirmed the highly crystalline nature of $NaCoO_2$ material. These analyses provided a crucial insight into the atomic arrangement, revealing a high degree of crystallinity. The clear and sharp lattice fringes **Figures 4.6 (c-*d*)** indicated well-ordered atomic layers, critical for improving the electrochemical properties of the cathode material. Hence, the combined TEM and HRTEM analyses provided a comprehensive understanding of the morphology and structural integrity of $NaCoO_2$, highlighting its potential as a cathode for SIBs.

4.3.1.6 Raman Analysis of $NaCoO_2$

The Raman spectra analysis for $NaCoO_2$ was performed to explore the local atomic interaction and the structural integrity of $NaCoO_2$, by

exploring its specific possible vibrational modes as shown in **Figure 3.6 (*e*)**. The spectrum was obtained in a wave number range of 100-1200 cm^{-1}. Five Raman active modes of "$3E_{2g}+E_{1g}+A_{1g}$" were shown by the D_6h symmetry elements of the hexagonal symmetry of $NaCoO_2$ for Na and O elements.[17] As a result, five significant peaks were observed at 188.3, 464.3, 512.9, 602.1, and 666.4 cm^{-1} wave numbers corresponding to E_{1g} (O), E_{2g} (O), E_{2g} (Na), E_{2g} (Na), and A_{1g} (O) Raman active modes, respectively. Here, the E_{1g} Raman active mode corresponded to the in-plane vibration of 'O' atoms, whereas the A_{1g} mode corresponded to the vibration of 'O' atoms in the direction of the out-of-plane. Similarly, the E_{2g} Raman active modes corresponded to the combined vibration of 'O' and 'Na' atoms in the lattice of $NaCoO_2$. All the modes were in good agreement with the reported literature [13,17].

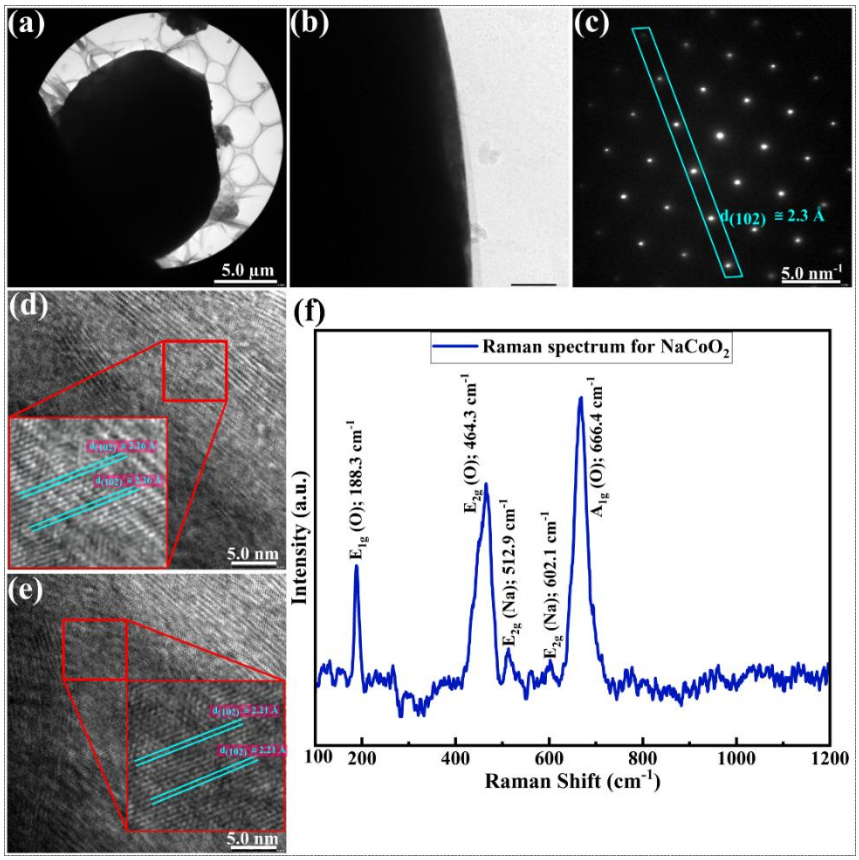

Figure 4.6 (a) TEM image; **(b)** SAED pattern; **(c-d)** HRTEM images; and **(e)** Raman spectrum of $NaCoO_2$ calcinated at 800ºC.

4.3.2 Analyses of Electrochemical Performances

4.3.2.1 CV Analysis

The redox activities for $NaCoO_2$ in Na/1M-$NaClO_4$/$NaCoO_2$ cells were investigated through the CV as shown in **Figures 4.7 (*a-d*)**. The CV analyses were performed with scan rates of 0.05, 0.1, 1.0, and 5 mV/s for three consecutive charge/discharge cycles, respectively, within a 2.0-4.2V voltage window. **Figure 4.7 (*a*)** represents the three charge/discharge CV profiles of $NaCoO_2$ at the lowest scan rate of 0.01 mV/s. The oxidation and reduction peaks for all three subsequent cycles were observed at the same potentials, moreover overlapping with each other, indicating excellent structural stability of the cathode during the sodiation/desodiation process. The anodic/cathodic peak pairs corresponding to Co^{3+}/Co^{4+} at 2.413/2.283, 2.466/2.41, 2.564/2.52, 2.615/2.583, 2.696/2.652, 2.969/2.94, 3.157/3.145, 3.279/3.245, 3.67/3.633, and 3.98/3.936 were due to the multiple phase transition involving *P'3, P3, O'3, O3, O2, and O2-O1* phases having different sodium contents[19–21] during the intercalation/deintercalation process. Along with these stable phase transitions, the consistency of cycles in **Figure 4.7 (*a*)** revealed the sustainability of a stable single phase of $NaCoO_2$ during the overall charge/discharge cycles. This further represented the ultra-reversibility of redox reaction. Further, the redox peaks were sharper beyond 2.8 V due to the better kinetics of Na^+-ions at higher potentials. **Figure 4.7 (*b*)** represents the CV profile at other scan rates of 0.1, 1.0, and 5.0 mV/s. Similar features were also observed at these scan rates. The area of these CV curves and the respective anodic and cathodic peak current densities increased with the increase in the values of scan rates, indicating the rapid electron kinetics and diffusion control behaviour. The CV profiles indicated that $NaCoO_2$ possesses a *P2*-phase structure which supported XRD analysis [22].

The Power-Law equation [23,24] shown in **equation 4.4,** provided relation between the current of the highest oxidation/reduction peaks (I_p) and the scan rate (υ) in CV analysis was used to investigate the reaction

kinetics and behaviour of $NaCoO_2$ cathode. In this **equation 4.4**, these assumptions are taken: (i) electrochemical system satisfies semi-infinite linear diffusion, and there is no appreciable ohmic drop, (ii) the electrode/electrolyte interface is ideal with no side reactions affecting the CV response, and (iii) Capacitive and diffusion-controlled processes can be separated using the exponent *b*.

$$I_p = av^b \quad \text{…. …. …. (4.4)}$$

Here, the constant parameters '*a*' and '*b*', were calculated as the y-intercept and slope, respectively, from the linear graph of $log(I_p)$ and $log(\upsilon)$ as shown in **Figure 4.7 (c)**. The slope '*b*' close to 0.5 indicates the battery-type behaviour of the cathode material, whereas the '*b*' value close to '1' indicates the capacitive-type behaviour. The intermediate value between these two limits indicates the combined characteristic of the cathode material in the electrochemical performance [23]. We calculated the *b*-values for the $NaCoO_2$ cathode as 0.644 and 0.645 for the oxidation and reduction processes, respectively. This signified that $NaCoO_2$ mostly demonstrated the battery-type behaviour with efficient charge transfer during intercalation/deintercalation of the redox process.

As the *b*-values are observed as 0.644 and 0.645 for anodic and cathodic processes, we extended the CV analysis to calculate the percentage of diffusion contribution (*i.e.,* battery-type) and capacitive-type characteristics of the cathode material through Dunn's plotting[25] as shown in **Figure 4.7 (d)**. Dunn's plot taken for 5 mV/s scan rate indicated that $NaCoO_2$ as a cathode material in Na/1M-$NaClO_4$/$NaCoO_2$ cell exhibited 99.48% of diffusion-controlled characteristics with a negligible amount of (only 0.52%) capacitive behaviour for the electrochemical performance as shown in **Figure 4.7 (d)**.

4.3.2.2 EIS Analysis

The EIS analysis of Na/1M-$NaClO_4$/$NaCoO_2$ was carried out before and after CV to investigate the ion diffusion properties, state of health,

charge kinetics, and the electrode-electrolyte interfacial reaction of $NaCoO_2$ cathode material. **Figures 4.7 (e-f)** represents the Nyquist plot in a frequency range of 0.01 Hz to 100 kHz. The Nyquist plot before CV is shown in **Figure 4.7 (e-f)** representing three semicircles corresponding to different resistances offered to the charge transfer in the fabricated cell. The below total equivalent circuit (**equation 4.5)** was used to fit the experimentally obtained EIS data before CV.

$$\text{Equivalent circuit} = R_s + \frac{Q_1}{R_{sei}} + \frac{Q_2}{R_{ct}} + \frac{C_1}{R_d} \quad \ldots\ldots\ldots\ldots (4.5)$$

The total impedance of the above-fitted circuit was given by **equation 4.6**.

$$Z(f) = R_s + \frac{R_{sei}}{R_{sei}Q_1(i2\pi f)^{a_1}+1} + \frac{R_{ct}}{R_{ct}Q_2(i2\pi f)^{a_2}+1} + \frac{R_d}{1+i2\pi f R_d C_1} \ldots\ldots (4.6)$$

Wheere, 'R_s' is the electrolyte solution resistance, 'R_{sei}' is resistance from SEI, 'R_{ct}' is the charge transfer resistance at the electrode-electrolyte interface, 'R_d' is the resistance resulting due to the diffusion-related process, 'Q_1' and 'Q_2' are the constant phase elements (CPEs), 'a_1' and 'a_2' are the exponent constants, and 'C_1' is the capacitive element. These parameters from the fitted equivalent circuit are given in **Table 4.5**.

Table 4.5: EIS parameters of the equivalent circuit of $NaCoO_2$.

Parameters	Values before CV
$\mathbf{R_S}$ (Ω)	4.371
$\mathbf{R_{sei}}$ (Ω)	32.016
$\mathbf{R_{ct}}$ (Ω)	179.558
$\mathbf{R_d}$ (Ω)	15.014
$\mathbf{Q_1}$ ($F.s^{(a-1)}$)	11.046
$\mathbf{Q_2}$ ($F.s^{(a-1)}$)	0.005
$\mathbf{C_1}$ (F)	$0.146x10^{-3}$
$\boldsymbol{a_1}$	0.820
$\boldsymbol{a_2}$	0.342

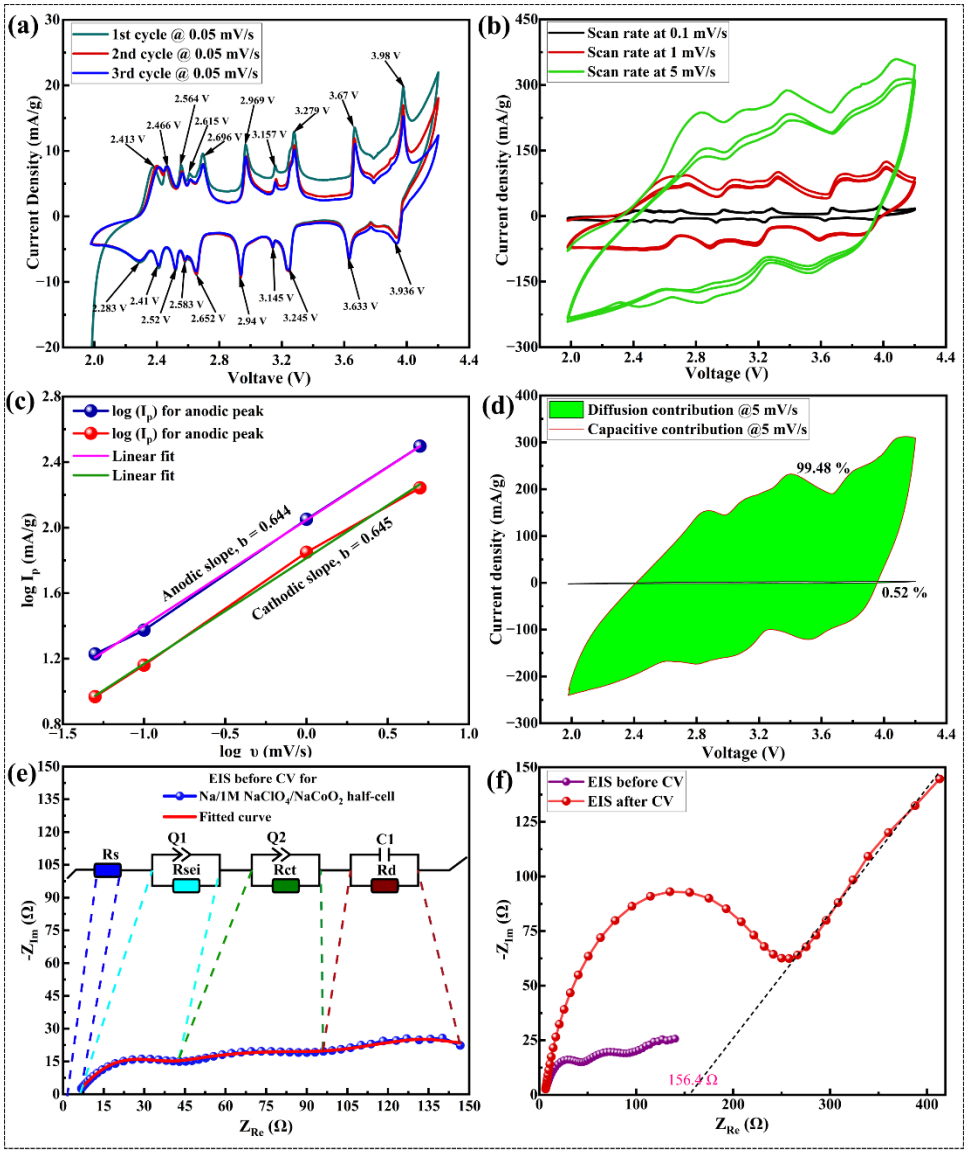

Figure 4.7 CV profiles of $NaCoO_2$ at **(a)** 0.05, **(b)** 0.2, 1.0, and 5.0 mV/s; **(c)** *log (υ) vs. log(I_p)* plotting, **(d)** Duun's plotting of $NaCoO_2$; **(e)** Nyquist plot and equivalent circuit of $NaCoO_2$ before CV; **(f)** Nyquist plot of $NaCoO_2$ before and after CV in Na/1M-$NaClO_4$/$NaCoO_2$ cell.

The solution resistance 'R_s' and the charge transfer resistance 'R_{ct}' remain matters of interest for the EIS analysis. $NaCoO_2$ demonstrated R_s of 4.371 Ω before CV, indicating good electrolyte conductivity. R_{ct} before CV was found as 179.558 Ω. This small R_{ct} indicated a good state of health and better charge kinetics at the electrode-electrolyte interface. The combined Nyquist plot of $NaCoO_2$, before and after CV, is shown in **Figure 4.7 (f)**.

R_s and R_{ct} after CV were found to be 5.416 and 227.4 Ω as shown in **Figure 4.7 (f)**. This indicated that the solution resistance remains almost the same, whereas the charge transfer resistance increased to a small extent after the CV. These further revealed that a very negligible resistance increased in the electrolyte solution. The increase in the charge transfer resistance after CV could be attributed to the formation of SEI as the passivation layer [26,27]. Still, these resistances offered to the cell were very small, indicating the improved interfacial conductivity for the faster charge transfer at the electrolyte and electrode owing to the formation of efficient SEI. These charge transfer resistances were used to calculate the double layer capacitance (C_{dl}) for $NaCoO_2$ cathode material as given in **equation 3.7** [16] for before and after CV and are tabulated in **Table 4.6.**

$$C_{dl} = \frac{1}{2\pi . R_{ct} f_{max}} \qquad \ldots\ldots\ldots\ldots (4.7)$$

Table 4.6: EIS parameters for $NaCoO_2$, before and after CV.

Parameters	This work		Early reported	
	Before CV	After CV	Before cycling	After Cycling
R_S (Ω)	4.371	5.416	66.29	78.29
R_{ct} (Ω)	179.558	227.4	2664.91	422.32
f_{max} (Hz)	100000	100000	100000	100000
C_{dl} (F)	8.864×10^{-9}	6.999×10^{-9}	0.598×10^{-9}	3.771×10^{-9}

EIS was used to calculate Na^+-ion diffusion coefficient (D_{Na+}) with the help of **equation (4.8)** [14]**.** Where, T (absolute temperature= 298.15 K for our study), R (universal gas constant =8.314 J/K.mol), n (number of electrons transferred=1 for $NaCoO_2$ owing to Co^{3+}/Co^{4+} redox couple), F (Faradays constant=96485.332 C/mol), A (area of the electrode=2.011 cm^2 for our study), C (concentration of sodium-ions=0.0461 mol/cm^3 calculated with the help of density obtained during the XRD analysis), σ is the Warburg factor, i.e., the slope of the real axis vs. $\omega^{-1/2}$ line extrapolated from Nyquist plot (σ = 156.4 Ω, **Figure 4.7(b)**). The D_{Na+} for $NaCoO_2$ cathode material in the fabricated half-cell after the CV is calculated as 1.686×10^{-16} cm^2/s.

$$D_{Na^+} = \frac{T^2 R^2}{2n^4 F^4 A^2 C^2 \sigma^2} \qquad \ldots\ldots\ldots\ldots (4.8)$$

4.3.2.3 Analysis of GCD Performance

The GCD was performed at 0.1, 0.15, 0.2, 0.3, 0.5, and 1.0C in the voltage range of 2.0-4.0V as shown in **Figure 4.8**. An excellent rate-tolerance of $NaCoO_2$ was observed. **Figure 4.8 (a)** represents the charge/discharge specific capacity values of $NaCoO_2$ cathode at 0.1C rate. The cathode material of interest exhibited the discharge-specific capacities of 152.48, 155.85, 152.04, 153.52, and 152.85 mAh/g at the 1^{st}, 2^{nd}, 3^{rd}, 4^{th}, and 5^{th} cycles, respectively at 0.1C rate, which is given in **Table 4.7**. This high value of discharge-specific capacity at 0.1C with its consistency (remains between 152 -156) is the highest one at the same C-rate among other know derivatives (**Table 4.7)**. At the initial cycle, we obtained a discharge-specific capacity of 152.48 mAh/g, which increased to 155.85 mAh/g in the 2^{nd} cycle, and then reduced to 152.04 mAh/g and then remained at almost the same values at 0.1C. This could be attributed to the formation of a stable SEI layer during the 1^{st} two cycles. Interestingly, after the 2^{nd} cycle, the discharge specific capacity at 0.1C attained almost a steady state (**Figure 4.8 (a)**), indicating the ultra-stability for the structure of the cathode material.

The rate capability analysis of the same cell was performed at the other higher scan rates of 0.15, 0.2, 0.3, 0.5, and 1.0 C as shown in **Figures 4.8 (b-c)**. The highest charge/discharge specific capacities are represented in **Figure 4.8 (b)**, which were 181.96/155.85, 148.76/136.98, 94.81/100.6, 86.14/84.78, 81.62/78.31, and 76.1/72.99 mAh/g at 0.1, 0.15, 0.2, 0.3, 0.5, and 0.1C, respectively. The specific capacity values for $NaCoO_2$ cathode synthesized in this thesis were notably superior or comparable to those reported in earlier literature on pristine $NaCoO_2$ and its sodium-deficient derivatives, as summarized in **Table 4.8**. For instance, hierarchical microspheres of Na_xCoO_2 synthesized via sodiation and calcination by Gao *et al.* demonstrated discharge capacities of 116.7, ~107, and ~100 mAh/g at 0.4, 1.0, and 2.0 C, respectively, in 1M $NaClO_4$ electrolyte [28].

Table 4.7: Specific capacities and Coulombic efficiencies of $NaCoO_2$.

C-rates	Cycle number	Charge specific capacity (mAh/g)	Discharge specific capacity (mAh/g)	Coulombic Efficiency (%)
0.1 C	1st	175.01	152.48	87.127
	2nd	181.96	155.85	85.651
	3rd	176.64	152.04	86.072
	4th	170.87	153.51	89.839
	5th	168.92	152.85	90.486
0.15 C	1st	148.76	136.98	92.079
	2nd	144.84	135.96	93.87
	3rd	142.58	135.08	94.739
	4th	137.72	113.91	82.716
	5th	100.36	97.7	97.346
0.2 C	1st	94.81	100.6	106.102
	2nd	94.51	98.79	104.524
	3rd	92.64	95.11	102.669
	4th	92.76	97.85	105.491
	5th	93.47	96.31	103.042
0.3 C	1st	91.4	84.78	92.757
	2nd	86.14	84.78	98.419
	3rd	85.83	84.54	98.5
	4th	84.22	83.16	98.74
	5th	84.56	83.3	98.505
0.5 C	1st	81.62	78.31	95.938
	2nd	78.7	77.68	98.711
	3rd	78.37	77.61	99.032
	4th	78.04	77.32	99.08
	5th	78.29	77.99	99.621
1.0 C	1st	76.1	72.46	95.219
	2nd	72.79	72.33	99.376
	3rd	72.84	72.42	99.421
	4th	72.78	72.35	99.406
	5th	72.75	72.3	99.385

Similarly, the solid-state reaction-based synthesis of $NaCoO_2$ by Shiprath *et al.* exhibited a discharge specific capacity of 89 mAh/g at 0.1 C in a 2M NaOH solution [11]. This smaller value for discharge specific capacity in the aqueous electrolyte is due to the performance of $NaCoO_2$

within the limited voltage window of 0.1 V, which will further bring constrains in high energy and high-power density-based applications. Boddu *et al.* achieved a maximum discharge capacity of 99 mAh/g at 0.1 C for *P2*-$NaCoO_2$ synthesized via sol-gel in 1M $NaClO_4$ [13]. The hydrothermal synthesis of $Na_{0.67}CoO_2$ arrays by Gao *et al.* showed an areal discharge capacity of 1.66 mAh/cm² at a constant current rate of 0.5 mA/cm² in 1M $NaClO_4$ [12]. Additionally, inverse microemulsion-based Na_xCoO_2 synthesized by Reddy *et al.* demonstrated an initial discharge capacity of 161 mAh/g at 0.1 C during the 1st cycle, however their subsequent cycles revealed significant capacity fading. Specifically, the discharge capacities at 0.1C for the 2nd, 3rd, 4th, 5th, and 6th cycles dropped to approximately 147, 143, 128, 140, and 128 mAh/g, respectively. This high-capacity fading, coupled with a more than 20% reduction in specific capacity by the 6th cycle, indicated that the material synthesized by Reddy *et al.* suffers from instability during charge/discharge process at 0.1C. Moreover, at 0.2C, the material displayed only 80 mAh/g discharge capacity during the 1st cycle, which further decreased to 65 mAh/g by the 3rd cycle, demonstrating additional capacity fading under higher current densities.[14] In contrast, the $NaCoO_2$ cathode material synthesized in this thesis showed a remarkable consistency in the discharge specific capacities for all the cycles of their respective C-rates. In this study, $NaCoO_2$ exhibited a specific capacity of 155.85 mAh/g at 0.1C, and importantly, it demonstrated exceptional consistent discharge capacities ranging between 152-156 mAh/g throughout all the five cycles at the same current rate. Furthermore, at 0.2C, our material exhibited a discharge specific capacity of 100.6 mAh/g, which remained almost stable over all the five cycles without significant capacity fading.

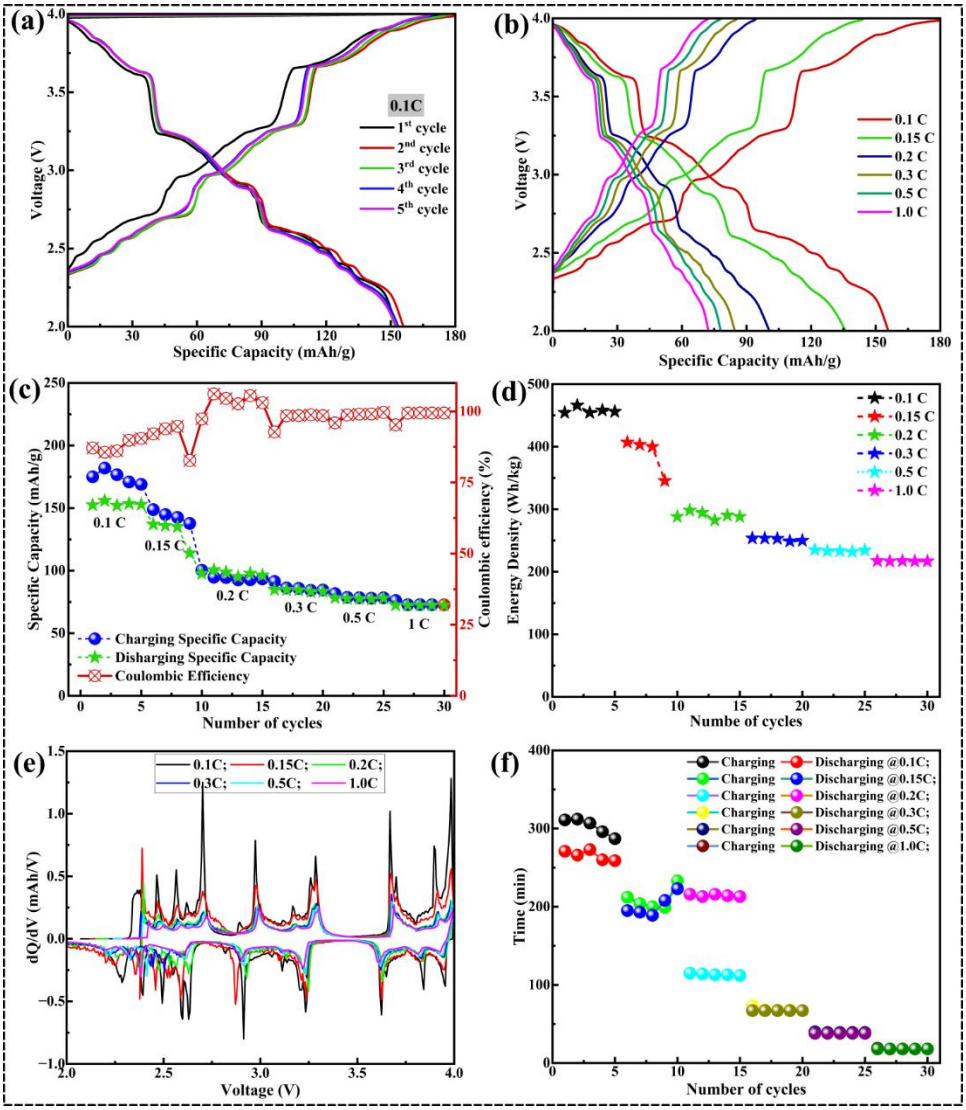

Figure 4.8 GCD curve **(a)** for five cycles at 0.1C, **(b)** at 0.1, 0.15, 0.2, 0.3, 0.5, and 1C; **(c)** C-rate performance; **(d)** discharge energy density; **(e)** *dQ/dV* curve; **(f)** charge-discharge time of $NaCoO_2$ cathode in Na/1M-$NaClO_4$/$NaCoO_2$ cell.

Other notable reports include $Na_{0.71}CoO_2$ with 120 mAh/g at 0.02 C.,[29] *P2*-$Na_{0.74}CoO_2$ with 110.2 and 107 mAh/g at 0.05 and 0.01 C,[30] respectively, and sol-gel-synthesized Na_xCoO_2 with 126 mAh/g at 0.1 C by Reddy *et al.*[16]. The two-step solvothermal synthesis of *P2*-$Na_{0.7}CoO_2$ achieved 125 mAh/g at 0.04 C [31] and 137.7 mAh/g at 10 mA/g [32], while biosynthesized $Na_{0.57}CoO_2$ showed 57 mAh/g at 0.7 C in aqueous Na_2SO_4 electrolyte.[33] All these results are given in **Table 4.8**. $NaCoO_2$ presented

in this thesis demonstrated improved performance compared to the previously reported pristine $NaCoO_2$ and its Na_xCoO_2 derivatives.

Table 4.8: Comparison table for the electrochemical performances of Na_xCoO_2 cathode materials for SIBs.

Cathode material	Synthesis Methode	Specific capacity (mAh/g)	Electrolyte	Voltage (V)	Ref.
P2-Na_xCoO_2	Facile sodiation, calcination	116.7 mAh/g @ 0.4C ~107 mAh/g @ 1.0C ~100 mAh/g @ 2.0C	1M $NaClO_4$ in EC:DMC:EMC=1 :1:1, 2vol% FEC	2.0-3.8	[28]
$NaCoO_2$	Solid state reaction	89 mAh/g @ 0.1C 79 mAh/g @ 0.2 C 34 mAh/g @ 1.0C	2M NaOH	0.0-1.0	[11]
P2-$NaCoO_2$	Sol-gel	99 mAh/g @ 0.1C 96 mAh/g @ 0.5C 85 mAh/g @ 1.0C	1M $NaClO_4$ in EC:PC=1:1	2.0-4.0	[13]
$Na_{0.67}CoO_2$ array	Hydrothermal process	1.66 mAh/cm^2@0.5 mA/cm^2 123.6 mAh/g @ 1.4C 100.5 mAh/g @ 2.1 C	1M $NaClO_4$ in EC:DMC:EMC=1 :1:1 with 2 vol % FEC	2.0-3.8	[12]
Na_xCoO_2	Inverse microemulsion	161 @0.1C @ 1st cycle 129 @ 0.1C@ 4th cycle 80 mAh/g @ 0.2C	1M $NaClO_4$ in EC:PC=1:1	2.0-4.2	[14]
$Na_{0.71}CoO_2$	Hydrothermal	120 mAh/g @ 0.02C ~102 mAh/g @ 0.04C	1M $NaClO_4$ in PC	2.0-3.9V	[29]
$Na_{0.74}CoO_2$	Solid state reaction	110.2 mAh/g @ 0.05C 107 mAh/g @ 0.1C	1M $NaClO_4$ in EC:DMC=1:1	2.0-3.8	[30]
Na_xCoO_2	Sol-gel	126 mAh/g @ 0.1C 108 mAh/g @ 0.2C 77 mAh/g @ 0.5C	1M $NaClO_4$ in EC:PC=1:1	2.0-4.2	[16]
P2-$Na_{0.7}CoO_2$	Two-step solvothermal method	125 mAh/g @ 0.04C 112 mAh/g @ 0.8C 84 mAh/g @ 8C	1M $NaClO_4$ in EC:DEC=1:1 with 5 wt. % FEC	2.0-3.8	[31]
P2-$Na_{0.7}CoO_2$	Two-step solvothermal	137.7 mAh/g@10 mA/g 69.7 mAh/g@500 mA/g	1M $NaClO_4$	2.0-3.8	[32]
$Na_{0.57}CoO_2$	Biosynthesis	57 mAh/g@0.7C at 1st cycle 47 mAh/g@0.7C at 4th cycle	Aqueous Na_2SO_4	0.0-1.8	[33]
$NaCoO_2$	Sol-gel	155.9 mAh/g@0.1C 152.9 mAh/g@0.1C (5th cycle) 136.98 mAh/g@ 0.15C 100.6 mAh/g @ 0.2C 78.3 mAh/g @ 0.5C	1M $NaClO_4$ in EC/PC=1:1	2.0-4.0	This work

In 2023, C. Hakim *et al.* synthesized a series of $Na_{0.7}Co_xMn_yNi_zO_2$ as partially cobalt-substituted cathode materials [34]. According to their study, *P2*-$Na_{0.7}Co_{0.5}Mn_{0.33}Ni_{0.16}O_2$, *P2*-$Na_{0.7}Co_{0.4}Mn_{0.43}Ni_{0.16}O_2$, *P2*-$Na_{0.7}Co_{0.3}Mn_{0.53}Ni_{0.16}O_2$, *P2/P3*-$Na_{0.7}Co_{0.4}Mn_{0.33}Ni_{0.26}O_2$, and *P2/P3*-$Na_{0.3}Co_{0.3}Mn_{0.33}Ni_{0.36}O_2$ delivered the highest discharge capacities of 100, 97, 88, 91, and 120 mAh/g, respectively at 0.1C, revealing that the specific capacity decreases with decreasing Co content in the cathode material [34]. *P2*-$Na_{0.67}Co_{0.5}Mn_{0.5}O_2$, studied by Zhu *et al.* [35] demonstrated 147 mAh/g discharge capacity at 0.1C. The electrochemical studies by Wang *et al.* on *P2*- $Na_{2/3}CoO_2$, and $Na_{2/3}Co_{0.5}Mn_{0.5}O_2$ reported highest discharge specific capacities of about 115, and 125 mAh/g, respectively at 0.1C [36].

Completely Co replaced cathode material, such as *O3*-$NaCrO_2$, $NaCrO_2$ surface modified with PVDF, and $La_2(CO_3)_3.8H_2O$ exhibited highest discharge capacities ranging between 111.4-117.7 mAh/g at 0.2C [37]. Additionally, the sol-gel synthesized $NaCrO_2$, studied by Liang *et al.* [38], delivered an initial discharge capacity of 120.7 mAh/g at 0.2C, and discharge capacities of 117.8, 110.3, 98.3, and 82.1 mAh/g at 2, 10, 30, and 50C, respectively. The $NaCrO_2$ nanowires cathode synthesized by Ling *et al.* exhibited discharge capacities of about 122.6, 121.9, and 123.5 mAh/g over three consecutive cycles at 0.1 C [39]. Hence, compared to previous results, $NaCoO_2$, in this thesis work, exhibited better initial discharge-specific capacity and C-rate performance by retaining almost consistent discharge-specific capacities at all the cycles of the respective C-rates.

The discharge energy densities for all the discharge cycles of various scan rates for $NaCoO_2$ as a potential cathode material for SIBs are shown in **Figure 4.8 (d).** $NaCoO_2$ exhibited the highest discharge energy density value of 466.04 Wh/kg at 0.1C. The other highest discharge energy densities are 406.96, 298.05, 253.66, 234.95, and 217.28 Wh/kg at 0.15, 0.2, 0.3, 0.5, and 1.0 C, respectively. High values of discharge energy density indicated the application of $NaCoO_2$ as a cathode for the fabrication of lightweight and compact batteries with long operational time.

The *dQ/dV* for the second cycles of all the C-rates are shown in **Figure 4.8 (e)**, demonstrating the consistency of oxidation and reduction peaks at the same voltages as observed in CV. This consistency indicated a high degree of reproducibility and stability in the redox processes, regardless of the charging or discharging rates. Furthermore, the close alignment between the *dQ/dV* peaks and CV confirmed the strong correlation between GCD and CV results. This further supported the potential of $NaCoO_2$ as a promising cathode material for SIBs, capable of sustaining high performance across a range of operational conditions. **Figure 4.8 (f)** illustrates the charge and discharge duration during the GCD cycles of $NaCoO_2$ at various C-rates. At higher C-rates such as 0.3 C, 0.5 C, and 1.0 C, the charge and discharge times were nearly identical across all five cycles, indicating stable and consistent electrochemical behaviour under these conditions. However, at lower C-rates like 0.1C and 0.15C, the charging time exceeds the discharging time, with a more pronounced difference observed at 0.1C compared to 0.15C. This discrepancy suggested that at lower C-rates, the cell experienced slower ion kinetics during charging, leading to longer charging durations relative to discharging. However, at 0.2C, the discharge duration was almost twice that of the charging across all five cycles. This can be attributed to the potential asymmetry in the electrode reaction kinetics or the gradual buildup of polarization during the charging process. This imbalance may result in more efficient utilization of the cathode material during discharge, thereby enhancing the discharge capacity relative to the charge capacity. This imbalance may result in more efficient utilization of the cathode material during discharge, thereby enhancing the discharge capacity relative to the charge capacity. Consequently, the extended discharge duration at 0.2 C suggests that $NaCoO_2$ can deliver improved electrochemical performance, particularly in terms of sustaining higher specific capacities and maintaining efficient charge-discharge cycles over extended application.

4.4 Conclusions

In conclusion, in this chapter of the thesis work, a phase pure *P2*-$NaCoO_2$ was synthesized by improving the calcination temperature via the sol-gel technique. An extensive physicochemical characterization revealed a well-ordered, highly crystalline, and *P6₃/mmc* hexagonal symmetry of $NaCoO_2$ for the improved calcination temperature of 800ºC for 12 hr, suitable for highly reversible Na^+ intercalation/deintercalation in SIBs. $NaCoO_2$ exhibited a desired stoichiometry with a hexagonal particle shape in the particle size distribution of 5.07-23.99 μm with an average particle size of 12.091 μm. Further physical and chemical analyses supported each other and indicated the presence of respective elements with their standard characteristics and vibrational modes in the symmetry elements. The CV analysis of the $NaCoO_2$ cathode demonstrated multiple redox peaks for Co^{3+}/Co^{4+} redox couple corresponding to a multiphase transition with ultra-high structural and electrochemical stabilities. The power law and Dunn's plotting revealed the battery type and the diffusion-controlled characteristics of the cathode material. $NaCoO_2$ as a cathode possessed a very small value for the solution and charge transfer resistance, indicating the good state of health and conductivity of the electrolyte and overall cell. The fabricated cell exhibited a very small value of $8.864x10^{-9}$ and $8.864x10^{-9}$ F of double-layer capacitance before and after CV, respectively, representing the potential application of high energy density and slow discharge of the cell. It exhibited a high discharge capacity of 155.85 mAh/g at 0.1 C with an excellent discharge capacity retention for all the C-rates. The discharge-specific capacities remain almost the same for all the discharge cycles of the respective C-rate. The cathode material demonstrates outstanding discharge-specific capacity retention at higher C-rates by showing a high specific capacity of 136.98, 100.6, 84.78, 78.31, and 72.46 at 0.15, 0.2, 0.3, 0.5, and 1.0C, respectively. The highest achieved discharge-specific capacities and their capacity retention at all the C-rates were much better than the previously reported literature. $NaCoO_2$

demonstrated the highest discharge energy density of 466.04 Wh/kg at 0.1C. The discharge duration at 0.2C was almost twice than the charging duration. The high value of discharge-specific capacity, energy density, and this consistency over various C-rates, is due to the improved calcination temperature which yielded a highly crystalline *P2*-$NaCoO_2$ with the desired stoichiometry and uniform particle shape throughout the material. The above analyses revealed the potential utilization of $NaCoO_2$ as the high-capacity cathode material for the development of lightweight and compact batteries with long operational stability.

4.5 References

[1] V.R.R. Boddu, D. Puthusseri, P.M. Shirage, P. Mathur, V.G. Pol, Layered NaxCoO2-based cathodes for advanced Na-ion batteries: review on challenges and advancements, Ionics. 27 (2021) 4549–4572. https://doi.org/10.1007/s11581-021-04265-w.

[2] Q. Liu, Z. Hu, M. Chen, C. Zou, H. Jin, S. Wang, S.L. Chou, Y. Liu, S.X. Dou, The Cathode Choice for Commercialization of Sodium-Ion Batteries: Layered Transition Metal Oxides versus Prussian Blue Analogs, Adv. Funct. Mater. 30 (2020) 1909530. https://doi.org/10.1002/adfm.201909530.

[3] Z. Liu, XijunXu, S. Ji, LiyanZeng, D. Zhang, J. Liu, Recent Progress of P2-Type Layered Transition-Metal Oxide Cathodes for Sodium-Ion Batteries, Chem. Eur. J. 26 (2020) 7747 –7766. https://doi.org/doi.org/10.1002/chem.201905131.

[4] Q. Liu, Z. Hu, W. Li, C. Zou, H. Jin, S. Wang, S. Chou, S.X. Dou, Sodium transition metal oxides: The preferred cathode choice for future sodium-ion batteries?, Energy Environ. Sci. 14 (2021) 158–179. https://doi.org/10.1039/d0ee02997a.

[5] R.M. Gao, Z.J. Zheng, P.F. Wang, C.Y. Wang, H. Ye, F.F. Cao, Recent advances and prospects of layered transition metal oxide cathodes for sodium-ion batteries, Energy Storage Mater. 30 (2020)

9–26. https://doi.org/10.1016/j.ensm.2020.04.040.

[6] Q. Wang, S. Chu, S. Guo, Progress on multiphase layered transition metal oxide cathodes of sodium ion batteries, Chin. Chem. Lett. 31 (2020) 2167–2176. https://doi.org/10.1016/j.cclet.2019.12.008.

[7] F. Wei, Q. Zhang, P. Zhang, W. Tian, K. Dai, L. Zhang, J. Mao, G. Shao, Review—Research Progress on Layered Transition Metal Oxide Cathode Materials for Sodium Ion Batteries, J. Electrochem. Soc. 168 (2021) 050524. https://doi.org/10.1149/1945-7111/abf9bf.

[8] A. Kanwade, S. Gupta, A. Kankane, M.K. Tiwari, A. Srivastava, J.A. Kumar Satrughna, S. Chand Yadav, P.M. Shirage, Transition metal oxides as a cathode for indispensable Na-ion batteries, RSC Adv. 12 (2022) 23284–23310. https://doi.org/10.1039/d2ra03601k.

[9] M. Palanisamy, V.R. Reddy Boddu, P.M. Shirage, V.G. Pol, Discharge State of Layered P2-Type Cathode Reveals Unsafe than Charge Condition in Thermal Runaway Event for Sodium-Ion Batteries, ACS Appl. Mater. Interfaces. 13 (2021) 31594–31604. https://doi.org/10.1021/acsami.1c04482.

[10] N. Mattila, A.J. Karttunen, Lattice thermal conductivity of NaCoO2 and LiCoO2 intercalation materials studied by hybrid density functional theory studied by hybrid density functional theory, Mater. Res. Express. 7 (2020) 075502. https://doi.org/10.1088/2053-1591/aba3e5.

[11] K. Shiprath, H. Manjunatha, R. Venkata Nadh, T. Anil Babu, S. Ramesh, K. Chandra Babu Naidu, M. Ramesha, Synthesis and Electrochemical Characterization of NaCoO2 as Cathode Material in 2M NaOH Aqueous Electrolyte, ChemistrySelect. 6 (2021) 1874–1881. https://doi.org/10.1002/slct.202100294.

[12] L. Gao, S. Chen, L. Zhang, X. Yang, High Areal Capacity Na0.67CoO2 Bundle Array Cathode Tailored for High-Performance Sodium-Ion Batteries, ChemElectroChem. 6 (2019) 947. https://doi.org/10.1002/celc.201900031.

[13] V.R. Reddy Boddu, M. Palanisamy, L. Sinha, S.C. Yadav, V.G. Pol, P.M. Shirage, Hysteresis abated P2-type NaCoO2 cathode reveals highly reversible multiple phase transitions for high-rate sodium-ion batteries, Sustain. Energy Fuels. 5 (2021) 3219–3228. https://doi.org/10.1039/d1se00490e.

[14] B. Venkata Rami Reddy, S. Gopukumar, NaxCoO2 Cathode Material: Synthesized by Inverse Micro- Emulsion Method for Sodium Ion Batteries, ECS Trans. 53 (2013) 49–58. https://doi.org/10.1149/ma2013-01/4/139.

[15] A. Căpraru, E.A. Moacă, C. Păcurariu, R. Ianoş, R. Lazău, L. Barbu-Tudoran, Development and characterization of magnetic iron oxide nanoparticles using microwave for the combustion reaction ignition, as possible candidates for biomedical applications, Powder Technol. 394 (2021) 1026–1038. https://doi.org/10.1016/j.powtec.2021.08.093.

[16] B.V. Rami Reddy, R. Ravikumar, C. Nithya, S. Gopukumar, High performance NaxCoO2 as a cathode material for rechargeable sodium batteries, J. Mater. Chem. A. 3 (2015) 18059–18063. https://doi.org/10.1039/c5ta03173g.

[17] A. Bhide, K. Hariharan, Physicochemical properties of NaxCoO2 as a cathode for solid state sodium battery, Solid State Ion. 192 (2011) 360–363. https://doi.org/10.1016/j.ssi.2010.04.022.

[18] M.M. Faras, S.S. Patil, P.S. Patil, A.P. Torane, Unleashing the Potential of Binder-Free Hydrothermally Synthesized Marigold-Like ZnCo2O4 for Supercapacitors, J. Energy Storage. 74 (2023) 109490. https://doi.org/10.1016/j.est.2023.109490.

[19] C. Delmas, J.-J. Braconnier, C. Fouassier, P. Hagenmuller, ELECTROCHEMICAL INTERCALATION OF SODIUM IN NaxCoO2 BRONZES, Solid State Ion. 3/4 (1981) 165–169. https://doi.org/10.1016/0167-2738(88)90351-7.

[20] H. Hasegawa, Y. Ishado, S. Okada, M. Mizuhata, H. Maki, M.

Matsui, Stabilized Phase Transition Process of Layered NaxCoO2 via Ca-Substitution, J. Electrochem. Soc. 168 (2021) 010509. https://doi.org/10.1149/1945-7111/abd451.

[21] S. Song, Y. Wang, R.C. Davis, Z. Ren, X. Xiao, G. Yang, D. Wang, J. Bao, Q. Zhang, S. Chen, Z. Ren, Electrochemical Insight into NaxCoO2 for the Oxygen Evolution Reaction and the Oxygen Reduction Reaction, Chem. Mater. 33 (2021) 6299–6310. https://doi.org/10.1021/acs.chemmater.1c00008.

[22] L.W. Shacklette, T.R. Jow, L. Townsend, Rechargeable Electrodes from Sodium Cobalt Bronzes, J. Electrochem. Sac. 135 (1988) 2669–2674. https://doi.org/10.1149/1.2095407.

[23] N. Raeisi-Kheirabadi, A. Nezamzadeh-Ejhieh, H. Aghaei, Cyclic and Linear Sweep Voltammetric Studies of a Modified Carbon Paste Electrode with Nickel Oxide Nanoparticles toward Tamoxifen: Effects of Surface Modification on Electrode Response Kinetics, ACS Omega. 7 (2022) 31413–31423. https://doi.org/10.1021/acsomega.2c03441.

[24] A.R. Kanwade, A.K.S. Jena, S.M. Rajore, S.S. Mali, J. V Patil, C.K. Hong, P.M. Shirage, Revealing the potential of graphene-embedded Na3Fe2(PO4)3 for enhanced sodium-ion battery performance, J. Mater. Sci. Energy. 59 (2024) 8956–8972. https://doi.org/10.1007/s10853-024-09698-y.

[25] R. Raavi, S. Archana, P. Adinarayana Reddy, P. Elumalai, Performances of dual carbon multi-ion supercapacitors in aqueous and non-aqueous electrolytes, Energy Adv. 2 (2023) 385–397. https://doi.org/10.1039/d2ya00271j.

[26] S.M. Oh, J. Song, S. Lee, I.C. Jang, Effect of current rate on the formation of the solid electrolyte interphase layer at the graphite anode in lithium-ion batteries, Electrochim. Acta. 397 (2021) 139269. https://doi.org/10.1016/j.electacta.2021.139269.

[27] S. Kiani, H. Gharibi, S. Javadian, M. Zhiani, H. Kashani, The effect

of the SEI layer on the electrochemical impedance in the graphite/Li[Ni0.5Mn0.3Co0.2]O2 lithium-ion full cells, Appl. Surf. Sci. 633 (2023) 157638. https://doi.org/10.1016/j.apsusc.2023.157638.

[28] L. Gao, S. Chen, H. Hu, H. Cheng, L. Zhang, X. Yang, Hierarchical NaxCoO2 microspheres with low surface area toward high performance sodium ion batteries, Mater. Lett. 260 (2020) 126965. https://doi.org/10.1016/j.matlet.2019.126965.

[29] M. D'Arienzo, R. Ruffo, R. Scotti, F. Morazzoni, C.M. Mari, S. Polizzi, Layered Na 0.71CoO2: a powerful candidate for viable and high performance Na-batteries, Phys. Chem. Chem. Phys. 14 (2012) 5945–5952. https://doi.org/10.1039/c2cp40699c.

[30] J.J. Ding, Y.N. Zhou, Q. Sun, X.Q. Yu, X.Q. Yang, Z.W. Fu, Electrochemical properties of P2-phase Na0.74CoO2 compounds as cathode material for rechargeable sodium-ion batteries, Electrochim. Acta. 87 (2013) 388–393. https://doi.org/10.1016/j.electacta.2012.09.058.

[31] Yongjin Fang, X.-Y. Yu, X.W. Lou, A Practical High-Energy Cathode for Sodium-Ion Batteries Based on Uniform P2-Na0.7CoO2 Microspheres, Angew.Chem. Int. Ed. 56 (2017) 5801 –5805. https://doi.org/10. 1002/anie.201702024.

[32] B. Peng, Z. Sun, S. Jiao, J. Li, G. Wang, Y. Li, X. Jin, X. Wang, J. Li, G. Zhang, Facile self-templated synthesis of P2-type Na0.7CoO2 microsheets as a long-term cathode for high-energy sodium-ion batteries, J. Mater. Chem. A. 7 (2019) 13922–13927. https://doi.org/10.1039/c9ta02966d.

[33] A.C. Nwanya, M.M. Ndipingwi, F.I. Ezema, E.I. Iwuoha, M. Maaza, Bio-synthesized P2-Na0.57CoO2 nanoparticles as cathode for aqueous sodium ion battery, J. Electroanal. Chem. 878 (2020) 114600. https://doi.org/10.1016/j.jelechem.2020.114600.

[34] C. Hakim, H.D. Asfaw, R. Younesi, D. Brandell, K. Edstrom, I.

Saadoune, Development of P2 or P2/P3 cathode materials for sodium-ion batteries by controlling the Ni and Mn contents in Na0.7CoxMnyNizO2 layered oxide, Electrochim. Acta. 438 (2023) 141540. https://doi.org/10.1016/j.electacta.2022.141540.

[35] Y.E. Zhu, X. Qi, X. Chen, X. Zhou, X. Zhang, J. Wei, Y. Hu, Z. Zhou, A P2-Na0.67Co0.5Mn0.5O2 cathode material with excellent rate capability and cycling stability for sodium ion batteries, J. Mater. Chem. A. 4 (2016) 11103–11109. https://doi.org/10.1039/c6ta02845d.

[36] X. Wang, M. Tamaru, M. Okubo, A. Yamada, Electrode Properties of P2−Na2/3MnyCo1−yO2 as Cathode Materials for Sodium-Ion Batteries, J. Phys. Chem. C. 117 (2013) 15545−15551. https://doi.org/10.1149/ma2010-03/1/550.

[37] J. Wu, G. Hu, K. Dua, Z. Peng, M. Huang, J. Fan, Y. Gong, D. Guan, Y. Shi, R. Liu, Y. Cao, Inhibiting electrochemical phase transition of NaCrO2 with long-cycle stability by surface fluorination treatment, Electrochim. Acta. 403 (2022) 139641.

[38] J. Liang, L. Liu, X. Liu, X. Meng, L. Zeng, J. Liu, J. Li, Z. Shi, O3-Type NaCrO2 as a Superior Cathode Material for Sodium/Potassium-Ion Batteries Ensured by High Structural Reversibility, ACS Appl. Mater. Interfaces. 13 (2021) 22635−22645. https://doi.org/10.1021/acsami.1c04997.

[39] L. Liang, X. Sun, D.K. Denis, J. Zhang, L. Hou, Y. Liu, C. Yuan, Ultralong Layered NaCrO2 Nanowires: A Competitive Wide-Temperature-Operating Cathode for Extraordinary High-Rate Sodium-Ion Batteries, ACS Appl. Mater. Interfaces. 11 (2019) 4037−4046. https://doi.org/10.1021/acsami.8b20149.

CHAPTER 5

Multi-Transition Metal Co-substituted-$Na_xCo_{0.5}Fe_{0.25}Mn_{0.25}O_2$ as a High Cycle Life Cathode for Sodium-Ion Batteries

This chapter provides an investigation into the reduction of Co content to 50% of the original TM oxide by co-substituting it 50% with Fe and Mn. Hence, this chapter presents the synthesis of multi-TM co-substituted $Na_xCo_{0.5}Fe_{0.25}Mn_{0.25}O_2$ through a solid-state method and explores its physicochemical and electrochemical features as a cathode material for SIBs. Physicochemical characterization revealed the P3-$Na_xCo_{0.5}Fe_{0.25}Mn_{0.25}O_2$ structure with multiple crystal symmetries and high-order crystallinity, suitable for enhanced Na^+-ion intercalation and deintercalation. CV study revealed M^{3+}/M^{4+} (where $M=Co_{0.5}Fe_{0.25}Mn_{0.25}$) redox couple with an excellent structural reversibility. The EIS analysis suggested excellent compatibility of the electrolyte with the cathode, showing a good state of health, a low value of resistance offered to the cell, and a very negligible double-layer capacitance. The GCD interpretations reveal that $Na_xCo_{0.5}Fe_{0.25}Mn_{0.25}O_2$ delivered a significant rate capability and a high discharge capacity of 94.22 mAh/g at 0.05C by maintaining stable performance across a range of C-rates. The material exhibited high Coulombic efficiency and impressive energy densities, with a maximum discharge energy density of 279.82 Wh/kg at 0.05C. Considerably, $Na_xCo_{0.5}Fe_{0.25}Mn_{0.25}O_2$ demonstrated excellent cycle life, retaining 92.2, 78.4, 53.9, 39.4, and 28.3% of initial discharge capacity at 100^{th}, 200^{th}, 300^{th}, 400^{th}, and 500^{th} cycles, respectively, owing to the synergistic effect of co-substituted multi-transitional metals.

5.1 Introduction

There are many works reported on single TM-based Na_xCoO_2 , Na_xFeO_2 , Na_xMnO_2 , and Co, Fe, and Mn co-substituted cathode materials [1–6]. *P*2-Na_xCoO_2 has shown promising initial specific capacities and satisfactory C-rate performance and capacity retention over numerous cycles [7–11]. Due to the toxicity, high cost, and environmental concerns associated with Co, research is shifting toward earth-abundant TM like Mn and Fe. Na_xMnO_2, with 3D Na^+-ion diffusion pathways and layered structure, offers high initial capacities (*e.g.,* 190 mAh/g for β-$NaMnO_2$) [12,13], but cycling stability is hindered by the Jahn-Teller effect of Mn^{3+} state [12]. Orthorhombic $Na_{0.44}MnO_2$ demonstrates better cycling stability compared to β-$NaMnO_2$ [2,14]. Similarly, Na_xFeO_2 leverages the Fe^{3+}/Fe^{4+} redox couple but suffers from phase transitions, water reactivity, and capacity fading [15,16]. To address these limitations and reduce Co content, co-substituted multi-TM oxides are being explored with a focus on enhancing structural stability, improving electrochemical performance, cycle life, and reducing the overall cost.

The *O*3- $Na[Fe_{1/2}Mn_{1/2}]O_2$ and *P2*-$Na_{2/3}[Mn_{1/2}Fe_{1/2}]O_2$ reported by Yabuuchi *et al.* [17] exhibited a high discharge capacity of ~110 and ~190 mAh/g, respectively at 12 mA/g based on M^{3+}/M^{4+} ($M=Fe_{0.5}Mn_{0.5}$) redox couple. However, it exhibited poor cyclability and high-capacity loss and retained only ~74% and 64% of its initial capacities at the 30^{th} cycle at 13 mA/g. Similarly, *P2*-$Na_{0.5}[Ni_{0.23}Fe_{0.13}Mn_{0.63}]O_2$ studied by Hasa *et al.* [18] exhibited an initial capacity of ~200 and 175 mAh/g at 0.33C and 0.5C, respectively. An initial capacity retention of ~72% is achieved for 100 cycles at 0.5C due to the use of Ni. At 5C, it maintained a capacity of 60 mAh/g. *P2-type* $Na_{0.67}Fe_{0.2}Ni_{0.15}Mn_{0.65}O_2$ studied by Yuan *et al.* [19] demonstrated a capacity of 208 mAh/g and retained ~71% capacity over 50 cycles. Although the combination of Mn and Fe shows an enhanced initial specific capacity, the high and fast capacity fading, even at a low number of cycles, is a severe challenge. The combination of Co and Mn in

$Na_{0.67}Co_{1/2}Mn_{1/2}O_2$ investigated by Zhu *et al.* [6] exhibited a high capacity of 147 mAh/g at 0.1C and satisfying capacity retention of about 100% for over 100 cycles at 1C. $Na_{2/3}Mn_{0.5}Co_{0.5}O_2$, synthesized by Yamada *et al.* [20] achieved a high discharge capacity of 123 mAh/g at 30 mA/g, however, the capacity reduces to 85 mAh/g showing a poor initial capacity retention of only ~61% of the initial capacity at a low cycle number of 30. This indicated that the co-substitution of Mn and Co could enhance the cycle life performance of the cathode material. Nevertheless, for practical applications, further improvements in both cyclic life and high-rate performance are essential. Again, effectively controlling phase transitions during the desodiation and sodiation processes was another critical challenge for making SIBs viable for real-world applications. Hence, despite considerable progress, there is still significant challenges in identifying cathodes that offer a combination of satisfying electrochemical performance and robust structural and cycle life stability for SIBs.

Mn-based layered cathodes are known to suffer from challenges such as high-capacity fading, structural strain caused by the Jahn–Teller effect of Mn^{3+} ions, and possible Mn dissolution in the electrolyte [1,2,12,13,21,22]. However, recent advancements such as doping, partial elemental substitution, surface and defect engineering, electrolyte optimization, *etc.,* provided potential and actionable pathways to enhance the stability and high-capacity retention of the Mn-based cathode materials while minimizing the structural strain caused by the Jahn-Teller effect of Mn^{3+} [1,6,13]. This Jahn-Teller effect arises due to the asymmetric electron occupancy in the high energy e_g orbitals that lead to the distortion in the MnO_6 octahedral units and an irreversible phase transition. This John-Taller effect and the electrolyte decomposition in such Mn-based layered oxides could be mitigated through the effective strategy of multi-elemental doping to reduce the significant volume changes. As a result, in this chapter of the thesis work, we have attempted to mitigate these issues through multi-TM co-substitution of Co and Fe alongside Mn in $Na_xCo_{0.5}Fe_{0.25}Mn_{0.25}O_2$

cathode material for SIBs. With the high amount substitution of Co^{3+} and Fe^{3+} ions, the concentration of Jahn-Teller-active Mn^{3+} ions gets reduced as a result the structural strain associated with the lattice gets minimized giving rise to a stabilized lattice structure. Further, the synergistic effect of multiple TM enhances the structural integrity of the material and provides better Na^{+}-ion diffusion kinetics that help to reduce the high capacity fading during the cycling process. Again, the $Na_xCo_{0.5}Fe_{0.25}Mn_{0.25}O_2$ as cathode is synthesized at high temperature of calcination promoted a strong metal oxide bonding and high crystalline that stabilized the host structure to suppress its dissolution in the electrolyte.

Hence synergistic effect of multiple TM co-substitution significantly enhances electrochemical performances. Based on the advantages of high structural integrity and electronic conductivity of Co, the abundance, and cycle life enhancement features of Fe, and the cost-effectiveness and high working voltage window of Mn, we co-substituted these elements in $Na_xCo_{0.5}Fe_{0.25}Mn_{0.25}O_2$. Co, Fe, and Mn were substituted in a proportion of 2:1:1 to minimize Co content while enhancing the synergistic effect of these metals in optimizing performance. It was synthesized using a simple solid-state method with a two-step heating approach. Fe and Mn were selected for co-substitution in $Na_xCo_{0.5}Fe_{0.25}Mn_{0.25}O_2$ owing to their abundance, economical cost, and electrochemical activity via the Fe^{3+}/Fe^{4+} and Mn^{3+}/Mn^{4+} redox couples. Notably, Fe and Mn are both TMs with partially filled 3d orbitals that introduce electronic interactions and spin states susceptible to affecting the charge compensation mechanism and Na^{+}-ion diffusion. Specifically, Mn^{3+} is Jahn-Teller active, and its cooperative distortion results in structural strain; however, through co-substitution with Fe^{3+} and Co^{3+}, Mn^{3+} concentration is decreased, thus suppressing Jahn-Teller-induced lattice instabilities. In terms of magnetism, whereas magnetic interactions (those resulting from localized 3d electrons on Mn and Fe) are in secondary position to electrochemical properties in this research, they indirectly

influence electronic conductivity and charge delocalization, thus providing structural stability upon cycling. Substitution with a non-magnetic ion (Al^{3+}, Ti^{4+}, or Mg^{2+}) can inhibit structural distortions by playing the role of an electrochemically inactive stabilizer. Nevertheless, such non-magnetic substitutions tend to dilute the redox-active sites, reducing the overall specific capacity. Our approach thus balanced the structural stability (through partial Co and Fe substitution) with the preservation of enough redox-active ions to maintain high capacity and rate performance. Therefore, the motivation for choosing Fe and Mn over nonmagnetic ions was to harness their redox activity, abundance, and synergistic stabilizing effects while keeping the negative effect of Mn^{3+} Jahn-Teller distortions to a bare minimum. Magnetism, while secondary, plays a supporting role through its influence on electron correlations and spin states in the transition-metal layers. Physicochemical analyses were done to investigate the structural, morphological, and chemical properties. The electrochemical performances of $Na_xCo_{0.5}Fe_{0.25}Mn_{0.25}O_2$ cathode for SIB were explored in sodium half-cells. It demonstrated a high discharge capacity of 94.22 mAh/g at 0.05C due to the M^{3+}/M^{4+} ($M=Co_{0.5}Fe_{0.25}Mn_{0.25}$) redox couple. Notably, it also showed a high discharge energy density of 279.82 Wh/kg at 0.05C and an outstanding C-rate performance. It also demonstrated an excellent cycle life by maintaining about 92.2, 78.4, 53.9, 39.4, and 28.3% of its initial discharge-specific capacities at the 100, 200, 300, 400, and 500th cycles, respectively. These results underscored the material's potential as a cost-effective cathode for SIBs.

5.2 Experimental Section

The experimental details, including preparation through solid-state method, advanced techniques for physicochemical characterizations, slurry preparation, drying, electrode cutting, fabrication of $Na_xCo_{0.5}Fe_{0.25}Mn_{0.25}O_2$ cathode in CR2032 half-cells, and the characterization techniques used for its electrochemical properties investigation are explained in the **Chapter 2.**

5.3 Results and Discussions

5.3.1 Phase Purity and Crystal Structure Studies

The XRD pattern of $Na_xCo_{0.5}Fe_{0.25}Mn_{0.25}O_2$ cathode material (black color) is depicted in **Figure 5.1 (a)**. It possessed a combination of rhombohedral and hexagonal phases of *R*-3m and *P*6$_3$/mmc symmetry, respectively. All the obtained peaks were well indexed to these symmetries, indicating the formation and a well-ordered crystalline arrangement of the material. The highest intense peaks for $Na_xCo_{0.5}Fe_{0.25}Mn_{0.25}O_2$ material were observed at the lattice planes of (*002*), (*006*), (*100*), (*101*), (*102*), *(103*), and (*015*) at 2θs of 16.04º, 32.29º, 35.70º, 37.03º, 38.38º, 40.44º, 41.72º, and 45.99º, respectively followed by other peaks as shown in the XRD pattern. Among them, the (*006*) lattice plane extending in 2θ from 31.62º to 33.20º had the highest FWHM and comparative intensity. This indicated that the maximum number of crystal lattices was most probably arranged in the (*006*) lattice plane. The reference XRD pattern of $Na_{0.6}CoO_2$ (red color), $Na_{0.61}CoO_2$ (green color), and $NaMnO_2$ (blue color) was used to match with the obtained peaks of $Na_xCo_{0.5}Fe_{0.25}Mn_{0.25}O_2$.

The structural refinement of $Na_xCo_{0.5}Fe_{0.25}Mn_{0.25}O_2$ is depicted in **Figure 5.1 (b)**. XRD pattern of $Na_xCo_{0.5}Fe_{0.25}Mn_{0.25}O_2$ was well-fitted to the referenced material with a chi-square of 2.64. This further indicated the high crystallinity and the formation of a double phase due to the co-substitution of Co, Fe, and Mn. **Table 5.1** represents the lattice parameters of $Na_xCo_{0.5}Fe_{0.25}Mn_{0.25}O_2$ from the refinement studies and was compared with those of pristine $NaCoO_2$ reported in the literature.

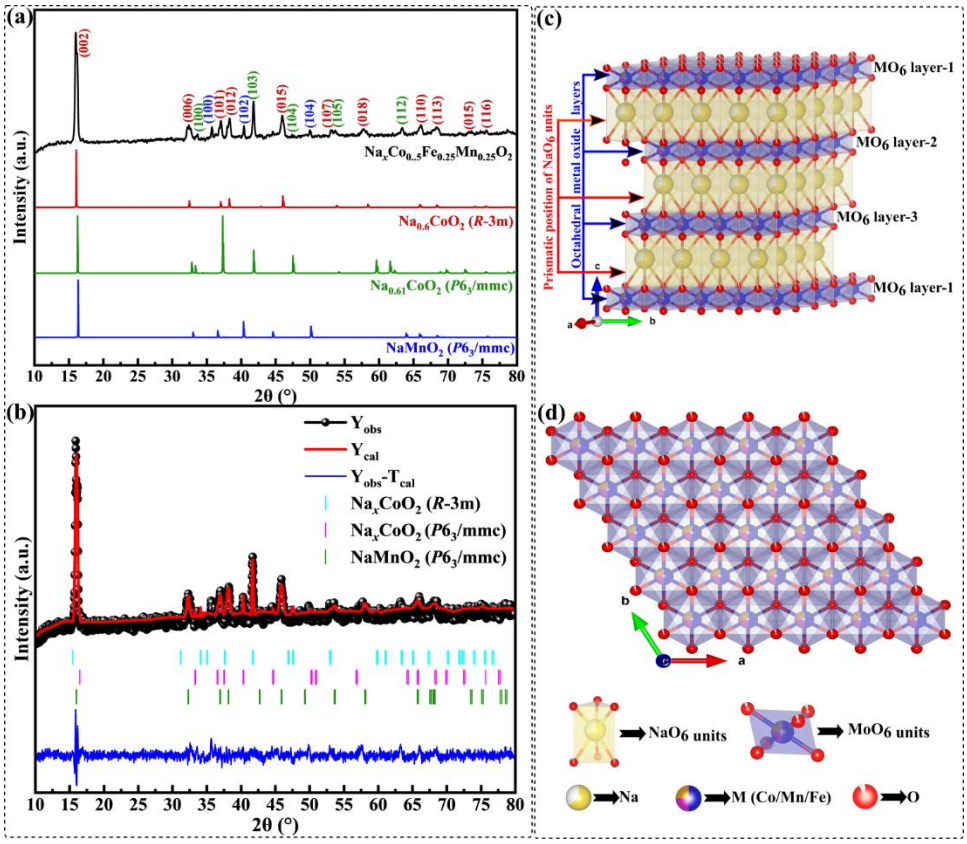

Figure 5.1 (a) XRD pattern of as-prepared $Na_xCo_{0.5}Fe_{0.25}Mn_{0.25}O_2$; **(b)** XRD structural refinement of $Na_xCo_{0.5}Fe_{0.25}Mn_{0.25}O_2$; **(c)** side view for the polyhedral crystal structures; and **(d)** top view for the polyhedral crystal structures of *P3*-type $Na_xCo_{0.5}Fe_{0.25}Mn_{0.25}O_2$.

Table 5.1: Refinement lattice information of $Na_xCo_{0.5}Fe_{0.25}Mn_{0.25}O_2$.

Parameters	**$Na_xCo_{0.5}Fe_{0.25}Mn_{0.25}O_2$**	**$NaCoO_2$**
***a* (Å)**	2.840	2.833[23], 2.82[24],
***b* (Å)**	2.840	2.833[23], 2.82[24],
***c* (Å)**	16.634	10.89[24], 10.880[23]
α (°)	90	90[23,24]
β (°)	90	90[23,24]
γ (°)	120	120[23,24]
V (Å^3)	116.198	75.07[23,24]
ρ (g/cm^3)	7.497	-
Symmetry	*R*-3m + *P*6$_3$/mmc	*P*6$_3$/mmc[23,24]

The side and top view of the polyhedral lattice structure of $Na_xCo_{0.5}Fe_{0.25}Mn_{0.25}O_2$ material are demonstrated in **Figures 5.1 (c-d)**. It possessed three district MO_6 (M=$Co_{0.5}Fe_{0.25}Mn_{0.25}$) octahedral layers and the NaO_6 octahedral were arranged in between these MO_6 layers in a prismatic manner, forming a *P*3-$Na_xCo_{0.5}Fe_{0.25}Mn_{0.25}O_2$ structure. In this configuration, Na^+-ions occupied prismatic sites that were strategically situated between adjacent metal oxide sheets of CoO_6, FeO_6, and MnO_6 polyhedral units in a layered architecture. **Table 5.2** represents the lattice arrangement in $Na_xCo0_{.5}Fe_{0.25}Mn_{0.25}O_2$ including the position of atoms, multiplicity, and occupancy through the XRD refinement. Here X, Y, and Z are the cartesian coordinates and *a*, *b*, and *c* are their respective lattice constants as given in **Table 5.1**.

Table 5.2: Lattice arrangement information for $Na_xCo0_{.5}Fe_{0.25}Mn_{0.25}O_2$ for phase *R*-3m from the XRD refinement.

Lattices	Multiplicities	X/*a*	Y/*b*	Z/*c*	Occupancies
O2	3	0.000	0.000	0.618	1.000
O1	3	0.000	0.000	0.382	0.926
Co1	3	0.000	0.000	0.000	0.502
Mn1	3	0.000	0.000	0.000	0.251
Fe1	3	0.000	0.000	0.000	0.241
Na1	3	0.000	0.000	0.844	0.652

5.3.2 Particle Morphology and Composition Studies

FESEM images of the particles of $Na_xCo_{0.5}Fe_{0.25}Mn_{0.25}O_2$ at a magnification of 100,000x, 20,000x, and 10,000x are shown in **Figure 5.2 (a-c)**. These particles exhibited a smooth surface morphology with a combination of hexagonal and rodlike structures. The coexistence of morphologies was due to the presence of multiple phases as explained in the above phase purity and crystal analysis section. The smooth and uniform surface morphologies of $Na_xCo_{0.5}Fe_{0.25}Mn_{0.25}O_2$ facilitated fast ion transport and stable electrode-electrolyte interface formation. Although the

solid-state synthesis method has limitations as it produces large particle size with rough surface morphology, the particle size distribution of our synthesized $Na_xCo_{0.5}Fe_{0.25}Mn_{0.25}O_2$ material lied within a narrow range of 0.1-0.6 µm, having ~0.33 µm average size of the particles indicating the uniform, fine, and highly homogeneous formation as displayed in **Figure 5.2 (d)**. This uniformity in particle size is crucial for achieving consistent electrochemical behaviour and efficient Na^+-ion kinetics.

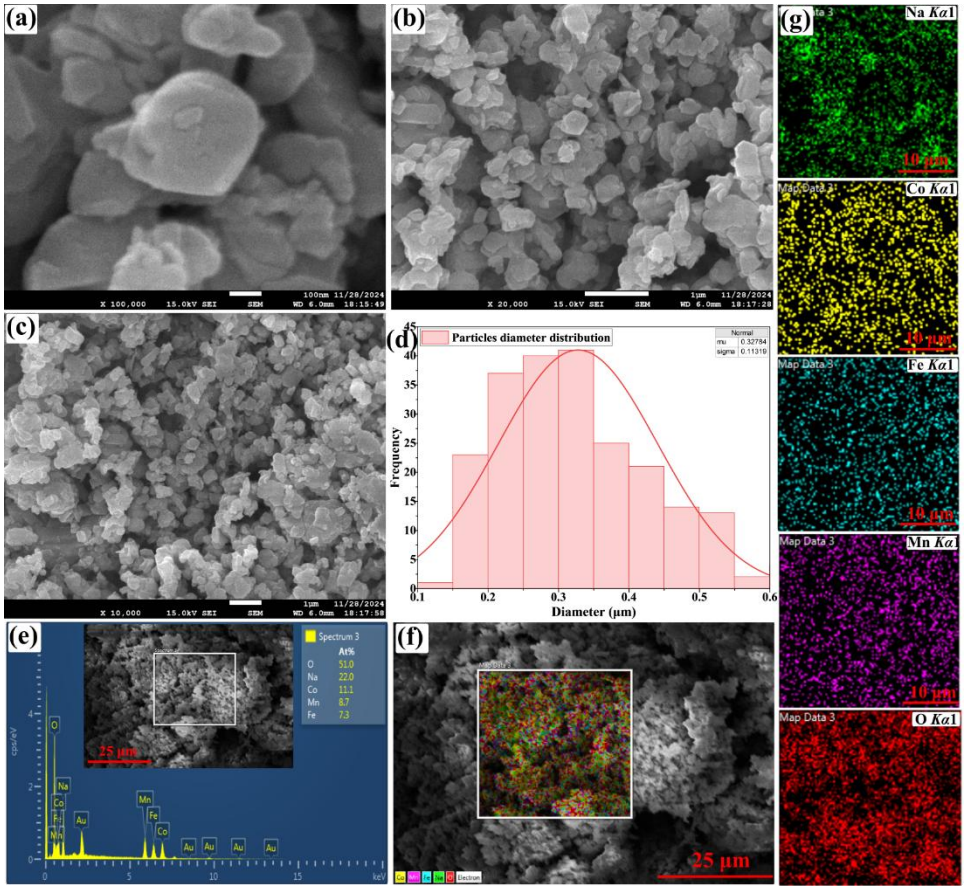

Figure 5.2 (a-c) FESEM images of $Na_xCo_{0.5}Fe_{0.25}Mn_{0.25}O_2$ at various magnifications; **(d) Particle** size distribution profile; **(e)** EDS profile; **(f-g)** color distribution profile and color mapping of Co, Fe, Mn, O, and Na in $Na_xCo_{0.5}Fe_{0.25}Mn_{0.25}O_2$ material.

The uniform particle size of $Na_xCo_{0.5}Fe_{0.25}Mn_{0.25}O_2$ resulted in due to the substitution of Co, Fe, and Mn promoted enhanced particle and crystal growth, resulting in higher crystallinity. The synergistic presence of

multiple symmetries, well-ordered crystallinity as analyzed through XRD and the formation of uniform particle distribution were expected to enhance Na^+-ion insertion/extraction during the cell performance. These features contributed to further enhance the structural stability and cycle life of $Na_xCo_{0.5}Fe_{0.25}Mn_{0.25}O_2$ cathode.

The uniformity in the spatial elemental distribution of Na, Co, Fe, Mn, and O throughout the materials and the nominal elemental composition of the material were studied through EDX and elemental color mapping as illustrated in **Figure 5.2 (e-g)**. The EDS spectrum for $Na_xCo_{0.5}Fe_{0.25}Mn_{0.25}O_2$ confirmed the presence of Na, Co, Fe, Mn and O in 22.0, 11.1, 7.3, 8.7, and 51.0 atomic%, respectively. With this, the synthesized material had a stoichiometry of $Na_{0.81}Co_{0.41}Fe_{0.27}Mn_{0.32}O_{1.88}$ which had near-stoichiometric proportions as our desired material. **Figure 5.3 (f)** represents the uniform and even elemental distribution of all the elements across the synthesized material, and further, the elemental mapping (**Figure 5.3 (g)**) highlights a homogeneous distribution of each element across the particles, clearly representing the uniform particle formation inside the material of interest.

5.3.3 TEM/HRTEM: Atomic Arrangement Analysis

Further detailed analysis for the structural morphology, shape, and size, lattice fringes, and ordered atomic arrangement of $Na_xCo_{0.5}Fe_{0.25}Mn_{0.25}O_2$ at the atomic level was performed through the TEM and HRTEM as depicted in **Figure 5.3.** The TEM images in **Figures 5.3 (a-b)** at different magnifications displayed the clear particle morphology and size of $Na_xCo_{0.5}Fe_{0.25}Mn_{0.25}O_2$. The TEM images also revealed the coexistence of hexagonal and rod-like morphology of particles and the sizes were consistent as explained in through FESEM. These different morphologies were due to the formation of hexagonal and rhombohedral phases of the material with the $P6_3/mms$ and $R\text{-}3m$ crystal symmetry. The SAED pattern of $Na_xCo_{0.5}Fe_{0.25}Mn_{0.25}O_2$, shown in **Figure 5.3 (c)**, illustrated the reciprocal lattice plane. The 2D-Brillouin zones in the

reciprocal lattice of SAED patterns are also observed to have a hexagonal shape supporting our above analyses. The measured *'d-spacing'* from the SAED pattern was ~2.6 Å corresponding to *(006)* planes of the *R*-3m crystal phase structure. Moreover, the SAED pattern demonstrated the crystalline nature of the material with desired symmetry. This analysis further supported our findings and explanations as discussed in the above XRD analysis.

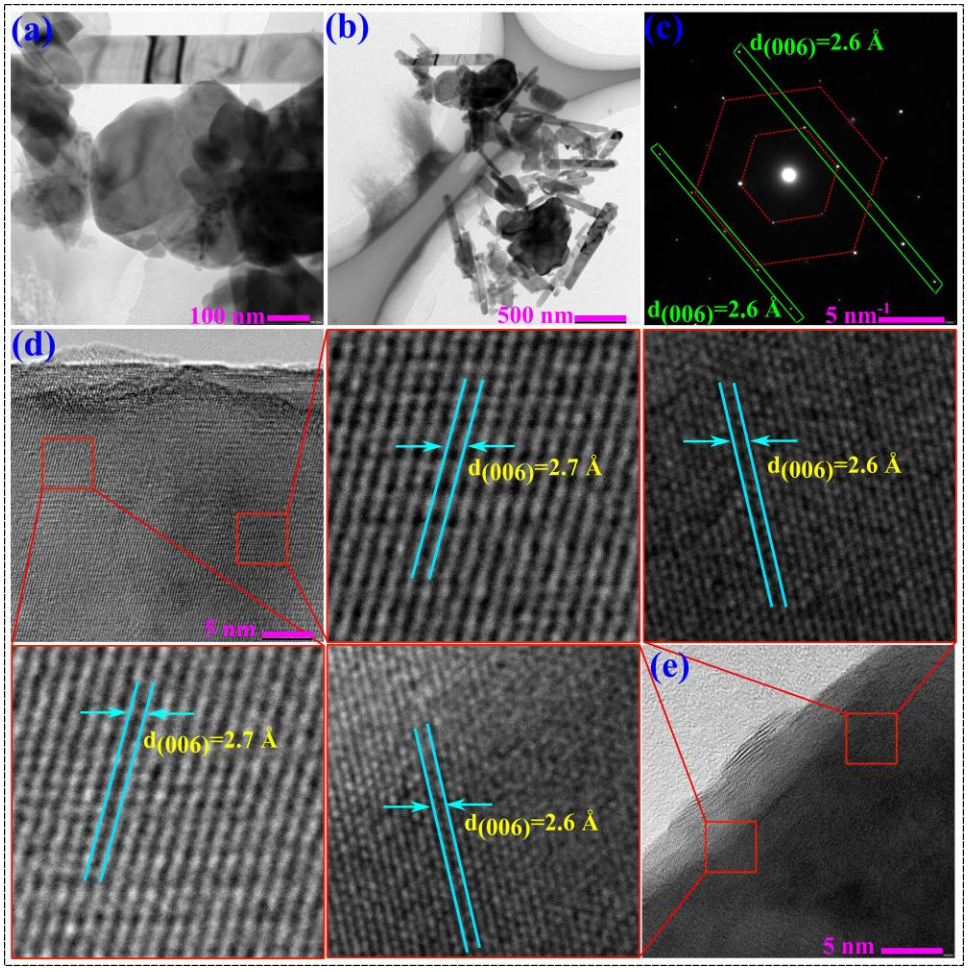

Figure 5.3 (a-b) TEM images; **(c)** SAED pattern; **(d-e)** HRTEM images at various locations of $Na_xCo_{0.5}Fe_{0.25}Mn_{0.25}O_2$.

The HRTEM images in **Figures 5.3 (d-e)** show distinct lattice fringes for atomic arrangements taken at various locations of different particles. The magnified view of the atomic arrangement in **Figure 5.3 (d)** clearly showed atomic lattice fringes, with a *'d-spacing'* of ~2.7 Å.

Similarly, the *'d*-spacing' value for the other particles was found to be ~2.6 Å as displayed in **Figure 5.3 (e).** The *d*-spacing value of ~2.6-2.7 Å was in resonance with the SAED profile and with the intense peak with high FWHM at *(006)* of XRD analysis. This consistency revealed the crystalline feature of $Na_xCo_{0.5}Fe_{0.25}Mn_{0.25}O_2$ material. The sharp and well-defined lattice fringes reflected orderly atomic arrangement, crucial for enhancing electrochemical properties such as fast Na^+-ion migration, structural stability, and enhancement of cycle life performance of $Na_xCo_{0.5}Fe_{0.25}Mn_{0.25}O_2$ cathode material for SIBs.

5.3.4 Chemical State Analysis Through XPS

The presence of individual elements and their chemical state analysis such as oxidation states in $Na_xCo_{0.5}Fe_{0.25}Mn_{0.25}O_2$ were done through XPS as depicted via **Figure 5.4**. XPS spectrum in **Figure 5.4 (a)**, spans over broad BE of 0-1300 eV, confirming the presence of all the expected elements. Apart from the main constituent elements, a distinct peak for electrons in the C-*1s* orbital was observed, which was attributed to the sample holder and used as a reference. The high-scan XPS spectra of the various atoms in $Na_xCo_{0.5}Fe_{0.25}Mn_{0.25}O_2$ are shown in **Figure 5.4 (b-f)**. The BE of electrons in Na-*1s* orbital was at 1070.5 eV, (**Figure 5.4 (b)**), representing the '+1' oxidation state of Na in $Na_xCo_{0.5}Fe_{0.25}Mn_{0.25}O_2$ material. Co-*2p* orbital of Co revealed the existence of Co^{3+} oxidation, with a spin-orbit coupling splitting into Co-$2p_{3/2}$ and Co-$2p_{1/2}$, with BE of 794.1 eV and 779.1 eV, and ΔE of 15 eV (**Figure 5 (c))**. High scan XPS spectrum of Fe-*2p* represents the Fe^{3+} oxidation state of Fe with a spin-orbital coupling splitting characteristic peak at 724.1 and 710.4 eV for Fe-$2p_{1/2}$ and Fe-$2p_{3/2}$, respectively having ΔE = 13.7 eV as shown in **Figure 5.4 (d)**. Similarly, the characteristic peaks for Mn-*2p* orbital were observed at 653.5 and 641.8 eV for the spin-down Fe-$2p_{1/2}$ and spin-up Fe-$2p_{3/2}$ orbitals, respectively with ΔE = 11.7 eV. These characteristic peaks of Mn revealed its '+3' oxidation state (**Figure 5.4 (e))**. The characteristic satellite peaks for all these TMs were observed at their respective locations. The position

of these characteristic satellite peaks further confirmed the +3 oxidation state TMs before battery operation. During the charging process, these '+3' oxidation states of Co, Fe, and Mn in $Na_xCo_{0.5}Fe_{0.25}Mn_{0.25}O_2$ gets transition to '+4' oxidation state, confirming that the electrochemical behaviour of $Na_xCo_{0.5}Fe_{0.25}Mn_{0.25}O_2$ cathode material in SIBs is primarily driven by the M^{3+}/M^{4+} ($M=Co_{0.5}Fe_{0.25}Mn_{0.25}$) redox couple.

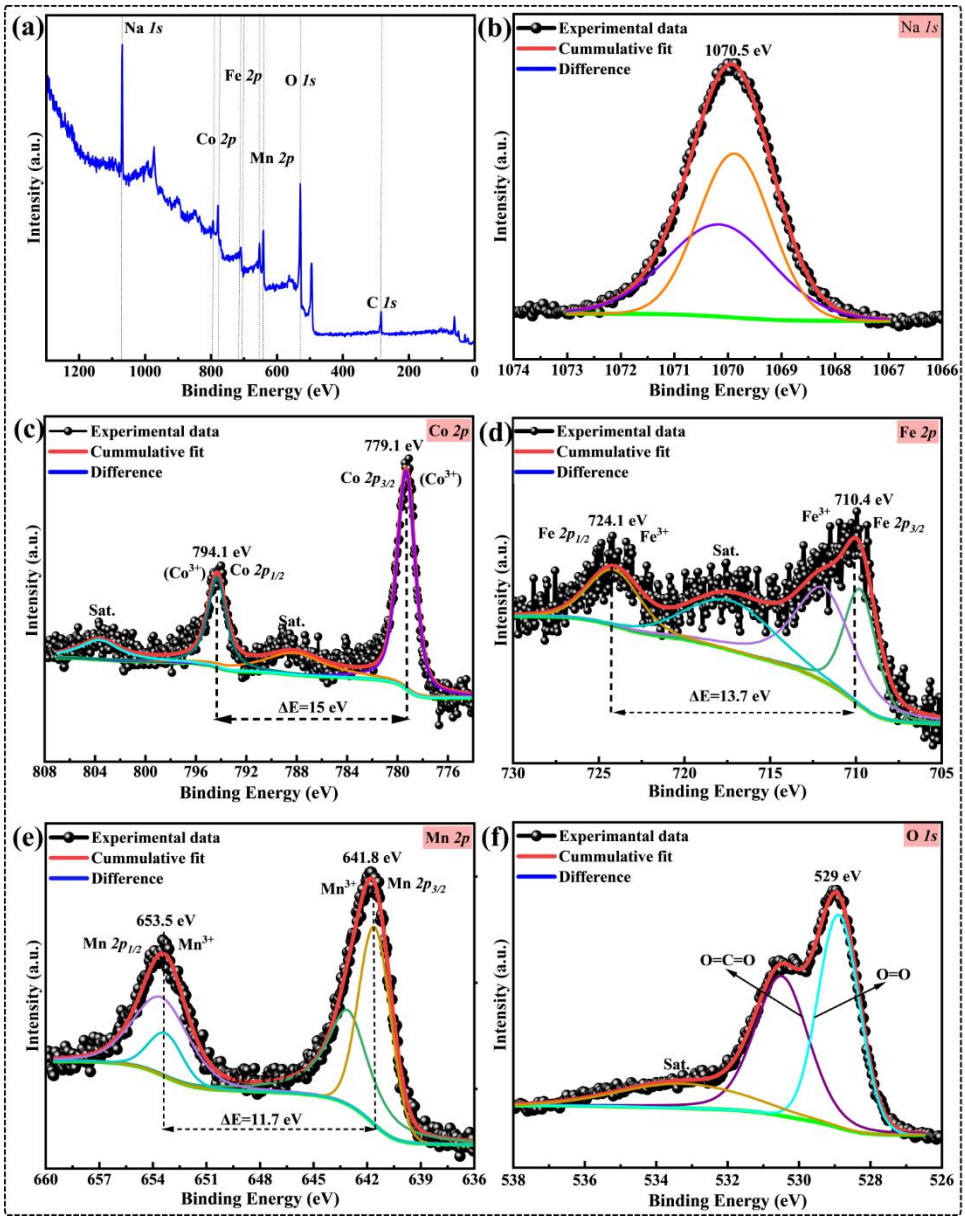

Figure 5.4 XPS spectra of **(a)** $Na_xCo_{0.5}Fe_{0.25}Mn_{0.25}O_2$; **(b)** Na-1*s*; **(c)** Co-2*p* orbital; **(d)** Fe-2*p* orbital; **(e)** Mn-2*p* orbital; and **(f)** O-1*s*.

The 'O-*1s*' XPS spectrum in **Figure 5.4 (f)** represents a major characteristic peak at 529 eV, along with a lower-intense peak corresponding to 'O=C=O' bonding, indicating the '-2' oxidation state of O in the as-synthesized material. These binding energies are summarized in **Table 5.3**. The comprehensive XPS study confirmed the existence and distribution of atoms and respective chemical states in $Na_xCo_{0.5}Fe_{0.25}Mn_{0.25}O_2$ for its potential application as cathode in SIBs.

Table 5.3: Electron BE of elements and their oxidation state in as prepared $Na_xCo_{0.5}Fe_{0.25}Mn_{0.25}O_2$ cathode material.

Elements	Orbital	Orbital splitting	BE characteristic peak (eV)	Oxidation state
Na	Na-*1s*	No	**1070.5**	+1
Co	Co-*2p*	Yes	Co-$2p_{1/2}$ (**794.1**), Co-$2p_{1/2}$ (**779.1**)	+3
Fe	Fe-*2p*	Yes	Fe-$2p_{1/2}$ (**724.1**), Fe-$2p_{1/2}$ (**710.4**)	+3
Mn	Mn-*2p*	Yes	Mn-$2p_{1/2}$ (**653.5**), Mn-$2p_{1/2}$ (**641.8**)	+3
O	O-*1s*	No	**529.0**	-2

5.4 Electrochemical Performances Analysis

5.4.1 CV Studies

Electrochemical redox behaviour of $Na_xCo_{0.5}Fe_{0.25}Mn_{0.25}O_2$ was studied using CV, as illustrated in **Figure 5.5.** CV measurements were conducted at four different scan rates of 0.1, 0.5, 1.0, and 5 mV/s in 2.0-4.2 V. The CV profile for the three charge and discharge cycles for the lowest scan rate of 0.1 mV/s is presented in **Figure 5.5 (a)**. The redox peaks for all cycles were located at identical positions of voltages and overlapped with one another, demonstrating the highly electrochemical reversible characteristics and the structural integrity of $Na_xCo_{0.5}Fe_{0.25}Mn_{0.25}O_2$ as cathode for SIBs during. The series of redox pairs of 2.41V/2.23V, 2.48V/2.37V, 2.57V/2.49V, 2.72V/2.63V, 2.98V/2.91V, 3.3V/3.22V, 3.39V/3.34V, 3.7V/3.61V, 3.92V/3.8V, and 3.99V/3.94V representing the oxidation/reduction peaks corresponded to the reversible multiple phase transition during battery performance.

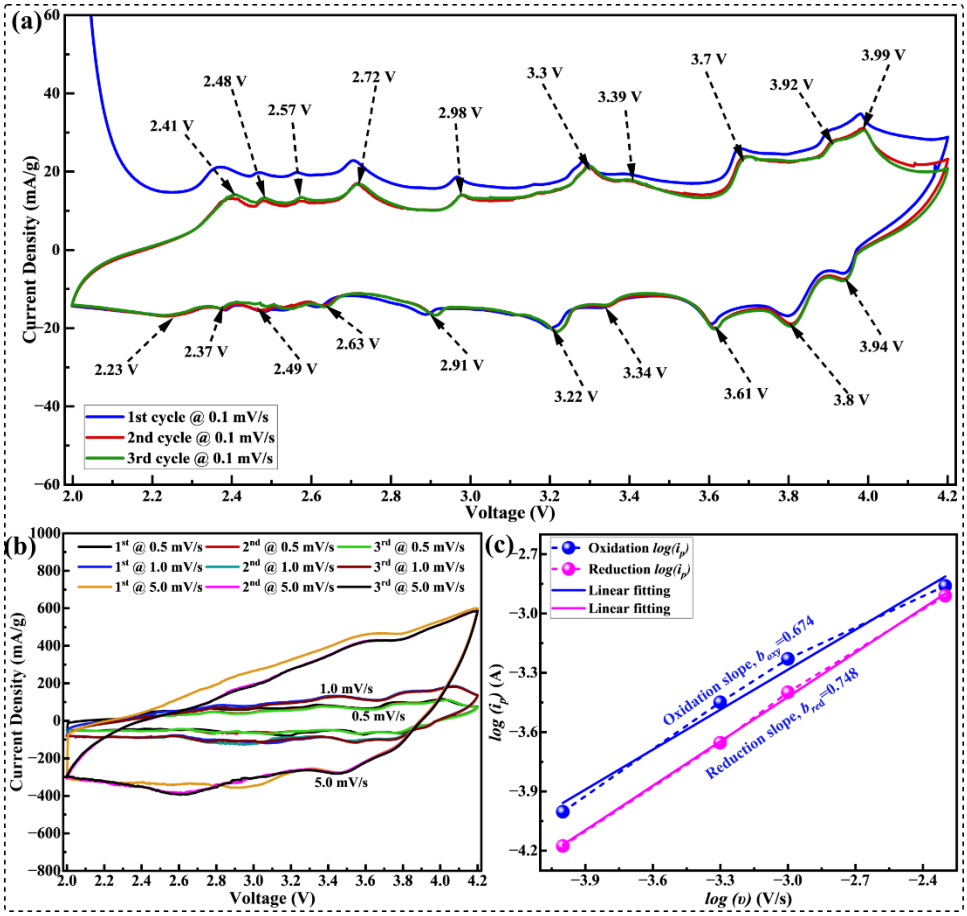

Figure 5.5 CV at **(a)** 0.1 mV/s, **(b)** 0.5 mV/s, 1.0 mV/s, and 5.0 mV/s; **(c)** *log (υ) versus log(i_p)* graph for $Na_xCo_{0.5}Fe_{0.25}Mn_{0.25}O_2$ cathode.

The redox process followed the same pathway and exhibited the redox pairs at the same voltage, representing the high structural integrity and stability of $Na_xCo_{0.5}Fe_{0.25}Mn_{0.25}O_2$ cathode. During the process of charging, the '+3' oxidation state of the TM elements oxidized into '+4', and during discharging these TM elements further reduced from the '+4' oxidation state to '+3'. Hence the electrochemical performances of $Na_xCo_{0.5}Fe_{0.25}Mn_{0.25}O_2$ cathode was due to the M^{3+}/M^{4+} (where, $M=Co_{0.5}Fe_{0.25}Mn_{0.25}$) redox couples and the peaks resulted in due to the multiple stable phase transitions during Na^+ ion extraction/insertion from/to the $Na_xCo_{0.5}Fe_{0.25}Mn_{0.25}O_2$ cathode material. The further CV graphs at other higher scans of 0.5, 1.0, and 5.0 V for their respective three charge/discharge cycles are represented in **Figure 5.5 (b)**. The redox peaks

were observed to be present at the same voltage with respect to Na/Na^+ for these higher scan rates as that of 0.1 mV/s, indicating the existence of stable phase of $Na_xCo_{0.5}Fe_{0.25}Mn_{0.25}O_2$ with exceptional reversibility in the redox reactions. This enhanced redox reversibility assisted in the high structural stability and an improved cycle life performance. Further, the increase in the area under the CV curve as well as the current densities of the redox peaks with an increase in the scan rates reflected the higher charge transfer and diffusion-controlled processes.

The CV analysis was extended to investigate the diffusion kinetics of Na^+-ions in using the Randles–Sevcik equation [25,26]. It provided a linear relationship between peak current (i_p) and the square root of scan rate ($v^{1/2}$) as given in **equation 5.1** and **5.2**.

$$i_p = \left(2.69 \times 10^5\right) A\, n\, (D\, n\, \upsilon)^{\frac{1}{2}} \qquad \ldots\ldots\ldots (5.1)$$

Or the diffusion constant of Na^+-ions is given by,

$$D = \left[\frac{1}{(2.69\times10^5)\, A\, C\, n^{\frac{3}{2}}} \cdot \left(\frac{i_p}{\upsilon^{\frac{1}{2}}}\right)\right]^2 \ldots\ldots\ldots (5.2)$$

Through the above equations, the Na^+-ion diffusion constant value for charging and discharging processes were found to be 3.612×10^{-10} and 1.468×10^{-10} cm^2/s, respectively. We further extended our study for the electrochemical behaviour of $Na_xCo_{0.5}Fe_{0.25}Mn_{0.25}O_2$ using the Power-Law equation (**equation 5.3**). Constants '*a*', and '*b*' were determined from the figure given in **Figure 5.5 (c)**. The value of *b*=0.5 or near 0.5 suggests battery-type behavior, *b*=1 or near 1 represents the capacitive behavior, and a 0.5 to 1 value reflects a combination of both behaviors.

$$i_{peak} = a.(v)^b \qquad \ldots\ldots\ldots (5.3)$$

For the $Na_xCo_{0.5}Fe_{0.25}Mn_{0.25}O_2$ cathode material, we obtained *'b'* values of 0.674 and 0.748 for the highest intense peak of oxidation and reduction, respectively, indicating that $Na_xCo_{0.5}Fe_{0.25}Mn_{0.25}O_2$ primarily showed inductive type behaviour during its electrochemical performances with an efficient charge transfer through the intercalation/deintercalation of Na^+-ions.

5.4.2 GCD Studies

Electrochemical features of $Na_xCo_{0.5}Fe_{0.25}Mn_{0.25}O_2$ as a potential cathode for SIB in Na/1M-$NaClO_4$/$Na_xCo_{0.5}Fe_{0.25}Mn_{0.25}O_2$ cell was analyzed through GCD at various current densities of 0.05 C (~11.95 mA/g), 0.1 C (~23.9 mA/g), 0.2 C (~47.79 mA/g), 0.3 C (~71.69 mA/g), 0.5 C (~119.49 mA/g), 0.8 C (191.18 mA/g), 1 C (~238.97 mA/g), and 2 C (~477.95 mA/g) in a voltage range of 2.0-4.2 V, as represented in **Figure 5.6**. The charge/discharge specific capacity of all the five respective cycles representing to these current rates are presented in **Figure 5.6 (a)**. $Na_xCo_{0.5}Fe_{0.25}Mn_{0.25}O_2$ as cathode material demonstrated excellent rate tolerance across all C-rates. A consistent charge/discharge capacity is detected for all five cycles of C-rates which highlights the stable electrochemical behaviour and structural integrity of $Na_xCo_{0.5}Fe_{0.25}Mn_{0.25}O_2$ cathode material. It exhibits the highest initial charge and discharge capacities of 114.52 and 94.22 mAh/g, respectively, at 0.05C. The other high charge/discharge capacities were 93.29/85.94, 85.98/78.94, 77.92/72.71, 71.19/65.59, 63.33/59.48, 58.16/56.29, and 52.13/47.6 at 0.1, 0.2, 0.5, 0.8, 1, and 2 C, respectively, as shown by the GCD profile in **Figure 5.6 (b)** and given in **Table 5.4**.

Figure 5.6 (c) represents *'dQ/dV'* pattern for the first charge/discharge cycles. The observed oxidation and reduction peaks appeared at identical voltages as in CV, highlighting the reproducibility of these redox activities. This consistency underscored the stability of the redox behaviour, irrespective of the applied charge/discharge rates. These findings additionally established $Na_xCo_{0.5}Fe_{0.25}Mn_{0.25}O_2$ as a highly potential cathode material for SIBs, demonstrating excellent performance in terms of high capacity, structural stability, and high cycle life performance.

Table 5.4: Specific capacities and Coulombic efficiencies of our material.

C-rates	Number of cycles	Specific capacity (mAh/g)		Coulombic Efficiency (%)
		Charging	Discharging	
0.05C	(1)	114.52	94.22	82.27
	(2)	105.99	93.17	87.90
	(3)	102.17	92.12	90.17
	(4)	98.7	92.24	93.46
	(5)	96.39	89.55	92.90
0.1C	(1)	93.29	85.94	92.12
	(2)	88.62	85.52	96.50
	(3)	88.01	85.21	96.83
	(4)	87.48	84.89	97.04
	(5)	87.09	84.49	97.01
0.2 C	(1)	85.98	78.94	91.81
	(2)	80.11	78.67	98.20
	(3)	79.78	78.38	98.24
	(4)	79.66	78.69	98.78
	(5)	79.86	77.87	97.52
0.3 C	(1)	77.92	72.71	93.31
	(2)	73.44	72.7	99.00
	(3)	73.42	72.43	98.66
	(4)	73.14	72.08	98.56
	(5)	72.82	71.85	98.67
0.5 C	(1)	71.19	65.59	92.14
	(2)	66.13	65.53	99.09
	(3)	66.04	65.34	98.90
	(4)	65.81	65.38	99.35
	(5)	65.85	65.23	99.06
0.8 C	(1)	63.66	59.48	93.43
	(2)	59.93	59.28	98.92
	(3)	59.61	59.16	99.24
	(4)	59.49	59.07	99.30
	(5)	59.37	58.99	99.35
1C	(1)	58.16	56.29	96.78
	(2)	56.6	56.14	99.18
	(3)	56.4	56.09	99.44
	(4)	56.35	56.03	99.44
	(5)	56.27	55.92	99.38
2C	(1)	52.13	47.6	91.31
	(2)	47.97	47.52	99.04
	(3)	47.69	47.33	99.25
	(4)	47.49	47.2	99.41
	(5)	47.33	47.12	99.56

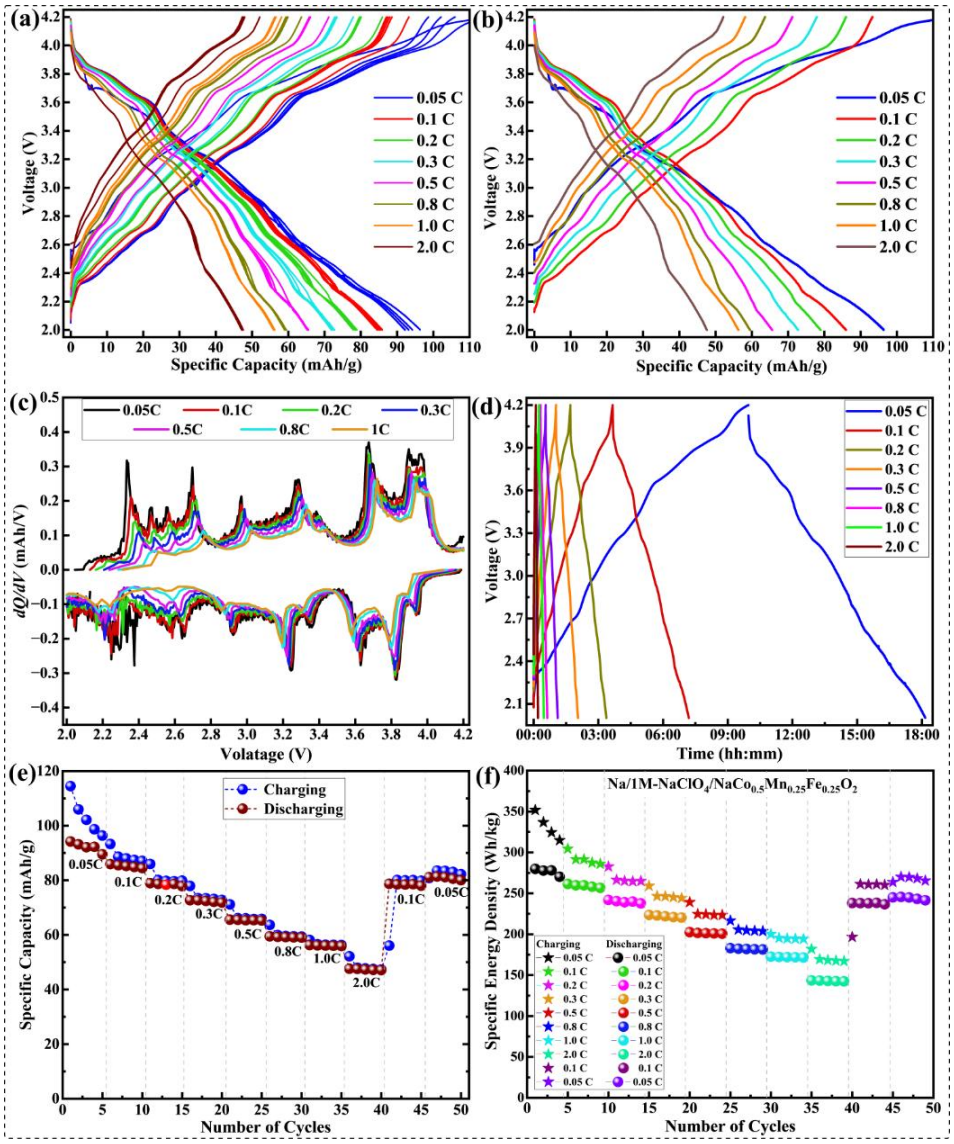

Figure 5.6 (a) GCD curve at 0.05, 0.1, 0.2, 0.3, 0.5, 0.8, 1, and 2 C, **(b)** GCD curve for highest specific capacities; **(c)** *dQ/dV profile;* **(d)** charge/discharge time profile; **(e)** C-rate performance; **(f)** charge/discharge energy density of $Na_xCo_{0.5}Fe_{0.25}Mn_{0.25}O_2$ cathode.

The charge and discharge duration profile for the 1st cycle during the GCD studies at different C-rates are represented in **Figure 5.6 (d)**. For all the charge/discharge cycles of different C-rates, the time for charging and discharging of the cell remains almost the same, suggesting the stable and reproducible electrochemical performance. At 0.05 C, it took about 9 hr 57 minutes to get fully charged and about 8 hr 11 minutes to get fully

discharged, whereas it took only 3 hours 39 minutes to fully charge and 3 hr 32 minutes to get fully discharged at 0.1 C. This high discharge time indicates the practical application of $Na_xCo_{0.5}Fe_{0.25}Mn_{0.25}O_2$ cathode material having long-term discharge applications.

The C-rate performance, representing the charge and discharge specific capacities the C-rates of 0.05C, 0.1C, 0.2C, 0.3C, 0.5 C, 0.8C, 1C, 2C, 0.1 C, and 0.05C are displayed in **Figure 5.6 (e)**. In addition, the exact values are also summarized in **Table 5.4**. $Na_xCo_{0.5}Fe_{0.25}Mn_{0.25}O_2$ showed nearly similar values of specific capacities at every cycle of current densities (*i.e.,* C-rates), suggesting that $Na_xCo_{0.5}Fe_{0.25}Mn_{0.25}O_2$ maintains high reversibility and retains its significant structural and electrochemical properties even under varied cycling conditions. An excellent Coulombic Efficiency retention was also found for each C-rates as presented in **Table 5.4**. At the higher C-rates, the rate-capability test showed diminishing capacity values, reflecting the expected performance drop due to higher charge/discharge rates. Further, the Coulombic efficiencies were much better at higher C-rates compared to the lower 0.05 C, which resulted in due to the lower side reactions at the higher C-rates. $Na_xCo_{0.5}Fe_{0.25}Mn_{0.25}O_2$ exhibited a good charge/discharge capacity retention, representing its excellent electrochemical performances. **Figure 5.6 (f)** demonstrates the charge/discharge energy densities across different scan rates for $Na_xCo_{0.5}Fe_{0.25}Mn_{0.25}O_2$. At a scan rate of 0.05C, it demonstrated the highest energy density for discharge as 279.82 Wh/kg. The next successive highest discharge energy densities were observed as 261.41, 241.9, 223.56, 202.57, 182.97, 172.56, and 143.54 Wh/kg at 0.1 C, 0.2 C, 0.3 C, 0.5 C, 0.8 C, 1 C, and 2 C, respectively as shown in **Figure 5.6 (f)**. The high discharge energy densities of $Na_xCo_{0.5}Fe_{0.25}Mn_{0.25}O_2$ cathode materials represented its potential implementation in the fabrication of dense batteries with lightweight.

5.4.3 Cycle Life Performance Analysis

The cycle life performance and capacity retention properties of $Na_xCo_{0.5}Fe_{0.25}Mn_{0.25}O_2$ are compellingly demonstrated in **Figure 5.7 (a).** Here, the cycling life measurements were performed under a constant charge/discharge current density of 0.2C in the voltage window of 2.0-4.2 V. The material of interest showed remarkable electrochemical stability over an extended cycling. In **Figure 5.7 (a),** the blue, green, and red dots represent the charging, discharging, and coulombic efficiency, respectively over the course of 500 charge/discharge cycles. $Na_xCo_{0.5}Fe_{0.25}Mn_{0.25}O_2$ as cathode material for SIBs demonstrated an excellent cycling performance by retaining a significant amount of initial discharge-specific capacities even after hundreds of charge/discharge cycles. Specifically, it retained about 92.2%, 78.4%, 53.9%, 39.4%, and 28.3% of its initial discharge capacities at the 100^{th}, 200^{th}, 300^{th}, 400^{th}, and 500^{th} cycles, respectively. The impressive initial discharge capacity retention of was attributed to the synergistic effect of multiple TMs incorporated into its crystal structure. The co-substitution of Co, Fe, and Mn TMs not only enhanced the electrochemical reversibility but also enhanced its structural stability for several cycles owing to their combined synergistic electrochemical reversible properties. Hence the strategic co-substitution of TM elements provided a robust crystal framework for repeated Na^+-ion intercalation/deintercalation, making $Na_xCo_{0.5}Fe_{0.25}Mn_{0.25}O_2$ a promising cathode material for SIBs.

5.4.4 EIS Analysis

The EIS studies for $Na_xCo_{0.5}Fe_{0.25}Mn_{0.25}O_2$ before CV, after CV, and after stability are displayed in **Figure 5.7 (b)**. The Nyquist plot revealed three distinct semicircle formations each representing the different electronic and charge resistances related to charge transfer, ion diffusion, and interfacial reactions in the battery system. Further, the equivalent circuit model given in **equation 5.4** (shown inside **Figure 5.7 (b)**) was employed to fit the experimental EIS data to analyse the underlying electrochemical

parameters. The total impedance (Z) calculated from the below polynomial given in **equation 5.5**.

$$\text{Equi. circuit} = R_1 + \frac{Q_2}{R_2} + \frac{Q_3}{R_3} + \frac{Q_4}{R_4} + W \qquad \ldots\ldots\ldots\ldots (5.4)$$

$$Z = R_1 + \frac{R_2}{R_2 Q_2 (2\pi i f)^{a_2+1}} + \frac{R_3}{R_3 Q_3 (2\pi i f)^{a_3+1}} + \frac{R_4}{R_4 Q_4 (2\pi i f)^{a_4+1}} + W \quad \ldots\ldots\ldots (5.5)$$

EIS parameters including R_1 (solution resistance), R_2 (charge transfer resistance), R_3 (SEI resistance), R_4 (diffusion-related resistance), Q_2, Q_3, Q_4 (CPEs), a_2, a_3, a_4 (exponent constants), and W (Warburg impedance) from the fitted and calculated equivalent model of a circuit are summarized in **Table 5.5**. Here, a key focus of the EIS analysis was the solution resistance (R_1) and charge transfer resistance (R_2), as they provided insights into the ionic conductivity and charge transfer. $Na_xCo_{0.5}Fe_{0.25}Mn_{0.25}O_2$ exhibited the solution resistance R_1 as only 8.411 **Ω** before CV which remained almost the same as 9.688 and 10.203 **Ω** after CV and after stability, respectively. This small change in R_1 indicated that the electrolyte used with the fabricated cell offers good conductivity for cell operation. The charge transfer resistance R_2 value was measured as 69.036 **Ω** before CV analysis which increased to 147.625 and 281.442 **Ω** after CV and after stability, respectively. This indicated that the migration of Na^+-ions becomes sluggish and observes higher resistance. This increase in transfer resistance was attributed to the prolonged cycling which induced structural degradation or minor phase transformations within the cathode material, contributing to the observed increase in charge transfer resistance. However, the SEI resistance, R_3 offered by the formation of the SEI increased significantly after the cycle life performance. The formation of SEI layer or surface passivation on the cathode material during repeated cycling resulted in a high increase in R_3 value. The SEI layer, while stabilizing the electrolyte-cathode interface, can act as a barrier to Na^+-ion migration, thereby increasing the R_3 resistance.

Table 5.5: Parameters obtained from EIS equivalent circuit.

Parameters	Obtained Values from data fitting		
	Before CV	**After CV**	**After Stability**
$\mathbf{R_1}$ (Ω)	8.411	9.688	10.203
$\mathbf{R_2}$ (Ω)	69.036	147.625	281.442
$\mathbf{R_3}$ (Ω)	18.129	25.598	180.416
$\mathbf{R_4}$ (Ω)	11.183	14.788	114.402
$\mathbf{Q_2}$ ($F.s^{(a-1)}$)	2.849×10^{-4}	1.382×10^{-5}	3.593×10^{-6}
$\mathbf{Q_3}$ ($F.s^{(a-1)}$)	4.616×10^{-5}	4.517×10^{-3}	1.561×10^{-4}
$\mathbf{Q_4}$ ($F.s^{(a-1)}$)	3.99×10^{-3}	4.825×10^{-6}	9.811×10^{-4}
a_2	0.425	0.756	0.864
a_3	1	0.918	0.56
a_4	1	0.821	0.993
W ($\Omega.s^{-1/2}$)	12.216	14.106	10.583

EIS analysis was used for calculating double layer capacitance (C_{dl}) through **equation 5.6** and was found to be 2.305×10^{-8} and 5.655×10^{-9}, before CV and after cycle life performance, respectively. Low C_{dl} represented the outstanding conductivity of electrolytes.

$$C_{dl} = \frac{1}{2\pi.\mathrm{R}_2 f_{max}} \qquad \ldots\ldots\ldots\ldots (5.6)$$

The above EIS fitting contained multiple overlapping semicircles corresponding to a number of circuit elements making it highly complex within a similar frequency domain. To overcome this limitation, the Distribution of Relaxation Time (DRT), a reliable mathematical tool, was utilized to investigate cell behavior in the time domain by analyzing the polarization effects that took place in the similar frequency range.[25,27] DRT method transformed frequency-domain data into a relaxation spectrum, where each DRT peak represented an individual polarization process characterized by a time constant τ. In DRT, an infinite Voigt model having a series of parallel connection of resistances (R) and CPEs (Q) were used to fit the impedance profile and gives the time constant τ as given in **equation 5.7**, where $0 < \alpha < 1$ [25,28].

$$\tau = \frac{1}{(R\,Q)^{\alpha}} \qquad \ldots\ldots\ldots\ldots (5.7)$$

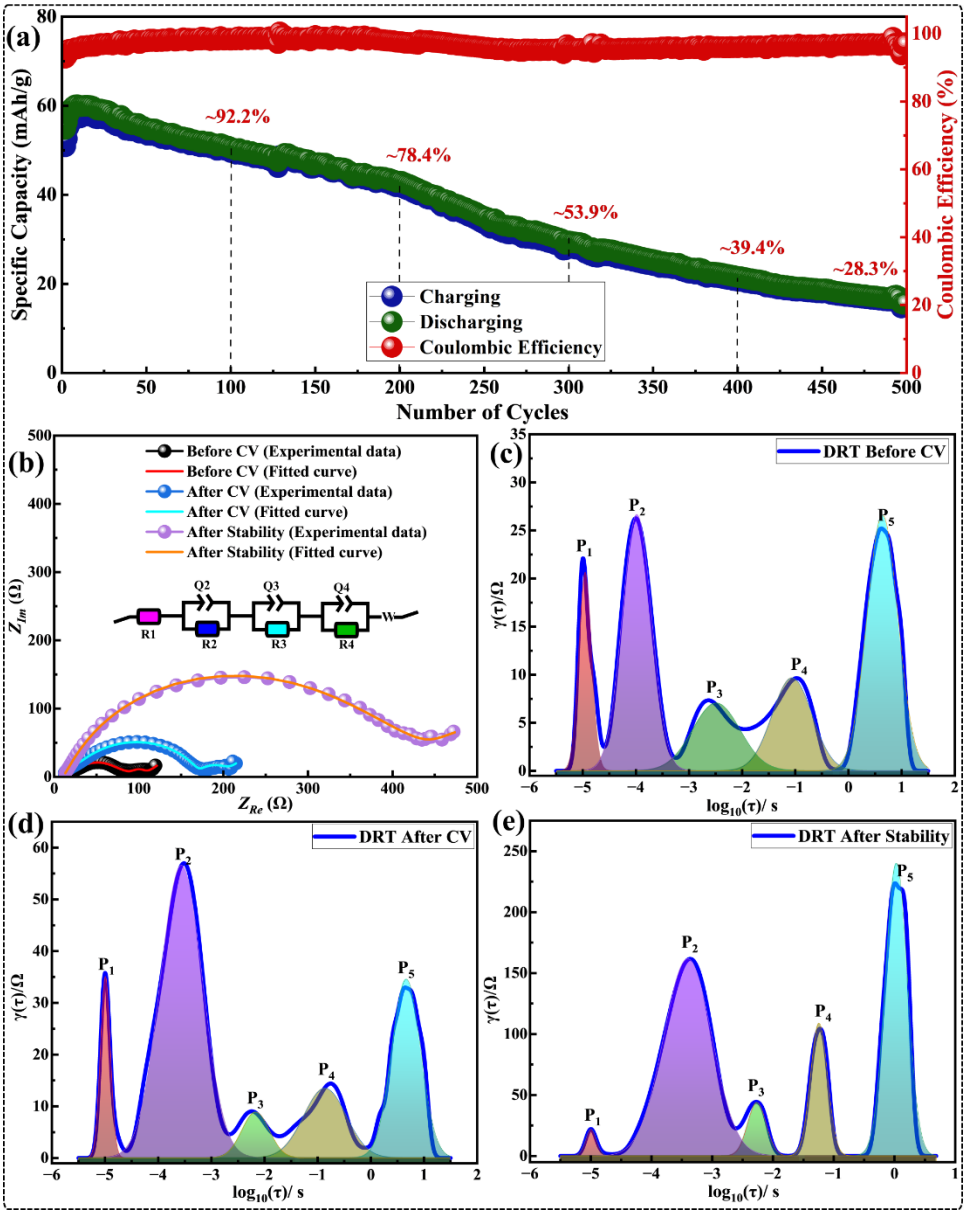

Figure 5.7 (a) Cycle life performance of $Na_xCo_{0.5}Fe_{0.25}Mn_{0.25}O_2$ cathode for 500 cycles; **(b)** EIS-Nyquist plot with equivalent circuit; DRT analysis **(c)** before CV, **(d)** after CV, and **(e)** after stability analysis for of $Na_xCo_{0.5}Fe_{0.25}Mn_{0.25}O_2$ cathode material in the sodium-half cell.

Hence, DRT allowed to resolve the closely overlapped processes with higher fidelity than equivalent circuit fitting or EIS representation. In DRT, the peak height, position, and area provide quantitative information about the reaction kinetics. In the literature, it is reported that the time constant $\log_{10}(\tau) \leq -3$ s represents the interparticle or contact resistances of

electrode particles with current collector; $\log_{10}(\tau)$ in between -3 to -2 s signifies active ion transport through the SEI layer, $\log_{10}(\tau)$ in between -2 to -1 s indicates interfacial charge transfer and $\log_{10}(\tau) \geq 10^{-1}$ s correspond to the ion diffusion process in bulk electrode [25,27]. **Figures 5.7 (c-e)** represents the DRT spectrum of Na/1M-$NaClO_4$/$Na_xCo_{0.5}Fe_{0.25}Mn_{0.25}O_2$ cell before CV, after CV, and after stability analyses, respectively. These DRT spectra derived from the impedance data revealed five distinct peaks (P_1 to P_5), each indicating specific electrochemical processes. The DRT peaks P_1 and P_2 corresponded to the contact resistance representing the high-frequency region semicircle of the EIS data. Peaks P_3 and P_4 corresponded to the charge transfer resistances across the SEI and electrode/electrolyte interfaces corresponded to the mid-frequency range of the EIS semicircle. Similarly, the DRT peak P_5 is assigned to ion diffusion within the bulk electrode at the low-frequency region of the EIS analysis. Thus, DRT offered high-resolution, quantitative insight into electrode kinetics, enabling deconvolution of overlapping processes, identification of rate-limiting steps, and separation of anodic and cathodic contributions.

Table 5.6: Electrochemical performance comparison of $Na_xCo_{0.5}Fe_{0.25}Mn_{0.25}O_2$ cathode with the existing similar materials.

Cathode name	Synthesis	Dis. capacity (mAh/g)	Cycle life	Potential range (V)	Ref.
$NaCoO_2$	Solgel	99 @ 0.1C	~91% @ 100th cycle	2.0-4.0V	[10]
$NaCoO_2$	Solid state	89 @ 0.1C 34 @ 1.0C	~75% @ 100th cycle	0.0-1.0V	[11]
Na_xCoO_2	Facile sodiation	116.7 @ 0.4C	~95% @ 300th cycle	2.0-3.8V	[7]
Na_xCoO_2	Solgel	126 @ 0.1C 77 @ 0.5C	~86% @ 50th cycle	2.0-4.2V	[24]
$Na_{0.67}CoO_2$	Hydrothermal	1.66 mAh/cm^2@0.5 mA/cm^2	~96 @ after 60 cycles	2.0-3.8 V	[29]
$Na_{0.57}CoO_2$	Biosynthesis	57 @ 0.7C	~79% @ 1000 cycle	0.0-1.8V	[30]
$Na_{0.70}CoO_2$	Solvothermal	~126.2 @ 0.1C	92.4% @ 300th cycles	2.0-4.0 V	[31]

$Na_{0.71}CoO_2$	Hydrothermal	~102 @ 0.04C	-	2.0-3.9V	[32]
$Na_{0.7}CoO_2$	Solvothermal	125 @ 0.04C	~86% @ 300th cycle	2.0-3.8V	[9]
$Na_{0.74}CoO_2$	Solid state	110.2@ 0.05C 107 @ 0.1C	~52.2% @ 40th cycle	2.0-3.8V	[33]
O3-$NaFeO_2$	Solid state	~91 @ 30 mA/g	~52% @ 11th cycles	2.0-3.8V	[34]
$NaFeO_2$	Solid-state	~80 @ 0.05C	~25% @ 50th cycle	2.0-3.8V	[35]
$NaFeO_2$	Solid-state	~85 @ 0.2 mA/cm^2	-	1.5-3.6 V	[36]
O3-$NaFeO_2$	Solid-state	~123 @ 80mA/g	~53% @ 20th cycle	2.0-4.0V	[37]
α-$NaMnO_2$	Solid state	~146 @ 0.2C	~73% @ 20th cycle	1.7-4.0 V	[21]
β-$NaMnO_2$	Solid state	~144.3 @ 1C	~41% @ 35th cycle	2.0-4.0V	[38]
$Na_{0.7}MnO_2$	Solid state	~101 @ 0.1C	~59% @ 50th cycle	2.0-3.8V	[39]
$Na_{0.67}Mn_{0.64}Al_{0.06}Co_{0.30}O_2$	Dealloying	114.1 @ 1000 mAh/g	~81% @ 200th cycle	1.5-4.0V	[40]
$NaMn_{0.33}Fe_{0.33}Ni_{0.33}O_2$@$TiO_2$	Solid state	~160 @ 0.1C	38.6% @ 500th cycle	1.5-4.2 V	[40]
$Na_{0.67}Ni_{0.2}Co_{0.2}Mn_{0.6}O_2$	Solvothermal	132.2 @ 0.2C	83% @ 200th cycle	1.5-4.2 V	[40]
$Na_xNi_{0.33}Co_{0.33}Mn_{0.33}O_2$	Solvothermal	142.8 @ 0.1C	93% @ 50 cycles	2.0-4.4 V	[31]
$NaFe_{1/3}Co_{2/3}O_2$	Solid state	199.6 @ 0.2C	83.06% @ 50th cycle	1.5-4.4 V	[31]
$NaFe_{1/2}Co_{1/2}O_2$	Solid state	148.1 @ 0.2C	72.65% @ 50th cycle	1.5-4.4 V	[31]
$NaFe_{2/3}Co_{1/3}O_2$	Solid state	111.2 @ 0.2C	55.29% @ 50th cycle	1.5-4.4 V	[31]
$NaTi_2(PO_4)_3$ coated $Na_{0.67}Co_{0.2}Mn_{0.8}O_2$	Sol-gel	70.7 @ 20C	86.7% @ 150th cycle	1.5-4.5 V	[40]
$NaFeO_2$@C	Solvothermal	89.6 @ 0.1C	87.3% @ 100th cycle	2.0-3.4 V	[40]
$Na_xCo_{0.5}Fe_{0.25}Mn_{0.25}O_2$	Solid state	94.22 @ 0.05 C ~86 @ 0.1 C	~92.2%@100th cycle ~78.4%@200th cycle ~54%@300th cycle ~39.4%@ 400th cycle ~28.3%@ 500th cycle	2.0-4.2 V	**This work**

Table 5.6 represents a comparison of the electrochemical performance of $Na_xCo_{0.5}Fe_{0.25}Mn_{0.25}O_2$ with previously reported pristine Na_xCoO_2**,** Na_xFeO_2**,** and Na_xMnO_2 along with combination of Co, Fe, or Mn. In contrast to these single-TM-based materials, $Na_xCo_{0.5}Fe_{0.25}Mn_{0.25}O_2$ exhibited significantly enhanced electrochemical characteristics, such as superior cycle life, higher initial specific capacity, improved C-rate performance, and an elevated working voltage. Further, the remarkable electrochemical performances of $Na_xCo_{0.5}Fe_{0.25}Mn_{0.25}O_2$ exhibiting a high discharge capacity of 94.22 mAh/g and energy density of 279.82 Wh/kg at 0.05 C, was competitive with many other similar layered cathode materials cathodes having multiple TMs. Some of its competitive layered metal oxides comprised of $Na_{0.67}Mn_{0.64}Al_{0.06}Co_{0.30}O_2$ (114.1 mAh/g initial capacity at 1000 mA/g, 81% capacity retention after 200 cycles) [40], $NaMn_{0.33}Fe_{0.33}Ni_{0.33}O_2$ with TiO_2 coating (160 mAh/g initial capacity, 36.8% capacity retention after 500 cycles) [40], $Na_{0.67}Ni_{0.2}Co_{0.2}Mn_{0.6}O_2$ (132.2 mAh/g initial capacity, 83% capacity retention after 200 cycles) [40], $Na_xNi_{0.33}Co_{0.33}Mn_{0.33}O_2$ (142.8 mAh/g initial capacity, 93% capacity retention after 50 cycles) [31], $NaFe_xCo_{1-x}O_2$ derivatives (initial capacities between 111-200 mAh/g at 0.2 and retains about 55-83% initial capacities at 50th cycle) [31], $Na_{0.67}Co_{0.2}Mn_{0.8}O_2$ coated with $NaTi_2(PO_4)_3$ (70.7 mAh/g capacity at 20C and retains ~87% capacity after 150 cycle), and so on as given in **Table 5.6**. Its comparison with other high number of metals substituted similar layered oxides includes *P2*-$Na_{0.67}Ni_{1/3}Mn_{2/3}O_2$ (150 mAh/g initial capacity, 90% retention after 100 cycles) and $NaNi_{0.4}Cu_{0.05}Mg_{0.05}Mn_{0.4}Ti_{0.1}O_2$. The extended cycle life performance of $Na_xCo_{0.5}Fe_{0.25}Mn_{0.25}O_2$ is comparable with other Fe/Mn-based oxide cathodes such as *O3*-$NaFe_{1/2}Mn_{1/2}O_2$/C suffering a rapid capacity decay to only 24 mAh/g after 40 cycles, indicating the advantages of multi-metal substitution in enhancing the structural long-term cycling stability.

The superior cycling stability of $Na_xCo_{0.5}Fe_{0.25}Mn_{0.25}O_2$ was due to the synergistic effect of the co-substitution of TMs, which enhanced the

Na^+-ion diffusion pathways, minimized lattice strain, and maintained the crystal's structural integrity. These collectively contributed to sustaining Na^+-ion migration processes with minimal structural distortion. Even after hundreds of cycles, it retained its good initial discharge capacity, demonstrating its excellent capacity retention and high structural stability. This remarkable performance highlighted the potential of $Na_xCo_{0.5}Fe_{0.25}Mn_{0.25}O_2$ cathode for advanced SIBs.

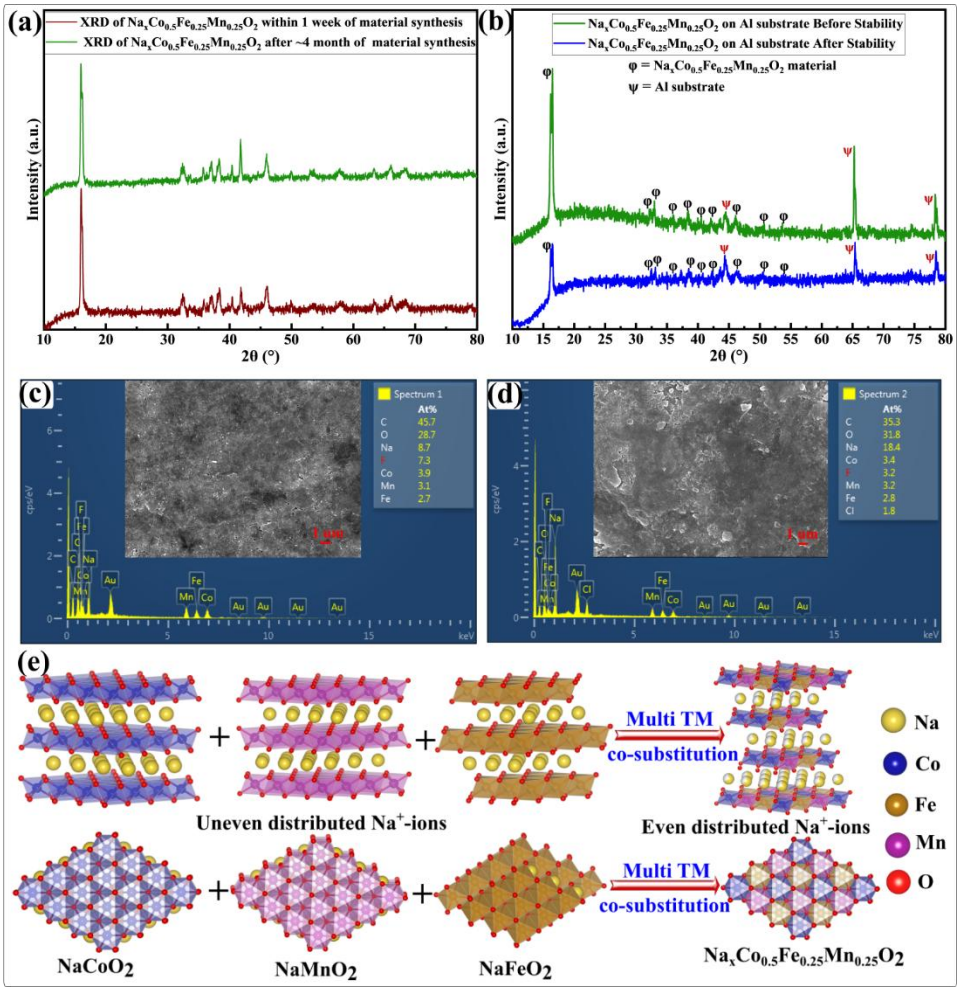

Figure 5.8 (a) XRD pattern of $Na_xCo_{0.5}Fe_{0.25}Mn_{0.25}O_2$ within one week and after four months of material synthesis, **(b)** Ex-situ XRD analysis of $Na_xCo_{0.5}Fe_{0.25}Mn_{0.25}O_2$ on Al substrate before and after stability testing, FESEM and EDS analysis of $Na_xCo_{0.5}Fe_{0.25}Mn_{0.25}O_2$ on Al substrate **(c)** before cell fabrication and **(d)** after stability testing, and **(e)** Mechanism of structural stability of $Na_xCo_{0.5}Fe_{0.25}Mn_{0.25}O_2$ cathode material.

The environmental stability of $Na_xCo_{0.5}Fe_{0.25}Mn_{0.}$was analyzed by performing XRD measurements within one week of material synthesis and subsequently after around four months of material synthesis as given in **Figure 5.8 (a)**. The XRD patterns obtained showed no noticeable changes, revealing that the crystal structure of $Na_xCo_{0.5}Fe_{0.25}Mn_{0.25}O_2$ remained stable over a long time. We conducted a comprehensive ex-situ postmortem analysis of the electrode after stability testing to analyse its structural stability during the cycling process. For this, we performed the XRD, FESEM, and EDS analysis of the coated active material as an electrode on Al substrate before the fabrication of the coin cell as well as for the electrode obtained by disassembling the coin cell after stability testing. The Ex-situ XRD analysis of electrodes before and after stability testing revealed the primary diffraction pattern of the active material in the electrode remained unchanged after cycling stability. This indicates the structural stability of $Na_xCo_{0.5}Fe_{0.5}Mn_{0.25}O_2$ cathode material.

The only noticeable difference in the diffraction pattern of the electrode after stability analysis was the increase in the relative intensity peak of the Al current collector which is likely due to the partial exposure of the substrate during electrode processing. The XRD pattern of the electrode before cell assembly (i.e., before stability testing) and after stability testing is given in **Figure 5.8 (b)**. The FESEM images of the electrodes before stability testing (**Figure 5.8 (c)** subfigure**)** and after stability testing (**Figure 5.8 (d)** subfigure**)** further confirmed that the surface morphology in both cases remains uniform. EDS analysis before stability (**Figure 5.8 (c)**) and after stability (**Figure 5.8 (d)**) supported these observations. Ex-situ analyses revealed the structural, phase, and composition identity after cycling testing.

5.5 Possible Reason for Enhanced Cyclic Life Performance

The enhanced cycle life performance of $Na_xCo_{0.5}Fe_{0.25}Mn_{0.25}O_2$ could be attributed to the synergistic existence of Co, Fe, and Mn. This helped in maintaining the crystal structure integrity and reducing the capacity fading during repeated Na^+-ion extraction/insertion. The detailed

mechanism of M^{3+}/M^{4+} *(*$M=Co_{0.5}Fe_{0.25}Mn_{0.25}$) redox couple of $Na_xCo_{0.5}Fe_{0.25}Mn_{0.25}O_2$ material for excellent structural reversibility in SIBs is shown in **Figure 5.8 (e)**. Here, the co-existence of Co, Fe, and Mn in the form of $M = Co_{0.5}Fe_{0.25}Mn_{0.25}$, leveraged complementary redox activity. The Co^{3+}/Co^{4+} redox couple provided a stable platform for minimal lattice strain. In layered $NaMO_2$ cathodes, Co^{3+} normally stabilizes in a low-spin state, while Co^{4+} may stabilize into intermediate- or mixed-spin states depending on the Na content and crystal field strength. This configuration suppresses significant Jahn-Teller distortions, thereby enhancing structural reversibility in $Na_xCo_{0.5}Fe_{0.25}Mn_{0.25}O_2$ [41]. Our electrochemical results, showing smooth phase transitions and stable cycling, are consistent with this behavior. The electronic conductivity of the material was enhanced due to Co^{3+}, which helped with efficient charge transfer. Hence, the presence of Co helped to obtain high-voltage stability of the material during the charging and discharging process [42]. Whereas the presence of Fe^{3+}/Fe^{4+} redox couple helped to obtain a high specific capacity. The '+3' oxidation state of Fe helps to reduce the lattice strain via charge compensation, resulting in enhanced crystal structural reversibility, improved cycle life performance, and reduced capacity fading [41]. One beautiful advantage of Fe in $Na_xCo_{0.5}Fe_{0.25}Mn_{0.25}O_2$ is the reduction of oxygen evolution during cycling, which was one of the common degradation reasons in the sodiated layered metal oxides [43]. Similarly, the presence of Mn^{3+}/Mn^{4+} redox couple in the lattice structure of $Na_xCo_{0.5}Fe_{0.25}Mn_{0.25}O_2$ acted as a structural pillar that suppressed the irreversible oxygen redox [42]. Further, during the charging/discharging process, Mn stabilized the host structure through the Mn-O covalent bonding and provided structural rigidity to the material [44].

Again, the coexistence of these elements in the M^{3+}/M^{4+} redox couple provided a uniform distribution of Na^+-ion in the lattice, minimized deleterious phase transition, and enhanced structural reversibility of $Na_xCo_{0.5}Fe_{0.25}Mn_{0.25}O_2$. It reduced volume change at the high charging voltage. Hence, the co-existence of Co^{3+}/Co^{4+}, Fe^{3+}/Fe^{4+}, and Mn^{3+}/Mn^{4+}

provided a multi-electron redox mechanism, uniform distribution of Na^+-ion, and a stable lattice framework which helped to provide excellent structural reversibility and improved capacity retention over a long cycle life. It optimized the Na layer spacing which mitigates irreversible phase transitions and maintains the structural integrity. The incorporation of Fe and Mn alongside Co brought a balance between electronic conductivity, enhanced electrochemical activities, and improvement in cycle life performance and distributed the local stress within the lattice, reducing microcrack formation and stabilizing the lattice structure. The Co^{3+}/Co^{4+} redox couple in $NaCoO_2$ is very reversible and structurally stable, providing smooth phase transitions and good cycling properties. In contrast, Fe^{3+}/Fe^{4+} tends to induce irreversible transitions and poor air/moisture stability, while Mn^{3+}/Mn^{4+} adds Jahn-Teller distortions that induce lattice strain and capacity loss. But by co-substitution of Fe and Mn with Co, these disadvantages are partially alleviated: Co^{3+} stabilizes the lattice, Fe^{3+} reduces cost, and Mn^{3+}/Mn^{4+} adds capacity. So, mixed valence Fe/Mn adds more complexity, but with Co, it finds the cost balance, stability, and performance balance.

5.6 Conclusions

This chapter provided an analysis of $Na_xCo_{0.5}Fe_{0.25}Mn_{0.25}O_2$ cathode synthesized via the solid-state method and highlighted its promising characteristics for SIBs. The detailed physicochemical characterization confirmed a well-ordered crystallinity with a multiphase crystal symmetry, which is beneficial for efficient Na^+-ion intercalation/deintercalation. The XRD, FESEM, and TEM analyses collectively demonstrated a uniform smooth morphology and confirmed the material multiphase and structural integrity. $Na_xCo_{0.5}Fe_{0.25}Mn_{0.25}O_2$ demonstrated excellent rate capability and stability across a range of C-rates, with a high discharge capacity of 94.22 mAh/g at 0.05 C and consistent performance at higher C-rates. The good Coulombic efficiency and high energy densities suggested its potential for lightweight, high-energy-density batteries. The stability of the material over

extended cycling, with significant retention of its capacity, underscored the effectiveness of using TM co-substitution to improve structural stability and electrochemical performance. These findings supported the suitability of $Na_xCo_{0.5}Fe_{0.25}Mn_{0.25}O_2$ cathode material for advanced SIB applications.

5.7 References

[1] Y. Liu, D. Wang, H. Li, P. Li, Y. Sun, Y. Liu, Y. Liu, B. Zhong, Z. Wu, X. Guo, Research progress in O3-type phase Fe/Mn/Cu-based layered cathode materials for sodium ion batteries, J. Mater. Chem. A. 10 (2022) 3869–3888. https://doi.org/10.1039/d1ta10329f.

[2] L. Rakočević, S. Štrbac, J. Potočnik, M. Popović, D. Jugović, I.S. Simatović, The NaxMnO2 materials prepared by a glycine-nitrate method as advanced cathode materials for aqueous sodium-ion rechargeable batteries, Ceram. Int. 47 (2021) 4595–4603. https://doi.org/10.1016/j.ceramint.2020.10.025.

[3] L. Durai, A. Gopalakrishnan, S. Badhulika, One-step solid-state reaction synthesis of β-NaFeO2 nanopebble as high capacity cathode material for sodium ion batteries, Mater. Lett. 270 (2020) 127739. https://doi.org/10.1016/j.matlet.2020.127739.

[4] V.R.R. Boddu, D. Puthusseri, P.M. Shirage, P. Mathur, V.G. Pol, Layered NaxCoO2-based cathodes for advanced Na-ion batteries: review on challenges and advancements, Ionics. 27 (2021) 4549–4572. https://doi.org/10.1007/s11581-021-04265-w.

[5] M. Palanisamy, V.R. Reddy Boddu, P.M. Shirage, V.G. Pol, Discharge State of Layered P2-Type Cathode Reveals Unsafe than Charge Condition in Thermal Runaway Event for Sodium-Ion Batteries, ACS Appl. Mater. Interfaces. 13 (2021) 31594–31604. https://doi.org/10.1021/acsami.1c04482.

[6] Y.E. Zhu, X. Qi, X. Chen, X. Zhou, X. Zhang, J. Wei, Y. Hu, Z. Zhou, A P2-Na0.67Co0.5Mn0.5O2 cathode material with excellent rate capability and cycling stability for sodium ion batteries, J. Mater.

Chem. A. 4 (2016) 11103–11109. https://doi.org/10.1039/c6ta02845d.

[7] L. Gao, S. Chen, H. Hu, H. Cheng, L. Zhang, X. Yang, Hierarchical NaxCoO2 microspheres with low surface area toward high performance sodium ion batteries, Mater. Lett. 260 (2020) 126965. https://doi.org/10.1016/j.matlet.2019.126965.

[8] B. Peng, Z. Sun, S. Jiao, J. Li, G. Wang, Y. Li, X. Jin, X. Wang, J. Li, G. Zhang, Facile self-templated synthesis of P2-type Na0.7CoO2 microsheets as a long-term cathode for high-energy sodium-ion batteries, J. Mater. Chem. A. 7 (2019) 13922–13927. https://doi.org/10.1039/c9ta02966d.

[9] Yongjin Fang, X.-Y. Yu, X.W. Lou, A Practical High-Energy Cathode for Sodium-Ion Batteries Based on Uniform P2-Na0.7CoO2 Microspheres, Angew.Chem. Int. Ed. 56 (2017) 5801 –5805. https://doi.org/10. 1002/anie.201702024.

[10] V.R. Reddy Boddu, M. Palanisamy, L. Sinha, S.C. Yadav, V.G. Pol, P.M. Shirage, Hysteresis abated P2-type NaCoO2 cathode reveals highly reversible multiple phase transitions for high-rate sodium-ion batteries, Sustain. Energy Fuels. 5 (2021) 3219–3228. https://doi.org/10.1039/d1se00490e.

[11] K. Shiprath, H. Manjunatha, R. Venkata Nadh, T. Anil Babu, S. Ramesh, K. Chandra Babu Naidu, M. Ramesha, Synthesis and Electrochemical Characterization of NaCoO2 as Cathode Material in 2M NaOH Aqueous Electrolyte, ChemistrySelect. 6 (2021) 1874–1881. https://doi.org/10.1002/slct.202100294.

[12] J. Billaud, R.J. Clement, A.R. Armstrong, J. Canales-Vazquez, P. Rozier, C.P. Grey, P.G. Bruce, β-NaMnO2 : A High-Performance Cathode for Sodium-Ion Batteries., J. Am. Chem. Soc. 136 (2014) 17243−17248. https://doi.org/10.1002/chin.201514014.

[13] N. Ortiz-Vitoriano, N.E. Drewett, E. Gonzalo, T. Rojo, High performance manganese-based layered oxide cathodes: Overcoming

the challenges of sodium ion batteries, Energy Environ. Sci. 10 (2017) 1051–1074. https://doi.org/10.1039/c7ee00566k.

[14] X. He, J. Wang, B. Qiu, E. Paillard, C. Ma, X. Cao, H. Liu, M.C. Stan, H. Liu, T. Gallash, Y.S. Meng, J. Li, Durable high-rate capability Na0.44MnO2 cathode material for sodium-ion batteries, Nano Energy. 27 (2016) 602–610. https://doi.org/10.1016/j.nanoen.2016.07.021.

[15] Y. Li, Y. Gao, X. Wang, X. Shen, Q. Kong, R. Yu, G. Lu, Z. Wang, L. Chen, Iron migration and oxygen oxidation during sodium extraction from NaFeO2, Nano Energy. 47 (2018) 519–526. https://doi.org/10.1016/j.nanoen.2018.03.007.

[16] P.F. Wang, Y. You, Y.X. Yin, Y.G. Guo, Layered Oxide Cathodes for Sodium-Ion Batteries: Phase Transition, Air Stability, and Performance, Adv. Energy Mater. 8 (2017) 1–23. https://doi.org/10.1002/aenm.201701912.

[17] N. Yabuuchi, M. Kajiyama, J. Iwatate, H. Nishikawa, S. Hitomi, R. Okuyama, R. Usui, Y. Yamada, S. Komaba, P2-type Nax [Fe1/2 Mn1/2[O2 made from earth-abundant elements for rechargeable NaÂ batteries, Nat. Mater. 11 (2012) 512–517. https://doi.org/10.1038/nmat3309.

[18] I. Hasa, D. Buchholz, S. Passerini, B. Scrosati, J. Hassoun, High Performance Na0.5[Ni0.23Fe0.13Mn0.63]O2 Cathode for Sodium-Ion Batteries, Adv. Energy Mater. 4 (2014) 1–7. https://doi.org/10.1002/aenm.201400083.

[19] D. Yuan, X. Hu, J. Qian, F. Pei, F. Wu, R. Mao, X. Ai, H. Yang, Y. Cao, P2-type Na0.67Mn0.65Fe0.2Ni0.15O2 Cathode Material with High-capacity for Sodium-ion Battery, Electrochim. Acta. 116 (2014) 300–305.

[20] X. Wang, M. Tamaru, M. Okubo, A. Yamada, Electrode Properties of P2−Na2/3MnyCo1−yO2 as Cathode Materials for Sodium-Ion Batteries, J. Phys. Chem. C. 117 (2013) 15545−15551.

https://doi.org/10.1149/ma2010-03/1/550.

[21] I.H. Jo, H.S. Ryu, D.G. Gu, J.S. Park, I.S. Ahn, H.J. Ahn, T.H. Nam, K.W. Kim, The effect of electrolyte on the electrochemical properties of Na/α-NaMnO2 batteries, Mater. Res. Bull. 58 (2014) 74–77. https://doi.org/10.1016/j.materresbull.2014.02.024.

[22] X. Ma, H. Chen, G. Ceder, Electrochemical Properties of Monoclinic NaMnO2, J. Electrochem. Soc. 158 (2011) A1307. https://doi.org/10.1149/2.035112jes.

[23] A. Bhide, K. Hariharan, Physicochemical properties of NaxCoO2 as a cathode for solid state sodium battery, Solid State Ion. 192 (2011) 360–363. https://doi.org/10.1016/j.ssi.2010.04.022.

[24] B.V. Rami Reddy, R. Ravikumar, C. Nithya, S. Gopukumar, High performance NaxCoO2 as a cathode material for rechargeable sodium batteries, J. Mater. Chem. A. 3 (2015) 18059–18063. https://doi.org/10.1039/c5ta03173g.

[25] J. Pati, R.S. Dhaka, Mixed polyanionic NaFe1.6V0.4(PO4)(SO4)2@CNT cathode for sodium-ion batteries: Electrochemical diffusion kinetics and distribution ofrelaxation time analysis at different temperatures, J. Power Sources. 609 (2024) 234646. https://doi.org/10.1016/j.jpowsour.2024.234646.

[26] M.M. Faras, S.S. Patil, P.S. Patil, A.P. Torane, Unleashing the Potential of Binder-Free Hydrothermally Synthesized Marigold-Like ZnCo2O4 for Supercapacitors, J. Energy Storage. 74 (2023) 109490. https://doi.org/10.1016/j.est.2023.109490.

[27] A. Maradesa, B. Py, T.H. Wan, M.B. Effat, F. Ciucci, Selecting the Regularization Parameter in the Distribution of Relaxation Times, J. Electrochem. Soc. 170 (2023) 030502. https://doi.org/10.1149/1945-7111/acbca4.

[28] T.H. Wan, M. Saccoccio, C. Chen, F. Ciucci, Influence of the Discretization Methods on the Distribution of Relaxation Times Deconvolution: Implementing Radial Basis Functions with

DRTtools, Electrochim. Acta. 184 (2015) 483–499. https://doi.org/10.1016/j.electacta.2015.09.097.

[29] L. Gao, S. Chen, L. Zhang, X. Yang, High Areal Capacity Na0.67CoO2 Bundle Array Cathode Tailored for High-Performance Sodium-Ion Batteries, ChemElectroChem. 6 (2019) 947. https://doi.org/10.1002/celc.201900031.

[30] A.C. Nwanya, M.M. Ndipingwi, F.I. Ezema, E.I. Iwuoha, M. Maaza, Bio-synthesized P2-Na0.57CoO2 nanoparticles as cathode for aqueous sodium ion battery, J. Electroanal. Chem. 878 (2020) 114600. https://doi.org/10.1016/j.jelechem.2020.114600.

[31] X. Tan, J. Zeng, L. Sun, C. Peng, Z. Li, S. Zou, Q. Shi, H. Wang, J. Liu, Current issues and corresponding optimizing strategies of layered oxide cathodes for sodium-ion batteries Xiang, InfoMat. (2024) e12636. https://doi.org/10.1002/inf2.12636.

[32] M. D'Arienzo, R. Ruffo, R. Scotti, F. Morazzoni, C.M. Mari, S. Polizzi, Layered Na 0.71CoO2: a powerful candidate for viable and high performance Na-batteries, Phys. Chem. Chem. Phys. 14 (2012) 5945–5952. https://doi.org/10.1039/c2cp40699c.

[33] J.J. Ding, Y.N. Zhou, Q. Sun, X.Q. Yu, X.Q. Yang, Z.W. Fu, Electrochemical properties of P2-phase Na0.74CoO2 compounds as cathode material for rechargeable sodium-ion batteries, Electrochim. Acta. 87 (2013) 388–393. https://doi.org/10.1016/j.electacta.2012.09.058.

[34] X. Wang, G. Liu, T. Iwao, M. Okubo, A. Yamada, Role of Ligand-to-Metal Charge Transfer in O3-Type NaFeO2−NaNiO2 Solid Solution for Enhanced Electrochemical Properties, J. Phys. Chem. C. 118 (2014) 2970−2976. https://doi.org/dx.doi.org/10.1021/jp411382r.

[35] N. Yabuuchi, M. Yano, H. Yoshida, S. Kuze, Synthesis and Electrode Performance of O3-Type NaFeO2-NaNi1/2Mn1/2O2 Solid Solution for Rechargeable Sodium Batteries, J. Electrochem.

Soc. 160 (2013) 3131–3137. https://doi.org/10.1149/2.018305jes.

[36] J. Zhao, L. Zhao, N. Dimov, S. Okada, T. Nishida, Electrochemical and Thermal Properties of α-NaFeO2 Cathode for Na-Ion Batteries, J. Electrochem. Sac. 160 (2013) 3077–3081. https://doi.org/10.1149/2.007305jes.

[37] J. Jayachitra, J.R. Joshua, A. Balamurugan, N. Sivakumar, V. Sharmila, S. Shanavas, M. Abu, M. Waqas, A. Baqais, High electrode performance of hydrothermally developed activated C coated O3–NaFeO2 electrode for Na-ion batteries applications, Ceram. Int. 49 (2023) 48–56. https://doi.org/10.1016/j.ceramint.2022.07.110.

[38] D. Nayak, P. Kumar, S. Ghosh, V. Adyam, Aluminium substituted β–type NaMn1-xAlxO2: A stable and enhanced electrochemical kinetic sodium-ion battery cathode Debasis, J. Power Sources. 438 (2019) 227025. https://doi.org/10.1016/j.jpowsour.2019.227025.

[39] M.A. Khan, D. Han, G. Lee, Y. Il Kim, Y.M. Kang, P2/O3 phase-integrated Na0.7MnO2 cathode materials for sodium-ion rechargeable batteries, J. Alloys Compd. 771 (2019) 987–993. https://doi.org/10.1016/j.jallcom.2018.09.033.

[40] C. Peng, X. Xu, F. Li, L. Xi, J. Zeng, X. Song, X. Wan, J. Zhao, J. Liu, Recent Progress of Promising Cathode Candidates for Sodium-Ion Batteries: Current Issues, Strategy, Challenge, and Prospects, Small Struct. 4 (2023) 2300150. https://doi.org/10.1002/sstr.202300150.

[41] H. Wang, L. Li, W. Han, H. Guo, I.A. Bobrikov, Y. Chai, X. Liu, Tuning the Oxygen Anionic Redox Reversibility in Na0.67Mn0.8Fe0.1Co0.1O2 Through Sn Doping, Renewables. 1 (2023) 253–265. https://doi.org/10.31635/renewables.023.202200013.

[42] Z. Liu, C. Peng, J. Wu, T. Yang, J. Zeng, F. Li, Regulating electron distribution of P2-type layered oxide cathodes for practical sodium-

ion batteries, Materials Today. 68 (2023) 22–33. https://doi.org/10.1016/j.mattod.2023.06.021.

[43] J. Park, G. Park, H.H. Kwak, S. Hong, J. Lee, Enhanced Rate Capability and Cycle Performance of Titanium- Batteries, ACS Omega. 3 (2018) 361−368. https://doi.org/10.1021/acsomega.7b01481.

[44] Z. Liu, J. Shen, S. Feng, Y. Huang, D. Wu, F. Li, Y. Zhu, M. Gu, Q. Liu, JunLiu, M. Zhu, Angew Chem Int Ed - 2021 - Liu - Ultralow Volume Change of P2-Type Layered Oxide Cathode for Na-Ion Batteries with.pdf, Angew.Chem. Int.Ed. 60 (2021) 20960– 20969. https://doi.org/10.1002/anie.202108109.

CHAPTER 6

3D Channel-based $Na_{1.35}CrO_4$ and Tunnel-Structured $Na_4Mn_{7.2}Cr_{1.8}O_{18}$ Metal Oxide Electrodes for Sodium-Ion Batteries

In this chapter, we have reduced the Co content by 100% with its complete substitution by either Cr or the combination of Cr and Mn. This chapter is composed of two parts: Part A for $Na_{1.35}CrO_4$ material, and Part B for $Na_4Mn_{7.2}Cr_{1.8}O_{18}$ cathode material for SIBs.

Chapter 6 (Part A)

Part A of this chapter explores $Na_{1.35}CrO_4$ as an active electrode for SIBs. $Na_{1.35}CrO_4$ was successfully synthesized using a citric acid-assisted sol-gel method, and its physicochemical and electrochemical properties were explored for SIBs. Extensive physicochemical analyses confirmed the phase purity, high crystallinity, and orthorhombic crystal symmetry of $Na_{1.35}CrO_4$, having well-controlled elemental stoichiometry and a smooth surface morphology, with nanoparticles of a particle size of 42.87 nm. $Na_{1.35}CrO_4$ coexisted in Cr^{6+} and Cr^{7+} oxidation states, with Cr^{6+} as the dominant one. CV revealed V_{OC} of ~1.842 V and consistent redox peaks within 0.0-3.0 V, representing its structural and phase stability. Power-law analysis showed battery-type features and diffusion-controlled charge transfer. EIS analysis revealed good electrolyte compatibility and charge transfer kinetics. It also exhibited a low double-layer capacitance, representing its suitability for high-energy-density applications. These investigations revealed that $Na_{1.35}CrO_4$ is a promising electrode for SIBs.

6.1 Introduction for $Na_{1.35}CrO_4$ Electrode

For the past few decades, several researchers have explored layered sodium-based intercalation compounds as low-cost and large-scale energy storage solutions. These compounds have received a great deal of attention for rechargeable SIBs [1–3]. In 1980, Hagenmuller *et al.* [4] revealed that $NaCrO_2$ could be used as a sodium-ion (Na^+ ion) extraction/insertion electrode. Later, Komaba *et al.* revisited this material and discovered that owing to the larger interplanar spacing of $NaCrO_2$ than $LiCrO_2$, Na^+ ions could be easily inserted into/extracted from the host structure [5,6]. Despite having a theoretical capacity of about 250 mAh/g, the practical achievable reversible capacity of $Na_{1-x}CrO_2$ (where $0 \leq x \geq 0.5$) was around 110 mAh/g with a 3V voltage window [5,6]. According to Dahn *et al.,* desodiated $Na_{0.5}CrO_2$ possesses remarkable thermal stability with a non-aqueous electrolyte system [7]. A 2D carbon-coated $NaCrO_2$ synthesized via a citric acid-assisted method showed slightly improved cycling stability compared to the pristine one. However, the rate capability of the material was not satisfactory. Although $NaCrO_2$, as a cathode for SIBs, delivers an initial discharge capacity of 100-110 mAh/g due to the Cr^{3+}/Cr^{4+} redox couple, it shows disadvantages of limited cycle stability and fast capacity fading. A thorough review of the literature on $NaCrO_2$ indicates that it has the potential to be a cathode material for SIBs [5–14].

However, the advancement of anode materials for SIBs has not kept pace with the progress seen in LIBs. The primary reason for this lag is the larger size of the Na^+ ion compared to that of the Li^+ ion. The radius of Na^+ ions is about 1.02 Å compared to the Li^+ ions' radius of 0.76 Å [15]. Due to this larger ionic radius, Na^+ ions require a higher interplanar distance for easy intercalation and deintercalation. As a result, most anode materials do not show Na^+ ion insertion and extraction properties, although they are suitable for Li^+ ion intercalation/deintercalation. Currently, graphite is widely used as an anode material for developing commercially available LIBs due to its high theoretical capacity of >360 mAh/g and its stable

structure [16,17]. However, the small interlayer spacing of graphite does not allow Na^+ ions to be easily intercalated and deintercalated in SIBs [18]. The larger Na^+ ion radius in SIBs results in sluggish kinetics that lead to structural degradation and poorer electrochemical performance than LIBs [19]. HC is a promising anode material for SIBs and demonstrates a high specific capacity of about 240 mAh/g at a current density of 0.5 A/g [16,20]. The other anode materials for SIBs are graphene and reduced graphene oxide (r-GO), showing a high specific capacity of ~160 and ~272 mAh/g, respectively [21,22]. However, the practical use of these anode materials in SIBs is limited due to low operating voltage and high-capacity fading. Although the low operating voltage of these anode materials could assist in obtaining a high energy density, it results in high dendrite formation, limited cycle life performance, and safety risks. Various anode materials, such as metal oxides, nitrides, phosphides, and sulfides, working on the principle of conversion reactions, are explored for SIBs to tackle these issues. These anode materials offer high capacity but cause structural degradation. Hence, anodes showing intercalation/deintercalation of Na^+ is preferred to minimize the volume changes and reduce the lattice strain.

Several metal oxide anode materials with Chromium (Cr) have been investigated for LIBs. Among them, $LiCrTiO_4$ and Cr_2O_3 are two anode materials with low cost and stable electrochemical properties due to the Cr^{3+}/Cr^{2+} redox couple. $LiCrTiO_4$ has notable ionic conductivity of 10^{-9} cm^2/s and a stable voltage plateau at 1.5 V [23,24]. However, there is no significant work has been performed on the TM-based anode for SIBs. K. Y. Chungs's group [25] investigated the electrochemical performances of Na_2CrO_4/C composite as an anode material for SIBs. This composite material exhibited a high capacity of 228 mAh/g at a current density of 0.1C and can retain ~72.8% of its initial capacity by the end of the 100^{th} cycle. At a higher current rate of 2.0C, it showed a discharge capacity of ~71mAh/g [25]. However, this composite material shows a critical issue of a transformation from a crystalline to an amorphous phase [25]. This phase

transition of the metal oxide anode material for SIBs could be attributed to the high-volume expansion, poor electronic conductivity, and the formation of undesirable byproducts during the cycling process. These issues must be solved by adopting innovative strategies of control over the particle size to form nanoparticles and applying defect engineering to improve the electronic conductivity and maintain structural stability [26]. The partial sodium deficiency as defect engineering and reducing the particle size to the nanoscale are known for their cost-effectiveness and are frequently used to obtain structural retention and improve the electronic conductivity of the material. As a result, TM oxides with partial sodium deficiency have emerged as a promising solution to mitigate capacity degradation during long-term cycling. Further, by reducing the grain size to the nanoscale, the Na^+ ion diffusion path is significantly shortened, facilitating faster sodium deintercalation/intercalation and improving the overall performance.

Chromium-based oxides are attractive for SIBs due to their multiple accessible oxidation states ($Cr^{3+}/Cr^{4+}/Cr^{6+}/Cr^{7+}$), which allow multi-electron redox reactions. The higher Cr oxidation states can support increased voltage profiles and enhanced energy density. Additionally, nanosized Cr-based oxides have exhibited good structural stability and good Na^+ diffusion, and hence they are good substitutes for Co-based layered oxides. In this chapter, we have adopted a sol-gel approach to synthesize sodium-deficient $Na_{1.35}CrO_4$ by successfully reducing the particle size to the nanoscale. This technique significantly reduced the crystallite and grain sizes of $Na_{1.35}CrO_4$ compared to the unmodified Na_2CrO_4. Physicochemical investigations revealed phase purity, high crystallinity, and orthorhombic symmetry of $Na_{1.35}CrO_4$ with the desired stoichiometry and uniform element distribution. The nanoparticle morphology of $Na_{1.35}CrO_4$ provided a high surface electrode-electrolyte contact area that enhanced the material's charge kinetics and structural stability. It exhibited both Cr^{6+} and Cr^{7+} oxidation states, with Cr^{6+} as the dominant one. The electrochemical feasibility study of $Na_{1.35}CrO_4$ as an active electrode in SIBs was performed

through Na-half cells. CV analysis showed stable redox peaks in a voltage window of 0.01-3.0 V, representing high structural and phase stability and diffusion-controlled charge kinetics. EIS represents its excellent charge transfer kinetics and low double-layer capacitance. These findings highlight the potential of $Na_{1.35}CrO_4$ as an active electrode material for SIBs.

6.2 Experimental Section for $Na_{1.35}CrO_4$ Electrode

The experimental details, such as the synthesis methodology, physicochemical characterization techniques, electrode preparation, cell fabrication, and electrochemical property analysis techniques for $Na_{1.35}CrO_4$ electrode in SIBs, are given in Chapter 2 of this thesis.

6.3 Results and Discussions for $Na_{1.35}CrO_4$ Electrode

6.3.1 Physicochemical Analyses for $Na_{1.35}CrO_4$ Electrode

6.3.1.1 Thermal Behavior Analysis of $Na_{1.35}CrO_4$

The thermal behavior, such as thermal stability, precursor decomposition, and weight retention as a function of increasing temperature for $Na_{1.35}CrO_4$ compound, was analyzed with the help of TGA, DTG, and DSC, as shown in **Figures 6.1 (*b-c*)**. These heat treatment analyses were performed in an N_2 environment in a wide temperature range from 30ºC to 1000ºC. The two major stages of weight loss are observed in the TGA curve (**Figure 6.1 (*b*), green spectrum**). The 1st stage of about 6.4% weight loss of the initial weight is due to the corresponding evaporation of the physically adsorbed and trapped water within 50-100ºC. The 2nd highest weight loss of approximately 15.4% occurs between 300-600ºC and is attributed to decomposition and gas evolution processes [27]. After 600ºC, no significant mass reduction occurred, signifying a thermally stable phase formation beyond this temperature. By the completion of 1000ºC, $Na_{1.35}CrO_4$ material retains about 76% of its initial weight.

The DTG analysis representing the mass loss rate as a function of the temperature rise is shown in **Figure 6.1 (*b*)** (red-colored spectrum) to

support the above TGA analysis. Two broad peaks in the DTG spectrum align well with the mass loss stages observed in TGA. This DTG analysis further provides a deeper understanding of the evaporation of trapped water and the thermal decomposition of nitrate precursors. The two most intense peaks, at ~66.3ºC and ~332.3ºC, represent the highest water evaporation and precursor decomposition rate. Further, no significant peaks in the DTG curve are observed after 600ºC. It shows a nearly horizontal line, indicating the high thermal stability of the mass retention of the material after this temperature.

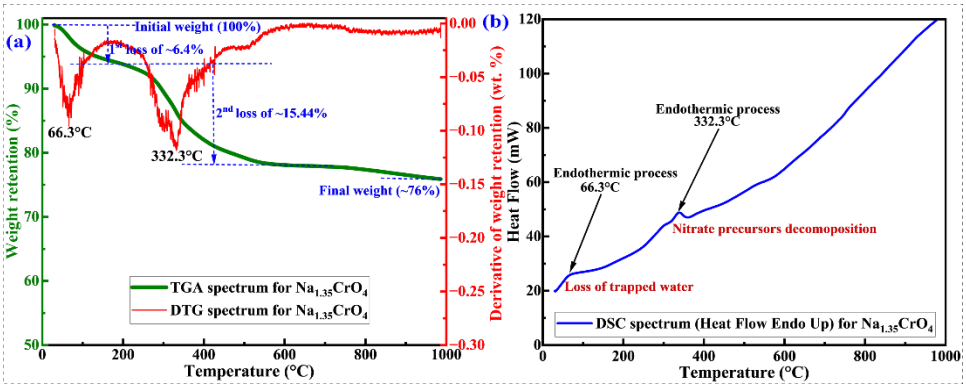

Figure 6.1 (a) TGA and DTG; and **(b)** DSC spectra of $Na_{1.35}CrO_4$ material.

The DSC spectrum in **Figure 6.1 (*c*)** reveals that the trapped water evaporation and the gas release processes are endothermic, with the peaks occurring at about 66ºC and 332ºC, respectively, confirming the thermal decomposition and volatilization of unwanted gases. TGA, DTG, and DSC analyses confirmed that the material could be calcinated beyond 600ºC to obtain a stable phase material. Following the above discussion, we selected 800ºC as the calcination temperature for synthesizing $Na_{1.35}CrO_4$ with high crystallinity and phase purity.

6.3.1.2 Phase Purity & Lattice Structure of $Na_{1.35}CrO_4$

Crystallographic information of $Na_{1.35}CrO_4$, such as phase purity, crystal structure, symmetry, and lattice parameters, is analyzed through XRD. **Figure 6.2 (*a*)** represents the experimentally obtained XRD profile of $Na_{1.35}CrO_4$ before annealing (green color pattern) and after calcination

(blue color). The XRD pattern of $Na_{1.35}CrO_4$ is further compared with the reference pristine Na_2CrO_4 (violet color). The observed peaks of our synthesized $Na_{1.35}CrO_4$ material are indexed with the orthorhombic symmetry-based pristine Na_2CrO_4 having the space group of *Cmcm,* as shown in **Figure 6.2 (*a*)**.[25] Compared to $Na_{1.35}CrO_4$ before annealing, $Na_{1.35}CrO_4$ material after calcination shows highly intense peaks at the same 2θ values as those of the reference Na_2CrO_4 material. The consistent appearance of peak positions is due to the final formation of the orthorhombic lattice-based structure of $Na_{1.35}CrO_4$ due to nucleation. $Na_{1.35}CrO_4$ shows clear and intense peaks, which are situated as those of the corresponding reference material. It represents the high crystallinity and the phase-pure synthesis of $Na_{1.35}CrO_4$ material. In addition to all the desired peaks of $Na_{1.35}CrO_4$, two additional peaks (represented by "***" in the XRD pattern) are also observed as a secondary phase. The occurrence of additional peaks could be attributed to the presence of a local deficiency of Na atoms in $Na_{1.35}CrO_4$ in comparison to Na_2CrO_4, resulting in a small amount of $Na_2Cr_4O_{13}$ (*i.e.,* $Na_{0.5}CrO_{3.25}$) as a secondary phase.

Table 6.1: Lattice parameter of $Na_{1.35}CrO_4$ from refinement.

Lattice parameters	**Units**	**Na_2CrO_4 From literature**	**$Na_{1.35}CrO_4$ (This work)**
a	Å	5.8612 [25]	5.8609
b		9.2847 [25]	9.2569
c		7.1429 [25]	7.1439
α	degree	90 [25]	90
β		90 [25]	90
γ		90 [25]	90
Unit cell volume	$Å^3$	388.708 [25]	387.585
Density	g/cm^3	-	2.985
Symmetry, space group	-	Orthorhombic [25] *Cmcm*, 63	Orthorhombic, *Cmcm*, 63

An extended XRD analysis is further performed to refine the material's structure and obtain crystallographic information. This

refinement process was carried out with the reference Na_2CrO_4 material through FullProf software, where we used the pseudo-Voigt profile shaping function and linear interpolation background correction, as represented in **Figure 6.2 (*b*)**. In the refinement, the experimentally obtained XRD peaks of $Na_{1.35}CrO_4$ nicely align and fit with Na_2CrO_4 as the reference material. We also included the secondary $Na_2Cr_4O_{18}$ during the refinement process as the secondary phase and performed the two-phase refinement process. With a good fit of the observed and calculated XRD peaks, the chi-square value reduced to 4.87, indicating the quality and clarity of the structural refinement process. Through this refinement, we calculated that $Na_{1.35}CrO_4$ has unit cell parameters of approximately a=5.861 Å, b=9.257 Å, c=7.144 Å, $\alpha=\beta=\gamma=90^{o}$, and a unit cell volume of 387.585 $Å^3$, resulting in the formation of an orthorhombic crystal structure with a lattice space group symmetry of *Cmcm* (space group number of 63). All these calculated lattice parameters for $Na_{1.35}CrO_4$ are summarized in **Table 6.1** and compared with the reference Na_2CrO_4 material.

Crystallite size for $Na_{1.35}CrO_4$ was calculated through the Debye-Scherrer formula by considering the highest intensity (130) plane [28]. The calculated crystallite size of $Na_{1.35}CrO_4$ was 54.56 nm. The crystallite size of $Na_{1.35}CrO_4$ material is smaller compared to the pristine Na_2CrO_4 and Na_2CrO_4/C composite, having the crystallite sizes of 198.9 and 72.2 nm, respectively, as studied by Ghulam [25]. The observation of reduced crystallite size could be attributed to the high FWHM, which can be attributed to the sol-gel-based synthesis. This reduced crystallite size of $Na_{1.35}CrO_4$ will enhance the electrochemical properties for energy storage by providing more interaction between the ion-conducting electrolyte and the active material surface [25].

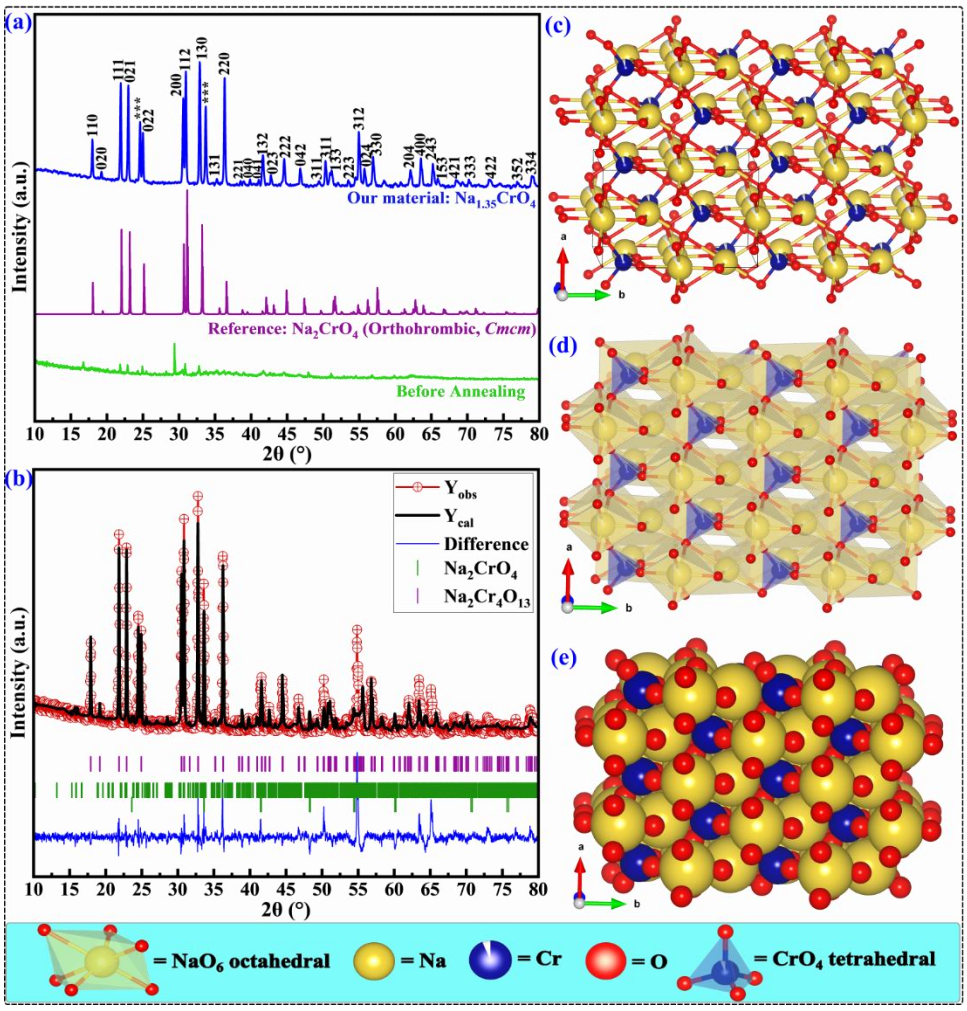

Figure 6.2 (a) XRD pattern of $Na_{1.35}CrO_4$ and reference Na_2CrO_4; **(b)** structural refinement; **(c-e)** Crystal structures of $Na_{1.35}CrO_4$.

The ball-and-stick, polyhedral, and space-filling views of the crystal structure of $Na_{1.35}CrO_4$ material obtained through the crystallographic information from the structural refinement are presented in **Figures 6.2 (*c*), 6.2 (*d*), and 6.2 (*e*)**, respectively. These crystal structures comprise tetrahedral chromium-oxygen (CrO_4) and sodium-oxygen (NaO_6) octahedral units. The sodium atoms are located in a zigzag channel between alternate CrO_4 units. With this structural arrangement, the crystal forms a eD structure suitable for easily migrating sodium atoms between the CrO_4 units. **Table 6.2** summarizes the atomic details, including atom types, atomic reciprocal coordinates, occupancies, site positions, and multiplicity values of the constituent elements in $Na_{1.35}CrO_4$.

Table 6.2: Atomic details from structural refinement of $Na_{1.35}CrO_4$.

Atom	Atom type	Reciprocal coordinates			Occupancy	Sites	Multiplicity
		x	*y*	*z*			
Na0	Na	0.000	0.193	0.750	1.000	4c	4
Na1	Na	0.000	0.500	0.000	0.886	4b	4
Cr2	Cr	0.000	0.151	0.250	0.941	4c	4
O3	O	0.000	0.250	0.062	1.215	8f	8
O4	O	0.231	0.0397	0.250	1.345	8g	8

6.3.1.3 Particle Morphology and Size Analyses of $Na_{1.35}CrO_4$

The FESEM is employed to observe and analyze the smoothness and morphology of the particle surface, such as the shape and size of the $Na_{1.35}CrO_4$ material. The nominal atomic percentage of elements, chemical stoichiometry, and composition in the synthesized $Na_{1.35}CrO_4$ material are studied through EDS. **Figures 6.3 (*a-c*)** show the FESEM images of particle size and surface morphologies of the synthesized $Na_{1.35}CrO_4$ at magnifications of 150,000×, 60,000×, and 15,000× of the original size, respectively. The particles are on the nanometer scale and have a highly smooth surface. The particles are mostly of disc-like structure and are individually detectable (**Figures 6.3 (*a-b*)**). The particles are arranged in linear patterns, forming a highly porous (**Figure 6.3 (*c*)**) structure of $Na_{1.35}CrO_4$ material. **Figure 6.3 (*d*)** represents the particle size distribution profile for $Na_{1.35}CrO_4$. The particle size varies in the range of 20 nm to 75 nm, with an average particle size of 42.87 nm. The particle size of the synthesized $Na_{1.35}CrO_4$ is smaller than the particle size of pure Na_2CrO_4 material, having a particle size range of 25-84 nm.[25] The formation of nanometer-size-based particles of $Na_{1.35}CrO_4$ will assist in providing a high surface-to-volume ratio and an increased active contact of the electrode with the electrolytes, which will enhance the electrochemical performance of $Na_{1.35}CrO_4$ as an electrode for SIBs.

Figure 6.3 (*e*) represents the EDS profile of $Na_{1.35}CrO_4$ and confirms the presence of the constituent elements Na, Cr, and O, which are subsequently used for the analysis of nominal atomic percentages of elements and the stoichiometric composition in the synthesized $Na_{1.35}CrO_4$.

The atomic percentages of Na, Cr, and O in $Na_{1.35}CrO_4$ through EDS are observed to be 30.3, 12.9, and 56.8%, respectively, yielding a stoichiometry of Na:Cr:O = 2.35:1:4.4, corresponding to a nominal $Na_{2.35}CrO_{4.4}$. The inset in **Figure 6.3 (*e*)** represents the selected portion of $Na_{1.35}CrO_4$ used for EDS spectrum. The uniformity of element distribution over the material's surface was analyzed through color mapping (**Figure 6.3 (*f*)**). This color mapping facility was integrated with FESEM technique and detected the *Kα* electron radiations of the respective elements. The color mapping of a particular portion of the material showed that the Na, Cr, and O atoms are evenly distributed over the $Na_{1.35}CrO_4$ surface. Furthermore, **Figures 6.3 (*g-i*)** demonstrate the color mapping of individual elements in the magnified portion of the material, supporting the uniform distribution of constituent elements in $Na_{1.35}CrO_4$. This even distribution of elements is crucial for the material's formation phase purity in a nanoscale particle size range.

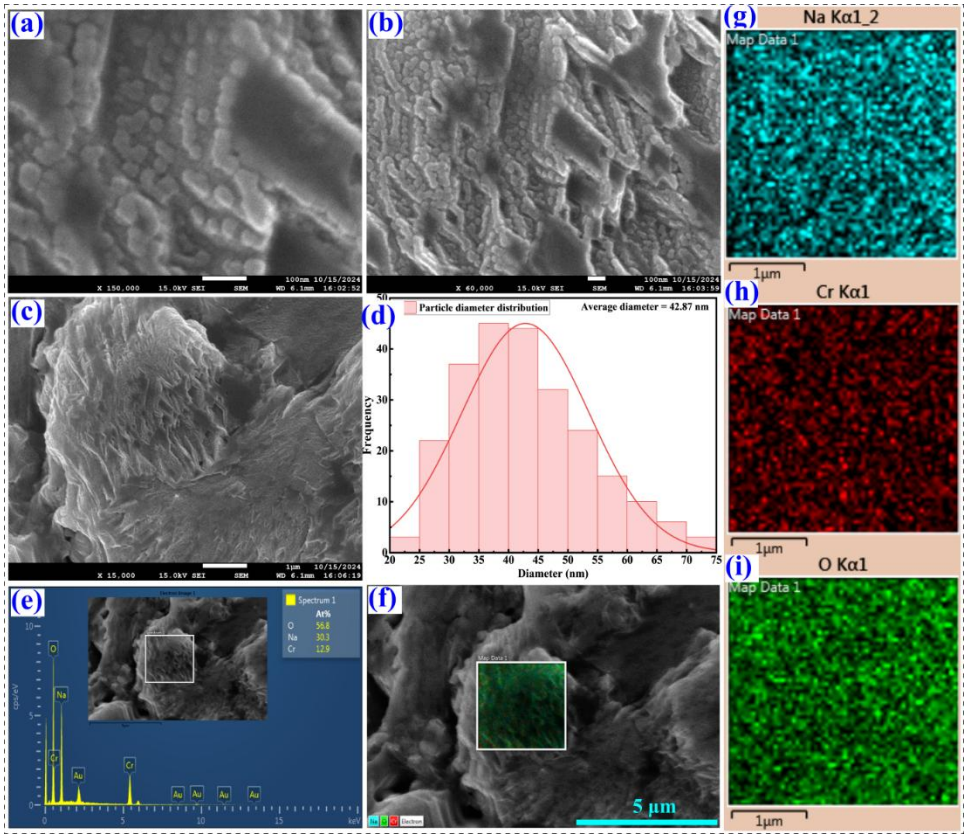

Figure 6.3 (a-c) FESEM images; (d) Particle size distribution profile; **(e)** EDS profile; and **(f-i)** Color mapping of $Na_{1.35}CrO_4$.

6.3.1.4 Quantitative Elemental Analysis of $Na_{1.35}CrO_4$

Although a nominal composition of the material is calculated from the above EDS analysis, it is not a quantitative analysis technique. To obtain the exact composition and an accurate stoichiometry of the synthesized material, ICP-OES is conducted as a quantitative elemental analysis technique. ICP-OES is performed using an Agilent SPS 4 autosampler by considering the wavelengths of metal elements Na and Cr as 589.592 and 267.716 nm, respectively. The analyte calibration process was performed in three standard solutions of 5, 10, and 20 ppm concentrations. The quantitative results observed from the ICP-OES analysis are given in **Table 6.3**, indicating the formation of the material with the required stoichiometry and an empirical formula of $Na_{1.35}CrO_4$.

Table 6.3: Quantitative results from ICP-OES interpretation.

Parameters	Values
Concentration of Na	1.87 ppm
Concentration of Cr	3.14 ppm
Number of moles per liter for Na	0.0604 mmol/L
Number of moles per liter for Cr	0.0813 mmol/L
Stoichiometry (Na: Cr)	1.35: 1
Empirical molecular formula	$Na_{1.35}CrO_4$

The observed discrepancy in the elemental compositions obtained through ICP-OES ($Na_{1.35}CrO_4$) and SEM-EDS ($Na_{2.35}CrO_{4.4}$) likely arises primarily due to their inherent methodological differences, including working principles, sensitivity limits, and sampling depths. ICP-OES provides a high-precision and bulk-sensitive quantitative analysis of elemental composition by digesting the sample in acid and analyzing it in a diluted solution with a high detection limit from ppm to ppb [29]. Hence, the composition $Na_{1.35}CrO_4$ obtained through ICP-OES reflects the actual and highly precise stoichiometry of the entire bulk material. In contrast, SEM-EDS is a surface-sensitive technique. It provides semi-quantitative accuracy of surface analysis, particularly limited in detecting light elements such as sodium and oxygen, with a detection limit of about 0.1 to 1 atomic%

[30]. SEM-EDS analysis is typically sensitive to samples only in the near-surface region and localized enrichment (including surface oxides and adsorbed Na^+ ions). The compositional results through SEM-EDS can be influenced by surface inhomogeneities, grain morphology, matrix effects such as Au coating, challenges in detecting light elements like oxygen and sodium, and local compositional fluctuations. Additionally, the overestimation of sodium in SEM-EDS is a known issue, often attributed to the higher mobility and potential surface enrichment of alkali metals during their exposure to the electron beam. Hence, while SEM-EDS demonstrates a semi-quantitative surface analysis and provides crucial information regarding the elemental presence in the material, it also possesses several limitations, as discussed above. Therefore, to obtain a highly accurate and comprehensive understanding of the chemical composition, both SEM-EDS and ICP-OES analyses are conducted. ICP-OES results are used as the primary reference for compositional analysis.

6.3.1.5 Chemical State Analysis of $Na_{1.35}CrO_4$

The oxidation states of elements and the chemical bonding of $Na_{1.35}CrO_4$ are studied using XPS. **Figure 6.4 (*a*)** shows the wide scan XPS spectrum of $Na_{1.35}CrO_4$ in a wide binding BE range of 0-1400 eV. The presence of the characteristic XPS peaks for Na, Cr, O, and C is observed in the wide scan XPS spectrum, indicating the existence of the respective elements. The occurrence of the C-*1s* peak could be attributed to the use of a sample holder consisting of a carbon-coated Cu grid. Further, the C-*1s* peak is used as the reference peak, and all other peaks are calculated with respect to this reference peak. **Figures 6.4 (*b-e*)** represent the core-level XPS spectra of Na-*1s*, Cr-*2p*, O-*1s*, and C-*1s* orbitals, respectively.

Figure 6.4 (*b*) for Na-*1s* showed a single intense peak at the BE of 1070.59 eV, corresponding to the characteristic peaks of Na-1s and the '+1' oxidation state. The deconvoluted XPS spectrum of Na-*1s* represents the Na-O bonding [25]. **Figure 6.4 (*c*)** represents the deconvoluted XPS spectrum of Cr-*2p*. Due to the presence of spin-down (-½) and spin-up (+½)

electrons in Cr-*2p* orbital, a spin-orbit coupling process occurs with the formation of Cr-$2p_{1/2}$ and Cr-$2p_{3/2}$ orbitals, respectively. These peaks are further split into major and minor peaks, respectively. The major peak of Cr-$2p_{3/2}$ is observed at the BE of 579.37 eV, followed by a minor peak at 576.11 eV. Similarly, the Cr-$2p_{1/2}$ split into the major peak at 588.51 eV, followed by a minor peak at 585.83 eV, as shown in **Figure 6.4 (*c*)**. The major peaks of Cr-$2p_{1/2}$ and Cr-$2p_{1/2}$ are separated by a BE difference of 9.14 eV, corresponding to the Cr^{6+} oxidation state [25]. Similarly, the minor peaks of Cr-$2p_{1/2}$ and Cr-$2p_{1/2}$ are separated by an energy difference of 9.72 eV, representing the existence of the Cr^{7+} oxidation state.

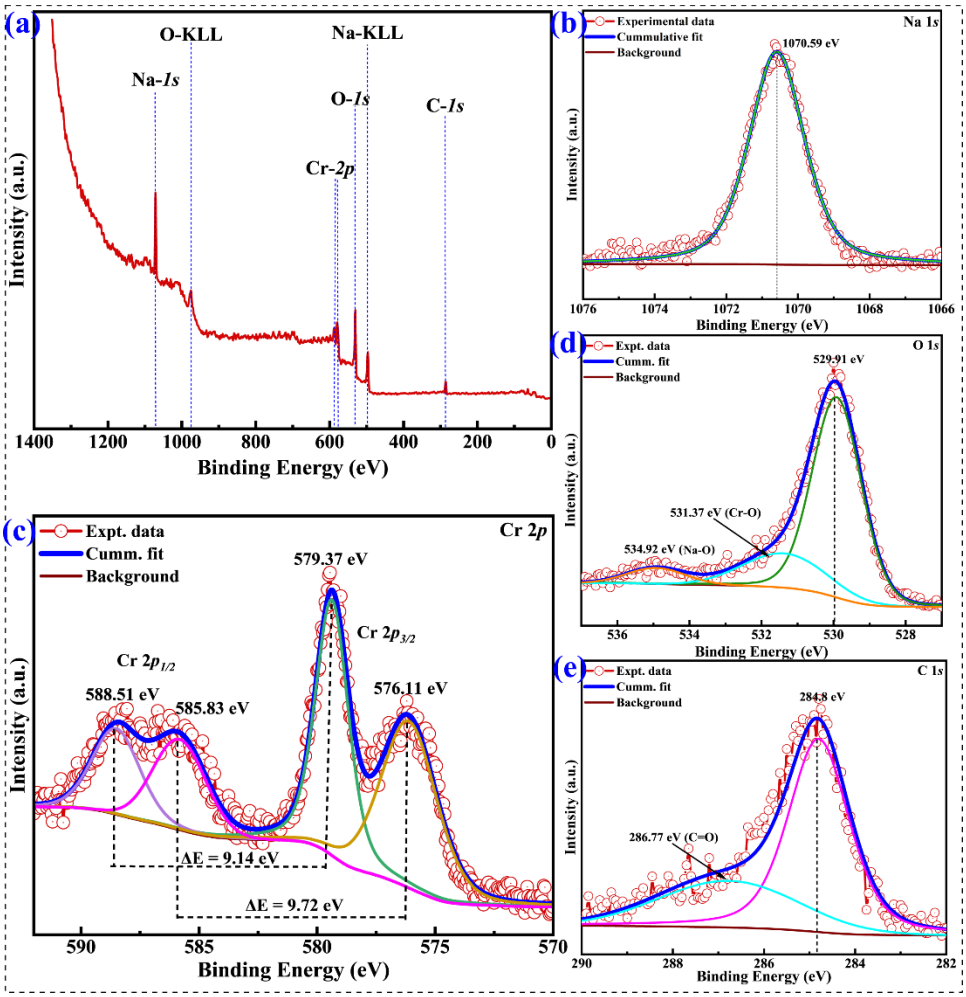

Figure 6.4 Wide scan XPS spectrum of **(a)** $Na_{1.35}CrO_4$, **(b)** Na-1s, **(c)** Cr-2p, **(d)** O-1s, and **(e)** C-1s orbitals in $Na_{1.35}CrO_4$ material.

Hence, Cr is present in both the Cr^{6+} and Cr^{7+} oxidation states, with Cr^{6+} as the dominant one in the synthesized $Na_{1.35}CrO_4$ material. The deconvoluted XPS spectrum of O-*1s* in **Figure 6.4 (*d*)** shows the formation of three peaks. The highest intense peak of O-*1s* at 529.91 eV corresponds to the chemisorbed oxygen, whereas the lower intense peaks of O-*1s* at 531.37 and 534.92 eV correspond to the Cr-O and Na-O metal bonds, respectively. **Figure 6.4 (*e*)** indicates the deconvoluted of C-*1s*. The highest intense peak at 284.8 eV belongs to the standard C-C bonding, and the lowest intense peak at BE at 286.77 eV corresponds to carbon bonding with oxygen, such as C=O or O-C=O. Hence, XPS analysis indicates the coexistence of Cr^{6+} and Cr^{7+} oxidation states of Cr in $Na_{1.35}CrO_4$, with Cr^{6+} as the dominant oxidation state.

It is necessary to remember that the hexavalent chromium Cr(VI)-based materials are highly toxic and may bring severe health-related issues to the biological system upon exposure [31]. The existence of Cr^{6+} in $Na_{1.35}CrO_4$ electrode will constrain its direct commercialization in battery technology. However, despite its high toxicity due to the presence of Cr^{6+}, many convincing scientific reasons exist to investigate Cr(VI)-based materials, including our $Na_{1.35}CrO_4$ electrode for battery industries. Their multi-electron transfer reaction and structure-property relationships provide a promising opportunity to enhance the electrochemical properties for an improved energy storage performance [25,32].

6.3.2 Electrochemical Analyses of $Na_{1.35}CrO_4$ Electrode

6.3.2.1 Redox Activity Analysis of $Na_{1.35}CrO_4$

The CV profiles of $Na_{1.35}CrO_4$ in the Na-half cell are shown in **Figure 6.5**. $Na_{1.35}CrO_4$, used as the active electrode material, with Na metal chips serving as reference and counter electrode in the Na-half cell, demonstrated an open circuit voltage (V_{OC}) of about 1.842 V with respect to the Na/Na^+. This V_{OC} is lower than the standard reduction potential of metal sodium, indicating that $Na_{1.35}CrO_4$ in the Na-half-cell works like a negative electrode. CV studies are carried out at various scan rates of 0.05

mV/s, 0.1 mV/s, and 0.5 mV/s for the three discharge and charge cycles in a voltage window of 0.01 V to 3.0 V.

The CV profile of $Na_{1.35}CrO_4$ electrode-based Na-half-cell at 0.05 mV/s scan rate is given in **Figure 6.5 (*a*)** for three consecutive cycles of charging/discharging processes. The 1st cycle corresponds to forming the SEI layer. During the discharging process, $Na_{1.35}CrO_4$ loses electrons (e^-) and sodium ions (Na^+ ions), forming CrO_4^{2-} ions in the host structure of the material. These Na^+ ions travel through the electrolyte to the sodium metal chip used as a counter and reference electrode. Meanwhile, e^- migrates through an external circuit and combines with these Na^+ ions to form metallic sodium at the counter electrode. During the discharging process, $Na_{1.35}CrO_4$ exhibits three prominent reduction peaks at the potentials of 1.529, 0.669, and 0.061 V with respect to Na^+/Na, as shown in the 2nd charge/discharge CV profile at 0.05 mV/s. The reverse process occurs during the charging process with the oxidation of sodium metal counter electrode to Na^+ ions and electrons (e^-). These Na^+ ions travel back to the active electrode via the ion-conducting electrolyte and are reinserted into the structure. The CrO_4^{2-} framework incorporates these Na^+ ions and the electrons to restore the original composition of $Na_{1.35}CrO_4$ [25]. This process results in the formation of three oxidation peaks at 2.097, 1.299, and 0.086 V with respect to Na/Na^+. The formation of multiple redox pairs indicates that the sodium extraction and insertion process in $Na_{1.35}CrO_4$ electrode proceeds via complex steps. Further, the redox peaks for the 3rd charge/discharge cycle occurred at similar potentials as the 2nd cycle, indicating the high electrochemical reversibility and structural stability of the $Na_{1.35}CrO_4$ electrode for SIBs.

Further, we performed the CV analysis at higher scan rates of 0.1 mV/s and 0.5 mV/s for three cycles, as shown in **Figure 6.5 (*b*)**. Similar redox characteristics are observed at other higher scan rates, such as 0.05 mV/s. It is observed that with the increase in the scan rates, the oxidation peaks shift towards higher voltages, and the reduction peaks shift towards

lower voltages. The area under the CV and the magnitude of redox peaks increase with the increase in scan rates due to diffusion behavior and fast electron kinetics at higher scan rates. At all the corresponding scan rates, redox peaks are consistent at a similar potential, further expressing the phase stability of $Na_{1.35}CrO_4$.

The EES behavior of $Na_{1.35}CrO_4$ for SIBs is investigated through CV analysis with the help of the Power-law relationship, **Figure 6.5 (*c*)**. Here, slope '*b*' provides crucial information regarding whether the electrode exhibits battery-type or capacitor-type behavior. A value of *b* as exactly 0.5 or close to it suggests the pure battery-type charge kinetics of the electrode material. In contrast, its exact value of 1 represents the pure capacitive type of performance of the electrode, and any value between 0.5-1 corresponds to a mixture of battery and capacitive type performance. $Na_{1.35}CrO_4$ shows slope values of 0.48 for the charging and 0.59 for the discharging processes, indicating $Na_{1.35}CrO_4$ exhibits battery-type performance rather than capacitive charge kinetics. The analysis further strengthens the application of $Na_{1.35}CrO_4$ as an active electrode for SIBs. **Figure 6.5 (*d*)** represents the stacking order of elements for cell fabrication and connection with AutoLab potentiostat electrochemical workstation for CV analysis. In the setup, the working electrode (WE) and sample (S) are connected together to the $Na_{1.35}CrO_4$ electrode side of the coin cell, whereas the counter electrode (CE) and the reference electrode (RE) are connected together to the Na-metal chip side of the coin cell.

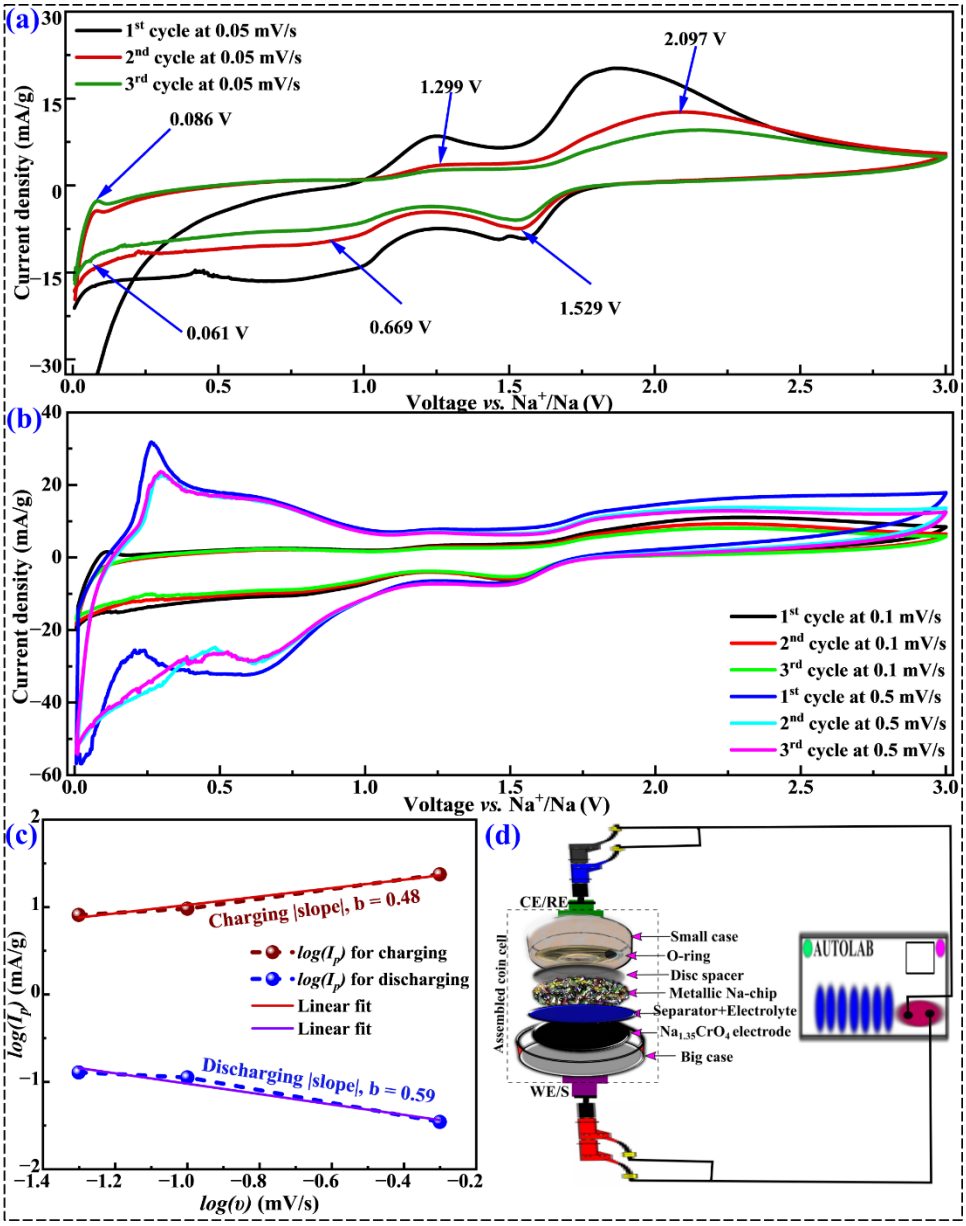

Figure 6.5 CV profile at (a) 0.05 mV/s; (b) 0.1 mV/s and 0.5 mV/s; (c) logarithm of peak current vs. scan rates; (d) Coin-cell configuration and Auto-lab setup for cyclic CV measurement of $Na_{1.35}CrO_4$.

6.3.2.2 EIS Analyses of $Na_{1.35}CrO_4$

EIS was performed before and after the CV analyses to observe the charge kinetics, resistances due to reactions at the electrode-electrolyte interface, and state of health for $Na_{1.35}CrO_4$ as an electrode for SIBs. The EIS analyses conducted before and after CV in a frequency range of 100,000

Hz to 0.1 Hz are shown in **Figure 6.6**. As interpreted from **Figure 6.6 (*a(i)*)**, the fabricated cell has several components such as copper foil serving as a current collector for the active electrode, $Na_{1.35}CrO_4$ as active electrode, SEI layer at the active electrode side, electrolyte, separator, thin film SEI layer at the counter electrode side, Na chip serving as counter electrode and reference, and the aluminum foil current collector from the counter electrode. Each of these components could be analyzed in different equivalent circuits, giving various resistances, as depicted in **Figure 6.6 (*a(ii)*)** [33]. However, the charge resistance contribution from current collectors R_{Cu} and R_{Al}, electrodes $R_{Act.\ ele}$ and $R_{Cou.\ ele}$, electrolyte R_{Elec}, and separator R_{Sep} could be summed up to form a bulk resistance represented by R_1 [33]. This bulk resistance R_1 is also known as the solution resistance and provides crucial information about the compatibility of electrolytes with electrodes. The value of R_1 indicates that the electrolyte is a better choice and is desirable. Similarly, the resistance at the interfaces, such as SEI at the active electrode ($R_{SEI\ act.\ ele}$) and thin film at the cathode ($R_{SEI\ cou.\ ele}$), can be represented together by a single resistance R_2 known as resistance due to the SEI. Further, the kinetics of electrochemical reactions at the electrode-electrolyte interface results in an additional and important resistance, R_3, known as the charge transfer resistance and sometimes represented as R_{CT} [33]. With these, the actual impedimetric profile for the real fabricated half-cell is closer to the equivalent circuit, as shown in **Figure 6.6 (*a(iii)*)**. The resistances R_1, R_2, and R_3 occur at higher, middle, and lower frequencies, respectively.

The Nyquist plot of EIS analysis for before and after CV in **Figure 6.6 (*b*)** represents the formation of two semicircles attributed to interfacial characteristics and the charge transfer of Na^+ ions. The starting position of the 1st semicircles at higher frequencies represents the value of the solution or bulk resistance R_1. The diameter of the 1st semicircle at high frequencies corresponds to interfacial characteristics of the SEI, which resulted in the formation of organic layers due to the electrolyte decomposition at

electrodes, and its resistance is represented as R_2. Similarly, the diameter of the 2nd semicircle at lower frequencies represents the charge transfer resistance R_3. The Nyquist plots before and after CV show similar values for the solution resistance. However, the resistance due to the SEI layer and charge transfer is higher in the Nyquist plot after CV than before CV analysis (**Figure 6.6 (*b*)**).

The individual Nyquist plot and EIS analyses before and after CV are represented in **Figures 6.6 (c)** and **6.6 (d)** for a better understanding. An equivalent circuit was used to fit experimental data, as shown in their respective inset figures. **Table 6.4** provides the values for equivalent circuit parameters obtained through circuit fitting.

Table 6.4: Equivalent circuit EIS parameters of $Na_{1.35}CrO_4$.

Elements	Units	Before CV	After CV
$\mathbf{R_1}$	Ω	2.496	2.54
$\mathbf{R_2}$	Ω	115.1	633.8
$\mathbf{R_3}$	Ω	54.32	573.2
$\mathbf{Q_2}$	F s^{a-1}	4.184×10^{-6}	9.933×10^{-4}
$\mathbf{Q_3}$	F s^{a-1}	2.241×10^{-3}	1.025×10^{-5}
a_2	-	0.9073	0.7315
a_3	-	0.6581	0.8486
f_{min}	Hz	0.1	0.1
f_{max}	kHz	100	100
C_{dl}	F	2.93×10^{-8}	2.777×10^{-9}

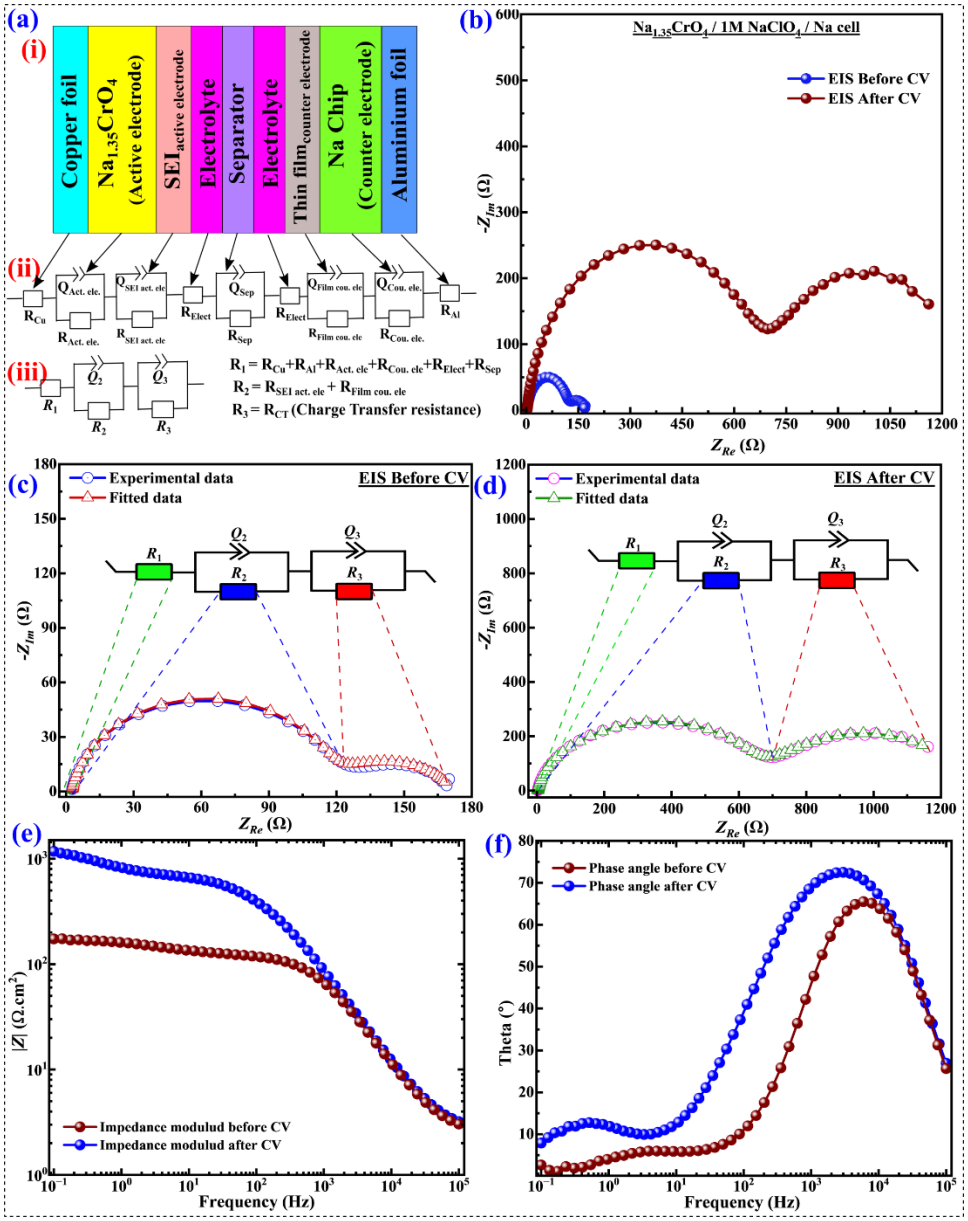

Figure 6.6 (a) Cell components and their respective resistance contributions; Electrochemical impedance study analyses of $Na_{1.35}CrO_4$ electrode **(b)** combined Nyquist plot for before and after CV; **(c)** Nyquist plot before CV; **(d)** Nyquist plot after CV; **(e)** Bode modulus; and **(f)** Bode phase angle.

The values of solution resistance R_1 before CV (2.494 Ω) and after CV (2.54 Ω) remain nearly the same and are relatively small, indicating the good conductivity of the electrolyte and its compatibility with the

$Na_{1.35}CrO_4$ electrode. The resistance offered by the SEI layers R_2 before CV is 115.1 Ω, which increased to 633.8 Ω after CV. This increase in the R_2 value is due to the formation of stable SEI layers at both electrode surfaces during the charge and discharge processes of the CV analysis. However, these R_2 values are still low, which signifies good charge kinetics and a healthy state of the $Na_{1.35}CrO_4$ electrode. Similarly, the charge transfer resistance R_2 before CV is about 54.32 Ω, which increased to about 573.2 Ω after CV due to the decomposition of organic electrolyte and the formation of thin film solid organic layers at the electrode. Despite this increase, the values remain small, representing the high charge kinetics of Na^+ ions. Compared to the charge transfer resistance of 311 Ω and 1091 Ω before and after cell cycling analyses for Na_2CrO_4/C as determined by Ali *et al.*[25], the small resistances of our material represent an enhanced interfacial conductivity and improved charge transfer of the fabricated cell. Further, the R_2 values are used to determine the capacitance of the double layer (C_{dl}) [27]. The values of C_{dl} before and after CV analyses were determined to be approximately 2.930×10^{-8} and 2.777×10^{-9} F, respectively, and are given in **Table 6.4**.

Figures 6.6 (*e*) and **6.6 (*f*)** represent the Bode modulus and Bode phase angle, respectively, for $Na_{1.35}CrO_4$ electrode for both before and after CV analyses. A slight increase is observed in both the Bode modulus and Bode phase angle after CV testing, representing a degradation in electrochemical performance after the charge-discharge process during CV testing. The rise in impedance modulus magnitude signifies an increase in R_3 that further results in increased interfacial polarization due to the passivation layer at the electrode. Further, after CV analysis, the Bode phase angle increase represents a shift toward more capacitive electrode behavior. This higher phase angle shifting could be attributed to the thin surface film formation.

6.4 Conclusions and Future Perspectives of $Na_{1.35}CrO_4$

In conclusion, for the first time, phase-pure $Na_{1.35}CrO_4$ has been successfully synthesized as an active electrode material for SIBs through a simple sol-gel method. Comprehensive physicochemical characterizations such as XRD, FESEM, EDS, ICP-OES, and XPS were carried out to investigate its various physical and chemical properties. These physicochemical analyses demonstrate the phase purity, high crystallinity, and well-ordered nature of $Na_{1.35}CrO_4$ with orthorhombic symmetry of the *Cmcm* space group, suitable for SIB application. Sol-gel-based synthesized $Na_{1.35}CrO_4$ exhibited a disc-like nanoparticle morphology and controlled stoichiometry. The nanoparticles range from 20 to 75 nm, with an average particle size of 42.87 nm, providing a highly active electrode-electrolyte contact surface. The EDS revealed a uniform distribution of elements all over the material surface. The XPS revealed the coexistence of Cr^{6+} and Cr^{7+} oxidation states, with Cr^{6+} as the dominant oxidation state. The detailed investigation of physical and chemical analyses is mutually supportive, signifying the elemental composition and structural integrity of $Na_{1.35}CrO_4$. Electrochemical studies, such as CV and EIS for $Na_{1.35}CrO_4$, were performed using fabricated sodium half-cells. The CV analysis demonstrated a V_{OC} of ~1.842 V and a working voltage window of 0.01 V to 3.0 V with multiple redox peaks. CV demonstrated a consistent occurrence of redox peaks at similar potential, representing the phase stability of $Na_{1.35}CrO_4$. The Power-law analysis of the CV data demonstrates diffusion-controlled, battery-type behavior. At the same time, the EIS investigation indicated a low resistance from SEI layers and charge transfer resistance, revealing good electrolyte compatibility and excellent charge transfer kinetics. Furthermore, the low C_{dl} suggests the potential of $Na_{1.35}CrO_4$ for high-energy-density applications. All the above analyses revealed that $Na_{1.35}CrO_4$ could be a potential active electrode material for SIBs.

Despite these promising findings for $Na_{1.35}CrO_4$ as an active electrode material for SIBs, further research is necessary to fully optimize and evaluate the electrochemical performance of $Na_{1.35}CrO_4$ for practical applications. The future direction for this material could be focused on galvanostatic charge-discharge analysis to investigate the specific capacity, rate capability, energy density, stability, and cycle life performance. Additionally, further research could investigate the effects of defect engineering, such as surface modifications, substitutional doping, and composite formation, to improve the Na^+ ion charge kinetics, material stability, and electrochemical performance. This study primarily explores $Na_{1.35}CrO_4$ as an active electrode for SIBs. However, the existence of hexavalent Cr in $Na_{1.35}CrO_4$ makes it improbable for industrial commercialization for battery technology. Hence, future research could focus on exploring stabilization strategies, including surface modification, protective matrix encapsulation, and chemical bonding, to significantly reduce the toxic nature of Cr(VI)-based compounds by mitigating the mobility and bioavailability of Cr(VI). The Cr^{6+}-based compounds are well known for their toxicity and environmental impact; hence, a thorough investigation could be focused on assessing the possible secondary pollution, including battery leakage. Exploring such environmental safety regarding the electrodes is important for real-life applications. Hence, more future work should focus on the rigorous environmental assessments of secondary pollution, including battery leakage, to comprehensively understand the safety implications of such materials. Moreover, future studies could be conducted on integrating $Na_{1.35}CrO_4$ electrodes into the full-cell fabrication of SIBs.

Chapter 6 (Part B)

Tunnel-Structured $Na_4Mn_{7.2}Cr_{1.8}O_{18}$ Metal Oxide Electrodes for Sodium-Ion Batteries

Part B of this chapter represents the partial Cr-doping in $Na_4Mn_9O_{18}$ to synthesize a tunnel-structured $Na_4Mn_{7.2}Cr_{1.8}O_{18}$ through a conventional solid-state method, followed by comprehensive physicochemical and electrochemical characterizations as a cathode for SIBs. Here we have completely replaced Co with Mn and Cr. The additional selection of the tunnel structure over the layered structure was preferred due to its high structural stability and limited phase transitions. The partial substitution of Mn^{3+} with Cr effectively reduced the Jahn-Teller distortions and stabilized the material for efficient Na^+ ion diffusion. Detailed physicochemical investigations confirmed the phase purity, uniform rod-like morphology, desired stoichiometry, and favourable bonding environment of $Na_4Mn_{7.2}Cr_{1.8}O_{18}$. Its electrochemical characterizations in a sodium half-cell configuration revealed charge and discharge specific capacities of ~105 mAh/g and 74 mAh/g, respectively, at 0.05C within a 2.0-4.0 V and about 76% capacity retention after 200 cycles at 0.2C. CV demonstrated a high redox activity, Na^+ ion diffusion, and pseudocapacitive behavior. The EIS and DRT studies revealed low resistances due to various physical processes and stable charge transfer resistance before and after cycle life testing, alongside a low double-layer capacitance, representing robust interfacial charge migration. These results support $Na_4Mn_{7.2}Cr_{1.8}O_{18}$ as a potential cathode for the fabrication of sustainable SIBs.

6.5 Introduction for $Na_4Mn_{7.2}Cr_{1.8}O_{18}$ Cathode

Cathode materials, also known as positive electrodes, play a vital role in developing SIBs. In the past few decades, various cathode materials have been explored for their potential applications in SIBs. Each of these materials exhibits distinct properties. Sodiated manganese oxides of the chemical form $Na_4Mn_9O_{18}$ (also known as $Na_{0.44}Mn_2$) are considered as promising positive electrodes for SIBs [34]. Na_xMnO_2 either exist in the tunnel structure such as $Na_4Mn_9O_{18}$ (*i.e.,* Na_xMnO_2 for $0.22<x<0.66$), or in *P2* structure (Na_xMnO_2 for $x>0.66$). Among them, the tunnel-structured $Na_4Mn_9O_{18}$ is the most promising cathode for SIBs based on its highly favorable crystalline framework for Na^+ ion intercalation/deintercalation. Amongst $Na_{0.44}MnO_2$ (*i.e.,* $Na_4Mn_9O_{18}$) is one of the most studied cathodes with a tunnel structure lattice framework and provides a high theoretical capacity of ~121 mAh/g [35,36]. The $Na_4Mn_9O_{18}$ nanowire studied by Anh Tan *et al.* [34] demonstrated a discharge capacity of ~90 mAh/g at 0.2C in a 2.0 V - 4.0 V voltage window. It retained a consistency in discharge capacities for 30 cycles. Zhenzhen *et al.* [37] investigated the electrochemical performance of $Na_4Mn_9O_{18}$/carbon-nanotube embedded reduced graphene oxide ternary composite cathode with respect to the zinc anode. It delivered a discharge capacity of 96.2 mAh/g and retained ~68% of its discharge capacity at the 150^{th} charge-discharge cycle [37]. Similarly, the work carried out by Guanghui *et al.* [38] on $Na_4Mn_9O_{18}$/reduced graphene oxide cathode and zinc anode exhibited a reversible discharge capacity of about 83, 43, 33, 24, 16, and 13 mAh/g at 0.1, 0.2, 0.5, 1. 2, and 5 A/g current densities, respectively, and capable of retaining ~72% of the capacity by 160 cycles. The $Na_4Mn_9O_{18}$ cathode material in aqueous electrolyte of 1M Na_2SO_4 and activated carbon counter electrode delivered a maximum specific capacity of 45 mAh/g at 0.125C. Similarly, the electrochemical process study of the $Na_4Mn_9O_{18}$ cathode with respect to the $Hg/HgSO_4$ reference electrode by Tevar *et al.* [39] in aqueous electrolyte exhibited a specific capacity of 35 mAh/g at 25 mA/g. The rod-like particle

morphology of $Na_4Mn_9O_{18}$ as cathode material for SIBs provided a high surface area for effective redox reactions and short diffusion paths that facilitated rapid ion transport, providing enhanced rate capability and charge/discharge efficiency. Furthermore, $Na_4Mn_9O_{18}$ is observed to have two phases of α-$Na_4Mn_9O_{18}$ and β-$Na_4Mn_9O_{18}$. The α-$Na_4Mn_9O_{18}$ has a monoclinic crystal lattice structure with a *C2/m* space group, and its structure is composed of Na atoms sandwiched between the MnO_2 layers. On the other hand, β-$Na_4Mn_9O_{18}$ exhibits the orthorhombic lattice symmetry with a space group of *Pmnm*, and its crystal structure is composed of an arrangement of Na atoms and MnO_2 slabs in a zigzag pattern, forming a tunnel structure [40,41].

The electrochemical performance of α-$Na_4Mn_9O_{18}$, having a layered structure, is limited by the Jahn-Teller (JT) effect, which is associated with the formation of $Mn^{4+}O_6$ octahedra from $Mn^{3+}O_6$ octahedra during the cycling process [40,41]. This JT effect arises from the relatively large ionic radius of Na^+ ions, which induces distortions in the crystal lattice. However, the β-$Na_4Mn_9O_{18}$, having orthorhombic symmetry, shows a significant reduction in the JT effect, which enhances the cathode material's structural stability, cycle life, and rate performance. Although β-$Na_4Mn_9O_{18}$ exhibits a considerable decrease of the JT effect compared to the α-$Na_4Mn_9O_{18}$, it undergoes a partial transformation into α-$Na_4Mn_9O_{18}$ during prolonged repeated cycling [35,36,39–41]. The formation of a tunnel-like structure for Na^+ ion migration shows a reduction in this JT effect. Several research studies have also been extended to explore other strategies to address this issue of structural instability due to the JT effect [35,36,39–41]. One such promising approach is the partial substitution of cation with Mn^{3+} ions. The studies by Shishkin *et al.* show that the partial doping of Cu cations can reduce this JT effect and provide a stabilized structure [42]. Further, theoretical studies revealed that the partial substitution of Mn with other TM elements (such as Sc, Ti, V, Cr, Fe, Co, Ni, and Zn), post-TMs such as Al, and alkali metal such as Mg can also stabilize the $Na_4Mn_9O_{18}$ cathode [42].

However, a detailed experimental study is required to investigate the effect of these TMs in enhancing the structural stability and rate performance of $Na_4Mn_9O_{18}$ cathode for SIBs.

The selection of Cr as a partial dopant in Mn-based tunnel structures is due to its structural and electronic advantages. Cr^{3+}, having the d^3 electronic structure, is not subject to Jahn-Teller distortion and therefore suppresses the instability usually inherent in Mn^{3+}. Its ionic radius is almost the same as that of Mn^{3+}, facilitating substitution without severe lattice strain, and contributing additionally to electronic conductivity and Na^+-ion diffusion. These characteristics together stabilize the tunnel structure and enhance long-term electrochemical performance. This study successfully incorporates Cr as a partial dopant at the Mn^{3+} site to form *β*-$Na_4Mn_{7.2}Cr_{1.8}O_{18}$, with doping levels of 20% of the primary TM atom. The selection of Cr as a dopant is based on the consideration of both literature analysis and the structural and electrochemical advantages of Cr. The DFT calculation performed by Shishkin et al. revealed that the partial substitution of several TMs, such as Sc, Ti, V, Cr, Fe, Co, Ni, Cu, and Zn, can effectively stabilize the different polymorphs of Mn-based cathodes for SIBs by modifying the local electronic environment and influencing the formation energy.[42] Among these, Cr was one of the most cost-effective and easily available elements that exhibited the highest structural stabilization after Ti. However, Ti exhibits a redox couple at a very low voltage that restricts its usage for high-voltage cathode synthesis. Further, Ti does not suppress JT distortion as Cr^{3+} does. As a result, in our study, we chose Cr as a dopant in $Na_4Mn_9O_{18}$ to form $Na_4Mn_{7.2}Cr_{1.8}O_{18}$ cathode. Several unique properties of Cr make it a suitable dopant at the location of Mn. The ionic radius of Cr (0.615 Å for Cr^{3+} with VI coordination) is close to that of Mn (0.645 Å for Mn^{3+} with VI coordination), making it a structurally compatible substitution into the MnO_6 unit without significant lattice distortion. Further, Cr^{3+} does not exhibit JT distortion due to its d^3-electron configuration, and its partial substitution helps in significant structural stabilization by reducing the JT

effect of Mn^{3+} during the prolonged cycle life performance. Moreover, Cr enhances the electronic conductivity of TM oxide cathodes by lowering the bandgap.[43,44] Again, the Cr dopant also improves the Na^+ ion diffusion by widening the interplanar spacing [45]. All these properties make Cr a potential dopant for the synthesis of $Na_4Mn_{7.2}Cr_{1.2}O_{18}$ cathode material for SIBs. Further, Cr-doping provided a zigzag-like tunnel structure for Na^+ ion migration and intercalated and deintercalated maximum Na^+ ions in the cathode material to enhance the prolonged cycle life performance. In our study, $Na_4Mn_{7.2}Cr_{1.8}O_{18}$ as cathode material in SIB configuration achieved a notable enhancement in electrochemical performance, Na^+ ion diffusion kinetics, and long cycle life performance compared to the undoped $Na_4Mn_9O_{18}$ counterpart. The $Na_4Mn_{7.2}Cr_{1.8}O_{18}$ cathode demonstrated an impressive discharge capacity of about 74 mAh/g at 0.05C within the 2.0-4.0 V voltage range versus Na/Na^+. Further, it exhibited excellent rate capability and cycling stability. Even after 200 charge-discharge cycles at 0.2 C, the discharge capacity retention was approximately 76%. CV and EIS studies revealed that Cr doping raises the average discharge potential and enhances the Na^+ ion diffusion coefficient. Moreover, Cr doping in $Na_4Mn_{7.2}Cr_{1.8}O_{18}$ cathode mitigated the JT distortion and improved the electrochemical stability and performance.

6.6 Experimental Section for $Na_4Mn_{7.2}Cr_{1.8}O_{18}$ Cathode

The experimental details, such as the materials synthesis approach, physicochemical characterization techniques, electrode preparation, cell assembly, and electrochemical property analysis techniques for $Na_4Mn_{7.2}Cr_{1.8}O_{18}$ cathode in SIBs, are explained in detail in Chapter 2.

6.7 Results and Discussion for $Na_4Mn_{7.2}Cr_{1.8}O_{18}$ Cathode

6.7.1 Physicochemical Analyses for $Na_4Mn_{7.2}Cr_{1.8}O_{18}$ Cathode

6.7.1.1 Thermal Behavior of $Na_4Mn_{7.2}Cr_{1.8}O_{18}$

The thermal behavior of $Na_4Mn_{7.2}Cr_{1.8}O_{18}$ material before the calcination process was analyzed through TGA and DTG, as shown in **Figure 6.7**. The material exhibited a complex three-stage decomposition process between approximately 30°C and 1000°C. The first stage, mass loss, was observed between 35 and 135°C with a total mass loss of 4.3% and is attributed to the removal of absorbed and trapped water. It is further represented by endothermic peaks in the DTG curve at 63 and 109°C. The second stage mass loss occurred between 135-550°C, where a substantial 2.5% mass loss took place owing to the decomposition of precursors, accompanied by gas evolution. The peak in the DTG curve at 495°C indicates the rapid mass loss rate corresponding to this decomposition process.

The third stage mass loss, spanning 550-920°C, involved only a 2.3% mass loss due to nucleation and desired $Na_4Mn_{7.2}Cr_{1.8}O_{18}$ phase formation, likely represented by a parallel line to the temperature axis of the DTG curve, reflecting a more gradual structural reorganization. By the end of 1000°C, the material still retained about 89.1% of its initial mass. This high mass retention indicated the excellent thermal stability of the material. Between temperatures 550-920°C, the DTG curve plateaus approached zero and a very low percentage of mass loss (as analyzed through TGA), indicating the formation of a stable phase. The stability of the material at higher temperatures is important for its performance in SIBs. Based on these thermal characteristics, 700, 800, and 900°C calcination temperatures were strategically selected for synthesizing materials with enhanced stability. These temperatures ensured complete phase formation and stability of $Na_4Mn_{7.2}Cr_{1.8}O_{18}$ as a cathode material.

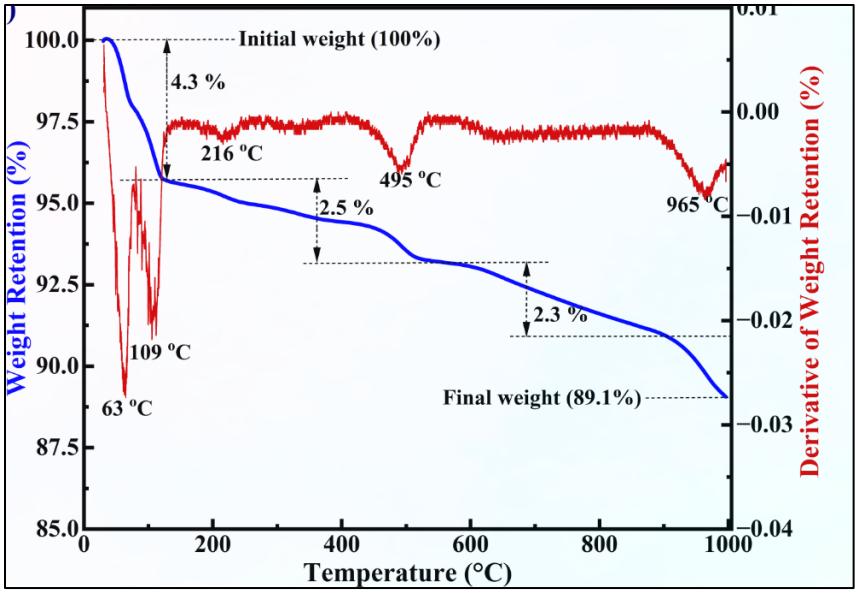

Figure 6.7 Thermal behavior of $Na_4Mn_{7.2}Cr_{1.8}O_{18}$ from ~30ºC to ~1000ºC.

6.7.1.2 Phase Purity and Lattice of $Na_4Mn_{7.2}Cr_{1.8}O_{18}$

The phase purity synthesis analyses of $Na_4Mn_{7.2}Cr_{1.8}O_{18}$ cathode were performed using powder-XRD for the samples calcinated at three distinct temperatures of 700°C (black colored pattern), 800°C (red colored pattern), and 900°C (green colored pattern) as shown in **Figure 6.8 (a)**. These XRD patterns of synthesized $Na_4Mn_{7.2}Cr_{1.8}O_{18}$ materials were compared with the standard $Na_4Mn_9O_{18}$ CIF file from the Materials Project, having orthorhombic crystal symmetry [34,37,46] as shown by the blue-colored pattern in **Figure 6.8 (a)**. The XRD analysis revealed significant variations in the formation of the material's purity across the calcination temperatures, signifying insights into the optimal synthesis calcination.

The XRD patterns demonstrated a clear evolution of crystalline structure with increasing calcination temperature. The $Na_4Mn_{7.2}Cr_{1.8}O_{18}$@700°C sample revealed the presence of all the corresponding peaks as those of the reference $Na_4Mn_9O_{18}$ material. In addition to the phase pure peaks, $Na_4Mn_{7.2}Cr_{1.8}O_{18}$@700°C also showed the presence of some additional peaks corresponding to impurities, as represented by the "***" symbol. From the Rietveld refinement on the XRD data of the sample calcined at 700°C, it was found that these impurity phases

were due to the presence of secondary impurities such as $NaCr_3O_8$ and $Na_2Cr_4O_{18,}$ constituting approximately 2.14% of the total composition. These impurity phases could be attributed to the incomplete reaction or insufficient diffusion kinetics at this lower temperature. This indicates that 700°C is insufficient for the complete phase transformation and impurity elimination. $Na_4Mn_{7.2}Cr_{1.8}O_{18}$@800°C demonstrated the optimal phase-pure crystalline phase formation, with all observed peaks precisely matching the standard $Na_4Mn_9O_{18,}$ having a tunnel structure for Na^+ ion migration as reference material with no detectable impurities. The well-defined prominent peaks and the absence of impurity peaks strongly suggested the formation of a single-phase of $Na_4Mn_{7.2}Cr_{1.8}O_{18}$ material at 800°C [38,39,47]. Conversely, $Na_4Mn_{7.2}Cr_{1.8}O_{18}$@900°C displayed the lack of several characteristic XRD peaks represented by dotted circles. This degradation of crystallinity at higher calcination temperatures is likely due to excessive sodium loss at high temperatures. Sodium volatilizes at higher temperatures, which disrupts the structural stability and stoichiometry of the material, leading to defects, reduced long-range order, phase impurity, and poor crystallinity [48]. This suggests that at this elevated temperature, the desired phase of $Na_4Mn_{7.2}Cr_{1.8}O_{18}$ decomposed, and the crystallinity nature decreased, emphasizing the importance of not exceeding the optimal calcination temperature. The comprehensive XRD analysis revealed 800°C as the optimal calcination for phase-pure $Na_4Mn_{7.2}Cr_{1.8}O_{18}$.

We extended our study on its structural refinement using FullProf, as shown in **Figure 6.8 (b)**. The Rietveld-refinement analysis confirmed the formation of the orthorhombic phase of $Na_4Mn_{7.2}Cr_{1.8}O_{18}$@800°C. This symmetry possesses the lattice parameters of 2.988, 9.092, and 26.429 Å with all the interaxial angles as 90º. The volume and density of the unit cell for this material were calculated from refinement as 718.09 $Å^3$ and 2.715 g/cm^3, respectively. All these obtained lattice parameters are given in **Table 6.5** and are compared with the previously studied $Na_4Mn_9O_{18}$ material.

Table 6.5: Crystallographic data obtained through refinement for $Na_4Mn_{7.2}Cr_{1.8}O_{18}$@800°C.

Crystallographic Parameters	Reference $Na_4Mn_9O_{18}$	This work $Na_4Mn_{7.2}Cr_{1.8}O_{18}$
***Lattice parameters* (Å)**	2.92, 9.224, 26.52, 9.09, 26.46, 2.82 [47]; 9.084, 26.311, 2.822 [49]	2.988, 9.092, 26.429
***α, β, γ* (°)**	90 [47,49]	90
***Unit cell volume* ($Å^3$)**	714.452; 678.27 [47]; 674.6 [49]	718.09
***Density* (g/cm^3)**	-	2.715
Crystal symmetry	Orthorhombic [47,49]	Orthorhombic

Figure 6.8 (*c*) demonstrates the lattice structure of $Na_4Mn_{7.2}Cr_{1.8}O_{18}$@800°C obtained from the XRD structural refinement. The unit cell of $Na_4Mn_{7.2}Cr_{1.8}O_{18}$@800°C contains four Na positions as represented by *Na1*, *Na2*, *Na3*, and *Na4*, and single chains of edge-linked MnO_5 square pyramids, double and triple chains of edge-linked MnO_6 octahedra, and double and triple chains of edge-linked CrO_4 tetrahedra as shown in **Figure 6.8 (*c*)**. The single, double, and triple polyhedra formed two 3D tunnels: a large S-shaped and a small six-sided tunnel.[47,49] This is attributed to the coexistence of Mn^{3+} and Mn^{4+} inside the lattice structure of $Na_4Mn_{7.2}Cr_{1.8}O_{18}$. Here, the *Na2*, *Na3*, and *Na4* reside in these large S-shaped tunnels, whereas the *Na1* occupies the six-sided tunnels, as shown in **Figure 6.8 (*c*)**. The *Na1* is coordinated by nine O atoms, and the Na^+ ions are positioned on the mirror plane perpendicular to the crystallographic *c*-axis. In addition to reducing the JT effect, the Cr-doping extends the large S-shaped tunnel suitable for Na^+ ion migration.

$$D = \frac{0.9\,\lambda}{\beta \cos(\theta)} \qquad \text{……. (6.1)}$$

The crystallite size (D) of $Na_4Mn_{7.2}Cr_{1.8}O_{18}$@800°C corresponding to the highest intense peak through the Debye Scherrer formula[27,28] (as given in **equation 6.1**) was found as ~22.43 nm. Here, λ=0.1542 nm is the corresponding x-ray wavelength, β is the FWHM of the highest intense peak, and θ is the Bragg's angle. Hence, the comprehensive XRD analysis, structural refinement, and a detailed crystal structure investigation

identified that 800ºC is the optimal calcination condition for the phase-pure synthesis of $Na_4Mn_{7.2}Cr_{1.8}O_{18}$, containing a similar phase to that of the $Na_4Mn_9O_{18}$ reference material. These insights are essential for understanding the electrochemical performances of $Na_4Mn_{7.2}Cr_{1.8}O_{18}$ as a potential cathode material for SIBs and further improving its electrochemical activities.

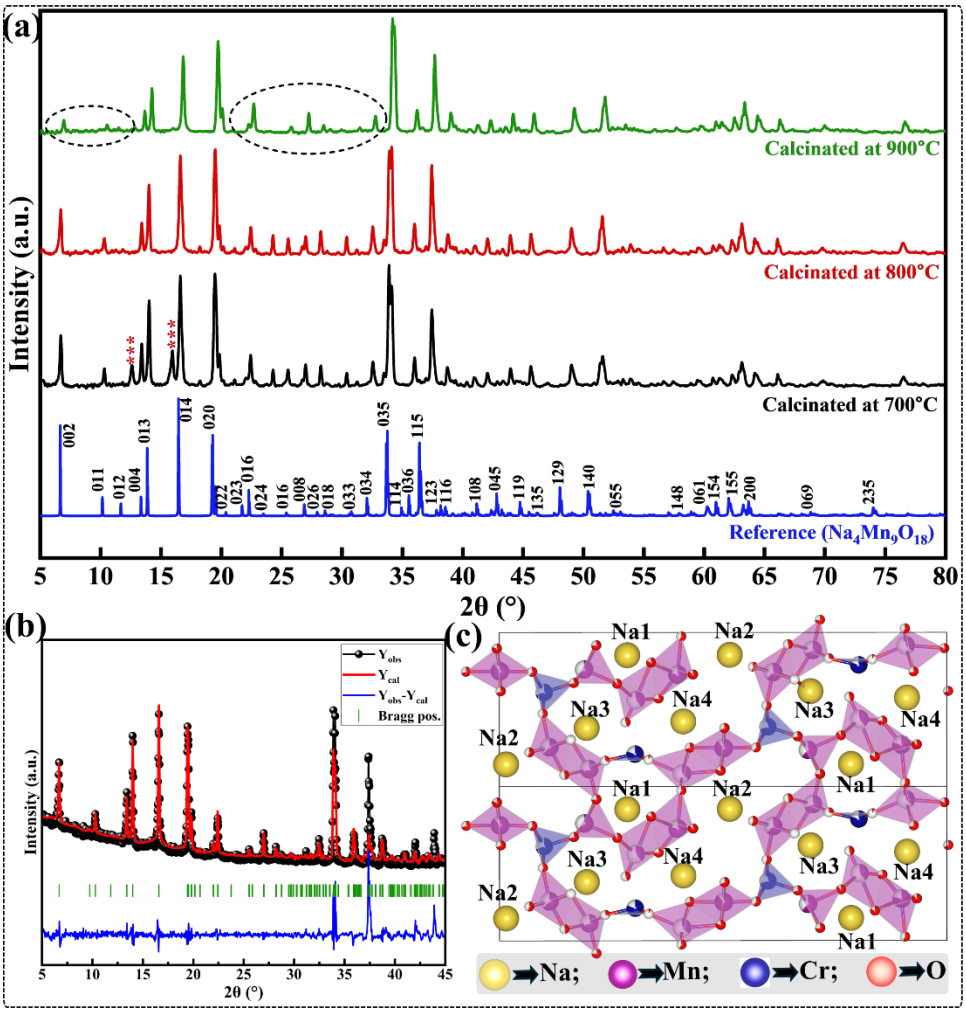

Figure 6.8 (a) XRD patterns of $Na_4Mn_{7.2}Cr_{1.8}O_{18}$ and reference $Na_4Mn_9O_{18}$; (b) Structural refinement; and (c) The lattice structure of $Na_4Mn_{7.2}Cr_{1.8}O_{18}$@800°C obtained through structural refinement.

6.7.1.3 Surface Morphology of $Na_4Mn_{7.2}Cr_{1.8}O_{18}$

Comprehensive qualitative analyses of particle surface morphology, shape, size, elemental distribution, and nominal chemical composition of all

the synthesized materials with different calcination temperatures were conducted using FESEM and EDS and are compared with the $Na_4Mn_9O_{18}$ material from the literature. **Figure 6.9 (*a, c, e, g*)** represents the particle morphologies of $Na_4Mn_{7.2}Cr_{1.8}O_{18}$ before calcination, calcinated at 700ºC for 12h, 800ºC for 12h, and 900ºC for 12h, respectively, at 30,000 times magnification of their original size. All these materials have a smooth surface morphology. $Na_4Mn_{7.2}Cr_{1.8}O_{18}$ material before calcination showed an irregular particle shape, and most of them were of disc-like shape, as shown in **Figure 6.9 (*a*)**. The particle size distribution of $Na_4Mn_{7.2}Cr_{1.8}O_{18}$ before calcination in **Figure 6.9 (*b*)** indicates that the particles exhibited a wide range of sizes varying from 0.4 to 1.7 μm and with 0.918 μm average particle size. This indicates that further calcination was required.

The FESEM images of $Na_4Mn_{7.2}Cr_{1.8}O_{18}$@700°C shown in **Figure 6.9 (*c*)** revealed that the particles at 700°C start to agglomerate and form a rod-like morphology. However, most particles still showed an undefined shape and size, significantly deviating from $Na_4Mn_9O_{18}$, which contains a rod-like morphology. This indicates that a higher calcination temperature was needed for better morphology. The diameter size distribution profile of $Na_4Mn_{7.2}Cr_{1.8}O_{18}$@700°C spanned over a size range of 0.1 μm to 0.7 μm and an average particle diameter of 0.302 μm (**Figure 6.9 (*d*)**). On the other hand, $Na_4Mn_{7.2}Cr_{1.8}O_{18}$@800°C revealed the formation of smooth surface morphology of the particles, with almost all the particles having a uniform rod-like shape (**Figure 6.9 (*e*)**), like the reference undoped $Na_4Mn_9O_{18}$ material. This morphological analysis supported the XRD results, confirming the formation of the desired orthorhombic phase $Na_4Mn_{7.2}Cr_{1.8}O_{18}$@800°C with tunnel-like features for Na^+ ion migration. The diameter of these rod-like $Na_4Mn_{7.2}Cr_{1.8}O_{18}$@800°C particles ranged from 0.1 to 0.6 μm, with an average particle size of 0.265 μm as shown in **Figure 6.9 (*f*)**. This particle diameter distribution range was very narrow, with a good Gaussian normal distribution function fitting, indicating the uniform formation of particles at this calcination temperature of 800°C.

Although $Na_4Mn_{7.2}Cr_{1.8}O_{18}$@900°C particles in **Figure 6.9 (g)** exhibited a rod-like morphology as that of undoped $Na_4Mn_9O_{18}$ material, [34,47,50] their diameter varied significantly from particle to particle. The diameter of $Na_4Mn_{7.2}Cr_{1.8}O_{18}$@900°C particles spanned over a wide range of 0.0 to 0.1 to 0.6 µm (**Figure 6.9 (*h*)**), indicating that at this temperature, several particles break their symmetry and crystallinity as confirmed through the above XRD analysis. Hence, from this qualitative morphological analysis, it was confirmed that $Na_4Mn_{7.2}Cr_{1.8}O_{18}$ calcinated at 800°C for 12h showed uniform and better morphology like $Na_4Mn_9O_{18}$ material.

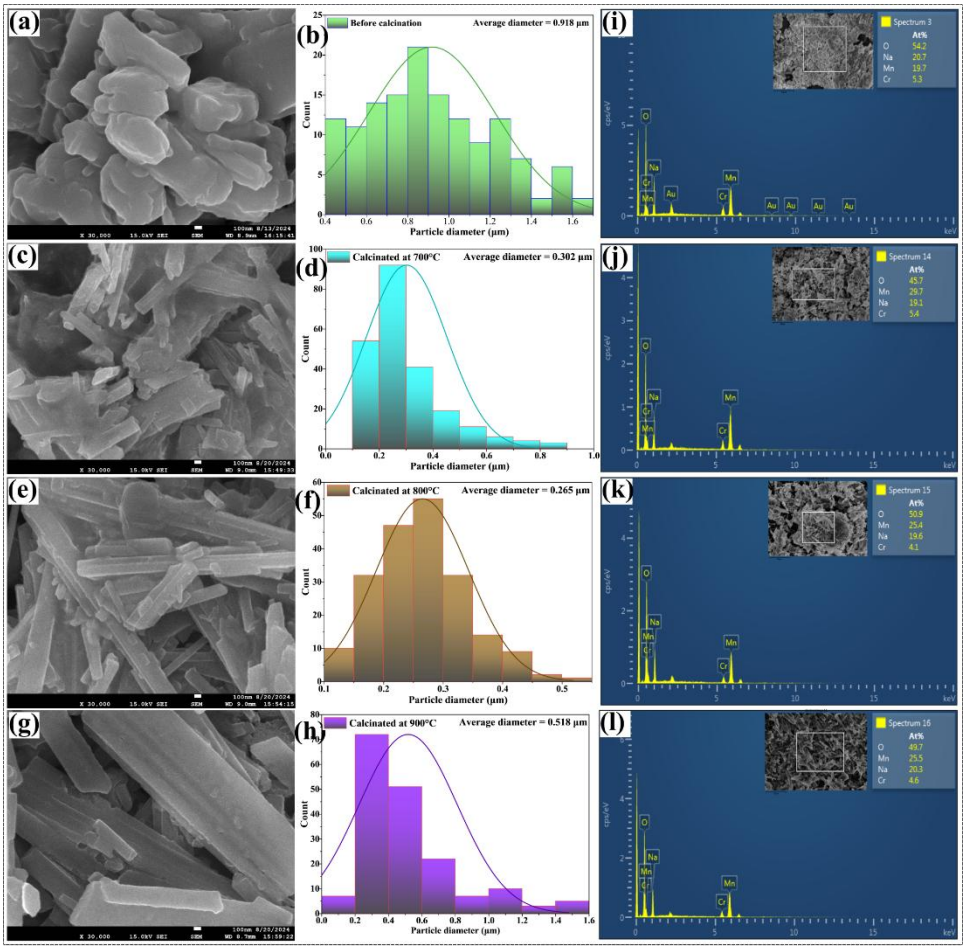

Figure 6.9 FESEM images (a) before calcination and calcinated at (c) 700°C, (e) 800°C and (g) 900°C; (b) particle diameter distribution profile (b) before calcination and calcinated at (d) 700°C, (f) 800°C and (h) 900°C; and EDS profiles (i) before calcination and calcinated at (j) 700°C, (k) 800°C and (l) 900°C of $Na_4Mn_{7.2}Cr_{1.8}O_{18}$ material.

The qualitative analysis of elemental composition and distribution in $Na_4Mn_{7.2}Cr_{1.8}O_{18}$ before and after calcination at 700°C, 800°C, and 900°C for 12 h is analyzed using EDS, as illustrated in **Figure 6.9 (*i-l*)**. The EDS spectrum of $Na_4Mn_{7.2}Cr_{1.8}O_{18}$ confirms the presence of elements in near-stoichiometric proportions. The primary elements, such as Na, Cr, Mn, and O of $Na_4Mn_{7.2}Cr_{1.8}O_{18}$ materials, are uniformly distributed throughout the surface of the synthesized materials. The EDS spectrum of $Na_4Mn_{7.2}Cr_{1.8}O_{18}$ before calcination in **Figure 6.9 (*i*)** reveals that Na, Cr, Mn, and O content is about 20.7, 5.3, 19.7, and 52.2%, respectively. Similarly, the EDS study for $Na_4Mn_{7.2}Cr_{1.8}O_{18}$@700°C (**Figure 6.9 (*j*)**) reveals the existence of Na, Cr, Mn, and O as 19.1, 5.4, 29.7, and 45.7%, respectively. These values for $Na_4Mn_{7.2}Cr_{1.8}O_{18}$@800°C (**Figure 6.9 (*k*)**) materials are about 19.6, 4.1, 25.4, and 50.9%, respectively. And that of $Na_4Mn_{7.2}Cr_{1.8}O_{18}$@900°C (**Figure 6.9 (l)**) is found to be 20.3, 4.6, 25.5, and 49.7, respectively. Through EDS, it is found that all the $Na_4Mn_{7.2}Cr_{1.8}O_{18}$ materials before calcination and calcinated at 700, 800, and 900ºC possessed nearly the desired stoichiometry of surface elements as shown in **Table 6.6**.

Table 6.6: EDS-based atomic% in $Na_4Mn_{7.2}Cr_{1.8}O_{18}$.

% of atoms	$Na_4Mn_{7.2}Cr_{1.8}O_{18}$			
	before calcination	@700ºC	@800ºC	@ 900ºC
Na	20.7	19.1	19.6	20.3
Mn	19.7	29.7	25.4	25.5
Cr	5.3	5.4	4.1	4.6
O	54.2	45.7	50.9	49.7

6.7.1.4 Quantitative Stoichiometry of $Na_4Mn_{7.2}Cr_{1.8}O_{18}$

To obtain the exact stoichiometry and true composition of the synthesized material, ICP-OES was employed as a quantitative elemental analysis technique. The ICP-OES [27] was carried out through an Agilent SPS 4 autosampler, with specific wavelengths for metal elements such as sodium at 589.592 nm, chromium at 283.563 nm, and manganese at 257.610 nm. The samples for ICP-OES were prepared by digesting the powder

samples in a combination of nitric acid (HNO_3) and hydrochloric acid (HCl) in a 3:1 volume ratio and diluted in DI water to form about 10 ppm of the concentration. The calibration process involved the preparation of three standard solutions with concentrations of 5, 10, and 20 ppm to ensure accurate quantification of the elements. The quantitative results from the ICP-OES analysis are presented in **Table 6.7**. All three samples of $Na_4Mn_{7.2}Cr_{1.8}O_{18}$ synthesized with a calcination temperature of 700ºC, 800ºC, and 900ºC show almost similar stoichiometry and the empirical molecular formula. However, the material synthesized with a calcination temperature of 800ºC exhibited the most required stoichiometry with an empirical formula of $Na_{4.81}Mn_{6.80}Cr_{1.8}O_{18}$, suggesting almost the needed proportion of TM elements as that of $Na_4Mn_{7.2}Cr_{1.8}O_{18}$ material. Compared to $Na_4Mn_{7.2}Cr_{1.8}O_{18}$@700°C and $Na_4Mn_{7.2}Cr_{1.8}O_{18}$@900°C, the stoichiometry of the alkali atom Na, chalcogen O and the TM elements Mn and Cr in $Na_4Mn_{7.2}Cr_{1.8}O_{18}$@800°C was found to be more similar to the reference $Na_4Mn_9O_{18}$ material.

The discrepancy between the stoichiometry obtained through SEM-EDS and ICP-OES is due to the inherent differences in the working principles, sensitivity, and sampling depth of these two techniques. Although SEM-EDS is useful for identifying the presence of elements and their relative concentrations, it is a semiquantitative and surface-sensitive technique whose results can be influenced by grain morphology, surface inhomogeneities, Au coating, and local compositional variations. Moreover, EDS is prone to overestimating Na content due to its surface enrichment and higher mobility under the electron beam [30,51]. In contrast, ICP-OES is a highly quantitative and bulk-sensitive analytical technique. It involves complete digestion of the sample in acid and analysis of the resulting solution, providing highly accurate elemental quantification with detection limits ranging from ppm to ppb [29]. Hence, ICP-OES reflects the true stoichiometry of the entire bulk material. Therefore, while

EDS provides useful information about surface elemental distribution, the ICP-OES reflects the accurate compositional analysis of $Na_4Mn_{7.2}Cr_{1.2}O_{18}$.

Table 6.7: Concentration, stoichiometry, and empirical molecular formula for $Na_4Mn_{7.2}Cr_{1.8}O_{18}$ materials through ICP-OES analysis.

$Na_4Mn_{7.2}Cr_{1.8}O_{18}$ calcinated at	**Concentration (ppm)**			**Stoichiometry (Na : Mn : Cr)**	**Probable Molecular formula**
	Na	**Mn**	**Cr**		
700ºC for 12h	1.32	4.74	1.20	2.49 **:** 3.74 **:** 1 ≈ (4.482 : 6.732 : 1.8)	**$Na_{4.48}Mn_{6.73}Cr_{1.8}O_{18}$**
800ºC for 12h	1.97	6.67	1.67	2.67 : 3.78 : 1 ≈ (4.81 **:** 6.804 **:** 1.8)	**$Na_{4.81}Mn_{6.80}Cr_{1.8}O_{18}$**
900ºC for 12h	2.02	6.08	1.68	2.72 : 3.43 : 1 ≈ (4.896 : 6.174 : 1.8)	**$Na_{4.9}Mn_{6.17}Cr_{1.8}O_{18}$**

6.7.1.5 Raman Scattering of $Na_4Mn_{7.2}Cr_{1.8}O_{18}$

The critical insight of the crystalline framework and vibrational properties of $Na_4Mn_{7.2}Cr_{1.8}O_{18}$ material was investigated through Raman spectroscopy, as shown in **Figure 6.10 (*a*)**. The distinct Raman scattering vibrational peaks at 550-700 cm^{-1} and ~850 cm^{-1} are attributed to Mn-O and Cr-O bonding environments within the crystal matrix of the material. $Na_4Mn_{7.2}Cr_{1.8}O_{18}$@700°C exhibited three low-intensity peaks between 550-700 cm^{-1}, similar to those of the reference $Na_4Mn_9O_{18}$. In contrast, $Na_4Mn_{7.2}Cr_{1.8}O_{18}$@800°C possessed an additional peak at 848.8 cm^{-1} corresponding to the Cr-O vibration in addition to Raman peaks between 550-700 cm^{-1}. However, $Na_4Mn_{7.2}Cr_{1.8}O_{18}$@900°C demonstrated a single Raman peak at ~636 cm^{-1}. The Raman scattering peaks at 568.2, 647.1, and 672.1 cm^{-1} of the above materials correspond to the A_{1g} vibrational mode of Mn-O and Cr-O bonding environments of their respective MnO_6 and CrO_6 octahedral units [52]. The Raman scattering peak at ~597 cm^{-1} could be attributed to the Mn-O vibration in the basal plane of the MnO_6 octahedral unit [53]. The additional Raman scattering peak of $Na_4Mn_{7.2}Cr_{1.8}O_{18}$@800°C at 848.8 cm^{-1} further corresponds to the Cr-O vibration [54]. The lack of Raman Scattering peaks of $Na_4Mn_{7.2}Cr_{1.8}O_{18}$@900°C material compared to the $Na_4Mn_9O_{18}$ indicated

the distortion of octahedral units as explained in the above XRD and FESEM sections. Further, the significant number and intensity of vibrational modes of $Na_4Mn_{7.2}Cr_{1.8}O_{18}$@800°C are similar to those of $Na_4Mn_9O_{18}$, revealing a better synthesis of phase-pure material at 800°C.

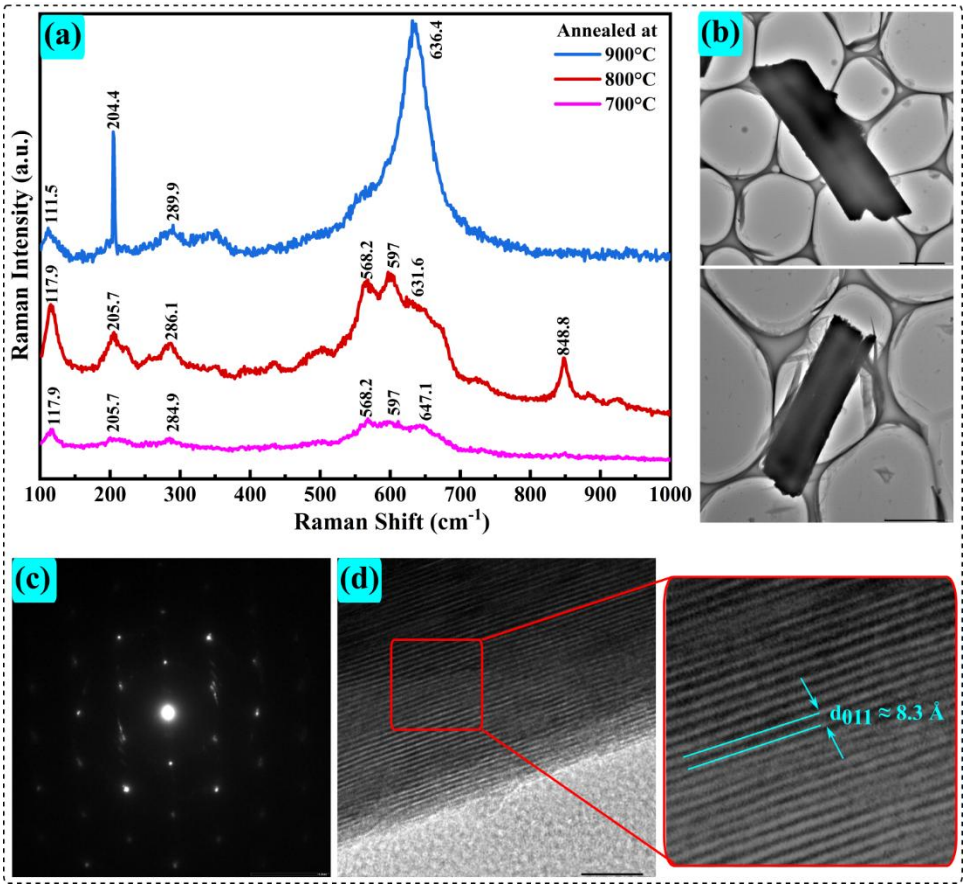

Figure 6.10 (a) Raman spectra of $Na_4Mn_{7.2}Cr_{1.8}O_{18}$ calcinated at 700ºC (pink), 800ºC (red), and 900ºC (blue); (b) TEM images; (c) SAED pattern; and (d) HRTEM image of $Na_4Mn_{7.2}Cr_{1.8}O_{18}$@800°C.

From XRD, FESEM, ICP OES, EDS, and Raman scattering, $Na_4Mn_{7.2}Cr_{1.8}O_{18}$ synthesized at 800°C exhibited a more well-defined phase and superior structural characteristics similar to the undoped $Na_4Mn_9O_{18}$, compared to its counterparts synthesized at 700°C and 900°C for 12 h. Consequently, all the subsequent analyses from this point onwards were focused exclusively on $Na_4Mn_{7.2}Cr_{1.8}O_{18}$@800°C material.

6.7.1.6 TEM and HRTEM Analyses $Na_4Mn_{7.2}Cr_{1.8}O_{18}$

The fine TEM images of $Na_4Mn_{7.2}Cr_{1.8}O_{18}$@800°C are shown in **Figure 6.10 (*b*),** exhibiting the rod-shaped morphology. The particle shape and size analysed through TEM are inconsistent with FESEM. The SAED pattern in **Figure 6.10 (*c*)** represents a well-recognizable spotty diffraction pattern consisting of distinct, sharp spots arranged in a regular array. It corresponded to the orthorhombic symmetry and the highly single-crystal lattice nature of $Na_4Mn_{7.2}Cr_{1.8}O_{18}$@800°C material, similar to that of its undoped $Na_4Mn_9O_{14}$ counterpart. The further single lattice-based atomic plane orientation of $Na_4Mn_{7.2}Cr_{1.8}O_{18}$@800°C was observed via the HRTEM, as shown in **Figure 6.10 (*d*)**. The atomic columns and the lattice fringes were found to be arranged in a specific direction with an interplanar spacing of 8.3 Å (**Figure 6.10 (*d*)**). The observed d-spacing value corresponds to the *(011)* plane of the material, as indicated in the XRD analysis. This strong agreement further substantiated the highly crystalline nature of $Na_4Mn_{7.2}Cr_{1.8}O_{18}$@800°C cathode material. The sharp atomic column lattice fringes indicated a highly ordered atomic arrangement, crucial for enhancing the electrochemical performance.

6.7.1.7 Chemical State Analysis of $Na_4Mn_{7.2}Cr_{1.8}O_{18}$

The oxidation states of elements and chemical bonding in $Na_4Mn_{7.2}Cr_{1.8}O_{18}$@800°C were analyzed through XPS. **Figure 6.11 (*a*)** presents the wide-scan XPS spectrum over a BE range of 0–1200 eV, confirming the presence of the characteristic peaks in $Na_4Mn_{7.2}Cr_{1.8}O_{18}$@800°C. Here, the C-*1s* peak serves as a reference for BE calibration. The core level XPS spectra of Na-*1s*, Cr-*2p*, Mn-*2p*, O-*1s*, and C-*1s* are given in **Figure 6.11 (*b-f*),** respectively. The high-resolution Na-*1s* XPS spectrum (**Figure 6.11 (*b*)**) exhibits a highly intense peak at 1070.3 eV corresponding to the core level electrons from Na (*i.e.,* Na_e) followed by a weak peak corresponding to Na-O-M (where, M = Mn/Cr) coordination environments, suggesting the successful incorporation of Na into the crystal structure of $Na_4Mn_{7.2}Cr_{1.8}O_{18}$.

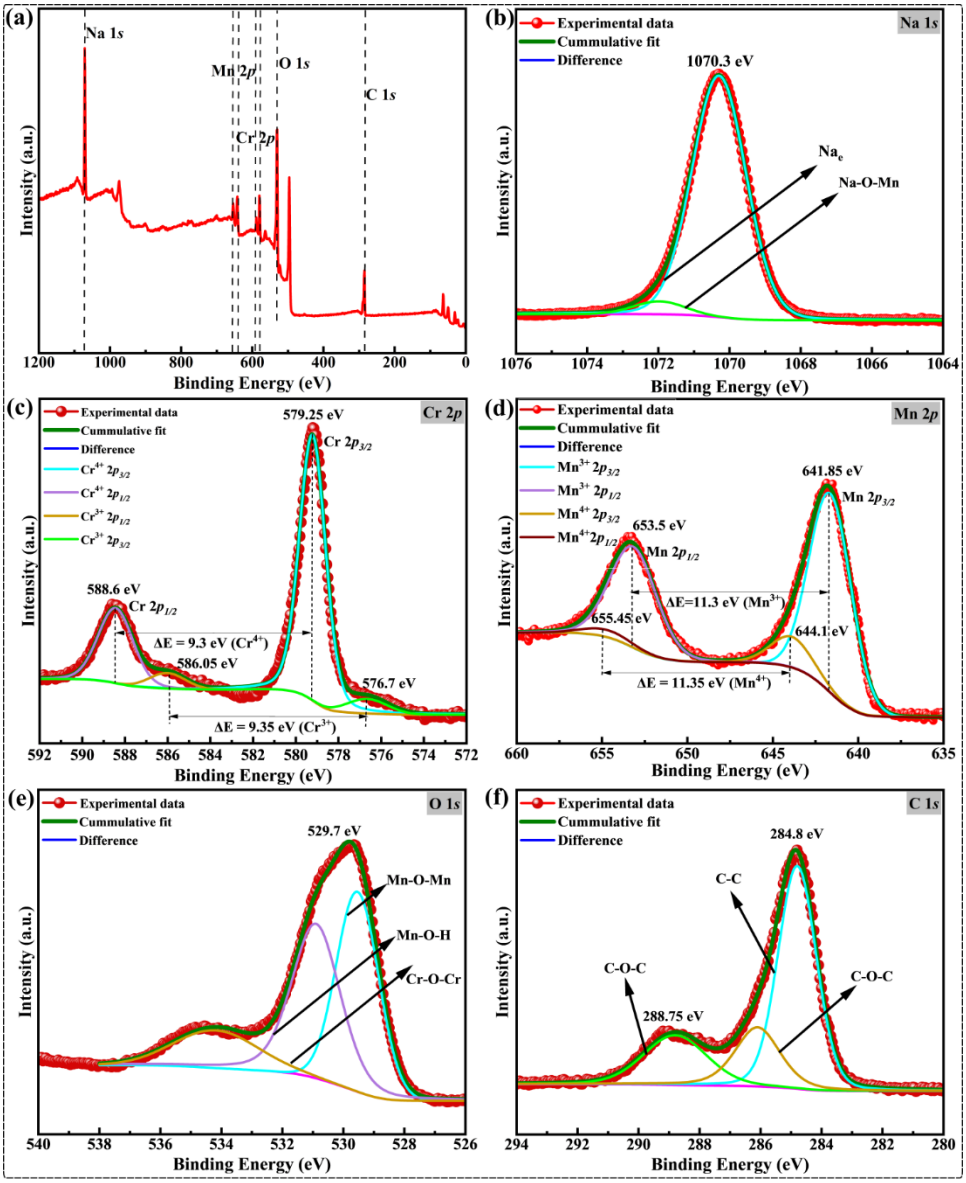

Figure 6.11 (a) Wide scan XPS spectra of $Na_4Mn_{7.2}Cr_{1.8}O_{18}$@800°C; Narrow scan XPS spectra of **(b)** Na-*1s*; **(c)** Cr-*2p*; **(d)** Mn-*2p*; **(e)** O-*1s*; and **(f)** C-1*s* orbitals.

The oxidation states of TM were identified in the Cr-*2p* and Mn-*2p* spectra, as shown in **Figure 6.11 (*c*)** and **6.11 (*d*)**, respectively. The high-resolution Cr-*2p* XPS spectra demonstrated characteristic spin-orbit splitting with Cr-$2p_{1/2}$ at 588.6 eV and Cr-$2p_{3/2}$ at 579.25 eV. Its deconvolution revealed the coexistence of Cr^{3+} and Cr^{4+} oxidation states with BE separation values (ΔE) of 9.35 eV and 9.3 eV, respectively. At the

same time, the high-resolution XPS spectrum of Mn-*2p* revealed a spin-orbit splitting with Mn-$2p_{1/2}$ at 653.5 eV and Mn-$2p_{3/2}$ at 641.85 eV, respectively. Its deconvolution results represented the coexistence of Mn^{3+} and Mn^{4+} oxidation states with ΔE values of 11.35 eV and 11.3 eV, respectively. The mixed-valence oxidation state character of Mn and Cr is advantageous for obtaining high redox activity during cell operation.

The high-resolution XPS spectrum of O-*1s* spectrum **Figure 6.11 (*e*)** was situated at 529.7 eV and revealed its various chemical environments. The deconvoluted components represented the Mn-O-Mn, Cr-O-Cr, and Mn-O-H bonding environments, confirming the formation of the polyhedral structure of metal-oxygen coordination in the crystal framework. The occurrence of hydroxyl groups (Mn-O-H) indicated minor surface hydration, commonly resulting in oxide materials. The high-resolution deconvoluted spectrum of C-*1s* (**Figure 6.11 (*f*)**) with a central peak at 284.8 eV corresponded to the C-C bonding environment. Meanwhile, the secondary C-*1s* peak at 288.75 eV represented the C=O=C bonds [55]. Overall, the XPS analysis confirmed the successful synthesis of $Na_4Mn_{7.2}Cr_{1.8}O_{18}$ with the expected oxidation states and bonding environment. Moreover, the BE for XPS peaks of $Na_4Mn_{7.2}Cr_{1.8}O_{18}$@800ºC sample was found to be situated at a BE almost similar to that of the XPS peaks in the undoped $Na_4Mn_9O_{18}$ material. This further correlated the oxidation states and the structural bonding environment similarity of Cr-doped $Na_4Mn_{7.2}Cr_{1.8}O_{18}$ with its undoped $Na_4Mn_9O_{18}$ counterpart.

6.8 Electrochemical Analyses for $Na_4Mn_{7.2}Cr_{1.8}O_{18}$ Cathode

6.8.1 CV Analysis for $Na_4Mn_{7.2}Cr_{1.8}O_{18}$ Cathode

To further obtain a deeper understanding of the redox mechanisms for the electrochemical behavior of $Na_{(s)}$ | 1M $NaClO_{4(solvent)}$ | $Na_4Mn_{7.2}Cr_{1.8}O_{18}$ half-cell, we conducted a CV study through the AutoLab electrochemical workstation by connecting the coin cell as shown in **Figure 6.12 (*a*)**. CV analysis is a widely utilized electroanalytical technique that

makes it easy to characterize redox-active materials by probing electron transfer-driven chemical transformations. In addition to identifying redox processes, the CV analysis technique provides essential information about the charge kinetics and thermodynamics of the ions taking part in the redox reactions. **Figure 6.12 (*b*)** represents the CV profile of the synthesized half-cell at a scan rate of 0.1 mV/s within a potential window spanning from 2.0 V to 4.0 V. It showed the existence of five pairs of redox peaks, the oxidation (*i.e.,* anodic) peaks are represented by *O*, and the reduction (*i.e.,* cathodic) peaks are represented by *R*, respectively. The redox peaks at 2.625 V/2.276 V, 2.796 V/2.535 V, 3.136 V/2.823 V, 3.338 V/ 3.163 V, and 3.526 V/3.379 V corresponded to the Mn^{3+}/Mn^{4+} and Cr^{3+}/Cr^{4+} redox couples that play an essential role in charge storage mechanisms. These peaks represented the redox processes during the forward and reversed potential scans and confirmed the electrochemical reversibility of $Na_4Mn_{7.2}Cr_{1.8}O_{18}$ cathode material. Similarly, **Figure 6.12 (*c*)** corresponds to the CV curves at potential scan rates of 0.2, 0.5, and 1.0 mV/s within the same potential window. The peak current and the area under the CV increased with the scan rate and could be attributed to the high electron exchange and ion diffusion rate in the $Na_4Mn_{7.2}Cr_{1.8}O_{18}$ cathode with an increase in scan rate.

The linear correlation between anodic/cathodic peak current (i_p) and the square root of scan rate ($\nu^{1/2}$), as represented in **Figure 6.12 (*d*),** provided the value of $i_p/v^{1/2}$. By considering the Na^+ ion diffusion as the rate-limiting step and the interface charge transfer resistance as negligible, the Na^+ ion diffusion coefficient D_{Na^+} value can be calculated from the Randles-Sevcik equation [56] (**equations 6.2** and **6.3).**

$$i_p = 2.69 \times 10^5 \; C \; A \; n^{\frac{3}{2}} \; v^{\frac{1}{2}} \; D_{Na+}^{\frac{1}{2}} \qquad \text{……. (6.2)}$$

Or the Na^+ ion diffusion constant D_{Na^+}:

$$D_{Na+} = \left[\frac{1}{(2.69\times10^5) \; C \; A \; n^{\frac{3}{2}}} \left(\frac{i_p}{v^{\frac{1}{2}}} \right) \right]^2 \qquad \text{……. (6.3)}$$

The D_{Na+} for $Na_4Mn_{7.2}Cr_{1.8}O_{18}$ cathode for the highest anodic and cathodic peaks of the charging and discharging processes were calculated as

3.713×10^{-11} and 5.42×10^{-11} cm^2/s, respectively. We used the power law equation[28,56,57] as given below in **equation 6.4,** to understand the underlying charge storage mechanism of $Na_4Mn_{7.2}Cr_{1.8}O_{18}$ cathode material quantitatively and to distinguish between surface-controlled (pseudo-capacitive) and/or diffusion-controlled (Faradaic) nature.

$$i_p = av^b \qquad \textbf{……. (6.4)}$$

By taking the logarithm of both sides, the above equation reduces to,

$$\log i_p = b \log (v) + \log (a) \qquad \textbf{……. (6.5)}$$

Here, *a* and *b* are the empirical constants and are obtained from the intercept and slope from the linear graph of *log* (i_p) on the y-axis and *log (v)* on the x-axis, respectively, as represented in **Figure 6.12 (*e*)**. The value of slope *b* signifies the nature of the charge storage mechanism of the electrode in the cell. If the value b = 0.5, it indicates a purely diffusion-controlled Faradaic charge storage process, whereas b = 1 indicates a diffusion-controlled charge storage process. Values between 0.5 and 1 represent the hybrid pseudo-capacitive behavior with the coexistence of surface-controlled and diffusion-controlled charge storage [28,56,57]. The calculated *b* values for $Na_4Mn_{7.2}Cr_{1.8}O_{18}$ cathode material were found to be about 0.789 and 0.801 for the anodic and cathodic processes, respectively, clearly reflecting the pseudo-capacitive energy storage characteristics of $Na_4Mn_{7.2}Cr_{1.8}O_{18}$ cathode. The incorporation of Cr into the Mn-based cathode materials significantly influences the pseudocapacitive behavior through synergistic structural and electrochemical effects [58]. The partial substitution of Mn^{3+} with Cr^{3+} into $Na_4Mn_9O_{18}$ to form $Na_4Mn_{7.2}Cr_{1.8}O_{18}$ stabilizes the lattice structure by reducing the JT distortion. This structural stabilization improves cycling performance and elevates the average Mn oxidation state, enhancing Mn^{3+}/Mn^{4+} redox activity. Further, Cr^{3+}/Cr^{4+} redox introduces additional redox-active sites and local lattice distortions, which enhance Na^+ ion diffusion kinetics and promote surface-controlled

faradaic reactions. These effects contribute to an increased pseudocapacitive contribution, as evidenced by CV analysis showing higher b-values. These modifications collectively position $Na_4Mn_{7.2}Cr_{1.8}O_{18}$ as a high-performance cathode for SIBs.

To further quantitatively analyze the pseudo-capacitance contribution, we evaluated the percentages of capacitive and diffusive contributions at a particular voltage using the following relationship of **equation 6.6** [56].

$$i = k_1 v + k_2 v^{\frac{1}{2}} \qquad \text{..... (6.6)}$$

On further rearranging,

$$\frac{i}{v^{\frac{1}{2}}} = k_1 v^{\frac{1}{2}} + k_2 \qquad \text{..... (6.7)}$$

The above **equation 6.7** provides a linear relationship between $i/\nu^{1/2}$ and $\nu^{1/2}$ as shown in **Figure 6.12 (*f*)**, whose slope k_1 and intercept k_2 facilitate the quantitative calculation of diffusive and faradic contributions. By the approach of the above method, the capacitive and diffusive contribution portions of the total current at 0.1 mV/s scan rate are shown by the blue and green shaded regions, respectively, in **Figure 6.12 (*g*).** Quantitatively, at the lowest scan rate of 0.1 mV/s, $Na_4Mn_{7.2}Cr_{1.8}O_{18}$ cathode material demonstrated a diffusive and capacitive contribution of 58 and 42%, respectively, of the total current contribution for the anodic process. Similarly, **Figure 6.12 (*h*)** represents the bar diagram for capacitive and diffusive contributions of anodic current with respect to scan rates, and **Figure 6.12 (*i*)** demonstrates the bar diagram for capacitive and diffusive contributions of currents, respectively, at all the scan rates. At low scan rates of 0.1 mV/s, diffusion-controlled processes dominated; however, with the increase in scan rate, the capacitive contribution progressively becomes more prominent. This trend was because, under high scan rates, ions do not get sufficient time to penetrate the electrode fully, which increases the fast surface redox reactions [56].

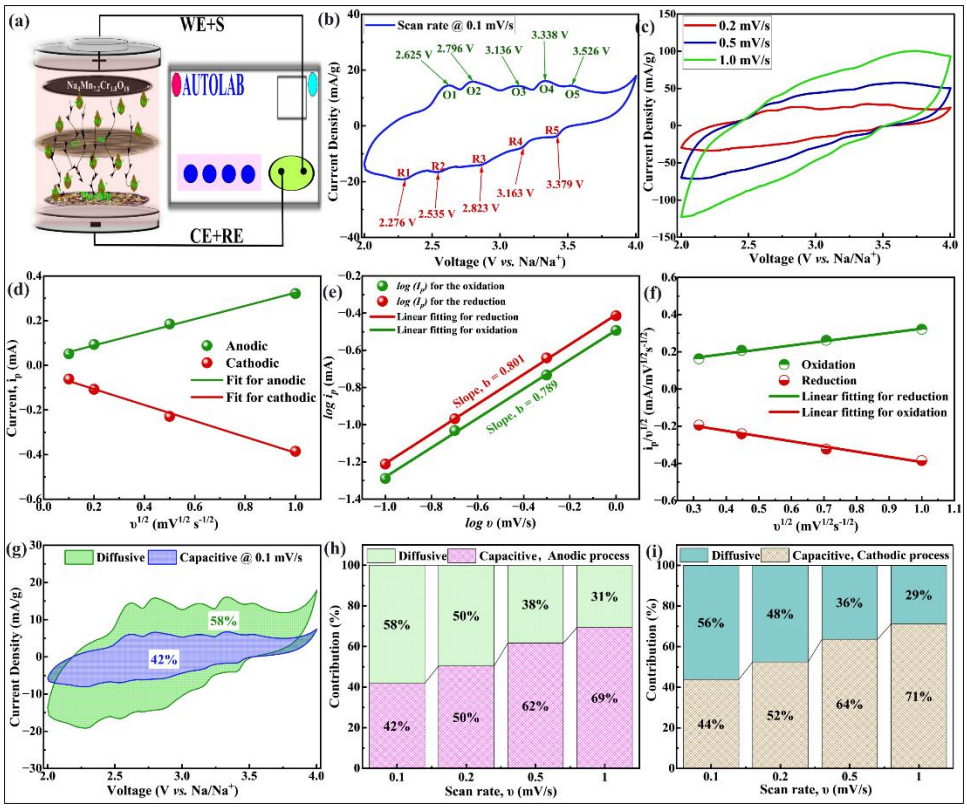

Figure 6.12 (a) AutoLab electrochemical workstation connection for CV study; CV at scan rates of (b) 0.1 mV/s; (c) 0.2, 0.5, and 1.0 mV/s; (d) i_p vs. $\nu^{1/2}$; (e) log(i_p) vs. log(ν); (f) $\nu^{1/2}$ vs. $i_p/\nu^{1/2}$; (g) anodic capacitive and diffusive contribution at 0.1 mV/s; bar diagram for capacitive and diffusive contributions for (h) anodic current (i) cathodic current.

6.8.2 GCD Analyses for $Na_4Mn_{7.2}Cr_{1.8}O_{18}$ Cathode

The GCD performance analyses of $Na_4Mn_{7.2}Cr_{1.8}O_{18}$ cathode were thoroughly investigated in Na/1M-$NaClO_4$/$Na_4Mn_{7.2}Cr_{1.8}O_{18}$ cell at varying current densities corresponding to different C-rates within the potential range of 2.0 V to 4.0 V, as illustrated in **Figure 6.13**. The results demonstrated the good rate performance and high structural stability of the cathode under a wide range of current rates. **Figure 6.13 (*a*)** represents the GCD profile for five consecutive charge and discharge processes. At 0.05 C, $Na_4Mn_{7.2}Cr_{1.8}O_{18}$ demonstrated the highest discharge capacity value of 73.86 mAh/g, corresponding to the charge capacity of 105.4 mAh/g, and by the end of the 5th cycle, its discharge capacity became 68.42 mAh/g,

corresponding to a charge capacity of 72.73 mAh/g. The charge and discharge capacities for all five GCD cycles of the respective C-rates are shown in **Figure 6.13 (*a*)**. Here, 1C corresponds to the current density of ~263.4 mA/g. Interestingly, the value of charge and discharge specific capacities for all five cycles remained almost the same, with a high value of Coulombic efficiency approaching ~100%, indicating high electrochemical reversibility and structural stability of the material. The formulas for calculating the theoretical and experimental specific capacities of the electrode material are given in **equations 6.8** and **6.9**, respectively.

Theoretical specific capacity (C_{th}) in mAh/g: $C_{th} = \frac{n\,F}{M}$**……. (6.8)**

Experimental specific capacity (C_{exp}) in mAh/g: $C_{exp} = \frac{I.\Delta t}{m}$**…. (6.9)**

In the above equations, '*n*' is the number of electrons transferred, '*F*' is the Faradays constant in (26801.39 mAh/g), '*M*' is the molecular weight of the electrode in g/mol, '*I*' is the charge/discharge current in mA, 'Δt' is the charge/discharge time in hours, and '*m*' is the electrodeactive mass in mg.

To further assess the rate tolerance of $Na_4Mn_{7.2}Cr_{1.8}O_{18}$ cathode, the rate performance providing charge/discharge capacities and Coulombic efficiencies were performed at increasing C-rates of 0.05 C, 0.1 C, 0.2 C, 0.3 C, 0.5 C, 1 C, 2 C, and further back to 1 C and 0.1 C, as shown in **Figure 6.13 (*b*)**. A constant trend in the decrease in both charge and discharge capacities was observed with an increase in the C-rates from 0.05 C to 2 C. This type of electrochemical behavior is due to the limited availability period for deintercalation/intercalation of Na^+ ions at higher C-rates, which hinders the complete extraction and insertion of Na^+ ions from/to the active cathode material. On further reducing the C-rates from 2C to 1C and then back to 0.1C, the cathode material exhibited similar values for charge/discharge capacities, revealing the high-rate tolerance of the $Na_4Mn_{7.2}Cr_{1.8}O_{18}$ cathode. The values of specific discharge capacities of all five discharge cycles concerning current densities remained at the same level during the C-rate performance analysis, indicating the excellent electrochemical stability of $Na_4Mn_{7.2}Cr_{1.8}O_{18}$. Furthermore, a good

Coulombic efficiency approaching 100% was observed during all the C-rates. Coulombic efficiencies are calculated as per **equation 6.10**.

Coulombic Efficiency (CE): $$CE = \frac{Discharge\ capacity}{Charge\ capacity} \times 100 \ldots\ \textbf{(6.10)}$$

Average voltage V_{avg}: $$V_{avg} = \frac{1}{C_{max}} \int_0^{C_{max}} V(C)\, dC \quad \ldots\ \textbf{(6.11)}$$

The curve shown in **Figure 6.13 (*c*)** demonstrates the average voltage for the charging and discharging processes of the $Na_4Mn_{7.2}Cr_{1.8}O_{18}$ cathode for all the current density calculations. The average charge/discharge voltage (V_{avg}) in volts was calculated with the help of **equation 6.11**, where C_{max} is the maximum charge/discharge specific capacity in mAh/g and *V(C)* is the voltage as a function of a particular capacity. It could be observed that the value of the average voltage increased with an increase in the value of C-rates, whereas its value decreased with an increase in the C-rates for the discharging process. The discharge energy densities of the cathode material with respect to their corresponding current densities are given in **Figure 6.13 (*d*)**. The high energy densities associated with these specific capacities further supported $Na_4Mn_{7.2}Cr_{1.8}O_{18}$ as a promising cathode for SIBs. The highest discharge energy density of 193.51 Wh/kg was achieved at 0.05C, followed by discharge energy densities of 154.66, 126.95, 116.63, 98.15, 78.42, and 53.45 Wh/kg at 0.1, 0.2, 0.3, 0.5, 1, and 2C, respectively, as illustrated in **Figure 6.13 (*d*)**. This signified the potential of $Na_4Mn_{7.2}Cr_{1.8}O_{18}$ cathode in lightweight, compact, and high-energy SIBs. Here, the experimentally obtained values for discharge energy densities were calculated through **equation 6.12**, where 'C_{exp}' is the experimentally obtained discharge specific capacity in mAh/g and 'V_{avg}' is the average discharge voltage in volts.

Discharge energy density in Wh/kg: $$E = C_{exp} \times V_{avg} \quad \ldots\ \textbf{(6.12)}$$

Again, **Figure 6.13 (*e*)** demonstrates the *dQ/dV vs. V* pattern. It showed similar charge/discharge patterns to those of the CV curve. This result further reinforced the high consistency of CV with GCD and the high reversibility of the electrochemical features of $Na_4Mn_{7.2}Cr_{1.8}O_{18}$ cathode.

Similarly, **Figure 6.13 (*f*)** corresponds to the evolution of charge and discharge durations across C-rates. At all the C-rates, the charge and discharge durations were almost symmetric, indicating stable Na^+ ion kinetics. The charge and discharge duration profile of $Na_4Mn_{7.2}Cr_{1.8}O_{18}$ cathode in the fabricated sodium half-cell at different C-rates from 0.05C to 2.0C revealed its significant rate-dependent electrochemical features. At the lowest 0.05C rate, the material demonstrated a prolonged charging profile that extends nearly 6 hours to reach 4.0V, followed by a gradual discharge lasting approximately six more hours until reaching 2.0V, exhibiting the whole voltage range and electrochemical kinetics of the cathode. As C-rates increased from the lowest 0.05C to the highest 2C, the charging-discharging times gradually decreased, with the highest rates at 1C and 2C completing the full charge and discharge cycles within 30 minutes. The characteristic slopes and plateaus in the voltage profiles between 2.0 - 4.0 V correspond to the reversible structural phase transitions of $Na_4Mn_{7.2}Cr_{1.8}O_{18}$ cathode material during the Na^+ ion intercalation/deintercalation.

The capacity retention and the cycle life performance of the $Na_4Mn_{7.2}Cr_{1.8}O_{18}$ cathode in $Na|1M\text{-}NaClO_4|Na_4Mn_{7.2}Cr_{1.8}O_{18}$ half-cell is performed at 0.3C (~79.02 mA/g) as shown in **Figure 6.13 (*g*)**, revealing an impressive electrochemical stability of the material over prolonged 200 charge/discharge cycles. With over 200 charge and discharge cycles, the cathode retained a high value of its initial capacity. Notably, $Na_4Mn_{7.2}Cr_{1.8}O_{18}$ retained about 86-88% of its initial discharge capacity by the end of 150 charge/discharge cycles. By the end of the 200^{th} cycle, it retained ~76% of its initial discharge-specific capacity, representing its excellent cycling performance and capacity retention behavior. $Na_4Mn_{7.2}Cr_{1.8}O_{18}$ cathode consistently demonstrated a remarkable coulombic efficiency, approaching 100% throughout 200 charge/discharge processes. This represents the highly reversible Na^+-ion insertion/extraction in the cathode material, formation of a stable electrode-electrolyte interface, and negligible parasitic side reactions, which are crucial for long-term

battery performance. The excellent capacity retention of over 75% after 200 cycles for $Na_4Mn_{7.2}Cr_{1.8}O_{18}$ highlights its long-term and efficient cathode performance for large-scale, cost-effective energy storage applications in SIBs. **Table 6.8** provides a comprehensive comparison of the synthesis methodology and the electrochemical performance, including the highest initial discharge capacity and capacity retention of the $Na_4Mn_{7.2}Cr_{1.2}O_{18}$ cathode with previously reported pristine $Na_4Mn_9O_{18}$ and its various composite derivatives for energy storage applications. In contrast to $Na_4Mn_9O_{18}$ and its different composite forms, the $Na_4Mn_{7.2}Cr_{1.2}O_{18}$ cathode material explored in this work exhibited significantly enhanced electrochemical performances, including excellent capacity retention.

Table 6.8: Features of $Na_4Mn_{7.2}Cr_{1.2}O_{18}$ & $Na_4Mn_9O_{18}$ derivatives.

Material name	Synthesis	Discharge Capacity	Capacity retention	Ref.
$Na_4Mn_9O_{18}$/RGO	Hydrothermal	83 mAh/g@0.1 A/g	68% at 160th@0.2 A/g	[38]
$Na_4Mn_9O_{18}$	Solid state	~50 mAh/g@0.1C	-	[47]
$Na_4Mn_9O_{18}$	Precipitation	73.8 mAh/g@4C	68.6% at 150th@4C	[55]
$Na_4Mn_9O_{18}$/CNT/RGO	Spray drying	96.2 mAh/g@4C	68.3% at 150th@4C	[37]
$Na_4Mn_9O_{18}$	Ball-mailing	45 mAh/g@0.125C	-	[46]
$Na_4Mn_9O_{18}$ NRs	Hydrothermal	~90 mAh//g@0.2C	~100% for 30@0.2C	[34]
$Na_4Mn_9O_{18}$	Solid state	~35 mAh/g@0.9C	~ 93% at 50th@0.9C	[39]
$Na_4Mn_9O_{18}$/RGO	Spray drying	61.7 mAh/g@4C	95.5% at 150th@4C	[50]
$Na_4Mn_9O_{18}$	Pechini	65 mAh/g@0.1C	-	[59]
$Na_4Mn_9O_{18}$	Spray drying	62.5 mAh/g@4C	64.5% at 150th@4C	[60]
$Na_4Mn_{7.2}Cr_{1.8}O_{18}$	Solid state method	73.9 mAh/g@0.05C	88% at 100th@2C 76% at 200th@2C	This work
RGO = Reduced graphene oxide, CNT = Carbon nanotube, NRs = Nanorods				

The rebound of capacity in **Figure 6.13 (*g*)** following multiple decay phases can be attributed to a combination of structural and electrochemical recovery processes that become prominent during the extended cycle life performance of $Na_4Mn_{7.2}Cr_{1.8}O_{18}$. The intermittent capacity rebounds are primarily due to progressive structural rearrangement within the tunnel structure framework [61]. Repeated sodiation/desodiation causes local lattice distortion, defect formation, and partial inaccessibility of active sites, leading to initial capacity fading. However, continued cycling permits progressive lattice strain relaxation and reorganization of disordered

regions, effectively restoring the Na^+ ion pathways and reactivating redox-active sites. Cr is electrochemically available over a prolonged charging and discharging process. This delayed redox activation, in addition to the primary Mn^{3+}/Mn^{4+} redox process, supports the resulting capacity rebound. Notably, the consistency in high coulombic efficiency (approximately 100%) during 200 cycles strongly suggests that capacity fluctuations are not caused by parasitic reactions or irreversible degradation but by reversible electrochemical and structural changes. Thus, the capacity rebound in **Figure 6.13 (*g*)** occurs due to lattice reorganization, redox reactivation, and enhanced electrode-electrolyte interface dynamics upon long-term cycling.

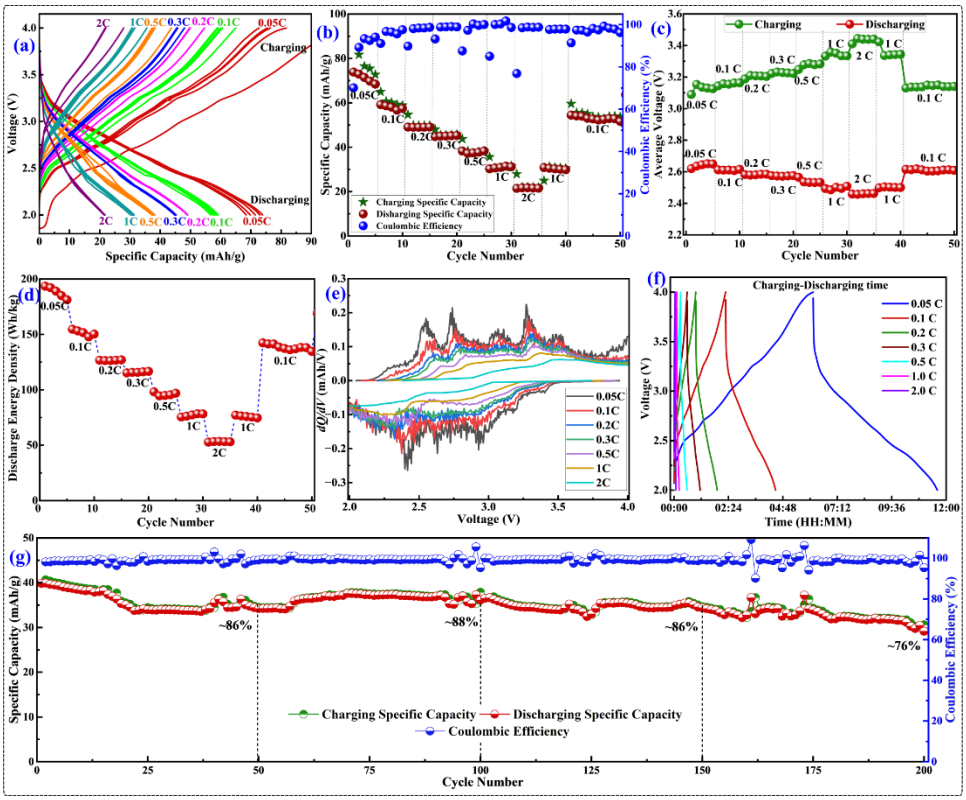

Figure 6.13 (a) GCD profile at various current densities; **(b)** C-rate performance; **(c)** Average voltage profile; **(d)** Energy density profile with respect to current densities; **(e)** The *dQ/dV* pattern profile; **(f)** Charge-discharge time profile; **(g)** Capacity retention over 200 charge-discharge cycles and their Coulombic Efficiency for $Na_4Mn_{7.2}Cr_{1.8}O_{18}$ cathode in SIB configuration.

6.8.3 EIS Analysis for $Na_4Mn_{7.2}Cr_{1.8}O_{18}$ Cathode

A comprehensive EIS study of $Na_4Mn_{7.2}Cr_{1.8}O_{18}$ cathode material in Na half-cell was performed to obtain critical insight into the electrode kinetics, state of health, charge transfer processes, and stability mechanisms. The EIS was carried out through the PGSTAT032N potentiostat electrochemical workstation with a frequency range of 0.01 Hz to 100 kHz. EIS spectra were obtained at three stages: (1) before CV analysis, (2) after CV analysis, and (3) after stability testing. In EIS, the total impedance was comprised of complex nonlinear least squares, as given in **equation 6.13**.

$$Z(\omega) = Z_{re}(\omega) + jZ_{im}(\omega) \qquad \text{..... (6.13)}$$

Here, $Z(\omega)$ is the total complex impedance as a function of frequency ω, j is the imaginary number, and Z_{re} and Z_{im} are the real and imaginary parts. **Figure 6.14 (*a*)** depicts the Nyquist plots of $Na_4Mn_{7.2}Cr_{1.8}O_{18}$ at different stages of electrochemical testing. The impedance spectra demonstrated the existence of characteristic features consisting of a high-frequency intercept with the real impedance axis, formation of semicircles in the high-to-medium frequencies, and a sloping line in the low-frequency region, corresponding to various electrochemical processes occurring at the electrode/electrolyte interfaces and within the bulk $Na_4Mn_{7.2}Cr_{1.8}O_{18}$ electrode. The equivalent circuit (given in **equation 6.14)** illustrated in **Figure 6.14 (*b*)** fits the experimental impedance data. Corresponding to the equivalent circuit, the total impedance in the form of resistances and CPEs was given by **equation 6.15**.

Equivalent Circuit: $$Z(\omega) = R_1 + \frac{Q_1}{R_2} + \frac{Q_2}{R_3} + \frac{Q_3}{R_4} \qquad \text{..... (6.14)}$$

$$Z(f) = R_1 + \frac{R_2}{1+(R_2\,Q_1\,(i2\pi\omega)^{a_1})} + \frac{R_3}{1+(R_3\,Q_2\,(i2\pi\omega)^{a_2})} + \frac{R_4}{1+(R_4\,Q_3\,(i2\pi\omega)^{a_3})}$$

.... (6.15)

The above equivalent circuit comprises four resistance elements (R_1 to R_4), three CPEs (Q_1 to Q_3), and a_1, a_2, and a_3 dimensionless exponent constants ($0 \leq a \leq 1$). The value of R_1 represents the combined resistance

resulting from the electrolyte and electrical contacts of the electrodes with the current collectors. The 2nd part, as the parallel connection of R_2/Q_1, represents the resistance from the SEI layer formed at the electrolyte and electrodes. The 3rd part R_3/Q_2 corresponds to the charge transfer resistance at the electrode-electrolyte interface, and the parallel connection of the 4th part R_4/Q_3 is attributed to the solid-state diffusion process of $Na_4Mn_{7.2}Cr_{1.8}O_{18}$ cathode. The value of impedance offered by the respective CPS is given by **equation 6.16**:

$$Z_{CPE} = \frac{1}{Q(j\omega)^a} \qquad \textbf{……. (6.16)}$$

The fitted values are shown in **Table 6.9**. R_1, commonly known as the solution resistance, remained almost the same and relatively very small in the range of 0-4 **Ω** before and after CV and after stability analyses, indicating the compatibility of electrolyte with the $Na_4Mn_{7.2}Cr_{1.8}O_{18}$ cathode. The R_2 (resistance offered by the SEI layer and R_3 (resistance due to charge transfer) are particularly critical for evaluating the ionic conductivity of the electrolyte and the kinetic efficiency of charge transfer processes. The resistance value due to the SEI layer R_2 remained almost the same as before CV and after CV, which were 31.08 and 39.71 **Ω**, respectively. However, this R_2 value increased significantly to 360.34 **Ω** after stability testing of the cell. This is due to the stable SEI layer formation during the charging and discharging process of the cell. The EIS before CV indicates a moderate charge transfer resistance R_3. After CV, the impedance profile changed notably, with the increase in R_3 value, suggesting enhanced charge transfer kinetics due to electrode activation. However, after the stability analysis, this charge transfer resistance R_3 remained slightly higher than before the CV analysis. This slight increase in R_3 after stability testing was due to structural changes or the growth of surface films during the long charging/discharging process.

Table 6.9: Fitted EIS parameters for CR-2032 type Na/1M $NaClO_4$/ $Na_4Mn_{7.2}Cr_{1.8}O_{18}$ cell.

Fitted EIS Parameters	Cr-2032 type Na/1M-$NaClO_4$/NCMO cell		
	Before CV	After CV	After Stability
R_1 (Ω)	2.120	3.646	0.103
Q_1 ($F.s^{(a-1)}$)	0.162	0.044	0.001
a_2	0.966	0.545	0.602
R_2 (Ω)	31.084	39.705	360.341
Q_2 ($F.s^{(a-1)}$)	0.001	26.092	29.939
a_3	0.467	0.812	0.904
R_3 (Ω)	51.310	167.566	67.779
Q_3 ($F.s^{(a-1)}$)	10.169	14.741	0.922
a_4	1	0.831	0.986
R_4 (Ω)	21.9939	26.790	4.023

The value of charge transfer resistance R_3 derived from EIS analysis was further expanded for the calculation of double layer capacitance (C_{dl}) of the system at all three stages using the following **equation 6.17** [27].

$$C_{dl} = \frac{1}{2\pi R_3 \omega_{max}} \qquad \text{……. (6.17)}$$

Through the above equation, the value of double-layer capacitance C_{dl}, before and after CV, and after stability testing, was calculated to be 3.102×10^{-9}, 9.498×10^{-10}, and 2.348×10^{-9} F, respectively, significantly indicating the charge accumulation capability of the electrode interface. The combination of low R values before and after stability testing and double-layer capacitance indicated that the $Na_4Mn_{7.2}Cr_{1.8}O_{18}$ cathode exhibits robust Na^+ ion transport properties and electrochemical stability, making it a potential electrode for SIBs in energy storage applications.

6.8.4 DRT Analysis for $Na_4Mn_{7.2}Cr_{1.8}O_{18}$ Cathode

Although the EIS is a potential electrochemical tool capable of understanding the interfacial and bulk properties of the electrode, analyzing the complex impedance involving the overlapping of semicircles within the same frequency domain becomes difficult or inaccurate. The EIS typically uses the models of equivalent circuits composed of several resistive and

capacitive elements; however, their interpretation becomes increasingly difficult due to the problem of isolating the individual contributions of distinct electrochemical processes [56]. To tackle these limitations, the DRT, an advanced mathematical tool, has evolved to deconvolute the impedance spectra into discrete relaxation processes in the time domain [56]. Mathematically, the DRT assumes an infinite Voigt circuit composed of an infinite series of resistance and constant phase (RQ) elements, each RQ pair contributing to a unique relaxation process whose time constant (τ) could be derived from **equation 6.18** [56].

$$\tau = (RQ)^{\frac{1}{\alpha}} \qquad \text{……. (6.18)}$$

The DRT approach calculates a normalized distribution function γ(τ) representing the contribution of each relaxation process across the time constant (τ) domain. The relation between impedance Z(ω) and the DRT function γ(τ) is given in **equation 6.19** [56].

$$Z(\omega) = R_s + R_p \int_{-\infty}^{\infty} \frac{\gamma(\tau)}{1+j\omega\tau} d \ln \tau \qquad \text{……. (6.19)}$$

R_s represents the uncompensated solution resistance at the high-frequency range, and R_p represents the total resistance due to the polarization contribution at the low-frequency range. To ensure that the area under each DRT peak corresponds quantitatively to the associated relaxation process, the DRT function γ(τ) is normalized as in **equation 6.20**.

$$\int_{-\infty}^{\infty} \gamma(\tau) d \ln \tau = 1 \qquad \text{……. (6.20)}$$

Considering any i^{th} DRT peak representing a discrete electrochemical process, the location of each peak reveals the characteristic relaxation time, while its area and intensity correspond to the magnitude of the resistance R_i. The capacitance C_i of the corresponding DRT peak is calculated by **equation 6.21**. This decomposition allows for the identification and understanding of individual kinetic processes [56].

$$C_i = \frac{T_i}{R_1} \qquad \text{……. (6.21)}$$

From the literature, it is evident that the time constant τ domain represents various resistances and their respective physical processes. For

example, the location of $\tau \leq 10^{-3}$ s corresponds to the resistance between the particle-current collector and the particle-particle of the electrode. The τ in between 10^{-3} and 10^{-2} s represents the resistance by the active ion transport through SEI (*i.e.,* resistance due to SEI layer formation), $10^{-2} < \tau < 10^{-1}$ s represents the charge transfer resistance, and $\tau \geq 10^{-1}$ s corresponds to the active ion diffusion process in the bulk electrode. **Figure 6.14 (*c*), 6.14 (*d*),** and **6.14 (*e*)** represent the DRT results for $Na_4Mn_{7.2}Cr_{1.8}O_{18}$ cathode before CV, after CV, and after stability testing, respectively, obtained by pyDRTtools [62]. The DRT before CV (**Figure 6.14 (*c*)**) possessesd five distinct DRT peaks (P_1-P_5). The DRT peaks P_1 and P_2 belong to the high-frequency domain and represent the electronic transport processes at the current collector-electrode interface and the particle-particle bulk electrode. The DRT Peak P_3 at the mid-frequency range corresponds to the SEI layer properties. The peak P_4 represents the charge transfer reaction at the electrode/electrolyte interface. The peak P_5 at the low-frequency domain corresponds to the solid-state diffusion processes [56,62].

After the CV analysis, the DRT profile **(Figure 6.14 (*d*)**) changed significantly with the appearance of peaks P_6-P_{10}. Notably, peaks P_6-P_8 shifted towards a higher time constant with a significant increase in intensity compared to their corresponding DRT peaks before CV. This could be attributed to electrode activation during the CV analysis, creating additional active sites for Na^+ ion intercalation. The DRT peaks P_{11}-P_{15} after stability **(Figure 6.14 (*e*)**) demonstrated higher impedance contributions with highly intense peaks at P_{13}-P_{15}. This increase was attributed to the formation of SEI, charge transfer resistance, and the resistance of the solid-state diffusion process due to electrolyte decomposition. This indicated the formation of additional resistive components during the long charging/discharging, resulting in irreversible structural changes or resistive SEI films.

Figures 6.14 (*f*), 6.14 (*g*), and **6.14 (*h*)** represent the DRT results with MAP analysis for before CV, after CV, and after stability, respectively. The MAP analysis revealed the mean values and confidence bounds for

each DRT peak and provided statistical reliability by estimating the uncertainty in the deconvoluted peaks [63]. The confidence bounds (represented by light grey shading) showed the reliability of the DRT peak through relaxation time distributions and the corresponding physical process of the electrode. The MAP analysis before CV (**Figure 6.14 (*f*)**) and after CV (**Figure 6.14 (*g*)**) revealed the occurrence of five distinct processes having relatively narrow confidence bounds, representing high reliability. The MAP profile after stability analysis (**Figure 6.14 (*h*)**) exhibited relatively broader confidence bounds, particularly in the mid and low-frequency domains, representing the increased uncertainty in the identification of physical processes at these time constants after a prolonged cycling process.

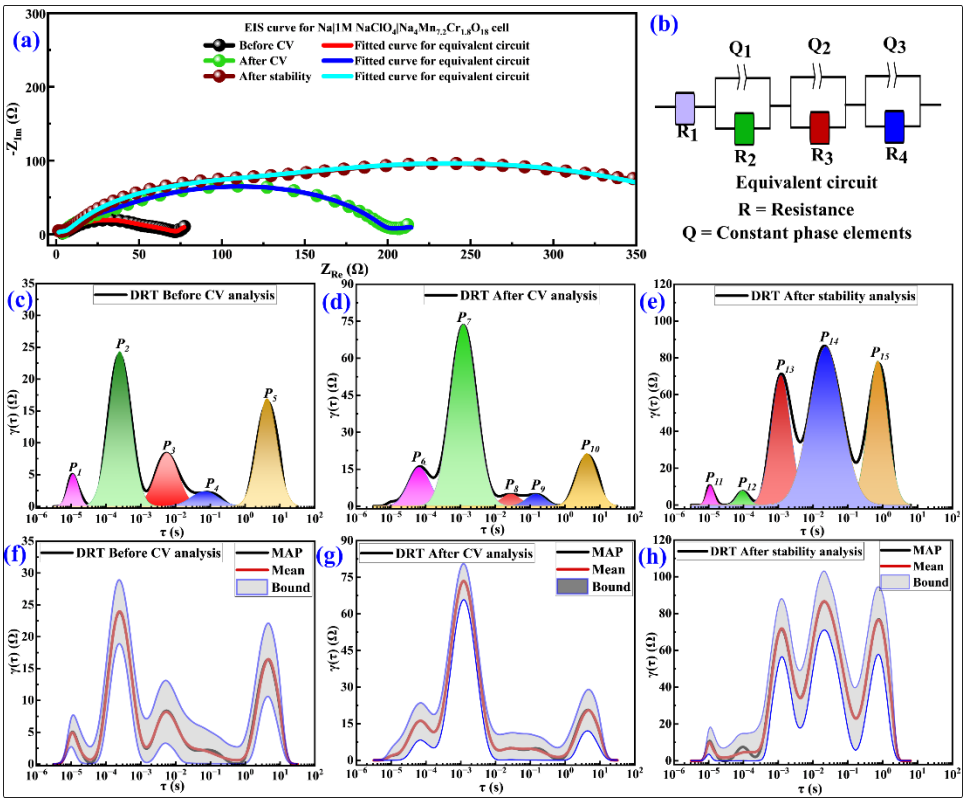

Figure 6.14 (a) Nyquist plots of $Na_4Mn_{7.2}Cr_{1.8}O_{18}$ before CV, after CV, and after stability; (b) Equivalent circuit; DRT spectra of $Na_4Mn_{7.2}Cr_{1.8}O_{18}$ (c) before CV, (d) after CV, and (e) after stability; MAP spectra of $Na_4Mn_{7.2}Cr_{1.8}O_{18}$ (f) before CV, (g) after CV, and (h) after stability

6.9 JT Distortion Mitigation via Cr-Doping in $Na_4Mn_{7.2}Cr_{1.8}O_{18}$

The mechanism by which Cr doping mitigates JT distortion in $Na_4Mn_{7.2}Cr_{1.2}O_{18}$ involves a sophisticated interplay of electronic configuration modification and structural stabilization. The mitigation of the JT is fundamentally attributed to the substitution of JT active Mn^{3+} ions (containing high-spin d^4 electrons in $t_{2g}^3\ e_g^1$ configuration) by JT inactive Cr^{3+} ions (having d^3 electrons in $t_{2g}^3\ e_g^0$ configuration). The Mn^{3+} centered MnO_6 octahedra units exhibit spontaneous asymmetric distortions (elongation in the z-axis) due to asymmetric occupation of degenerate high-energy e_g orbitals (dz^2 and dx^2-dy^2), resulting in the lattice strain as shown in **Figure 6.15 (a)** [64]. The Cr^{3+} substitution in the place of Mn^{3+} introduces electronically symmetric octahedra, as its d^3 electronic configuration is fully occupied by the lower energetic half-filled t_2g orbitals and avoids occupation of the high-energy e_g orbitals [65]. This electronic stabilization eliminates the axial distortion, which mitigates the JT effect, as shown in **Figure 6.15 (a)**. Again, Cr^{3+} has an ionic radius of 0.615 Å, which is compatible and smaller than that of Mn^{3+} (with an ionic radius of 0.645 Å). This reduces the bond-length mismatching and suppresses the structural distortion by inducing a local lattice contraction. **Figure 6.15 (a)** visually demonstrates this effect through the transition from an elongated to a more regular octahedron upon Cr substitution. The resulting symmetric bond length-based regular CrO_6 octahedral in $Na_4Mn_{7.2}Cr_{1.8}O_{18}$ not only reduces local strain but also enhances its structural stability.

Figure 6.15 (b) represents the ligand field orbital degeneracy diagrams. Cr^{3+} with its stable electron configuration, does not cause orbital degeneracy as Mn^{3+} does. This helps to maintain a more symmetrical octahedral structure and prevents the elongation-related destabilization of the dx^2-y^2 and dz^2 orbitals, which is common in MnO_6 octahedral units. The synergistic effect of these mechanisms resulted in significantly improved structural stability, enhanced capacity retention, and superior electrochemical performance of the $Na_4Mn_{7.2}Cr_{1.2}O_{18}$ cathode.

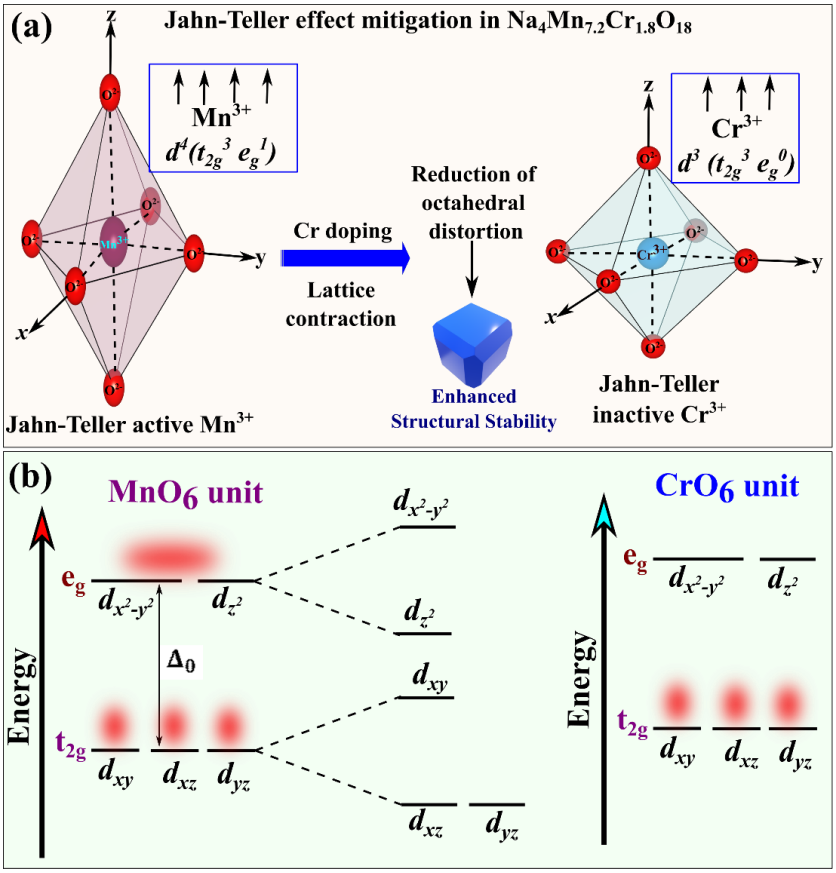

Figure 6.15 (a) Octahedral elongation in MnO_6 unit due to JT effect and mitigation of JT effect due to Cr-doping; **(b)** Pictorial representation of orbital degeneracy in MnO_6 and CrO_6 units.

6.10 Conclusions for $Na_4Mn_{7.2}Cr_{1.8}O_{18}$ Cathode

The partial incorporation of the Cr dopant at the Mn^{3+} site reduced the JT effect, resulting in a stable phase formation of the material with a zigzag-like tunnel structure for efficient Na^+ ion diffusion. Thorough physicochemical analyses, including TGA, DTG, XRD, FESEM, EDS, ICP-OES, Raman, TEM, SAED, HRTEM, and XPS, confirmed the phase purity, uniform rod-like morphology, appropriate stoichiometry, and needed bonding environment of $Na_4Mn_{7.2}Cr_{1.8}O_{18}$. It exhibited a notable discharge-specific capacity of ~74 mAh/g at 0.05C within a 2.0-4.0 V voltage vs. Na/Na^+. It also showed excellent rate capability and cycling stability, retaining about 76% of its initial discharge capacity even after 200

cycles at 0.3C. EIS and CV studies demonstrated that the partial Cr-doping enhanced structural stability, redox behavior, and average discharge potential and reduced resistance toward the cell. It also increased the Na^+ ion diffusion coefficient. CV analyses indicated the pseudocapacitive energy storage characteristics. $Na_4Mn_{7.2}Cr_{1.8}O_{18}$ exhibited a diffusive and capacitive contribution of 58% and 42%, respectively. The consistent coulombic efficiency, along with the low values of resistances, underscored the robust Na^+ ion migration and electrochemical stability of $Na_4Mn_{7.2}Cr_{1.8}O_{18}$. In this study, we have investigated a single doping level of 20% of Mn with Cr. This choice was inspired by previous studies [66]. However, a thorough analysis of a range of Cr doping levels is necessary to determine the optimal substitution amount.

6.11 References

[1] A. Kanwade, S. Gupta, A. Kankane, M.K. Tiwari, A. Srivastava, J.A. Kumar Satrughna, S. Chand Yadav, P.M. Shirage, Transition metal oxides as a cathode for indispensable Na-ion batteries, RSC Adv. 12 (2022) 23284–23310. https://doi.org/10.1039/d2ra03601k.

[2] P.F. Wang, Y. You, Y.X. Yin, Y.S. Wang, L.J. Wan, L. Gu, Y.G. Guo, Suppressing the P2–O2 Phase Transition of Na0.67Mn0.67Ni0.33O2by Magnesium Substitution for Improved Sodium-Ion Batteries, Angew.Chem. Int. Ed. 55 (2016) 7445–7449. https://doi.org/10.1002/anie.201602202.

[3] A.S. Shaikh, S.C. Yadav, A. Srivastava, A.R. Kanwade, M.K. Tiwari, S.M. Rajore, J.A.K. Satrughna, M. Dhonde, P.M. Shirage, Dynamic synergy of tin in the electron-transfer layer and absorber layer for advancing perovskite solar cells: a comprehensive review, Energy Adv. 3 (2024) 1505–1552. https://doi.org/10.1039/d4ya00204k.

[4] C. Delmas, C. Fouassier, P. Hangenmuller, STRUCTURAL CLASSIFICATION AND PROPERTIES OF THE LAYERED OXIDES, Physica. 99B (1980) 81–85. http://www.pubmedcentral.nih.gov/articlerender.fcgi?artid=2854659&tool=pmcentrez&rendertype=abstract%0Ahttp://www.pubmedcentral.nih.gov/articlerender.fcgi?artid=3100238&tool=pmcentrez&rendertype=abstract%0Ahttp://www.ncbi.nlm.nih.gov/pubmed/8423474.

[5] K. Kubota, I. Ikeuchi, T. Nakayama, C. Takei, N. Yabuuchi, H. Shiiba, M. Nakayama, S. Komaba, New Insight into Structural Evolution in Layered NaCrO2 during Electrochemical Sodium Extraction, J. Phys. Chem. C. 119 (2015) 166–175. https://doi.org/10.1021/jp5105888.

[6] S. Komaba, T. Nakayama, A. Ogata, T. Shimizu, C. Takei, S. Takada, A. Hokura, I. Nakai, Electrochemically Reversible Sodium Intercalation of Layered NaNi0.5Mn0.5O2 and NaCrO2, ECS Trans. 16 (2009) 43–55. https://doi.org/10.1149/1.3112727.

[7] X. Xia, J.R. Dahn, NaCrO2 is a Fundamentally Safe Positive Electrode Material for Sodium-Ion Batteries with Liquid Electrolytes, Electrochem. Solid-State Lett. 15 (2012) A1–A4. https://doi.org/10.1149/2.002201esl.

[8] J. Wu, G. Hu, K. Dua, Z. Peng, M. Huang, J. Fan, Y. Gong, D. Guan, Y. Shi, R. Liu, Y. Cao, Inhibiting electrochemical phase transition of NaCrO2 with long-cycle stability by surface fluorination treatment, Electrochim. Acta. 403 (2022) 139641.

[9] J. Wei, L. Shaw, W. Chen, First-principles comparative study of Cr migration in O3 and O/P hybrid-phased NaCrO2, Phys. Rev. Mater. 6 (2022) 095403. https://doi.org/10.1103/PhysRevMaterials.6.095403.

[10] I. Lee, G. Oh, S. Lee, T.Y. Yu, M.H. Alfaruqi, V. Mathew, B. Sambandam, Y.K. Sun, J.Y. Hwang, J. Kim, Cationic and transition metal co-substitution strategy of O3-type NaCrO2 cathode for high-energy sodium-ion batteries, Energy Storage Mater. 41 (2021) 183–195. https://doi.org/10.1016/j.ensm.2021.05.046.

[11] J. Liang, L. Liu, X. Liu, X. Meng, L. Zeng, J. Liu, J. Li, Z. Shi, O3-Type NaCrO2 as a Superior Cathode Material for Sodium/Potassium-Ion Batteries Ensured by High Structural Reversibility, ACS Appl. Mater. Interfaces. 13 (2021) 22635−22645. https://doi.org/10.1021/acsami.1c04997.

[12] L. Liang, X. Sun, D.K. Denis, J. Zhang, L. Hou, Y. Liu, C. Yuan, Ultralong Layered NaCrO2 Nanowires: A Competitive Wide-Temperature-Operating Cathode for Extraordinary High-Rate Sodium-Ion Batteries, ACS Appl. Mater. Interfaces. 11 (2019) 4037−4046. https://doi.org/10.1021/acsami.8b20149.

[13] C.Y. Yu, J.S. Park, H.G. Jung, K.Y. Chung, D. Aurbach, Y.K. Sun, S.T. Myung, NaCrO2 cathode for high-rate sodium-ion batteries, Energy Environ. Sci. 8 (2015) 2019–2026. https://doi.org/10.1039/c5ee00695c.

[14] C.L. Jakobsen, M. Brighi, B.P. Andersen, G. Ducrest, R. Černý, D.B. Ravnsbæk, Expanded solid-solution behavior and charge-discharge asymmetry in NaxCrO2 Na-ion battery electrodes, J. Power Sources. 535 (2022) 231317. https://doi.org/10.1016/j.jpowsour.2022.231317.

[15] A.R. Kanwade, A.K.S. Jena, S.M. Rajore, S.S. Mali, J. V Patil, C.K. Hong, P.M. Shirage, Revealing the potential of graphene-embedded Na3Fe2(PO4)3 for enhanced sodium-ion battery performance, J. Mater. Sci. Energy. 59 (2024) 8956–8972. https://doi.org/10.1007/s10853-024-09698-y.

[16] Y. Lou, X. Rao, J. Zhao, J. Chen, B. Li, L. Kuang, Q. Wang, S. Zhong, H. Wang, L. Wu, Graphite-like structure of disordered polynaphthalene hard carbon anode derived from the carbonization of perylene-3,4,9,10-tetracarboxylic dianhydride for fast-charging lithium-ion batteries, New J. Chem. 45 (2021) 16658–16669. https://doi.org/10.1039/d1nj02986j.

[17] S. Kiani, H. Gharibi, S. Javadian, M. Zhiani, H. Kashani, The effect of the SEI layer on the electrochemical impedance in the graphite/Li[Ni0.5Mn0.3Co0.2]O2 lithium-ion full cells, Appl. Surf. Sci. 633 (2023) 157638. https://doi.org/10.1016/j.apsusc.2023.157638.

[18] L. Zeng, F. Li, X. Xu, Z. Liu, J. fShen, D. Zhang, Y. Li, J. Liu, A Scalable Approach to Na2FeP2O7@Carbon/Expanded Graphite as a Low-Cost and High-Performance Cathode for Sodium-Ion Batteries, ChemElectroChem. 7 (2020) 3874–3882. https://doi.org/10.1002/celc.202001087.

[19] P. Thomas, J. Ghanbaja, D. Billaud, Electrochemical insertion of sodium in pitch-based carbon fibres in comparison with graphite in NaClO4-ethylene carbonate electrolyte, Electrochim. Acta. 45 (1999) 423–430. https://doi.org/10.1016/S0013-4686(99)00276-5.

[20] H. Van Nguyen, M. Le Nguyen, P.H. Tran, M. Van Tran, P.M.L. Le, Investigatiing the performance of full-cell using NaFe0.45Cu0.05Co0.5O2 cathode and hard carbon anode, Vietnam J. Sci. Technol. 60 (2022) 203–215.

[21] I.Y. Jeon, M.J. Ju, J. Xu, H.J. Choi, J.M. Seo, M.J. Kim, I.T. Choi, H.M. Kim, J.C. Kim, J.J. Lee, H.K. Liu, H.K. Kim, S. Dou, L. Dai, J.B. Baek, Edge-fluorinated graphene nanoplatelets as high performance electrodes for dye-sensitized solar cells and lithium ion batteries, Advanced Functional Materials. 25 (2015) 1170–1179. https://doi.org/10.1002/adfm.201403836.

[22] J. Jo, S. Lee, J. Gim, J. Song, S. Kim, V. Mathew, M.H. Alfaruqi, S. Kim, J. Lim, J. Kim, Facile synthesis of reduced graphene oxide by modified Hummer's method as anode material for Li-, Na- And K-ion secondary batteries, R. Soc. Open Sci. 6 (2019) 181978. https://doi.org/10.1098/rsos.181978.

[23] X. Gui, G. Hao, Weifeng, A comprehensive review of Cr, Ti-based anode materials for Li-ion batteries, Ionics. 26 (2019) 1081–1099. https://api.semanticscholar.org/CorpusID:209441427.

[24] X. Zhao, Q.-C. Zhuang, S.-D. Xu, Y.-X. Xu, Y.-L. Shi, X.-X. Zhang, Investigation of Cr2O3 as Anode Materials for Lithium-Ion Batteries by Electrochemical Impedance Spectroscopy, J. Electrochem. Soc. 162 (2015) A1156–A1162. https://doi.org/10.1149/2.0161507jes.

[25] G. Ali, M. Akbar, K.Y. Chung, Electrochemical investigations of a high-capacity Na2CrO4/C nanocomposite anode for sodium-ion batteries, Int. J. Energy Res. 46 (2022) 1803–1812. https://doi.org/DOI: 10.1002/er.7295.

[26] M.K. Tiwari, S. Chand Yadav, A. Kanwade, J.A. Kumar Satrughna, S.M. Rajore, P.M. Shirage, Advancements in lanthanide-based perovskite oxide semiconductors for gas sensing applications: a focus on doping effects and development, Anal. Methods. 15 (2023) 5754–5787. https://doi.org/10.1039/d3ay01420g.

[27] J.A.K. Satrughna, A.R. Kanwade, S.M. Rajore, M. Kumar, Y. Ito, A. Ogura, H. Lee, Y. Ohshita, P.M. Shirage, Sol-gel-based synthesis of high-capacity-NaCoO2 cathode for advanced sodium-ion batteries, Electrochim. Acta. 507 (2024) 145201. https://doi.org/10.1016/j.electacta.2024.145201.

[28] M.M. Faras, S.S. Patil, P.S. Patil, A.P. Torane, Unleashing the Potential of Binder-Free Hydrothermally Synthesized Marigold-Like ZnCo2O4 for Supercapacitors, J. Energy Storage. 74 (2023) 109490. https://doi.org/10.1016/j.est.2023.109490.

[29] A. Alomary, S. Belhadj, S. Obeidat, I. Al-momani, A. Attiyat, A comparison of SEM-EDS with ICP-OES for the Quantitative Elemental Determination of Algerian Mediterranean Sea Sediments, Jordan J. Chem. 7 (2012) 383–391. https://jjc.yu.edu.jo/index.php/jjc/article/view/199.

[30] I. Michalak, K. Chojnacka, K. Marycz, Using ICP-OES and SEM-EDX in biosorption studies, Microchim Acta. 172 (2011) 65–74. https://doi.org/10.1007/s00604-010-0468-0.

[31] J.D. Henderson, F.P. Filice, M.S.M. Li, Z. Ding, Tracking Live-Cell Response to Hexavalent Chromium Toxicity by using Scanning

Electrochemical Microscopy, ChemElectroChem. 4 (2017) 856–863. https://doi.org/10.1002/celc.201600783.

[32] M. Ahangari, M. Zhou, H. Luo, Review of Layered Transition Metal Oxide Materials for Cathodes in Sodium-Ion Batteries, Micromachines. 16 (2025) 137. https://doi.org/10.3390/mi16020137.

[33] A.C. Lazanas, M.I. Prodromidis, Electrochemical Impedance Spectroscopy-A Tutorial, ACS Meas. Sci. Au. 3 (2023) 162−193. https://doi.org/10.1021/acsmeasuresciau.2c00070.

[34] A.T. Ta, V.N. Nguyen, T.T.O. Nguyen, H.C. Le, D.T. Le, T.C. Dang, M.T. Man, S.H. Nguyen, D.L. Pham, Hydrothermal synthesis of Na4Mn9O18 nanowires for sodium ion batteries, Ceram. Int. 45 (2019) 17023–17028. https://doi.org/10.1016/j.ceramint.2019.05.252.

[35] N. Sheng, C. gong Han, Y. Lei, C. Zhu, Controlled synthesis of Na0.44MnO2 cathode material for sodium ion batteries with superior performance through urea-based solution combustion synthesis, Electrochim. Acta Acta. 283 (2018) 1560–1567. https://doi.org/10.1016/j.electacta.2018.07.120.

[36] E. Oz, S. Altin, S. Avci, Investigation of physical and electrochemical properties of Ni-doped Tunnel/P2 hybrid Na0.44MnO2 cathode material for sodium-ion batteries, J. Solid State Chem. 318 (2023) 123741. https://doi.org/10.1016/j.jssc.2022.123741.

[37] Z. Shan, Y. He, T. Tan, Y. Zhang, X. Wang, Preparation of Na4Mn9O18/carbon nanotube/reduced graphene oxide by spray drying as cathode materials for sodium ion batteries, Solid State Sci. 94 (2019) 77–84. https://doi.org/10.1016/j.solidstatesciences.2019.05.019.

[38] G. Yuan, J. Xiang, H. Jin, Y. Jin, L. Wu, Y. Zhang, A. Mentbayeva, Z. Bakenov, Flexible free-standing Na4Mn9O18/reduced graphene oxide composite film as a cathode for sodium rechargeable hybrid aqueous battery, Electrochim. Acta. 259 (2018) 647–654. https://doi.org/10.1016/j.electacta.2017.11.015.

[39] A.D. Tevar, J.F. Whitacre, Relating Synthesis Conditions and Electrochemical Performance for the Sodium Intercalation Compound Na4Mn9O18 in Aqueous Electrolyte, J. Electrochem. Soc. 157 (2010) A870–A875. https://doi.org/10.1149/1.3428667.

[40] Y. Zhang, L. Liu, S. Jamil, J. Xie, W. Liu, J. Xia, S. Nie, X. Wang, Al2O3 coated Na0.44MnO2 as high-voltage cathode for sodium ion

batteries, Appl. Surf. Sci. 494 (2019) 1156–1165. https://doi.org/10.1016/j.apsusc.2019.07.247.

[41] K. Dai, J. Mao, X. Song, V. Battaglia, G. Liu, Na0.44MnO2 with very fast sodium diffusion and stable cycling synthesized via polyvinylpyrrolidone-combustion method, J. Power Sources. 285 (2015) 161–168. https://doi.org/10.1016/j.jpowsour.2015.03.087.

[42] M. Shishkin, S. Kumakura, S. Sato, K. Kubota, S. Komaba, H. Sato, Unraveling the Role of Doping in Selective Stabilization of NaMnO2 Polymorphs : Combined Theoretical and Experimental Study, Chem. Mater. 30 (2018) 1257–1264. https://doi.org/10.1021/acs.chemmater.7b04394.

[43] J. Lee, S. Park, Y. Park, J. Song, B. Sambandam, V. Mathew, J.Y. Hwang, J. Kim, Chromium doping into NASICON-structured Na3V2(PO4)3 cathode for high-power Na-ion batteries, Chem. Eng. J. 422 (2021) 130052. https://doi.org/10.1016/j.cej.2021.130052.

[44] J. Liu, Y. Zhuang, Y. Liu, X. Wang, Z. Gu, D. Chen, X.-L. Wu, Chromium-containing polyanionic cathode materials for sodium-ion batteries: progress, challenges and opportunities, Mater. Chem. Front. 9 (2025) 1486–1500. https://doi.org/10.1039/d5qm00068h.

[45] H.D. Luong, H. Momida, V.A. Dinh, T. Oguchi, Understanding doping effects on P2 NaxMn1−yMyO2 (M = Li, Mg, Al, Ti, V, Cr, Fe, Co, Ni) cathode materials for Na-ion batteries, Phys. Rev. Mater. 6 (2022) 015802. https://doi.org/10.1103/PhysRevMaterials.6.015802.

[46] J.F. Whitacre, A. Tevar, S. Sharma, Na4Mn9O18 as a positive electrode material for an aqueous electrolyte sodium-ion energy storage device, Electrochem. Commun. 12 (2010) 463–466. https://doi.org/10.1016/j.elecom.2010.01.020.

[47] M. Soleimanzade, M. Bahdanchyk, M. Hashempour, M. Bestetti, F.M. Cernuschi, A. Vicenzo, Charging processes of Na4Mn9O18 electrode in aqueous electrolyte, Electrochim. Acta. 426 (2022) 140791. https://doi.org/10.1016/j.electacta.2022.140791.

[48] V.R. Reddy Boddu, M. Palanisamy, L. Sinha, S.C. Yadav, V.G. Pol, P.M. Shirage, Hysteresis abated P2-type NaCoO2 cathode reveals highly reversible multiple phase transitions for high-rate sodium-ion batteries, Sustain. Energy Fuels. 5 (2021) 3219–3228. https://doi.org/10.1039/d1se00490e.

[49] Q. Chu, X. Wang, Q. Li, X. Liu, The tunnel manganese oxide Na4.32Mn9O18: A new Na+ site discovered by single-crystal X-ray diffraction, Acta Cryst. 67 (2011) i10–i12.

https://doi.org/10.1107/S0108270110052856.
[50] F. Yin, Z. Liu, Y. Zhao, Y. Feng, Y. Zhang, Electrochemical Properties of an Na4Mn9O18-Reduced Graphene Oxide Composite Synthesized via Spray Drying for an Aqueous Sodium-Ion Battery, Nanomaterials. 7 (2017) 253. https://doi.org/10.3390/nano7090253.
[51] J.A.K. Satrughna, A.R. Kanwade, S.M. Rajore, P.M. Shirage, Exploring the Characteristics of Na1.35CrO4 as Active Electrode for Energy Storage Application in Sodium-Ion Batteries, Phys. Status Solidi RRL. (2025) 2500079. https://doi.org/10.1002/pssr.202500079.
[52] Z. Shi, Z. Wang, L.L. Shaw, M. Ashuri, On the Electrochemical Properties of Carbon-Coated NaCrO2 for Na-Ion Batteries, Batteries. 9 (2023) 433. https://doi.org/10.3390/batteries9090433.
[53] G. Brugnetti, C. Triolo, A. Massaro, I. Ostroman, N. Pianta, C. Ferrara, D. Sheptyakov, A. Bel, M. Pavone, S. Santangelo, R. Ruffo, Structural Evolution of Air-Exposed Layered Oxide Cathodes for Sodium-Ion Batteries: An Example of Ni-doped NaxMnO2, Chem. Mater. 35 (2023) 8440−8454. https://doi.org/10.1021/acs.chemmater.3c01196.
[54] R.L. Carter, C.E. Bricker, The Raman spectra of crystalline Na2CrO4 and Na2CrO4·4H2O, Spectrochimica Acta Part A: Molecular Spectroscopy. 30 (1974) 1793–1800. https://doi.org/10.1016/0584-8539(74)80130-3.
[55] Y. Song, Y. Chen, Z. Wang, W. Zhao, C. Qin, H. Yu, X. Wang, Z. Bakenov, Y. Zhang, Defective ZnOx@porous carbon nanofiber network inducing dendrite-free zinc plating as zinc metal anode for high-performance aqueous rechargeable Zn/Na4Mn9O18 battery based on hybrid electrolyte, J. Power Sources. 518 (2022) 230761. https://doi.org/10.1016/j.jpowsour.2021.230761.
[56] J. Pati, R.S. Dhaka, Mixed polyanionic NaFe1.6V0.4(PO4)(SO4)2@CNT cathode for sodium-ion batteries: Electrochemical diffusion kinetics and distribution ofrelaxation time analysis at different temperatures, J. Power Sources. 609 (2024) 234646. https://doi.org/10.1016/j.jpowsour.2024.234646.
[57] J.A.K. Satrughna, A.R. Kanwade, S.M. Rajore, M.K. Tiwari, Y. Ito, A. Ogura, H. Lee, Y. Ohshita, S.S. Mali, J. V Patil, C.K. Hong, P.M. Shirage, Unveiling the physicochemical and electrochemical features of sodium deficient-Na0.8Fe(SO4)2 as cathode for sodium-ion batteries, Next Research. 2 (2025) 100210. https://doi.org/10.1016/j.nexres.2025.100210.

[58] J. Jiang, W. Li, H. Deng, G. Gong, N. Li, Research on Improving the Electrochemical Performance of LiMn2O4 via Cr-Doping, J. Nanosci. Nanotechnol. 19 (2019) 125–129. https://doi.org/10.1166/jnn.2019.16386.

[59] D.J. Kim, R. Ponraj, A.G. Kannan, H.-W. Lee, R. Fathi, R. Ruffo, C.M. Mari, D.K. Kim, Diffusion behavior of sodium ions in Na0.44MnO2 in aqueous and non-aqueous electrolytes, J. Power Sources. 244 (2013) 758–763. https://doi.org/10.1016/j.jpowsour.2013.02.090.

[60] F. Yin, Z. Liu, S. Yang, Z. Shan, Y. Zhao, Y. Feng, C. Zhang, Na4Mn9O18/Carbon Nanotube Composite as a High Electrochemical Performance Material for Aqueous Sodium-Ion Batteries, Nanoscale Res. Lett. 12 (2017) 569. https://doi.org/10.1186/s11671-017-2340-1.

[61] Z. Wang, C. Tang, Z. Wang, Q. Zhang, P. Lv, K. Yu, J. Zheng, W. Wei, High-Energy Na4MnCr(PO4)3@C Cathode for Solid-State Sodium Metal Batteries, Energy Mater. Adv. 4 (2023) 0036. https://doi.org/10.34133/energymatadv.0036.

[62] A. Maradesa, B. Py, T.H. Wan, M.B. Effat, F. Ciucci, Selecting the Regularization Parameter in the Distribution of Relaxation Times, J. Electrochem. Soc. 170 (2023) 030502. https://doi.org/10.1149/1945-7111/acbca4.

[63] M.B. Effat, F. Ciucci, Bayesian and Hierarchical Bayesian Based Regularization for Deconvolving the Distribution of Relaxation Times from Electrochemical Impedance Spectroscopy Data, Electrochim. Acta. 247 (2017) 1117–1129. https://doi.org/10.1016/j.electacta.2017.07.050.

[64] K. Zhang, D. Kim, Z. Hu, M. Park, G. Noh, Y. Yang, J. Zhang, V.W. Lau, S. Chou, M. Cho, S. Choi, Y. Kang, Manganese based layered oxides with modulated electronic and thermodynamic properties for sodium ion batteries, Nat. Commun. 10 (2019) 5203. https://doi.org/10.1038/s41467-018-07646-4.

[65] A.A. Spivakov, L. Huang, Y. Chen, C. Lin, Facile Synthesis of Chromium-Doped Fe1.1Mn1.9O4 Nanoparticles and the Effect of Cr Content on Their Magnetic and Structural Properties, Nanomaterials. 13 (2023) 2203. https://doi.org/10.3390/ nano13152203.

[66] Z. Jingyu, L. Xingyu, Z. Xiaolin, W. Youwei, S. Erhong, L. Jianjun, Rate and Cycling Performance of Ti and Cu Doped β-NaMnO2 as Cathode of Sodium-ion Battery, J. Inorg. Mater. 39 (2024) 1404–1412. https://doi.org/10.15541/jim20240204.

CHAPTER 7

Conclusions and Scope for Future Work

The primary focus of this thesis work was to engineer, synthesize, optimize, and characterize high-performance cathode materials for SIBs with a special focus on sodiated layered/tunnel-structured TM oxides and polyanionic materials. By adopting the techniques of sol-gel and solid-state synthetic approaches, a wide range of layered, tunnel-type TM oxides and polyanionic cathode materials, including $NaCoO_2$, $Na_{0.8}Fe(SO_4)_2$, $Na_xCo_{0.5}Fe_{0.25}Mn_{0.25}O_2$, $Na_{1.35}CrO_4$, *and* $Na_4Mn_{7.2}Cr_{1.8}O_{18}$, *have been synthesized and thoroughly evaluated for SIBs. Focus was given on understanding the role of synthesis conditions, structure, compositional tuning, reducing Co content, and TM substitution in influencing the electrochemical properties, rate performance, energy density, and long-term cycling stability. The cathode materials exhibited encouraging properties such as high specific capacity, energy density, and excellent capacity retention, thus justifying their potential for real-world SIB applications. Special emphasis was given to understanding the correlations between physicochemical and electrochemical properties, allowing valuable insights into the structure-performance relationships. Hence, the outcomes of this thesis not only broaden the potential cathodes for SIBs but also contribute towards the basic understanding of principles of material design for future ESS.*

7.1 Brief Summary and Outcomes of the Thesis

Chapter 1 provided a comprehensive introduction to rechargeable battery technologies with a specific focus on SIBs as a potential substitute for the current LIBs for large-scale storage applications. The chapter discussed the fundamentals, history, working principles, components, and benefits of SIBs with a specific focus on the essential role of cathode materials in determining the battery performance. A detailed review of literature was presented on the different types of cathode materials, with special focus on layered oxides, tunnel-structured oxides, and polyanionic frameworks, discussing their structural properties, redox chemistry, and electrochemical features. The chapter concludes with the determination of the important research gaps and establishment of the objectives and scope of this thesis work that focuses on rational design and optimization of next-generation cathode materials for high-performance SIBs.

Chapter 2 briefly explained the experimental methods and sophisticated characterization techniques used in the synthesis and characterization of the cathode materials. Cathode materials such as $NaCoO_2$, $Na_{0.8}Fe(SO_4)_2$, $Na_xCo_{0.5}Fe_{0.25}Mn_{0.25}O_2$, $Na_{1.35}CrO_4$, and $Na_4Mn_{7.2}Cr_{1.8}O_{18}$ were prepared through sol-gel and solid-state methods under optimum conditions. A variety of physicochemical and electrochemical characterization techniques used to study the structural, morphological, and electrochemical attributes through XRD, SEM/TEM/HRTEM, EDS, ICP-OES, Raman spectroscopy, FTIR, XPS, TGA/DTG/DSC, CV, GCD, EIS, and DRT are discussed in detail to access a comprehensive insights into the sodium storage behaviour, redox activity, charge transport processes, and diffusion kinetics of the cathode materials.

Chapter 3 reported on $Na_{0.8}Fe(SO_4)_2$, a sodium-deficient 3D polyanionic material that was prepared through a citric acid-mediated sol-gel process. The material demonstrated a sturdy framework for improved Na^+ ion

kinetics, moderate specific capacity (~41 mAh/g), high voltage window, excellent Na^+-ion diffusion, and stable cyclic performance with up to 98% retention after 45 cycles. The 20% sodium vacancy was observed to enhance the Na^+-ion diffusion and rate performance, making it a cost-effective and environmentally friendly material for SIBs.

In **Chapter 4**, phase-pure $NaCoO_2$ was synthesized through a citric-acid-assisted sol-gel process by improving the calcination temperature. Various sophisticated structural characterization verified its high crystalline hexagonal symmetry (space group $P6_3/mmc$), and electrochemical analyses demonstrated high initial discharge capacity of ~156 mAh/g at 0.1C, consistency in capacity retention, superior rate capability, and an impressive energy density of 466 Wh/kg due to the improvement in the calcination temperature during the material synthesis. The material exhibited multiple redox transitions with the Co^{3+}/Co^{4+} couple and superior structural stability, which emphasized its possibility for lightweight and compact SIB applications.

In **Chapter 5**, $Na_xCo_{0.5}Fe_{0.25}Mn_{0.25}O_2$, as a multi-TM co-substituted layered oxide, was synthesized via solid-state reaction to reduce the Co content and understand the synergistic effect of multiple TM co-substitution. The physicochemical characterizations revealed its *P*3-type layered structure with superb crystallinity and structural reversibility. The cathode material for SIBs exhibited a high initial capacity of ~94 mAh/g at 0.05C, and superior cycle life by retaining ~92% of its capacity after 100 cycles and ~28% after 500 cycles, respectively, due to the synergistic redox activity of Co, Fe, and Mn. The synergistic effect of multiple TM co-substitution significantly reduced the irreversible phase transition and enhanced the cycling life performance during long-term cycling.

Chapter 6 represented the complete removal of Co with either Cr or the combination of Cr and Mn. Part A reported the synthesis of nanoparticle-structured $Na_{1.35}CrO_4$ with orthorhombic crystal structure. The study shows that the particle nano-structuring approach in $Na1_{.35}CrO_4$ materials makes it a suitable electrode for SIBs by demonstrating an V_{OC} of ~1.842 V and multiple redox peaks in 0-3 V for SIBs. $Na_{1.35}CrO_4$ material coexists with the Cr^{6+} and Cr^{7+} states and demonstrates good conductivity suitable for battery applications. Part B of Chapter 6 reported the successful incorporation of Cr doping in the tunnel-structured $Na_4Mn_{7.2}Cr_{1.8}O_{18}$ synthesized through a high-temperature solid-state method. Partial replacement of Mn^{3+} by Cr^{3+} significantly suppressed the Jahn-Teller distortions of Mn^{3+}, stabilized the tunnel structure, and enhanced the Na^+-ion diffusion kinetics. $Na_4Mn_{7.2}Cr_{1.8}O_{18,}$ as a potential cathode material for SIBs, exhibited a specific charge/discharge capacity of ~105/74 mAh/g at 0.05C and ~76% capacity retention at the 200^{th} cycle. EIS and DRT analyses confirmed its low charge-transfer resistance and superior interfacial stability, making it suitable for sustainable and long-life SIBs.

In summary, this thesis work can effectively demonstrate the engineering, synthesis, and optimization of the performance of several structurally different cathode materials for SIBs. The outcomes indicate how the material engineering techniques, such as improvement in the calcination temperature, stoichiometric tuning, multivalent replacement, framework stabilization, nano-structuring, and control over the phases of the cathode material, can effectively improve the sodium storage and electrochemical performance. The outcomes of the thesis provide useful information on structure-property relationships and open the pathway for future work on the development of low-cost, high-capacity, and long-cycle-life cathode materials for SIBs. These outcomes contribute to the development of secure, sustainable, and scalable SIB technologies as the next generation of future energy storage solutions, mainly in the integration of renewable energy, grid storage, and electric mobility.

7.1.1 Comparative Benchmarking of Cathode Materials

To further emphasize the importance of this work, the electrochemical performance of the as-synthesized cathode materials has been compared against other comparative representative sodium-ion battery cathode materials given in the literature. The comparative results are compiled in **Table 7.1.**

Table 7.1: Comparison of electrochemical performance of as-synthesized cathodes with some reported cathode materials for SIBs.

Materials	Max. Specific Capacity (mAh/g)	Voltage Range (V)	Capacity Retention (%@cycle@C)	Ref.
$NaFe(SO_4)_2$	63@0.1C	2.0-4.25	-	Ch.3
$NaFe(SO_4)_2$	78@0.1C	1.5-4.5	-	
$NaFe(SO_4)_{1.5}(SeO_4)_{0.5}$	45@0.1C	2.0-4.25	~50@5@0.1C	
$NaFe(SO_4)_{1.5}(PO_3F)_{0.5}$	39@0.1C	2.0-4.25	~70@30@0.1C	
$NaFe(SO_4)_{1.5}(HPO_4)_{0.5}$	39@0.1C	2.0-4.25	-10@30@0.1C	
$Na_{0.8}Fe(SO_4)_2$	41.17@0.2C	1.5-4.5	~70@45@0.1C ~98@45@1C	This work
P2-Na_xCoO_2	116.7@0.4C	2.0-3.8	-	Ch.4
$NaCoO_2$	89@0.1C	0.0-1.0	-	
P2-$NaCoO_2$	99@0.1C	2.0-4.0	-	
Na_xCoO_2	161@0.1C@ cycle 129@0.1C@4 cycle	2.0-4.2	-	
$Na_{0.71}CoO_2$	120@0.02C	2.0-3.9V	-	
$Na_{0.74}CoO_2$	110.2@0.05C	2.0-3.8	-	
Na_xCoO_2	126@0.1C	2.0-4.2	-	
P2-$Na_{0.7}CoO_2$	125@ 0.04C	2.0-3.8	-	
P2-$Na_{0.7}CoO_2$	137.7@10 mA/g	2.0-3.8	-	
$Na_{0.57}CoO_2$	57@0.7C	0.0-1.8	-	
$NaCoO_2$	156@0.1C@1 cycle 153@0.1C@5 cycle	2.0-4.0	-	This work
O3-$NaFeO_2$	~91 @ 30 mA/g	2.0-3.8	~52@11 cycles	Ch.5
$NaFeO_2$	~80 @ 0.05C	2.0-3.8	25@50 cycle	
$NaFeO_2$	~85 @ 0.2 mA/cm^2	1.5-3.6	-	
O3-$NaFeO_2$	~123 @ 80mA/g	2.0-4.0	53@20 cycle	
α-$NaMnO_2$	~146 @ 0.2C	1.7-4.0	73@20 cycle	
β-$NaMnO_2$	~144.3 @ 1C	2.0-4.0	41@35 cycle	
$Na_{0.7}MnO_2$	~101 @ 0.1C	2.0-3.8	59 @50 cycle	
$Na_{0.67}Mn_{0.64}Al_{0.06}Co_{0.30}O_2$	114.1@1000 mA/g	1.5-4.0	81@200 cycle	
$NaMn_{0.33}Fe_{0.33}Ni_{0.33}O_2$@$TiO_2$	~160 @ 0.1C	1.5-4.2	38.6@500 cycle	
$Na_{0.67}Ni_{0.2}Co_{0.2}Mn_{0.6}O_2$	132.2 @ 0.2C	1.5-4.2	83@200 cycle	
$Na_xNi_{0.33}Co_{0.33}Mn_{0.33}O_2$	142.8 @ 0.1C	2.0-4.4	93@50 cycles	
$NaFe_{1/3}Co_{2/3}O_2$	199.6 @ 0.2C	1.5-4.4	83.06@50 cycle	
$NaFe_{1/2}Co_{1/2}O_2$	148.1 @ 0.2C	1.5-4.4	72.7@50 cycle	

$NaFe_{2/3}Co_{1/3}O_2$	111.2 @ 0.2C	1.5-4.4	55.3@50 cycle	
$NaTi_2(PO_4)_3/Na_{0.67}Co_{0.2}Mn_{0.8}O_2$	70.7 @ 20C	1.5-4.5	86.7@150 cycle	
$NaFeO_2$@C	89.6 @ 0.1C	2.0-3.4	87.3@100 cycle	
$Na_xCo_{0.5}Fe_{0.25}Mn_{0.25}O_2$	94.22 @ 0.05 C ~86 @ 0.1 C	2.0-4.2	92.2@100 cycle 78.4@200 cycle 54@300 cycle	This work
$Na_4Mn_9O_{18}$/RGO	83 mAh/g@0.1 A/g	[38]	68@160@0.2A/g	Ch.6
$Na_4Mn_9O_{18}$	~50 mAh/g@0.1C	[47]	-	
$Na_4Mn_9O_{18}$	73.8 mAh/g@4C	[55]	68.6@150@4C	
$Na_4Mn_9O_{18}$/CNT/RGO	96.2 mAh/g@4C	[37]	68.3@150@4C	
$Na_4Mn_9O_{18}$	45 mAh/g@0.125C	[46]	-	
$Na_4Mn_9O_{18}$ NRs	~90 mAh//g@0.2C	[34]	100@30@0.2C	
$Na_4Mn_9O_{18}$	~35 mAh/g@0.9C	[39]	93@50@0.9C	
$Na_4Mn_9O_{18}$/RGO	61.7 mAh/g@4C	[50]	95.5@150@4C	
$Na_4Mn_9O_{18}$	65 mAh/g@0.1C	[59]	-	
$Na_4Mn_9O_{18}$	62.5 mAh/g@4C	[60]	64.5@150@4C	
$Na_4Mn_{7.2}Cr_{1.8}O_{18}$	73.9 mAh/g@0.05C		88@100@2C 76@200@2C	This work

From **Table 7.1,** it can be seen that cathode materials synthesized in the present work exhibit good competitive specific capacity and excellent cycle life against various reported cathode systems. This benchmarking comparison enhances the significance of the current work and establishes its potential impact on the improvement of SIB technology.

7.2 Outlook and Future Prospects

The research in this thesis significantly contributes to the advancement of SIBs, especially toward the synthesis of structurally varied and electrochemically stable cathode materials. By following a methodical design, synthesis, physicochemical, and electrochemical investigations of various cathodes, the present research lays a solid foundation for future SIBs. The materials studied in this thesis work possessed desirable properties like good reversible capacity, high cycle stability, improved redox activity, rapid Na^+-ion diffusion, and minimal interfacial resistance, suitable for sustainable, economical, and safe battery technologies. Although significant advancements have been made, future work could be focused on further investigating the sophisticated material design methods, such as heterointerface engineering, surface passivation, lattice substitution, carbon-based coating, and defect modulation to reduce irreversible phase

transitions, prevent volume expansion, and stabilize the electrode-electrolyte interfaces. The logical engineering of multicomponent TM systems with improved redox synergies and pathways for charge compensation can enhance structural stability, electronic conductivity, and Na^+-ion kinetics. Furthermore, the half-cell-based assessment of the cathode material synthesized in this thesis work needs to be performed in a full cell configuration with the optimized anodes, such as HC, high-voltage, and heat-stable electrolytes for real-world applications. At the same time, priority needs to be given to scalability, cost-effectiveness, and eco-friendliness of the cathode synthesis. Further, the computational thermodynamic calculation can accelerate the advancement and optimization of new cathode materials by tracing intricate structure-property-performance correlations over a variety of thermodynamically stable cathode materials.